Connecting stellar feedback in the first galaxies and cosmic reionisation

Aniket Bhagwat

München 2024

Connecting stellar feedback in the first galaxies and cosmic reionisation

Aniket Bhagwat

Dissertation
an der Fakultät für Physik
der Ludwig–Maximilians–Universität
München

vorgelegt von
Aniket Bhagwat
aus Nashik, India

München, den 23.09.2024

Erstgutachter: Prof. Dr. Volker Springel
Zweitgutachter: Prof. Dr. Klaus Dolag
Tag der mündlichen Prüfung: 27.11.2024

Perfection is the antithesis of authenticity

Contents

List of Figures

List of Tables

Zusammenfassung

Feedback von Supernovae und die von Sternen emittierte Strahlung spielen eine entscheidende Rolle bei der Entstehung des frühen Universums. Diese Rückkopplungsprozesse haben einen direkten Einfluss auf Gas- und Sternendynamik und hinterlassen erkennbare Signaturen in Beobachtungsdaten. Zum ersten Mal sind wir dank der Beobachtungen mit dem `JWST` in der Lage, das Universum mit hohem Rotverschiebungswert statistisch und mit beispielloser Auflösung zu untersuchen. Verschiedene Modi der stellaren Rückkopplung müssen berücksichtigt werden, um die neuesten Beobachtungen von Galaxien aus der Epoche der Reionisation (EoR) zu erklären. Es ist daher entscheidend, dass theoretische Modelle die Auswirkungen von Parameterwahlen und Variationen in den Rückkopplungsmodellen auf die beobachtbaren Eigenschaften des frühen Univsersums modellieren.

Im ersten Teil der Arbeit präsentiere ich `SPICE`, eine neue Reihe von Strahlungshydrodynamik-Simulationen, die sich auf die Epoche der Reionisation konzentrieren. `SPICE` verwendet `RAMSES-RT`, um die Ausbreitung stellaren Lichts zu verfolgen, mit dem Ziel, das interstellare Medium (ISM) bis auf Skalen von ≈ 28pc aufzulösen. Das Ziel dieser Simulationen ist es, systematisch eine Vielzahl von stellaren Rückkopplungsmodellen zu untersuchen, darunter „bursty“ und „smooth“ Modi der Supernova-Energieinjektionen. `SPICE` zeigt, dass subtile Unterschiede im Verhalten der Supernova-Rückkopplung tiefgreifende Auswirkungen auf die Reionisationsgeschichte haben können, wobei „bursty“ Rückkopplungen eine frühere Reionisation bewirken. `SPICE` verdeutlicht, dass die stellare Rückkopplung und ihre Stärke den morphologischen Mix der Galaxien bis $z = 5$ bestimmen. Während sternbildende Scheiben bei „smooth“ Supernova-Rückkopplung vorherrschen, erzeugt „bursty“ Feedback Systeme, die von Dispersion dominiert werden. Ich zeige eine starke Korrelation zwischen der Galaxienmorphologie und dem Anteil der Lyman-Kontinuum-Photonen, die der Galaxie entfliehen können, wobei dispersionsgestütze Galaxien 20 bis 50-am Mal höhere Anteile zeigen als als ihre rotationsdominierten Gegenstücke. Dieses Kapitel betont den Einfluss von Parameterwahlen auf grundlegende Eigenschaften des Universums, wie Reionisationsgeschichte, Galaxienmorphologien und Kinematik.

Im zweiten Teil der Arbeit modelliere ich den Strahlungstransport von Lyα- und UV-Photonen durch das komplexe, mehrphasige ISM von `SPICE`-Galaxien. Ziel dieses Projekts ist es, den Einfluss von Strahlungstransporteffekten (z.B. räumlich ausgedehnte Emission, Lyα-UV räumliche Versätze) und beobachtungstechnische Systematiken (z.B. falsch platzierte Spalten) auf die gemessenen Lyα-Äquivalentbreitenverteilungen (EW_0) zu verstehen. Ich finde, dass räumliche Lyα-UV-Versätze unabhängig vom Rückkopplungsmodell existie-

ren und häufig vorkommen, mit Medianwerten von $\approx 0.07 - 0.11''$. Räumliche Lyα-UV-Versätze werden als Hauptursache für den Verlust von Fluss bei `JWST-MSA`-Beobachtungen identifiziert, wobei die medianen Pseudo-Spalt-Verluste $\approx 65\%$ betragen und in $\approx 30\%$ der Fälle zu Verlusten von über 95% des Flusses führen. Selbst ohne solche räumlichen Versätze kann das Vorhandensein ausgedehnter Emission zu medianen Pseudo-Spalt-Verlusten von 40% führen. Darüber hinaus können komplexe Galaxienmorphologien oder falsch platzierte `JWST-MSA`-Pseudo-Spalten zu einer Unterschätzung des UV-Kontinuums führen, was zu fälschlicherweise hohen Schätzungen von EW_0 durch `JWST` führt. Sowohl Strahlungstransporteffekte als auch Beobachtungssystematiken haben einen starken Einfluss auf die Beobachtungen von Lyα von Galaxien während der Epoche der Reionisation.

Im dritten Teil der Arbeit präsentiere ich ein neuartiges Subgrid-Modell zur Vorhersage von [C II]-Leuchtstärken von `SPICE`-Galaxien. Ich zeige, dass [C II] als hervorragender Indikator für Sternentstehungsraten bei Galaxien mit „smooth“ Rückkopplungsformen fungiert, während bursty Rückkopplung zu einer Unterdrückung von L_{CII} führt. Galaxien mit glatteren Rückkopplungsformen produzieren steil abfallende radiale Profile, während Galaxien mit bursty Rückkopplung relativ flachere Profile aufweisen. Darüber hinaus führen „smooth“ Rückkopplungen zu breiten [C II]-Linien mit $\mathrm{FWHM}_{\mathrm{broad}} > 600\mathrm{km/s}$, während bursty Rückkopplung schmale Linien mit $\mathrm{FWHM}_{\mathrm{broad}} \approx 200 - 300\mathrm{km/s}$ erzeugt. Durch die Trennung von Galaxienpopulationen in bulgelastige und bulgearme zeige ich, dass bulgelastige Galaxien bevorzugt zentral konzentrierte Flächenhelligkeit und breite [C II]-Linien aufweisen, während bulgearme Galaxien flache Flächenhelligkeit und schmale [C II]-Linien zeigen, was eine weitere mögliche Erklärung für beobachtete breite [C II]-Linien in frühen Galaxien liefert.

Die in dieser Arbeit vorgestellten Simulationen und die Multiwellenlängenstudien ermöglichen eine detaillierte Untersuchung der Auswirkungen stellaren Feedbacks auf verschiedene Komponenten einer Galaxie. Zum ersten Mal ermöglicht `SPICE` somit eine systematische Untersuchung der relativen Unterschiede den verschiedenen stellaren Rückkopplungsmodellen und erlaubt robuste Vorhersagen über Galaxienbeobachtungen in der Epoche der Reionisation.

Abstract

Feedback from supernovae and the radiation emitted by stars play a pivotal role in shaping the early Universe. These feedback processes have a direct influence on gas and stellar dynamics, leaving discernible traces in observational data. For the first time, with observations from `JWST`, we are able to observe the high-redshift Universe statistically and at unprecedented resolution. Different modes of stellar feedback need to be invoked to explain the latest observations of reionisation-era galaxies. Therefore, it is imperative for theoretical models to forward model the impact of parameter choices and variations in feedback prescriptions on observable properties of the high-redshift Universe.

In the first part of the thesis, I present `SPICE`, a novel suite of radiation-hydrodynamical simulations targeting the epoch of reionisation (EoR). `SPICE` uses `RAMSES-RT` to track the propagation of stellar radiation with a focus on resolving the interstellar medium (ISM) down to $\approx$ 28pc scales. The goal of these simulations is to systematically probe a variety of stellar feedback models, including "bursty" and "smooth" modes of supernova energy injections. SPICE shows that subtle difference in the behavior of supernova feedback can drive profound difference in reionisation histories with burstier forms of feedback causing earlier reionisation. `SPICE` highlights that stellar feedback and its strength determine the morphological mix of galaxies emerging by z=5. While star-forming disks are prevalent if supernova feedback is smooth, bursty feedback generates dispersion-dominated systems. I present a strong correlation between galaxy morphology and Lyman continuum escape fractions of galaxies where dispersion-supported galaxies show 20-50 times higher escape fractions as compared to their rotation dominated-counterparts. This chapter emphasises the impact of parameter choices on fundamental properties of the Universe such as reionisation histories, galaxy morphologies and kinematics.

In the second part of the thesis, I model radiative transfer of Lyα and UV photons through the complex multi-phase ISM of `SPICE` galaxies. The goal of this project is to understand the effect of radiative transfer effects (e.g. extended emission, Lyα-UV spatial offsets) and observational systematics (e.g misplaced slits) on the measured Lyα equivalent width (EW_0) distributions. I find that spatial Lyα-UV offsets exist independently of feedback model, and are common with median values of $\approx 0.07-0.11''$. Spatial Lyα-UV offsets are identified as the leading cause of loss of flux for `JWST-MSA` observations, with median pseudo-slit losses of $\approx$ 65% with $\approx$ 30% cases suffering from >95% pseudo-slit losses. Even in the absence of such spatial offsets, the presence of extended emission can cause median pseudo-slit losses of 40%. Additionally, complex galaxy morphologies or misplaced JWST-

MSA pseudo-slit can lead to understimated UV continuum, resulting in spuriously high estimates of EW_0 from `JWST`. Both radiative transfer effects and observational systematics strongly affect observations of Lyα emitters during the EoR.

In the third part of the thesis, I present a novel sub-grid model to predict [C II] luminosities from `SPICE` galaxies. I show that [C II] acts as an excellent tracer for star-formation rates for galaxies with smooth forms of feedback while bursty feedback leads to a suppression in $L_{\rm CII}$. Galaxies with smoother forms of feedback produce steeply declining radial profiles while galaxies with burstier forms of feedback exhibit relatively flatter profiles. Additionally, smooth feedback leads to broad [C II] lines with $\mathrm{FWHM_{broad}} > 600$km/s while bursty feedback produces narrow lines $\mathrm{FWHM_{broad}} \approx 200 - 300$km/s. Separating galaxy populations into bulge-heavy and bulge-less, I show that bulge-heavy galaxies preferentially show centrally heavy surface brightness maps and broad [C II] line while bulge-less galaxies show flat surface brightness maps and narrow [C II] line, therefore, providing another potential explanation toward observed broad [C II] lines in high-redshift galaxies.

The simulations and the multi-wavelength studies presented in this thesis allow for a detailed study of the impact of stellar feedback on different components of a galaxy. Therefore, for the first time, `SPICE` enables a systematic study of relative differences in stellar feedback models and allows for robust predictions of galaxy observables in the EoR.

Chapter 1

The Universe: A multi-scale problem

> "People should try to understand theory before mindlessly running simulations"
>
> Eileen Herwig

Our quest to understand galaxies started with the proposition that they are "island universes" (Wright, 1750; Kant, 1755) that exist and evolve as isolated regions. With the advancements in telescoping engineering, early catalogues of objects (Messier, 1781; Herschel, 1802) revealed that these "nebulae" commonly inhabit the night sky. Edwin Hubble confirmed in the 1920s that these "nebulae" were indeed independent objects (Hubble, 1926, 1929b) that exist far away from our own galaxy. Furthermore, advances in the development of the standard model of cosmology (Friedmann, 1922; Lemaître, 1931b; Robertson, 1935; Walker, 1937) went hand-in-hand with these observations. Theoretical predictions of an expanding universe (Lemaître, 1927, 1931a; Eddington, 1933) were confirmed using observations (Hubble, 1929a) that showed a positive correlation between receding velocities of galaxies and their distance. This discovery of an expanding universe consequently inspired the development of the relativistic models based on the solutions of the Friedmann equations (Einstein & de Sitter, 1932) which suggest that the universe originated from an indefinitely hotter and denser state as compared to the current day. Further theoretical developments theorised the "beginning" as a hot big bang (Lemaître, 1931c; Lemaitre, 1949) followed by thermal conditions that would allow for synthesis of light elements (Gamow, 1946; Alpher et al., 1948; Peebles, 1968a). Furthermore, Alpher & Herman (1948) theorised the existence of a cosmic microwave background (CMB) which would be later detected as an excess signal in the microwave by Penzias & Wilson (1965). Dicke et al. (1965) realised that this excess signal (see also Peebles 1965, 1967) was indeed the CMB. Eventual detection of thermal fluctuations (spatial) in the CMB with COBE (Lindley, 1989) presented the first evidence of "seeds" of structure formation in the early universe.

In parallel, observations of galaxies allowed astronomers to use rotation curves of galaxies to estimate their mass. It was noted by Zwicky (1933) that the velocities of galaxies within the Coma cluster were much larger than estimated using the baryonic mass in the cluster. To explain this discrepancy, Zwicky (1933) theorised a "dark matter" component to galaxies that one could not observe electromagnetically. By the 1980s a wide range of observations (Zwicky, 1937; Kahn & Woltjer, 1959; Rubin & Ford, 1970; Einasto et al., 1974; Mathews, 1978; Faber & Gallagher, 1979) presented a flat outer rotation curve in galaxies and the existence of a non-baryonic "dark matter" component was agreed upon. Theoretical work by a number of authors (Lynden-Bell, 1967; Rees & Ostriker, 1977; Binney, 1977; Silk, 1977a,b,c; White & Rees, 1978; Fall & Efstathiou, 1980; Peebles, 1982) kick-started the field of galaxy formation and evolution in the late 1970s. Particularly, White & Rees (1978) laid out the key concepts of hierarchical galaxy formation which entails that galaxies form via cooling processes of the baryonic component inside the potential wells of dark matter halos. While alternative models were proposed such as modified Newtonian dynamics (Milgrom, 1983) or warm dark matter (Blumenthal et al., 1982), cold dark matter (CDM) became the widely accepted standard model for structure formation (Primack & Blumenthal, 1984; Davis et al., 1985) as it was already successful in correctly predicting masses of galaxies (Blumenthal et al., 1984). Various variants of cold dark matter were proposed (Holtzman, 1989) but observations of CMB temperature anisotropies with COBE (Lindley, 1989) narrowed the favored variants down to cold-hot dark matter and "ΛCDM" which is a CDM model in conjunction with a cosmological constant. Finally, with SN Ia observations confirming an accelerated expansion and a cosmological constant (Riess et al., 1998), the standard model of cosmology was widely accepted to be "ΛCDM" (see section 1.1) since the late 1990s.

Since the first numerical CDM simulations by Davis et al. (1985), rapid developments in numerics allowed for a gold rush of structure formation simulations (White et al., 1987a,b; Suto et al., 1992; Jenkins et al., 1998; Colberg et al., 2000; Springel et al., 2005). A great deal of effort has gone into modelling physical process within the galaxies into sub-grid models for galaxy formation simulations since they are crucial for a successful description of galaxy formation in a hierarchical ΛCDM universe. In the following decades, the field increasingly emphasized the interplay between observations and theoretical models, with each new discovery prompting revisions and refinements to our understanding of how galaxies form and evolve over cosmic time. We now describe galaxies as complex ecosystems that interact and co-evolve via a set of physical processes. Some of the key processes are gas accretion and shock heating (Binney, 1977; Bertschinger, 1985; Gnedin & Hui, 1998; Birnboim & Dekel, 2003), radiative cooling and heating (Peebles, 1968b; Katz et al., 1992; Efstathiou, 1992; Haardt & Madau, 1995; Abel et al., 1997; Ferland et al., 1998), star formation (Schmidt, 1959; Kennicutt, 1989; Krumholz & McKee, 2005; Bigiel et al., 2008), feedback from stars (Weaver et al., 1977; McKee & Ostriker, 1977; Chevalier & Clegg, 1985; Dekel & Silk, 1986; Walch et al., 2015), galaxy interactions (Gunn & Gott, 1972; Katz & White, 1993; Moore et al., 1996; Gnedin, 2003; Somerville et al., 2008; Angulo et al., 2008), chemical enrichment (Salpeter, 1955; Chabrier, 2003; Kobayashi et al., 2007) and transport of radiation (Shapiro & Giroux, 1987; Efstathiou, 1992; Gnedin, 2000; Okamoto et al., 2008). Modern numerical galaxy formation simulations are quite complete in that they include a majority of the aforementioned processes modelling in a self-consistent manner.

Therefore, numerical simulations provide an excellent laboratory on super-computers to test our models of galaxy formation and evolution in a systematic way.

The goal of this thesis is to employ cosmological radiation-hydrodynamical simulations to address the pressing question: *how and to what extent choice of stellar feedback models impact the physical insights gained from simulations?* The simulations presented in chapters 3 systematically target the connection between stellar feedback and galaxies in the epoch of reionisation. The goal of these simulations is to systematically probe a variety of stellar feedback models and model poorly-explored physical scenarios such as hypernova explosions and radiation pressure on dust. The simulations presented are then utilised to forward-model observables of high-redshift galaxies to test against observations from facilities such as `JWST`, `VLT` and `ALMA`. In this chapter, I briefly review the ΛCDM model (section 1.1) which is the standard model of cosmology assumed in this thesis and forms the theoretical basis of the physical processes included in the `SPICE` simulations. In sections 1.2, 1.3, 1.4, I present an overview of the theory of structure formation during cosmic reionisation, insights into the process of reionisation and review the current observational landscape, respectively. Finally in section 1.5, I conclude by listing some of the questions addressed in this thesis.

1.1 ΛCDM cosmology

ΛCDM is the standard model of cosmology used to describe the formation and growth of structure in the Universe. Within the ΛCDM paradigm, the Universe is homogeneous, isotropic and uniformly expanding on the largest scales. The geometry of the Universe is described by the Friedman-Lemaı̂tre-Robertson–Walker (FLRW; Friedmann, 1922; Lemaître, 1931b; Robertson, 1935; Walker, 1937) metric and its evolution is governed by Einstein's equations of General Relativity (Einstein, 1916). The model assumes that the universe is composed of four components: baryonic matter, cold dark matter (CDM), radiation, and dark energy (Λ).

The model is fully described using just six parameters, namely the total density of the universe, $\Omega_0 = \Omega_m + \Omega_\Lambda$ (where Ω_m and Ω_Λ represent matter and dark energy components), the Hubble constant, H_0, the baryon density parameter, Ω_b, the root-mean-square mass fluctuations on $8h^{-1}$ Mpc scale (where $h = H/100$), σ_8, and the spectral index of the primordial density fluctuation, n_s. These six parameters are directly derived from observations of the CMB anisotropies from space-based observatories. The CMB is a nearly isotropic background of black body radiation with an average temperature of ≈ 2.73 and fluctuations in temperature with an amplitude of $\Delta T/T \approx 10^{-5}$K. The angular power spectrum of these fluctuations has been measured to a very high degree of precision with various space missions like COBE (Lindley, 1989), WMAP (Bennett et al., 2003) and most recently Planck (Planck Collaboration et al., 2016a) as shown in Figure 1.1. The series of peaks seen at multipoles of $l > 30$ are caused by acoustic oscillations in the coupled radiation-matter fluid at the redshift of the CMB ($z \approx 1100$). These acoustic peaks hold information about physical processes and matter content in the very early Universe and

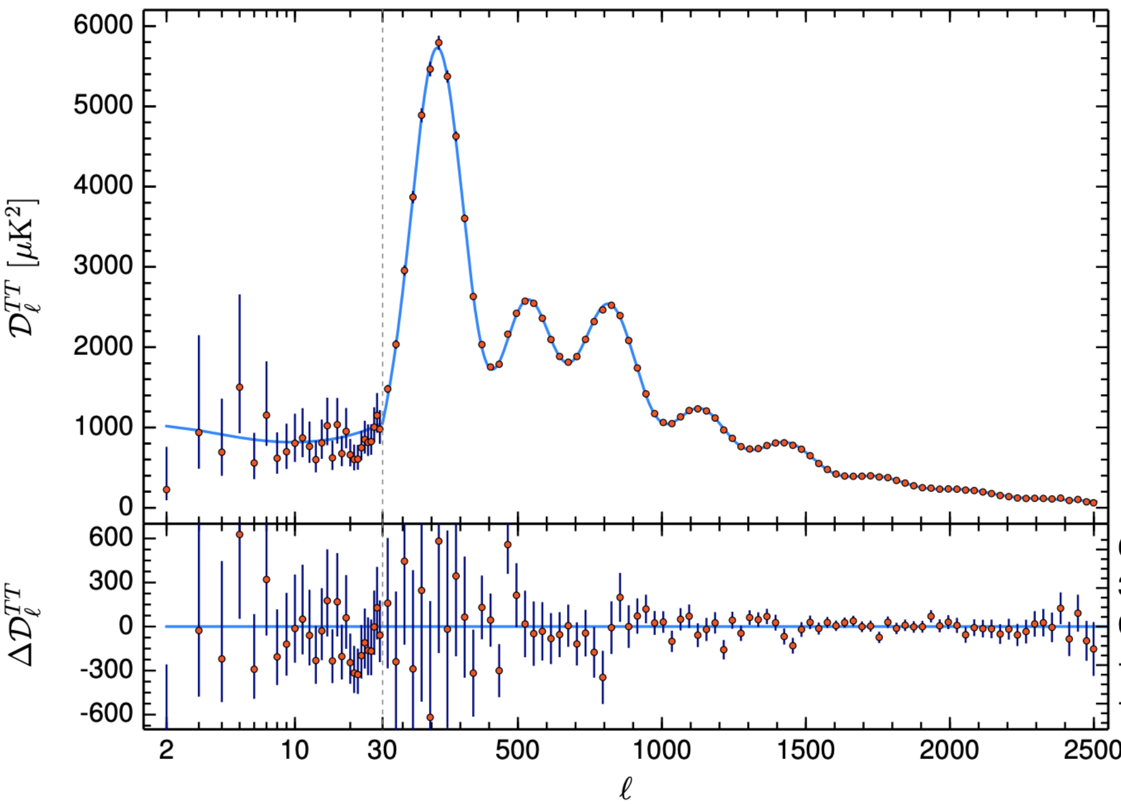

Figure 1.1: Power spectrum of the temperature fluctuations of the CMB as measured by the Planck satellite shown with solid points (Planck Collaboration et al., 2016a). The solid line refers to a fit obtained using a 6 parameter ΛCDM cosmology. This figure is adopted from Planck Collaboration et al. (2016a).

are used to place constraints on parameters of the ΛCDM model. Detailed analysis of the anisotropy data from the Planck satellite reveals that non-relativistic matter has a contribution of $\Omega_m = 0.3103 \pm 0.0054$ to the cosmic energy density, with dark energy contributing $\Omega_\Lambda = 0.6897 \pm 0.0054$. The baryonic component of the matter density is constrained to $\Omega_b \approx 0.0448$, showing that the Universe is dark and predominantly non-baryonic.

Furthermore, the nature of the dark energy component remains unknown, with the exception that it accelerates the expansion of the Universe (Riess et al., 1998). This would be equivalent to a positive cosmological constant in Einstein's equations of general relativity. Therefore, dark energy is theorised to follow an equation of state that writes as $P = w\rho c^2$, where $w = -1$, hence causing a net acceleration in the expansion of the universe.

The total energy density between the components adds up (Planck Collaboration et al., 2016a) to the critical density[1] as expected for a Friedmann universe, i.e. $\Omega = \Omega_m + \Omega_\Lambda \approx 1$, therefore implying we live in a flat Universe. The notion that we live in a flat Universe can

[1]Critical density here corresponds to the density of a spatially flat Universe given as $\rho = \frac{3H^2}{8\pi G}$

be explained by assuming that the Universe underwent a period of exponential expansion known as "cosmic inflation" (Guth, 1981), which also explains the degree of isotropy seen in observations of the CMB. Additionally, it alleviates the fine tuning problem associated with density of the Universe as measured at $z = 0$ to be the critical density. The remaining tiny perturbations in the CMB are naturally accounted for as a result of quantum fluctuations in the energy density of a scalar field referred to as the aforementioned "inflation". The density perturbations are described by a power spectrum $P_{\rm r}(k) \propto k^{n_s - 1}$ with a spectral index n_s. CMB observations constrain this index to be $n_s = 0.9668 \pm 0.0037$, in great agreement with predictions from inflationary models (Mukhanov & Chibisov, 1981).

As seen in Figure 1.1, the theoretical predictions for the power spectrum of the fluctuations from ΛCDM agree extremely well with observations from Planck. Therefore, ΛCDM remains the standard theory of cosmology to this date and has been adopted in this thesis. For details on the exact choice of cosmological parameters see Section 3.

Non-linear collapse and dark matter halos

At the redshift of the CMB, the universe consists of density fluctuations and free-streaming photons from the recombination epoch. Here I describe the current understanding of how complex cosmic structures emerged from an almost featureless Universe. In simple terms, galaxy formation and evolution is brought about by the gravitational collapse of dark matter. The initial density perturbations seeded by inflation in the dark matter distribution grow in mass and size through run-away gravitational collapse. When the density contrast satisfies $\Delta\rho/\rho \approx 1$, the perturbations decouple from the background Hubble flow (i.e. expansion of the Universe), undergo non-linear collapse and form virialised structures known as 'dark matter halos'.

Given the conditions of an initially Gaussian random field in an expanding Universe (as left behind by inflation), the number density of halos at a given halo mass as a function of redshift can be written as (Press & Schechter, 1974):

$$M\frac{dn}{dM} = \left(\frac{2}{\pi}\right)^{0.5} \frac{-d(ln\sigma)}{d(lnM)} \frac{\rho_0}{M} \nu_{\rm c} e^{-\nu_{\rm c}^2/2} \tag{1.1}$$

where ρ_0 is the mean density at given redshift, σ is the standard deviation of the density contrast smoothed through a certain window, and $\nu_{\rm c}$ is the minimum number of standard deviations of a collapsed fluctuation and M is the mass of the halo. Figure 1.2 shows the standard deviation of 1σ, 2σ, and 3σ fluctuations as a function of halo mass and compare this with the over-density at each redshift that corresponds to a collapsing object (horizontal lines, calculated as $\delta_c(t) = 1.686/D(z)$, where $D(z)$ is the growth factor as a function of redshift). Figure 1.2 and Equation 1.1 imply that the number of massive halos is exponentially suppressed at early times, while they are able to grow at later times. Comparing the halo masses that collapse at each redshift one can realise that the current scenario for structure formation is therefore hierarchical, in that smaller halos form earlier and massive halos form later. Since galaxies form within the potential wells of dark matter halos, it follows that low mass galaxies form at high redshifts too. An initially

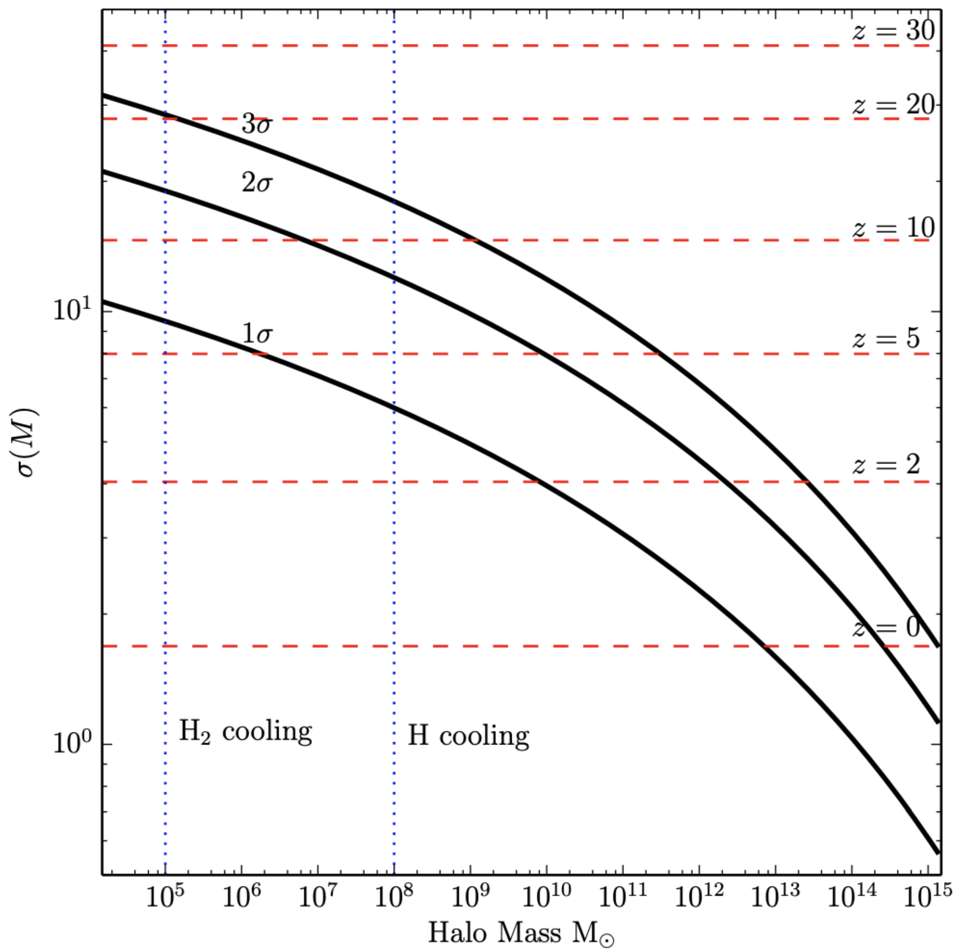

Figure 1.2: Collapse thresholds for cold dark matter halos as a function of halo mass. From bottom to top, the solid black lines show the 1σ, 2σ, and 3σ mass variance as a function of halo mass. The red horizontal lines represent over-density for collapse at different redshifts, computed as $\delta_c(t) = 1.686/D(z)$, where $D(z)$ is a redshift dependant growth factor. The intersection between the horizontal red lines and the solid black lines represents the fiducial halo mass at each redshift that is collapsing for each of the indicated mass variances. The dotted vertical blue lines indicate the approximate halo mass needed for a galaxy to form via molecular hydrogen or atomic hydrogen cooling. Plot is taken from Katz 2017.

homogeneous dark matter density field evolves into a complex network of nodes, filaments and voids knows as the "cosmic web". Virialised dark matter halos live along the filaments and the points of intersection of these filaments. Figure 1.3 shows the evolution of the dark matter density between $z = 30 - 2$ in the SPICE simulations (Bhagwat et al., 2024a) described in chapter 3.

In the current understanding of galaxy formation, dark matter and baryons start out well-mixed. Dark matter undergoes dissipationless gravitational collapse, leading to self-similar radial density profiles (Navarro et al., 1996). On the other hand, baryons can

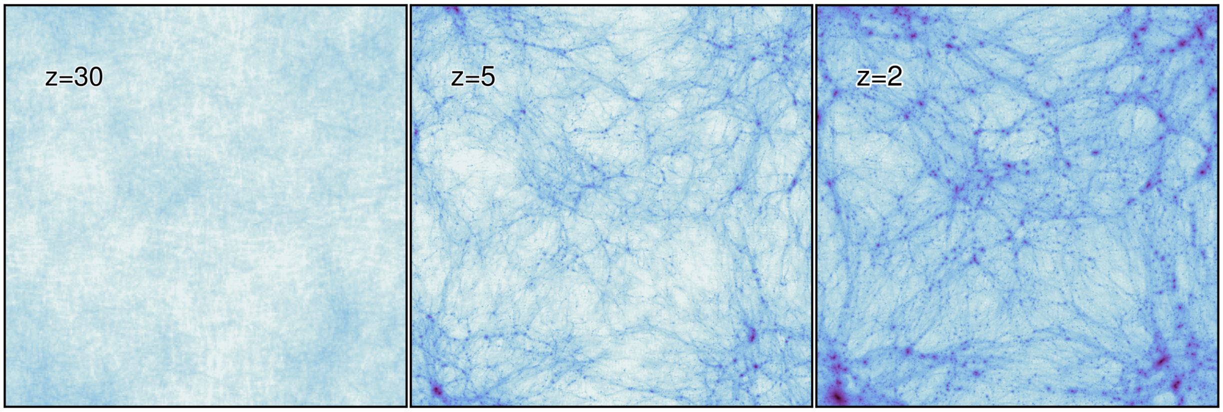

Figure 1.3: Evolution of the dark matter density between redshift 30 and 2 in the SPICE simulations. The figure demonstrates the growth of structure in the Universe from a relatively featureless universe at $z = 30$ to a complex web of large scale structure by $z = 5$.

dissipate their energy through various radiative cooling processes and collapse to the centers of dark matter halos (White & Rees, 1978). Thus, the minimum mass of a galaxy is determined by the gas' ability to cool and condense effectively within a dark matter halo (Rees & Ostriker, 1977; Silk, 1977a). I discuss the details of the baryonic physics that are included in galaxy formation models in the following section.

1.2 Baryonic processes in structure formation

The gas that collapses into the deepest parts of the potential wells of the host dark matter halos is decoupled from the evolution of the background Universe. Collapsing gas undergoes evolution via physical processes like cooling, heating, star-formation, feedback and accretion to produce galaxy populations which co-evolve with their environments. This thesis is focused on formation and evolution of galaxies during the epoch of reionisation (see section 1.3) therefore, I describe below the physical processes that affect the evolution of baryons (for a review see Ciardi & Ferrara 2005).

1.2.1 Cooling

Once the gas infalling into the dark matter potential wells reaches a sufficiently high density, dissipative forces begin to play a significant role such that baryons are able to become concentrated at the center of dark matter halos (White & Rees, 1978). The fate of the gas is determined by three characteristic timescales, namely, the cooling time ($t_{\rm cool}$), the free-fall time ($t_{\rm ff}$) and finally the Hubble time ($t_{\rm H}$). For a gas cloud with a number density n and temperature T, the associated timescales of cooling and free-fall can be written as $t_{\rm cool} = 3kT/(2n\Lambda(T))$ and $t_{\rm ff} = (3\pi/32G\rho)^{1/2}$ respectively, where k is the Boltzmann constant, $\Lambda(T)$ gives the cooling rate depending on the chemical composition of the gas cloud, G is the gravitational constant and ρ is the gas density. If the cooling

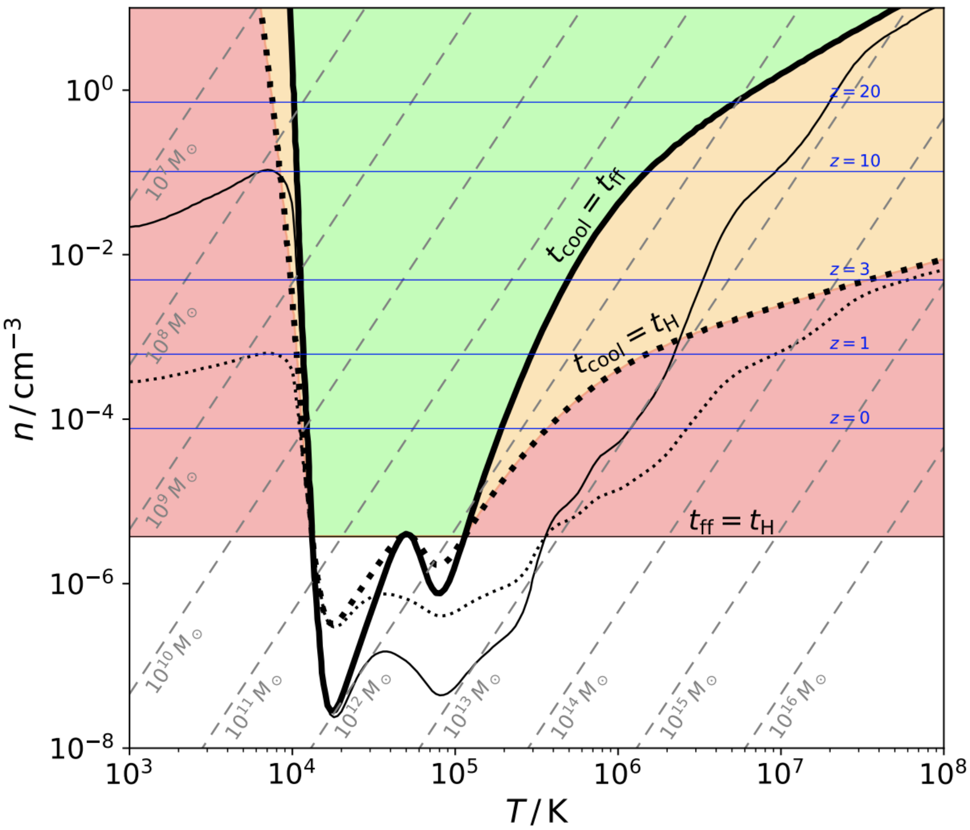

Figure 1.4: Number density n vs. gas temperature T for a cloud of gas. Clouds expand with the Universe for densities below the horizontal line at $n \sim 3 \times 10^{-6}\mathrm{cm}^{-3}$. The thick black line marks the phase space (T, n) values where the cooling timescale $t_{\rm cool}$ equals the dynamical timescale $t_{\rm ff}$ (solid), and the Hubble time scale $t_{\rm H}$ (dotted), for metal-free gas. Thin solid black line shows as before, but for Solar metallicity. Clouds in the red domain are virialised and therefore in hydrostatic equilibrium, however, their cooling times remain longer than the age of the Universe. In the orange shaded region, a could is in a quasi-static equilibrium, such that, the cloud can enter the green shaded region where pressure is unable to support the cloud. This leads to gravitational collapse on the free-fall timescale. Horizontal, blue lines mark typical densities of virialised halos at the indicated redshifts (with overdensities of $\Delta \sim 180$). Slanted, gray dashed lines show (T, n) values of halos with the indicated virial masses. This plot is taken from Laursen (2023).

time ($t_{\rm cool} \propto n^{-1}$) is shorter than the free-fall timescale ($t_{\rm ff} \propto n^{-1/2}$) of the cloud, then gas can collapse to the innermost regions of the dark matter halo, where processes like fragmentation and star-formation can take place.

The interaction between these timescales is demonstrated in Figure 1.4 along the $n-T$ plane. The plane can be divided into distinct domains where a virialised gas cloud may appear. The colors in each domain denote the dominating timescale: green indicates that $t_{\rm cool} < t_{\rm ff}$, and therefore dissipative forces dominate over dynamics allowing the gas to collapse freely, so that halos within the green domain can collapse and form galaxies. Gas clouds in the orange domain remain in a quasi-hydrodynamic equilibrium, while cooling and contracting in a slow but steady manner. These clouds may cross the $t_{\rm cool} = t_{\rm ff}$ line due to contraction and eventually collapse, and thus the ability of halos in the orange domain to form galaxies depends on their evolutionary tracks. Clouds in the red domains remain in hydrostatic equilibrium as their cooling times are longer than the Hubble time. Finally, the clouds below the horizontal $t_{\rm ff} = t_{\rm H}$ line are not virialised, and therefore are unable to withstand expansion of the Universe.

The first objects (often referred to as *minihalos*) initially collapse adiabatically, so that the gas cloud is heated up until thermal pressure prevents further collapse and the gas is shock-heated to its virial temperature ($T_{\rm vir} = \frac{\mu m_{\rm H}}{2k}\frac{GM}{R}$, where μ is the mean molecular weight of gas, m_H is the mass of a proton, M is the mass of the cloud and R is the radius of the cloud). At this time, the cooling in the metal-free gas is dominated by transitions of atomic (H) and molecular hydrogen (H_2). The latter is able to form below $z \approx 100$ as the CMB radiation intensity is weak enough for survival. H_2 can form via the following channels (McDowell, 1961; Abel et al., 1997):

$$\begin{aligned} H + e^- &\rightarrow H^- + h\nu \\ H^- + H &\rightarrow H_2 + e^- \end{aligned} \tag{1.2}$$

and

$$\begin{aligned} H^+ + H &\rightarrow H_2^+ + h\nu \\ H_2^+ + H &\rightarrow H_2 + H^+ \end{aligned} \tag{1.3}$$

Cooling from atomic hydrogen is most effective at temperatures of $T > 10^4$ K, while below this temperature molecular cooling dominates, and therefore the first bound objects are thought to be regulated by H_2 cooling (Haiman et al., 1996; Tegmark et al., 1997; Abel et al., 1997). The minimum halo mass that can support H_2 cooling and allow catastrophic collapse is estimated to be $\sim 10^5$ $M_\odot$ (Tegmark et al., 1997). H_2, however, is a fragile molecule and susceptible to destruction in the presence of Lyman-Werner (LW) radiation ($11.3 - 13.6$ eV). As soon as the first stars are born, a LW background forms which leads to H_2 destruction. The minimum halo mass that can support H_2 cooling is then increased to 10^7 $M_\odot$, as the LW background also heats up the gas to temperatures larger than the virial temperatures of H_2-cooling halos ($T > 10^4$ K). Therefore, gas can cool via atomic hydrogen cooling channels, producing halos that are dominated via atomic cooling and are more robust to the LW radiation fields (Oh & Haiman, 2002) . These halos are usually referred to as *"atomic cooling halos"* and set the stage for the formation of the first galaxies within them. Vertical dashed lines in Figure 1.2 show that the first atomic cooling halos (3σ peak with $M > 10^8$ $M_\odot$) formed between $z = 20 - 10$, therefore kick-starting the process of galaxy formation and assembly. Figure 1.5 illustrates the types of early galaxies hosted by dark matter halos of different masses.

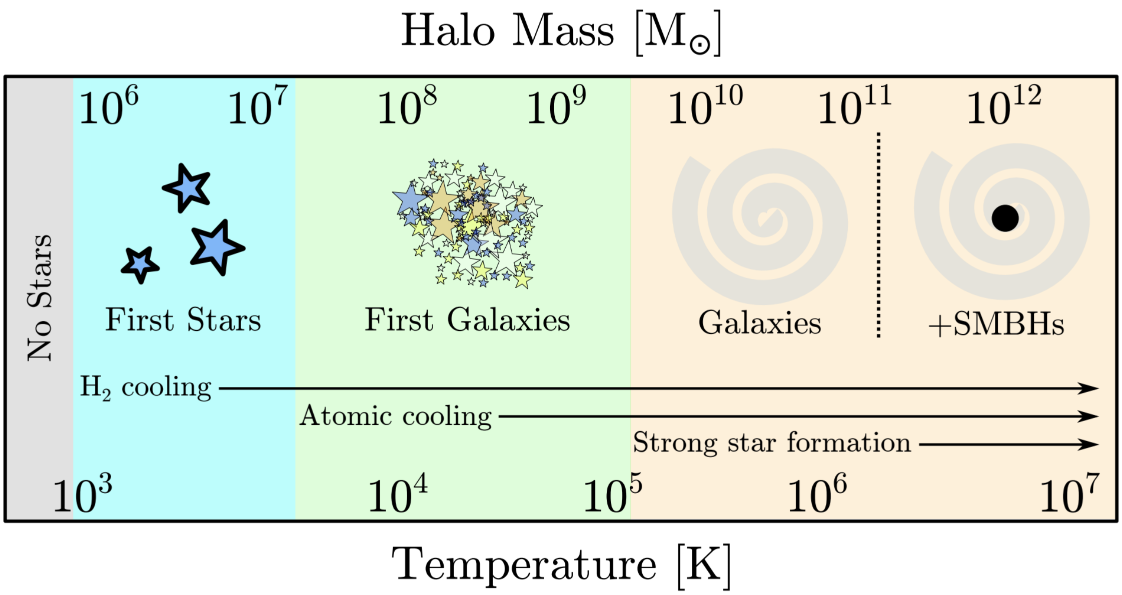

Figure 1.5: Mass scales and virial temperatures of dark matter halos that allow for the formation of the first stars, first galaxies and eventually the most massive galaxies in the Universe. This plot is taken from Wise 2019.

1.2.2 Star-formation in the first galaxies

A gas cloud that condenses to the center of a dark matter halo can become unstable to gravitational collapse. If the cloud accumulates enough mass such that the sound crossing time of the cloud is greater than the free-fall time, (i.e. if it satisfies the Jeans criterion, Jeans 1902) it is unstable to collapse and therefore is eligible for star-formation. This so called Jeans mass is given as:

$$\begin{aligned} M_{\mathrm{jeans}} &= \left(\frac{5kT}{G\mu m_{\mathrm{p}}}\right)^{3/2}\left(\frac{3}{4\pi\rho}\right)^{1/2} \\ &\approx 2M_{\odot}\left(\frac{c_{\mathrm{s}}}{0.2\ \mathrm{km/s}}\right)^{3}\left(\frac{n}{10^3\ \mathrm{cm^{-3}}}\right)^{-1/2} \end{aligned} \tag{1.4}$$

where c_{s} is the speed of sound in the cloud, k is the Boltzmann constant, n (or ρ) gives the number density (density) of gas, μ is the mean molecular weight, T is the temperature, m_{P} is proton mass and G is the gravitational constant. The phase of a Jeans unstable cloud is quite dynamic (Hoyle, 1953) in that fragmentation can occur such that all of the fragments are also Jeans unstable with slightly different densities and temperatures. The rate at which these fragments collapse depends on the chemical composition of the cloud and the density at which clouds become optically thick to cooling radiation (Lynden-Bell, 1967; Omukai et al., 2005).

During the initial collapse, primordial metal-free gas heats up to higher temperatures compared to metal-rich gas as seen at lower redshifts. Given that the Jeans mass scales as

$T^{3/2}$, the fragments in these first collapsing clouds will produce fragments with higher Jeans masses. Therefore, theoretical calculations have suggested that the first stars are expected to be more massive than stars observed in the local universe with mass of $10^2 - 10^3 M_\odot$ (Abel et al., 1999; Bromm et al., 1999; Abel et al., 2002; O'Shea & Norman, 2007). These first stars that form out of primordial H/He are referred to as Population III (Pop III) stars. The fragmentation leading to the formation of the first stars however, remains poorly understood. Therefore, the distribution of initial masses of formed stars (commonly know as the "IMF") remains uncertain. A widely used parameterisation of the Pop III IMF is written as (Larson, 1998)

$$\frac{dN}{d\log M_*} \propto \left(1 + M_*/M_\mathrm{c}\right)^{-1.35}, \tag{1.5}$$

where M_c is a characteristic mass related to the Jeans mass and M_* is the mass of the star. This IMF produces a top-heavy distribution at high redshifts as $M_c \propto M_\mathrm{Jeans} \propto T^{3/2}\rho^{-1/2}$ (see below). As Pop III stars evolve, they interact with their surroundings via various feedback processes (see section 1.2.3), including enrichment of inter-stellar medium (ISM) gas with the metals that form within Pop III stars. Metals in ISM gas provide additional cooling channels, consequently altering the fragmentation process within collapsing clouds and allowing for lower mass fragments to form. Therefore, leading to formation of stars with significantly lower masses. This marks the formation of stars with a more "conventional IMF" (e.g Chabrier 2003) i.e. transition into Population II (Pop II) star formation (Yoshii & Sabano, 1980; Bromm et al., 2001; Schneider et al., 2002; Smith & Sigurdsson, 2007; Xu et al., 2016; Tanaka & Hasegawa, 2021; Latif et al., 2022; Ventura et al., 2024). The critical metallicity for the transition from Pop III to Pop II star formation is estimated to be $Z_\mathrm{crit} = 10^{-4} - 10^{-3} Z_\odot$.

In the context of galaxy formation and cosmic reionisation, understanding when, where and how many stars formed are very pertinent questions. Averaged over the entire galaxy, one of the most striking features of star-formation is the *inefficiency* of the process. Gravitational collapse acts on the scales of t_ff, therefore, naively put, the star-formation rate of a galaxy should be $\dot{M}_* = M_\mathrm{gas}/t_\mathrm{ff}$. However, in observed galaxies, the depletion time of gas is estimated to be ~ 100 larger the one given by this equation (Kennicutt & Evans, 2012). A pre-factor called the "star-formation efficiency" (ϵ_ff) needs to be invoked to match observed rates. Therefore, star-forming clouds must somehow be supported against collapse and exist in a quasi-equilibrium state. Theoretical predictions suggest a dynamic picture with physical mechanisms like supersonic turbulence (Larson, 1981; Krumholz & McKee, 2005; Murray, 2011; Padoan & Nordlund, 2011; Federrath & Klessen, 2012; Naab & Ostriker, 2017) and stellar feedback (Hopkins et al., 2014; Somerville & Davé, 2015) regulating the evolution of star-forming clouds. In this picture, the timescales at which gravity, turbulence and feedback operate are not separable, with each being relevant to fully describe star-formation. Therefore, it remains key to include these processes in galaxy formation simulations to understand regulation of star-formation at different epochs in a self-consistent manner. This work focuses on cosmological simulations of the high redshift Universe including all of these physical mechanisms with a key focus on stellar feedback, which I describe below.

1.2.3 Stellar Feedback

The first stars that form in the Universe evolve while interacting with their surroundings via matter and radiation. The processes associated with star-formation that inject energy, mass and radiation into their surroundings are colloquially knows as “feedback” effects. These feedback mechanisms modify physical processes around them from ISM to IGM scales via ejected mass, injected momentum or radiative transfer effects. Feedback therefore is a back-reaction of a physical process on itself or on the underlying driving mechanisms. Feedback effects can both positively or negatively affect physical processes and therefore allow a complex mechanism like star-formation in a galaxy to be self-regulated. Below I motivate feedback as an essential ingredient of galaxy formation.

Is feedback a necessary ingredient of galaxy formation?

The incidence and evolution of a population of galaxies can be described using the luminosity function (LF). The LF gives the probability of finding a galaxy with a given luminosity per unit volume. However, to compare the importance of feedback on regulating galaxy formation, one needs to convert the luminosity function to a stellar mass function (SMF). For a detailed description of how observed galaxy luminosities are converted to SMFs, see Song et al. 2016; Weaver et al. 2023. The SMF is well described by a Schechter function, written as

$$\phi(M)dM = \phi_{\rm ch}\left(\frac{M}{M_{\rm ch}}\right)^{\alpha} e^{-\frac{M}{M_{\rm ch}}}dM, \tag{1.6}$$

where M is the stellar mass, and $M_{\rm ch}$ is the ”knee” of the Schechter function. It corresponds to the mass at which the function transitions from a power law with exponent α to an exponential function. $\phi_{\rm ch}$ is a normalisation which refers to the number density at $M_{\rm ch}$.

Figure 1.6 shows the number density of objects as a function of their respective masses (stellar and halo mass functions, SMF and HMF respectively). The dark-blue line shows the HMF at $z = 0.1$ (Sheth & Tormen, 2002; Klypin et al., 2011), the functional form is described in Laursen et al. (2019). Multiplying the masses in the HMF by the baryon fraction $f_b = \Omega_b/\Omega_m = 0.157$ shifts the HMF to the left (magenta line). This line represents the SMF if galaxies had star-formation efficiency of 1, i.e if all gas were converted to stars. However, the observed SMFs at $z = 0.1$ (Bernardi et al., 2013; Wright et al., 2017) demonstrate different trends, it is evident that the SMF is flatter at the low-mass end ($M < 10^11 M_\odot$) and much steeper at the high-mass end ($M > 10^{11} M_\odot$) as compared to the HMF. Moreover, contrary to expectations from the HMF, the majority of star-formation is found to be taking place in galaxies below the ”knee” in the SMF, while massive galaxies end up under-performing. Therefore, additional mechanisms that are able to quench star-formation need to be invoked to explain the “knee” in the SMF and flatter (steeper) slopes of the SMF as compared to the HMF at the low-mass (high-mass) end.

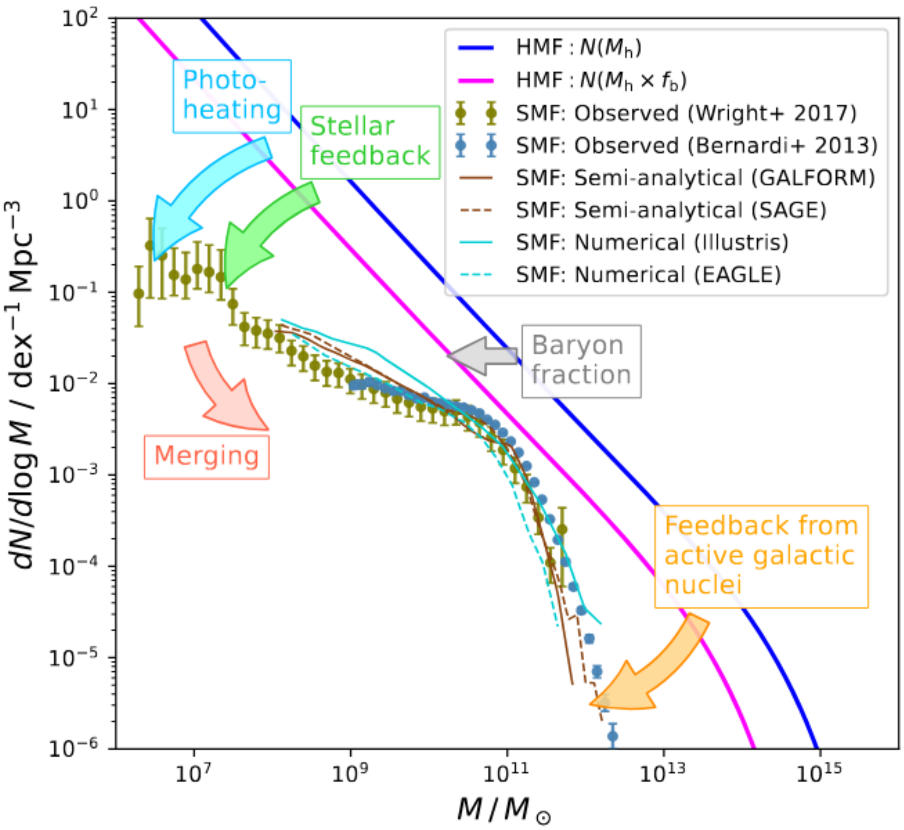

Figure 1.6: Number density of galaxies and halos as a function of respective mass. Theoretical predictions are shown for the total halo mass function (blue) and halo mass function multiplied with the baryon fraction (magenta), respectively. Stellar mass functions observed at $z = 0.1$ are shown at the low-mass end (olive points) and the high-mass end (steel blue points). At the low-mass end, photo-ionisation and stellar feedback are believed to suppress the mass function (blue and green arrows), while active galactic nuclei activity suppresses the high-mass end (orange arrow). Results from semi-analytical models (brown) and numerical (cyan) model show a good agreement with observations. This plot is taken from Laursen 2023.

Feedback mechanisms from stars and active galactic nuclei (AGN) are responsible for the observed SMF of galaxies. At the faint end, stellar feedback via mechanical injections and radiative photo-ionisation is thought to regulate star-formation. At the massive end, however, galaxies reside in much deeper potential wells, rendering stellar feedback ineffective. A more energetic feedback mechanism from AGN is favoured as a solution. Super-massive black holes (SMBH) accrete gas and consequently inject copious amounts of energy and radiation into their host galaxies, which efficiently quenches star-formation directly or by suppressing gas accretion. Models that invoke these feedback mechanisms (see figure 1.6) are able to capture the correct shape of the SMF. Therefore, numerous analytical, semi-numerical and fully coupled galaxy formation simulations suggest that feedback is essential to explain the observed galaxy populations. The focus of this thesis is on galaxies with masses below the "knee" where stellar feedback dominates, therefore, I introduce various types of stellar feedback below.

Types of feedback

Theoretical progress owing to analytical calculations and numerical simulations now provide us with a broad understanding of the types of feedback processes. These processes can be classified into radiative, mechanical and chemical feedback (each providing distinct channels for positive or negative effects). I briefly describe the processes below:

Mechanical feedback

Mechanical feedback is associated with the mass and energy deposited into the ISM as a result of life cycles of stars. Core-collapse SN are thought to play a key role in regulating the phases of the ISM and star-formation in a galaxy (Dekel & Silk, 1986; Navarro et al., 1996). At the end of the life of a star, typically $2-10M_{\odot}$ (Sukhbold et al., 2016) is ejected into the ambient ISM at ejected velocities of $v_{\rm ejecta} \sim 6000$kms s^{-1} (Janka, 2012), driving a shock into the ISM. Outside of injections of mass and chemical elements, SN events also heat up gas in the ambient ISM to $T > 10^6 K$ and thus are responsible for partly creating the hot-phase of a multi-phase ISM within the galaxy (McKee & Ostriker, 1977; Walch et al., 2015). SN mechanical feedback is important for driving galactic outflows, fountain flows, winds through low density channels (Chevalier & Clegg, 1985; Norman & Ikeuchi, 1989; Joung & Mac Low, 2006) and overall contribute to the kinetic energy budget of the ISM. It has been argued via numerical simulations that SN feedback can drive turbulence (Scalo & Elmegreen, 2004) within the ISM that can regulate both the scale heights of disks via turbulent pressure and star-formation rates (Ostriker & Shetty, 2011; Kim & Ostriker, 2015a).

Detailed studies on SN blast wave evolution (Chevalier, 1982; Ostriker & McKee, 1988; Blondin et al., 1998; Draine, 2011) have described multiple phases of the SN remnant. In the early free expansion phase, the momentum of SN ejecta is unable to directly accelerate gas to high velocities. Once the SN ejecta is able to sweep up cold ISM of mass comparable to the SN ejecta, the remnant enters the energy-conserving Sedov-Taylor phase (Taylor, 1950; Sedov, 1959). In this phase, $\sim 10^3$ times initially ejected mass is heated and ~ 10 times initially ejected radial momentum is generated depending on weather the expansion is adiabatic or not. Once radiative cooling losses dominates, a shell forms at the leading edge of the blast-wave and the amount of hot gas drops. No further radial momentum can be generated due to the radiative cooling and the remnant enters the momentum-conserving snowplough phase. Once the expansion velocity reaches the speed of sound of the ISM, the remnant propagates as a sound-wave within the ISM. This simple remnant evolution argument dictates that SN determine the thermal and dynamical evolution of the ISM (McKee & Ostriker, 1977).

The impact of SN mechanical feedback on star-formation is widely studied using subgrid models (e.g. Kimm & Cen, 2014; Kimm et al., 2015). Simulations have found that

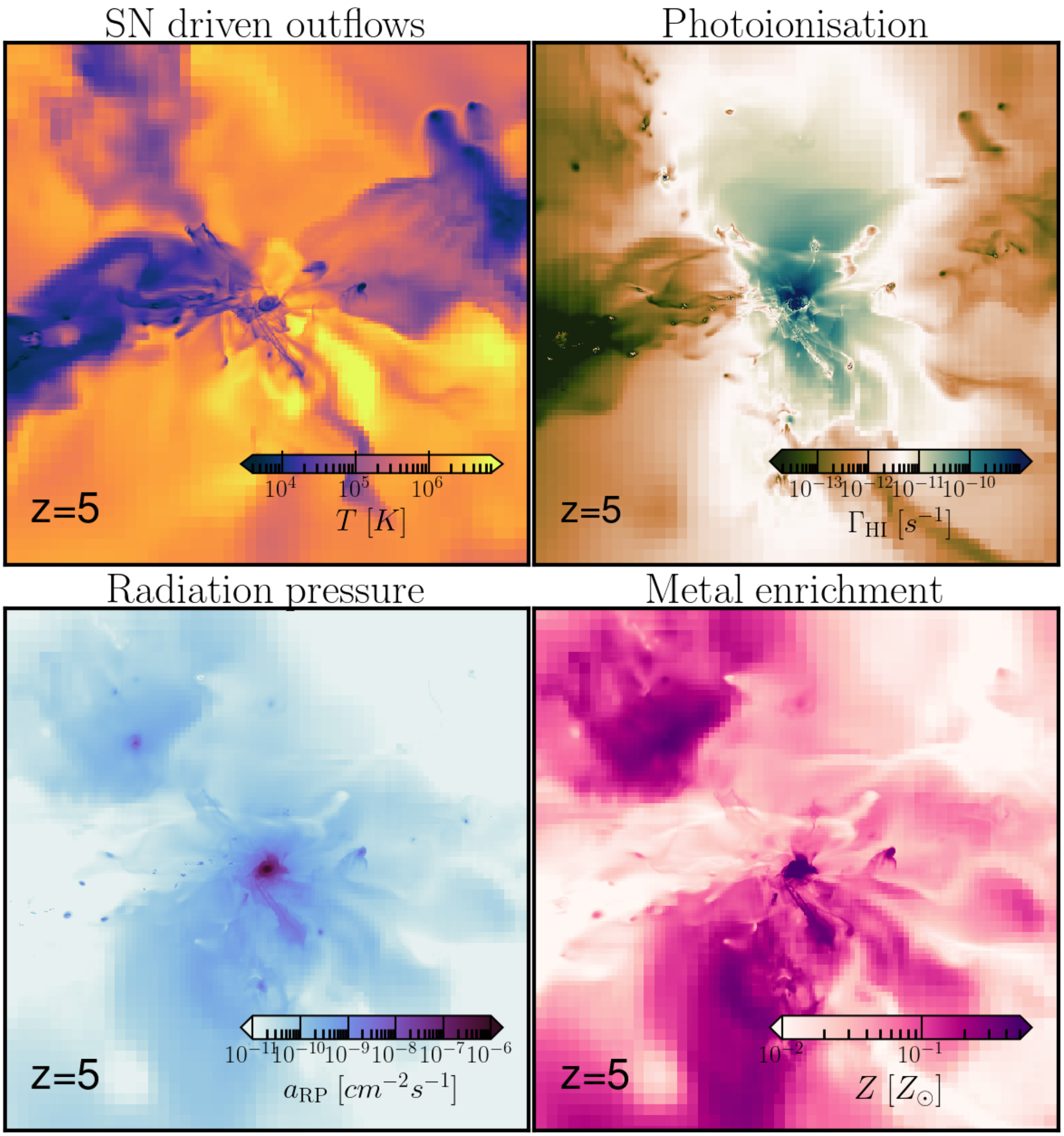

Figure 1.7: Various modes of stellar feedback included on-the-fly in the `SPICE` simulations: mechanical (top left panel), radiative (top right and bottom left panels) and chemical (bottom right panel). Each panel shows a region encompassing $1R_{\rm vir}$ of a $2 \times 10^{11} M_\odot$ halo at $z = 5$ taken from the `smooth-sn` model from SPICE (Bhagwat et al., 2024a). Outflowing hot ($T > 10^6$K) gas in the top left panel is generated by SN mechanical feedback, the photo-ionisation rate shown in top right panel results from escaping stellar radiation within a galaxy, radiation pressure depicted in the bottom left panel is due to coupling of stellar radiation with gas via dust and finally, metals generated by stars care carried out far into the CGM by SN driven outflows as depicted in the bottom left panel.

SN driven outflows are able to expel ISM gas. This suppresses star-formation by reducing available gas reservoir (e.g. Dubois & Teyssier, 2008; Puchwein & Springel, 2013; Fielding et al., 2018; Orr et al., 2019). Furthermore, feedback-driven turbulence in the ISM can provide both a positive and negative feedback effect on star-formation by either providing support against gravitational collapse, or by creating strong density contrasts allowing for rapid collapse, hence strongly regulating star formation efficiency (Krumholz & McKee, 2005; Ostriker et al., 2010; Faucher-Giguère et al., 2013; Gatto et al., 2016). By altering the phase of the ISM (which determines escape of ionising photons) SN feedback also directly affects the process of cosmic reionisation (Kimm et al., 2017; Trebitsch et al., 2018; Rosdahl et al., 2022a). Therefore, to fully describe high-redshift galaxy formation and cosmic reionisation, one needs to systematically study SN feedback and its impact on scales ranging from the ISM to the IGM.

Radiative feedback

Stars begin to emit copiously large amounts of radiation from birth and stellar evolution models dictate that the total energy released by young stars is dominated by stellar radiation (Leitherer et al., 1999). Before the onset of SN feedback ($t_{\rm SN} > 3$ Myr from birth), a young star already would have emitted $\sim 10^{53}$ erg in radiation as compared to $\sim 10^{51}$ erg which is the standard amount of energy injected by a SN event. Stellar radiation is coupled to gas via photo-ionisation, photo-heating and radiation pressure (both direct and via coupling to dust). Each of these affect gas in unique ways.

Ionising radiation from young stars is shown to suppresses radiative cooling (Efstathiou, 1992; Gnedin, 2000; Okamoto et al., 2008). Additionally, strong radiation fields can also reduce the baryon fraction of galaxies due to photo-heating/photo-ionisation, i.e gas can be evaporated out of the halo (Thoul & Weinberg, 1996; Machacek et al., 2001; Okamoto et al., 2008; Wise & Abel, 2008; Hasegawa & Semelin, 2012; Wise et al., 2012; Pawlik et al., 2013). Photo-evaporation is relevant in the first collapsing clouds which form Pop III objects as their virial temperatures are below the typical temperatures of photoionised gas ($T \approx 10^4$K). Consequently, photo-ionisation/photo-heating feedback can suppress Pop III star-formation. Additionally, soft-UV radiation fields in the Lyman-Werner bands ($11.2-13.6$eV) can build up and cause photo-dissociation of H_2 (Haiman et al., 1996; Ciardi et al., 2000a,b; Wise & Abel, 2008). Therefore, once the first generation of Pop III stars are born, suppression of molecular cooling in star-forming clouds can completely quench subsequent star-formation (Omukai & Nishi, 1999; Tashiro & Nishi, 2000; Glover & Brand, 2001; Oh & Haiman, 2002; Susa & Umemura, 2004). Finally, cosmic reionisation (which is an effective heating term in the IGM) causes an increase in the temperature of the gas. This heating suppresses galaxy formation by increasing the Jeans mass. The amplitude of this effect depends on the reionisation history (see Ciardi et al. 2000a). Overall, ionising radiative feedback dictates the transition from molecular to atomic cooling halos by altering cooling and the amount of cold gas available for star-formation.

Beyond the direct effects mentioned above, recent galaxy formation simulations suggest that accounting for radiative feedback can significantly enhance the coupling of the stellar feedback and momentum injection into the ISM (Hopkins et al., 2012; Agertz et al., 2013; Roškar et al., 2014). While its efficiency remains debated, radiative feedback is theorised to contribute to driving turbulence and galactic scale outflows (Murray et al., 2005; Murray, 2011; Agertz & Kravtsov, 2016; Geen et al., 2015). Radiation pressure on dust from "multi-scattered" IR radiation (i.e. when high energy photons are absorbed and re-emitted into IR) can add a large source of momentum into the ISM ($\dot{P}_{\rm rad} = (1 + \tau_{\rm IR})L/c$). Radiation-hydrodynamic (RHD) simulations, however, generally find that early stellar feedback including radiation pressure acts to suppress outflows through a reduction in star-formation and in supernova clustering (Kimm et al., 2018; Costa et al., 2019; Agertz et al., 2020). In summary, despite many promising leaps forward, the exact role of stellar radiation from young stars in regulating star-formation, driving outflows and modulating the speed of reionisation remains unclear. To further add to our understanding, accurate modeling of radiative feedback in galaxy formation simulations must be included.

Chemical feedback

The first stars (i.e. Pop III) are theorised to be composed exclusively of primordial elements. Nucleosynthesis in these stars produced the first generations of metals which eventually were recycled back into the ISM via stellar winds and supernova explosions, starting the process of chemical feedback. Chemical feedback entails enrichment, the transport and mixing of metals in the gaseous medium between the stars (Karlsson et al., 2013). Ejected metals are initially transported by supernova feedback followed by turbulent flows within galaxies. The efficiency of chemical feedback dictates how, when and where the transition from Pop III (metal-free stars) to Pop II (metal-enriched stars) star formation occurred (Schneider et al., 2002; Mackey et al., 2003; Maio et al., 2010, 2011). Chemical enrichment provides an additional channel of cooling in the ISM via metal-line cooling (Katz et al., 1992). Fine-structure line cooling allows for more efficient fragmentation (Yoshii & Sabano, 1980; Bromm et al., 2001) even in absence of H_2 leading to efficient Pop II star-formation.

1.3 Cosmic reionisation

About $380,000\,$yr after the Big Bang, protons and free electrons coalesce for the first time, leading to the formation of hydrogen and helium atoms. At this time, the Universe is largely neutral. The Universe then entered a timespan devoid of luminous sources known as the "dark ages". The formation of the first stars marks the end of the dark ages and the onset of the age of galaxy formation. A natural consequence of high redshift galaxy formation is the production, propagation and absorption of ionising radiation by hydrogen and helium. By $z = 5$ (e.g. Gaikwad et al., 2023), the vast majority of hydrogen has transitioned to an ionised state. This $\sim 1\,$Gyr period is known as the epoch of reionisation (EoR)[2] and represents the last major phase transition in the history of the universe.

[2] For the purpose of this thesis, we focus on reionisation of hydrogen

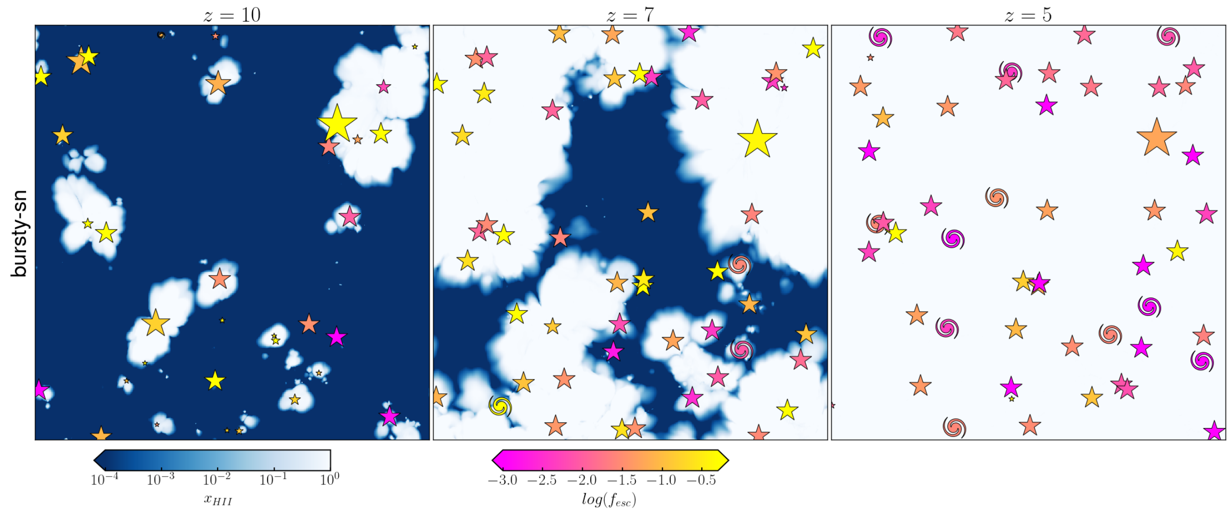

Figure 1.8: Evolution of the ionised hydrogen fraction ($x_{\rm HII}$) between $z = 10-5$ for the "bursty-sn" model of the SPICE simulations (Bhagwat et al., 2024c). We see the three phases of cosmic reionisation: pre-overlap (left panel), overlap (middle panel) and post-overlap (right panel). Each panel shows a thin slice of depth of 100 kpc cut along the z-axis of the simulation volume. Stars represent galaxies that reside within ionised bubbles powering their growth, the colors of the symbols represent the LyC escape fractions of galaxies and the symbols represent the galaxy morphologies (see chapter 3, section 3.3.6 for details).

The process of cosmic reionisation is thought to have occurred in an "inside-out" fashion, i.e. the dense regions ionise first, followed by the low density regions away from a galaxy. The reionisation process can be divided into three phases (pre-overlap, overlap and post-overlap), that describe the connectivity of ionised bubbles (or H II regions) (Gnedin, 2000). In the pre-overlap phase, young stellar populations within a galaxy produce an ionised bubble locally around themselves. Galaxy populations are typically separated by a neutral IGM and their evolution can be treated independently. During the overlap phase, ionised bubbles produced by multiple galaxies start to merge. This phase marks a dramatic increase in the mean free path of photons, as multiple galaxies contribute to the ionising flux of their overlapping bubbles, consequently speeding up reionisation. Finally, in the post-overlap phase, a vast majority of the IGM is fully ionised with neutral gas largely residing inside self-shielded regions within galaxies. Figure 1.8 demonstrates the phases of reionisation as captured by the SPICE simulations (Bhagwat et al., 2024c).

Cosmic reionisation is brought about by a complex interplay among the growth of structure, star-formation in galaxies, properties of stellar populations, the multi-phase structure of ISM, the ionisation properties of the circumgalactic medium (CGM) around galaxies and the time evolving strength of the LyC radiation emitted. Additionally, as previously discussed in section 1.2.3, it can drastically affect the formation of galaxies. Given the multitude of dynamical scales involved in reionisation, a wide range of questions remain open, such as: *What sources drive reionisation? How abundant are these sources? How did ionising radiation escape these sources? What is the timeline of reionisation?*

What is the topology of the ionised bubbles? How can one learn about the first galaxies from reionisation and vice-versa?

1.4 Observations into the epoch of reionisation

The high-redshift Universe has proven to be challenging to observe. Not only the galaxies themselves tend to be fainter (Bouwens et al., 2015), but a large portion of the radiation emitted from galaxies does not reach us due to the opacity of the IGM. In the last couple of decades, studies have used light from distant quasars (QSOs) to probe the intervening IGM. Observations of increasingly opaque Gunn-Peterson (Gunn & Gott, 1972) troughs in QSO spectra at $z > 6$ (Fan et al., 2006) have provided us with a strong constraint on the timing of the end stages and patchiness of reionisation (Becker et al., 2015; Greig et al., 2017). Absorption features due to neutral clouds with column densities of $N_{\rm HI} \sim 10^{12-16}\rm cm^{-2}$ appear redward of the Gunn-Peterson trough in QSO spectra (commonly referred to as the "Lyα forest") and are used to constraint $x_{\rm HI}$ and sizes of residual neutral patches (Mesinger, 2010; Greig et al., 2017). The clouds that produce the Lyα forest are susceptible to ionization and heating from the ultraviolet background (UVB) produced by galaxies and quasars and can act as thermometers for the IGM during the later stages of reionisation. Therefore, one can use the thermal state of the Lyα forest to constraint the timing and the spectrum of ionising sources (Hui & Gnedin, 1997; Schaye et al., 2000; McDonald et al., 2001; Bolton et al., 2010; Becker & Bolton, 2013).

The most direct measurement of reionisation, however, can, in principle be made using the 21 cm line of neutral hydrogen (Ewen & Purcell, 1951; Taylor, 1950; Field, 1959; Scott & Rees, 1990; Furlanetto, 2006). The 21 cm line provides for a great probe as it emanates from the neutral component of the IGM, and as such does not saturate at the highest redshifts. As 21 cm is only absorbed in very dense neutral clouds, one can observe this line along sightlines to bright radio loud sources. Absorption or emission by H I alters 21-cm differential brightness temperature (δT_b), defined as the spin temperature relative to the CMB temperature. δT_b additionally is a function of the local overdensity and $x_{\rm HI}$ (see Zaroubi 2012). Measurement of δT_b would place robust constraints on the $x_{\rm HI}$ evolution and the nature of ionising sources. In particular, features in evolution of δT_b give information on the X-ray and Lyα emissivities of the first sources like stars, galaxies and AGNs (Mirocha & Furlanetto, 2018; Ma et al., 2022). Various ongoing and future 21 cm experiments such as `PAPER` (Parsons et al., 2010), `LOFAR` (van Haarlem et al., 2013), `MWA` (Bowman et al., 2013), `HERA` (Neben et al., 2016), and `SKA` (Dewdney et al., 2009) aim to detect the 21 cm line in the coming decades.

To complete the picture of the high redshift universe, a comprehensive study of the sources of reionisation is key. While QSOs emit copious amounts of radiation, their number density disfavors them being the primary drivers of reionisation (Willott et al., 2010; Grissom et al., 2014; Kashikawa et al., 2015; Trebitsch et al., 2021). Therefore, it is widely accepted in literature that galaxies drive cosmic reionisation. Previously, deep spectroscopic surveys of galaxies deep into the EoR was not possible due to limitations in sensitivity and wavelength coverage. The Hubble Space Telescope (`HST`) largely relied on the photometric dropout techniques (Steidel et al., 1996) to find high redshift galaxies. HST has managed to find photometric candidates up to $z \sim 11$, deep into the EoR. At $z > 7$, only ~ 1000 galaxy candidates were previously detected, out of which only ~ 100 have been spectroscopically confirmed with ground-based telescopes like Keck, the Very Large Telescope (`VLT`), and the Atacama Large Millimeter/sub-millimetre Array (`ALMA`) (Robertson, 2022). Synergies between HST and the Spitzer Space Telescope enabled the first measurements of the rest-frame UV and optical spectral energy distributions of high redshift galaxies, allowing for estimates of the SFRs and stellar masses of the first galaxies. Using these observing facilities, various galaxy properties such as SFR (Stark et al., 2013), stellar mass (Duncan et al., 2014; Grazian et al., 2015; Stefanon et al., 2017), UV luminosity functions (UVLF) (Bouwens et al., 2015, 2022b; Harikane et al., 2022) and dust content (Schaerer & de Barros, 2010; Ouchi et al., 2013a) have been measured at $z > 6$.

Observations of Lyα emitters (LAEs) and visibility of LAEs (Stark et al., 2010; Pentericci et al., 2011; Stark et al., 2011; Pentericci et al., 2018) using ground-based follow ups of HST fields have added constraints on x_{HI} fractions. Additionally, presence of strong [O III] emission from these LAEs indicates efficient ionising photon production (Castellano et al., 2017; Harikane et al., 2018). Furthermore, follow-up observations of HST fields with `ALMA` have provided an unprecedented view into the ISM properties of reionisation-era galaxies. Infrared emission lines (e.g. [C II] 158 μm and [O III] 88 μm) detected by `ALMA` allow us to constrain the processes that regulate star-formation in galaxies that drive reionisation (Carniani et al., 2017; Pentericci et al., 2016).

With the successful deployment of the James Webb Space Telescope (`JWST`), the landscape of high-redshift observations has dramatically changed in last two years before the writing of this thesis. Deep spectroscopic surveys have allowed `JWST` to observe thousands of galaxies and hundreds of AGN up to $z \approx 14$. The expanded wavelength coverage ($\lambda \sim 1 - 28\mu m$) and high resolution allow for observations of rest-frame UV and optical emission lines, making the confirmation of galaxy redshifts easy. `JWST` is enabling us to now study the stellar mass (Barrufet et al., 2023; Gottumukkala et al., 2024; Wang et al., 2024), star-formation histories (Whitler et al., 2023; Endsley et al., 2023a; Atek et al., 2023; Simmonds et al., 2023a; Looser et al., 2023), ionisation state of the ISM (Rinaldi et al., 2023; Reddy et al., 2023; Sanders et al., 2023), metallicities (Vanzella et al., 2023; Curti et al., 2023; Nakajima et al., 2023; Morishita et al., 2023; D'Eugenio et al., 2024), outflow properties (Fujimoto et al., 2022; Carniani et al., 2023; Looser et al., 2023), ionising efficiencies (Prieto-Lyon et al., 2023; Endsley et al., 2023a,b; Simmonds et al., 2023a; Roberts-Borsani et al., 2024), structural and kinematic properties (Kartaltepe et al., 2023; Treu et al., 2023; Huertas-Company et al., 2023; Ito et al., 2024; Cutler et al., 2024; de Graaff et al., 2023) of galaxies at unprecedented resolution statistically at $z > 6$. Therefore, for the first time, we can characterise galaxies that drive reionisation and their physical properties. These observations provide invaluable constraints to compare theoretical models against.

In the context of cosmic reionisation, `JWST` has for the first time measured the ionising photon production of galaxies down to $M_{\mathrm{UV}} = -15.5$ (Atek et al., 2023) using both photometry and Balmer lines (Hα and Hβ) up to $z \approx 9$. Additionally, one can now potentially study ionised bubbles via the galaxy-IGM correlation (Garaldi et al., 2022; Kashino et al., 2023) and set limits on ionised bubble sizes via observations of Lyα emitters (Saxena et al., 2023b; Napolitano et al., 2024; Chen et al., 2024; Tang et al., 2024). It must be noted that uncertainties remain in both understanding of the instrument systematics and interpretations of observables (Bhagwat et al., 2024b; Narayanan et al., 2024a,b). Therefore, trends observed and constraints placed by `JWST` need to be tested against simulations to further our understanding of the high redshift Universe.

Owing to the characterisation of star-formation histories and emission line properties of galaxies, one of the most interesting questions posed in the light of `JWST` observations is: *What kind of feedback operates at high redshifts? Can we explain high-redshift galaxy properties and their evolution by invoking different modes of feedback?* Multiple studies suggest that galaxies that drive reionisation are likely to be low-mass galaxies with bursty star-formation histories (Asada et al., 2023a; Simmonds et al., 2023a; Endsley et al., 2023b; Atek et al., 2023). Additionally, morphological evolution of galaxies from disturbed systems to disk-like secularly evolving galaxies has been chalked down to the redshift evolution of burstiness of star-formation histories of galaxies (Ciesla et al., 2023). Therefore, a pertinent question that must be answered theoretically is: *How do variations in stellar feedback models influence our interpretations of the high-redshift universe?* In this thesis, I aim to answer these questions via simulations of the high-redshift universe. I describe the focus and methods employed in this thesis below.

1.5 Outline of this thesis

Numerical models of reionisation have become increasingly sophisticated in the last decade. Simulations of reionisation have begun to include galaxy scale physics, albeit in a sub-grid fashion to connect galaxy formation and reionisation. Different groups adopt varied approaches to their modelling with simulations such as `THESAN, CROC, CoDA` attempting to resolve the large scale reionisation process, whereas groups such as `SPHINX, SERRA, OBELISK` choose to resolve internal structures of galaxies. A common denominator among all these simulations is the extreme computing cost (tens of millions of CPU hours) involved in running RHD simulations. As a compromise, it is a normal practice to perform simulations for a single fiducial model at target resolution which is usually tuned to reproduce a specific observable (e.g. UV luminosity function at $z = 5$). Therefore, a systematic study of the effect of variations in input baryonic physics has remained relatively unexplored.

The approach taken in this thesis is to model galaxy formation and reionisation while resolving the multi-phase ISM in a cosmological volume. The emphasis of this thesis is on studying variations in supernova feedback prescriptions to quantify the impact of parameter choices and uncover observationally-testable connections between stellar feedback and the properties of the galaxies that drive reionisation.

Toward this goal, I perform a suite of simulations called `SPICE`, which includes (section 1.2.3) mechanical feedback from supernovae, radiative feedback in the form of ionising radiation (with on-the-fly radiation transport) and radiation pressure and chemical feedback via supernova ejecta. SPICE explores different models for SN feedback with variations in supernova delay times, supernova energies and the presence of hypernovae, predicted to exist in the metal-free conditions of the early universe (Kobayashi et al., 2006). Within the SPICE framework, I aim to quantify the imprints of different modes of feedback in observable properties of reionisation-era galaxies. By keeping all the ingredients of the simulation constant and varying only the feedback prescription, I am able to quantify *relative differences* between the feedback models, which ensure robust predictions and forward-modelling capabilities of the simulations.

The thesis is structured as follows:

- In Chapter 2, I describe the various methods used in the literature to simulate cosmic reionisation. Additionally, I describe the radiation transport method implemented in the radiation-hydrodynamics code `RAMSES-RT`, which is employed to simulate cosmic reionisation.

- In Chapter 3, I introduce `SPICE`, a novel suite of radiation-hydrodynamical simulations targeting galaxy formation and cosmic reionisation. I describe the ingredients of the simulations in detail, including the sub-grid models employed and stellar feedback variations. Furthermore, I present the global properties of the simulations in terms of galaxy populations, reionisation histories, and connection between galaxy morphologies and LyC escape fractions as a function of stellar feedback models.

- In Chapter 4, I use `SPICE` to study the imprints of stellar feedback on [C II] properties of high-redshift galaxies. I present a novel sub-grid model that uses radiation transport fluxes as output by the simulation along with the metallicity and non-equilibrium abundances of H I to predict emissivity of [C II] from each gas cell. I present global properties such as the $L_{\rm CII} - {\rm SFR}$ relation, the origin of [C II] suppression, and discuss the origin of broad [C II] lines as a function of stellar feedback. Finally, I test predictions from `SPICE` against observations of [C II] emitting galaxies from ALMA.

- In Chapter 5, I use `SPICE` to model Lyα properties of high-redshift galaxies to investigate the impact of radiative transfer effects (e.g. extended emission, Lyα-UV spatial offsets) and observational systematics (such as slit placement) on the measured Lyα equivalent widths (EW$_0$). I perform Monte Carlo radiative transfer of Lyα and UV photons for SPICE galaxies to forward model slit spectroscopy for ground-based slits and JWST-MSA pseudo-slits. Finally, I compare predictions from `SPICE` against ground-based (`VLT`, `Keck`, `MUSE`) and space-based observations (`JWST`) of Lyα emitters.

- In Chapter 6, I summarize the key results and discuss future directions and possible extensions of research presented in this thesis.

Chapter 2

Simulating cosmic reionisation

> "I'm implementing stuff that was implemented years ago only to find out this is not good enough to do what we wanted"
>
> Christian Partmann

2.1 Modelling techniques

In simplistic terms, modelling cosmic reionisation boils down to a photon counting exercise. The race between ionising photon production and sinks absorbing these photons describes the process of cosmic reionisation. Reionisation can be modelled with various levels of complexity with both analytical and numerical techniques (for a review see Gnedin & Madau 2022). Analytical models of reionisation are based on a set of equations that describe a statistical quantity (e.g volume-weighted HI fraction, x_{HI}) without necessarily a closed form solution. Numerical models of reionisation calculate a 3D realisation of the HI density field starting from initial conditions as described by random Gaussian fluctuations. I describe commonly used analytical (see 2.1.1, 2.1.2, 2.1.3) and numerical methods (see 2.1.4, 2.1.5, 2.1.6, 2.1.7) below. The choice of method is highly problem dependant and varies depending on the scale to be studied. I note that techniques described below are focused on simulations of reionisation while generally structure/galaxy formation simulations encompass a wider range of methods (see Teyssier & Commerçon 2019; Vogelsberger et al. 2020 for reviews).

2.1.1 The reionisation equation

The photon number counting exercise can be carried out by equating the volume of the ionised IGM to the rate of ionising photon production minus the rate of recombinations of

H II written as

$$N_{\rm ion}(t) = N_{\rm HII}(t) + \int_0^t N_{\rm HII}(t^{'})\frac{dt^{'}}{t_{\rm rec}(t')}, \tag{2.1}$$

where $t_{\rm rec}$ is the recombination time, $N_{\rm ion}$ is the number of ionising photons and $N_{\rm HII}$ is the number of ionised hydrogen atoms. The integral in the equation accounts for recombinations of H II. Averaging equation 2.1 over an "average" representative comoving volume of the Universe gives

$$\frac{1}{V}\frac{d}{dt}\langle N_{\rm ion}\rangle = \frac{1}{V}\frac{d}{dt}\langle N_{\rm HII}\rangle + \frac{1}{V}\langle\frac{N_{\rm HII}}{t_{\rm rec}}\rangle \tag{2.2}$$

Defining the ionised fraction of gas as $Q \equiv N_{\rm HII}/N_H = \langle n_{\rm HII}\rangle/\langle n_{\rm H}\rangle$ and rearranging equation 2.2 gives us the "reionisation equation" written as (Madau et al., 1999)

$$\frac{dQ}{dt} = \frac{\dot{n}_{\rm ion}}{\langle n_{\rm H}\rangle} - \frac{Q}{\bar{t}_{\rm rec}}, \tag{2.3}$$

where $\langle n_{\rm H}\rangle$ is the mean hydrogen density, $\dot{n}_{\rm ion}$ is the total ionising photon production rate and $\bar{t}_{\rm rec}$ is an effective recombination timescale. This equation is agnostic to the size, morphology, density and temperature of the patch of the Universe being studied. Equation 2.3 statistically describes the process of reionisation and is widely used (Haardt & Madau, 2012; Robertson et al., 2015; Khaire et al., 2016; Ishigaki et al., 2018) as it allows one to estimate the photon budget to achieve a reionisation history and explore various models essentially free-of-cost.

2.1.2 PDF based models

One can describe the ionisation state of the IGM using the volume-weighted PDF of IGM density $P_V(\Delta)$ (Miralda-Escudé et al., 2000). The premise of these models is that reionisation proceeds "outside-in" within ionised bubbles, i.e, into underdense voids first followed by dense self-shielded regions. The overlap of H II regions happens through low density channels between ionising sources while gas denser than a critical density ($\Delta_{\rm crit}(z)$) remains neutral due to self-shielding. At sub-horizon scales, the mean free path of ionising photons is decided by gas with density higher than $\Delta_{\rm crit}(z)$. Given a density PDF, the mass-averaged ionised fraction is written as

$$F_M(\Delta_{\rm crit}) = \int_0^{\Delta_{\rm crit}} \Delta P_V(\Delta) d\Delta. \tag{2.4}$$

Assuming a volume averaged recombination rate, Equation 2.1 for this model is written as

$$N_{\rm ion}(t) = F_M(\Delta_{\rm crit}) + \int_0^t \frac{dt}{\bar{t}_{\rm rec}}\int_0^{\Delta_{\rm crit}} \Delta^2 P_V(\Delta, t) d\Delta \tag{2.5}$$

For large Δ values, the recombination term dominates, while for small Δ ionisation dominates, hence, these models produce "outside-in" reionisation with outside referring to the low density regions that are the first to be reionised.

PDF based models have found applicability in studying quantities such as IGM optical depth and transmission of Lyα flux. The accuracy of PDF based models is anchored to our understanding of the shape of the PDF and the temperature-density relation is gas, there limiting their applicability to the post-reionisation IGM.

2.1.3 Excursion set models

PDF models as described previously usually assume a global uniform UV background and ignore the larger fluctuations in the density fields. Excursion set-based models, inspired by the Press-Schechter formalism (Press & Schechter, 1974) aim to provide a statistical representation of the fluctuating ionising field. These models connect the number of ionising photons available in a comoving radius R (or mass scales $M \equiv (4\pi/3)\overline{\rho}R^3$, where $\overline{\rho}$ is the mean density of the Universe) to the collapsed mass fraction in this volume. Following the extended Press-Schechter formalism, for Gaussian fluctuations on the scale of R, the fraction of collapsed mass ($f_{\rm coll}$) is given by

$$f_{\rm coll} = {\rm erfc}\left[\frac{\delta_c - \delta_R(z)}{\sqrt{2[\sigma^2_{\rm min} - \sigma_R(z)^2]}}\right], \tag{2.6}$$

where $\delta_R(z)$ and $\sigma(z)$ are the linear overdensity and rms fluctuations on the scales of R, δ_c is the density threshold for collapse according to linear-theory and $\sigma_{\rm min}$ is the rms density fluctuation at the smallest scale that can host an ionising source. The ionisation state of gas can then be determined by defining the ionising photon number needed to keep a volume ionised as

$$N_{\rm ion} = \zeta f_{\rm coll} N_H, \tag{2.7}$$

where $N_{\rm H}$ is the number of hydrogen atoms, ζ is a pre-factor to account for efficiency of ionising photon production. Therefore, after accounting for recombinations (substituting into Equation 2.1), a region of the Universe can be fully ionised if

$$\zeta f_{\rm coll} = 1 + \int_0^t x_{\rm HII} \frac{dt}{t_{\rm rec}}. \tag{2.8}$$

These equations (under the condition of $\delta_R > \delta_b(R, z)$) provide a constraint on the size of the H II regions, R where $\delta_b(R, z)$ gives a threshold for a region to be considered ionised. Such models predict the local x_{HI} and recombination rates therefore providing an estimate for size of ionised regions and topology of reionisation around a distribution sources of ionising photons.

2.1.4 Semi-numerical methods

Semi-numerical models are based on an analytical (excursion set) treatment of reionisation and operate under the assumption that cosmic reionisation starts in overdense regions. Under this assumption, a region of the IGM is ionised if the local number of ionising photons

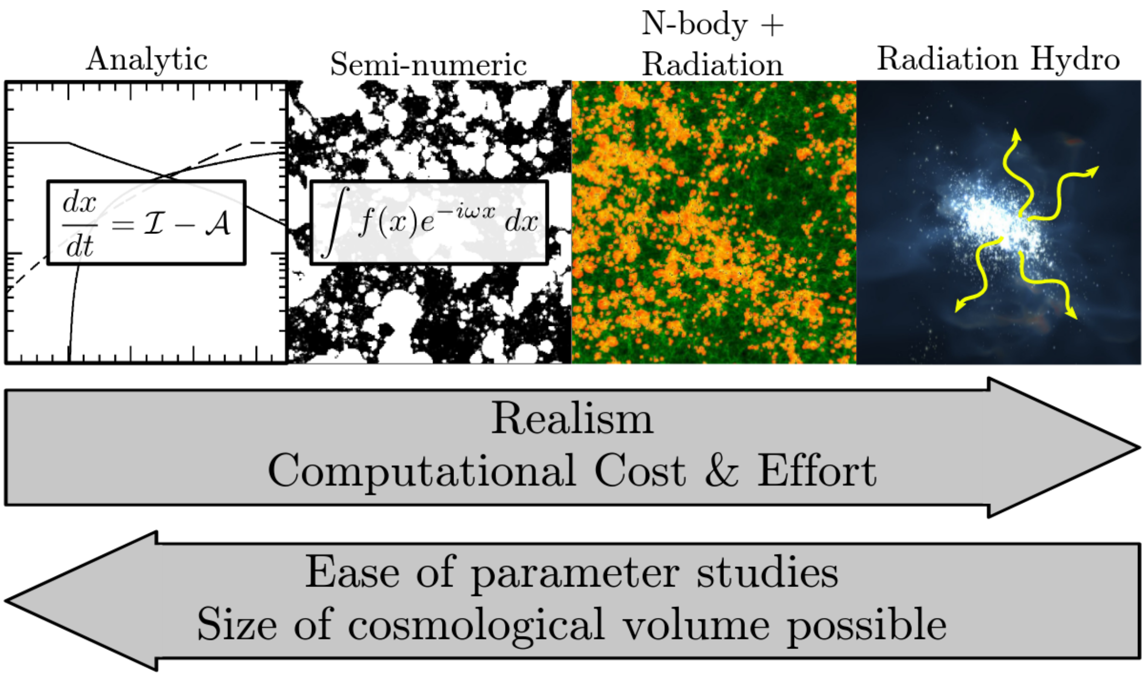

Figure 2.1: Four different modelling techniques commonly used to simulate cosmic reionisation: volume-averaged analytical models; semi-numerical methods; partially coupled radiation transport simulations that use matter distributions from N-body or hydrodynamical simulation ; fully coupled radiation hydrodynamic galaxy formation simulations. The increased physicality comes at the price of added computational cost, limiting the ability to explore variations in modelling of reionisation along with the relevant parameter space. This plot is taken from Wise (2019).

corrected for recombinations exceeds the number of baryons. These models tend to simulate 3D volumes and can accurately generate density and velocity following the Zel'dovich approximation and predict ionisation fractions without the need for accurately following underlying physics. The most widely used class of models in this category is `21cmFAST` (Mesinger et al., 2010) which is the go-to code used to make large scale reionisation-related field maps along with mock prediction for the 21 cm signal. Other semi-numeric codes include `ARTIST` (Molaro et al., 2019), `AMBER` (Trac et al., 2022) and `SCRIPT` (Maity & Choudhury, 2023).

2.1.5 N-body + Semi-analytical schemes

This approach involves using numerical dark-matter only simulations (N-body) combined with a semi-analytical model (SAM) to simulate galaxy formation and reionisation. These models are also able to compute the spatial distribution of neutral hydrogen therefore have a wide range of predictability. Various projects that use this scheme follow an excursion set-based formalism for the ionisation state of the IGM such as `ASTRAEUS` (Hutter et al., 2021), `DRAGONS` (Poole et al., 2016; Angel et al., 2016; Mutch et al., 2016). A key aspect of these projects is the large simulated volume ($\mathcal{O}(\sim 100\text{Mpc})$) which allows for converged ionised bubble distribution and reionisation histories (Iliev et al., 2014). The merit of schemes like `ASTRAEUS` and `DRAGONS` is that once the N-body simulations are produced, the SAMs are straightforward and cost-effective to run therefore allow parameter-space exploration in terms of galaxy formation parameters like strength of stellar feedback, star-formation efficiencies etc. Furthermore, codes like `GRIZZLY` (Thomas & Zaroubi, 2008; Ghara et al., 2015) allow for a novel approach for 1D radiative transfer on top of N-body simulations to simulate 21 cm emission during cosmic reionisation. These 1D radiative transfer simulations employ simulation volumes with sizes of ≥ 600Mpc and provides more accurate ionisation fields as compared to excursion set-based methods.

2.1.6 Partially coupled simulations

An intermediate compromise between the N-body+SAM technique and solving the radiative transfer equation self-consistently is a case where the radiation is not coupled to all the components in a simulation. An example of such a case would be simulations from Mellema et al. (2006); Iliev et al. (2006), which include radiative transfer but assume that the H I follows the dark matter density field. The gas dynamics remains unaffected by heating from UV radiation, and physical effects such as the suppression of gas accreting low-mass halos cannot be captured. The radiation sources are modelled with a semi-analytic model on top of the N-body/hydrodynamical simulation employed. Another method of partially coupling simulations is where radiative transfer solvers are run in post-processing on top of sophisticated galaxy formation hydrodynamical simulation as in Bauer et al. (2015). The obvious limitation of this method is that the gas dynamics does not respond to a spatially and temporally varying radiation field. Similar approach is post-processing with a Monte Carlo radiative transfer code like `CRASH` (Kulkarni et al., 2019a; Eide et al., 2020; Ma et al., 2022; Keating et al., 2020). The advantage of Monte Carlo codes is that one can extend the radiative transfer effects to X-rays and account for secondary ionisation. These methods serve as a cheaper alternative to exploit the full abilities of expensive DMO/hydrodynamical simulations to calculate the reionisation process in respective simulations.

2.1.7 Fully coupled simulations

The ultimate method to simulate the process of reionisation is to self-consistently couple gas physics and radiative transfer in a cosmological setting. Such models typically include most relevant physics like gravity, gas hydrodynamics, star-formation, stellar and AGN feedback and radiative transfer with a very large (typically 6-7 orders of magnitude) dynamical range of scales probed. With recent advancements in super-computing facilities, RHD codes such as `Arepo-RT` (Springel, 2010; Kannan et al., 2019), `RAMSES-RT` (Teyssier, 2002; Rosdahl et al., 2013a), `ENZO` (O'Shea et al., 2004) allow for simulating large volume with full radiative transfer on-the-fly. Radiative transfer algorithms in these codes solve for the evolution of the radiation field accounting for emission, absorption and scattering of photons. Existing algorithms solve for the evolution of the radiation field using "ray-tracing" methods or "moment-based" methods. For computing cost purposes, moment-based methods are the standard methods used which I describe in the following sections.

Fully coupled simulations largely fall into two main categories, those which resolve galactic scale heights sacrificing simulation volume (e.g `SPHINX`, `SERRA`, `OBELISK` (Rosdahl et al., 2018; Katz et al., 2018; Trebitsch et al., 2021; Pallottini & Ferrara, 2023)) and those which aim to capture the large scale reionisation process sacrificing on resolving galaxies (e.g `THESAN`, `CoDA`, `CROC` (Gnedin, 2014; Ocvirk et al., 2016; Kannan et al., 2022; Garaldi et al., 2022; Smith et al., 2022; Lewis et al., 2022)).

2.2 Radiation in an expanding universe

The temporal and spatial evolution of the specific intensity $I_\nu(t, x, n)$ in an expanding Universe is described using the radiative transfer equation written as (Gnedin & Ostriker, 1997; Abel et al., 1999; Petkova & Springel, 2009)

$$\frac{1}{c}\frac{\partial I_\nu}{\partial t} + \frac{\mathbf{n}}{a}\cdot\frac{\partial I_\nu}{\partial x} - \frac{H(t)}{c}\left(\nu\frac{\partial I_\nu}{\partial \nu} - 3I_\nu\right) = -\kappa_\nu I_\nu + S_\nu, \tag{2.9}$$

where x is the comoving coordinate, n is the unit vector along the direction of propagation of radiation, S_ν is the source term (in units of erg s^{-1} cm^{-3} Hz^{-1} sr^{-1}), c is the speed of light, a is the scale factor ($a(t) = 1/(1+z)$), $H(t)$ is the Hubble constant and κ_ν is the absorption coefficient. Equation 2.9 describes the classical radiative transfer equation in a static medium modified to take into account the change in path length due to expansion of the Universe (scale factor is added in the denominator of the second term) and cosmological redshift and dilution of intensity (third and fourth terms). In the limit where the length scale of interest is smaller than the cosmic horizon $L \ll c/H(t)$, one recovers the classical transfer equation. Equation 2.9 can be spatially and directionally averaged to obtain the mean specific background intensity ($\bar{J}_\nu$) written as

$$\frac{\partial \bar{J}_\nu}{\partial t} - H(t)\left(\nu\frac{\partial \bar{J}_\nu}{\partial \nu} - 3\bar{J}_\nu\right) = -c\bar{\kappa}_\nu\bar{J}_\nu + \frac{c}{4\pi}\epsilon_\nu, \tag{2.10}$$

where $\epsilon_\nu = 4\pi S_\nu$ is the mean volume emissivity. Solving for $\bar{J}_\nu$ we obtain

$$\bar{J}_\nu(t) = \frac{c}{4\pi}\int_0^t dt'\epsilon_{\nu'}dt'\left[\frac{a(t')}{a(t)}\right]^3 e^{-\bar{\tau}(\nu,t',t)}, \tag{2.11}$$

where $\nu' = \nu a(t)/a(t')$, along with

$$\bar{\tau} = c\int_{t'}^{t} dt''\bar{\kappa}_{\nu''}(t''), \tag{2.12}$$

where $\nu'' = \nu a(t)/a(t'')$. Therefore, a photon packet will suffer attenuation equal to $1/e$ after it travels a mean free path of $\lambda_{\rm mfp} = 1/\bar{\kappa}_\nu$. $\bar{\kappa}_\nu = \langle \kappa_\nu I_\nu \rangle / \bar{J}_\nu$ represents the specific intensity weighted mean opacity of gas.

Self-consistently solving equation 2.9 is difficult given that the equation has 7 dimensions (3D spatial coordinates, 2 angular coordinates, time and frequency), therefore, solving 2.9 in non-idealised scenarios is often computationally prohibitive. One therefore needs to adopt a method that allows for radiation transport in a cosmological simulation with a steep dynamical range in mass and physical resolution. The most common method adopted is to convert equation 2.9 into a hierarchy of moments of I_ν. Taking the zeroth and first angular moments of equation 2.9 one can describe the moment-based radiation transport equation as

$$\frac{1}{c}\frac{\partial J_\nu}{\partial t} + \frac{1}{a} \cdot \frac{\partial F^j_\nu}{\partial x^j} - \frac{H}{c}\left(\nu \frac{\partial J_\nu}{\partial \nu} - 3J_\nu\right) = -\kappa_\nu J_\nu + \tilde{S}_\nu, \tag{2.13}$$

and

$$\frac{1}{c}\frac{\partial F^i_\nu}{\partial t} + \frac{1}{a} \cdot \frac{\partial P^{ij}_\nu}{\partial x^j} - \frac{H}{c}\left(\nu \frac{\partial F^i_\nu}{\partial \nu} - 3F^i_\nu\right) = -\kappa_\nu F^i_\nu + Q^i_\nu, \tag{2.14}$$

where $J_\nu = \frac{1}{4\pi}\int d\Omega I_\nu(t, x, n)$ is the mean specific intensity, $F^i_\nu = \int d\Omega n^i I_\nu$ is the photon flux, $\tilde{S}_\nu$ is the angle averaged source term, Q^i_ν is flux source term. Finally, $P^{ij}_\nu = \int d\Omega n^i n^j I_\nu$ gives the radiation pressure tensor such that its trace is J_ν. This term is often expressed as a dimensionless tensor with a trace of unity known as the Eddington tensor, defined as

$$h^{ij} = P^{ij}_\nu / J_\nu. \tag{2.15}$$

However, computing the Eddington tensor just from the photon energy density and flux is not directly possible, therefore the hierarchy of moments is not closed. As a way around this issue, approximate schemes are employed such as the "M1 closure" or the "Optically thin variable Eddington tensor (OTVET)". I describe "M1 closure" method below as that is the method employed in this thesis. The M1 closure was introduced by Levermore (1984) with the ansatz for the Eddington tensor written as

$$h^{ij} = \frac{1-\alpha}{2}\delta^{ij} + \frac{3\alpha - 1}{2} n^i n^j, \tag{2.16}$$

where $n^i = F^i / \|F\|$ gives the unit vector along the direction of flux propagation,

$$\alpha = \frac{3 + 4f^2}{5 + 2\sqrt{4 - 3f^2}}, \tag{2.17}$$

and $f = \|F\| / J$. The term f represents the directionality of radiation at a given point and must have a value of $0 \leq f \leq 1$. Smaller values imply an isotropic radiation field whereas values close to 1 mean a highly directional field. One of the key advantages of using the M1 closure method is that it is purely local, i.e. evaluating it in a region of the simulation requires local quantities[1] along with the fact that it can retain directionality

[1]Using local quantities makes the simulation faster by avoiding additional communication steps

along the flow of radiation. M1 closure is widely used in cosmological simulation codes such as `AREPO-RT` and `RAMSES-RT`. In this thesis, I employ publicly available `RAMSES-RT` code to perform fully-coupled RHD simulations. The implementation of radiative transfer in `RAMSES-RT` is described below.

2.3 RAMSES-RT

`RAMSES-RT` (Rosdahl et al., 2013b; Rosdahl & Teyssier, 2015a) is a radiation-hydrodynamics extension of the Eulerian adaptive mesh refinement code `RAMSES`. `RAMSES-RT` solves the fully coupled gas hydrodynamics (see also Teyssier (2002)), the radiative transfer of stellar and AGN radiation along with self-gravity and dynamics of gas, dark-matter and stars. `RAMSES-RT` uses a first-order Godunov solver with M1 closure (see 2.2) for the Eddington tensor to solve the radiation transport equation. In numerical simulations performed with `RAMSES-RT`, timesteps are small enough such that $\Delta a_{\text{timestep}}/a \approx 1$, therefore, the change in the scale factor within a timestep is negligible $\bar{a} = 1$. Consequently, the second term in equation 2.9 reduces to $n \cdot \frac{\partial I_\nu}{\partial x}$. Finally, if the light crossing time within the simulation box is much shorter than the Hubble time, one can ignore the terms for cosmological redshifting and dilution of intensity. Therefore, equation 2.9 reduces to a non-cosmological form in this local approximation, written as (Mihalas & Mihalas, 1984)

$$\frac{1}{c}\frac{\partial I_\nu}{\partial t} + \mathbf{n} \cdot \frac{\partial I_\nu}{\partial x} = -\kappa_\nu I_\nu + S_\nu. \tag{2.18}$$

The moment-based RT equations in `RAMSES-RT` that govern the temporal evolution of the photon number densities and fluxes are written as

$$\frac{\partial N_\nu}{\partial t} + \nabla \cdot F_\nu = -\sum_j^{\text{ions}} n_j \sigma_{\nu j} c N_\nu + \dot{N}_\nu^* + \dot{N}_\nu^{\text{rec}} \tag{2.19}$$

and

$$\frac{\partial F_\nu}{\partial t} + c^2 \nabla \cdot \mathcal{P}_\nu = -\Sigma_j^{\text{ions}} n_j \sigma_{\nu j} c F_\nu, \tag{2.20}$$

where $\mathcal{P}_\nu$ is the pressure tensor to close the set of equations as described by equation 2.15 with the Eddington tensor given as in equation 2.16. The absorption coefficient is divided into constituent terms $n_j\sigma_{\nu j}$ where n_j is the number density of photo-absorbing species j and $\sigma_{\nu j}$ is the cross-section between photons of frequency ν and species j. The source term is split into components that indicate photon producing sources (stars, AGN) as $\dot{N}_\nu^*$ and the recombination term from gas is given by $\dot{N}_\nu^{\text{rec}}$. The equations stated above are continuous in frequency and therefore in a computational framework, need to be discretised such that RT is carried out in bins of frequency that are evolved separately. `RAMSES-RT` also tracks the non-equilibrium evolution of hydrogen and helium ionisation in each cell to consistently treat interactions of radiation and gas.

`RAMSES-RT` uses an operator-splitting strategy to solve equations 2.19-2.20. This involves decomposing the equations into three steps that are computed in a fixed sequence within each timestep Δt. The three steps are: photon injection, photon transport and thermochemisty. In the first step, radiation from various radiative sources (stars, AGN) is injected into the grid. This corresponds to N_i^* in equation 2.19. At a given time t and a timestep Δt, the discrete photon density update in a given cell is written as sum over all stellar sources in the cell:

$$N_i^{n+1} = N_i^n + \frac{f_{\rm esc}}{V} \sum_{\rm stars}^{cell} m_* [\Pi_i(\tau_*^{n+1}, Z_*) - \Pi_i(\tau_*^n, Z_*)], \tag{2.21}$$

where n denotes the timestep ($n = t$, $n+1 = t+\Delta t$), $f_{\rm esc}$ is the sub-grid escape fraction, V is the volume of the cell, m_*, τ_*, Z_* are the mass, age and metallicity fo the stellar particle. Finally, Π_i represents an interpolated model to describe the stellar photon output over its lifetime. `RAMSES-RT` typically reads stellar energy distributions (SED) to on-the-fly calculate the luminosities of stars to carry out the photon injection step.

In the photon transport step, the photons are transported as if they were freely flowing. The equation describing free-flowing photons is written as

$$\frac{\partial \mathcal{U}}{\partial t} + \nabla \mathcal{F}(\mathcal{U}) = 0, \tag{2.22}$$

where $\mathcal{U} = [N, F]$ and $\mathcal{F}(\mathcal{U}) = [F, c^2\mathcal{P}]$. Equation 2.22 is solved using an explicit conservative formalism which is written below (along x-axis) for simplicity as

$$\frac{\mathcal{U}_l^{n+1} - \mathcal{U}_l^n}{\Delta t} + \frac{\mathcal{F}_{l+1/2}^n - \mathcal{F}_{l-1/2}^n}{\Delta x} = 0, \tag{2.23}$$

where n is as before, l denotes the cell index along given axis. $\mathcal{F}_{l+1/2}$ and $\mathcal{F}_{l-1/2}$ denote inter cell fluxes calculated at cell interfaces. Therefore, once can calculate the updated cell state using this equation once the inter-cell fluxes are determined. The inter-cell fluxes in `RAMSES-RT` are computed using the so-called Global-Lax-Friedrich (GLF) function.

Finally, in the thermochemisty step, the interaction between photons and gas is calculated with zero divergence and radiation injection terms in equations 2.19 and 2.20. Absorption and emission of photons affect the gas via heating and cooling. To self-consistently solve for these interactions, `RAMSES-RT` evolves them with the thermal energy density ε of gas and the abundance of the species that interact with the photons. H I, He I and He II interact via photo-ionisations and their ionised counterparts via recombinations. The system of non-equilibrium thermochemisty equations solved by `RAMSES-RT` consists of

$$\frac{\partial N_i}{\partial t} = - \sum_j^{\rm HI,HeI,HeII} n_j \sigma_{ij}^B N_i + \sum_j^{\rm HII,HeII,HeIII} b_{ji}^{\rm rec} [\alpha_j^A - \alpha_j^B] n_j n_e, \tag{2.24}$$

$$\frac{\partial F_i}{\partial t} = - \sum_j^{\rm HI,HeI,HeII} n_j \sigma_{ij}^B G_i, \tag{2.25}$$

$$\frac{\partial \varepsilon}{\partial t} = \mathcal{H} + \mathcal{L} \tag{2.26}$$

$$n_{\mathrm{H}} \frac{\partial x_{\mathrm{HII}}}{\partial t} = n_{\mathrm{HI}} \left(\beta_{\mathrm{HI}} n_e + \sum_{\mathrm{i=1}}^{M} \sigma_{iHI}^{N} c N_i \right) - n_{\mathrm{HII}} \alpha_{\mathrm{HII}}^{A} n_e, \tag{2.27}$$

$$\begin{aligned} n_{\mathrm{He}} \frac{\partial x_{\mathrm{HeII}}}{\partial t} = n_{\mathrm{HeI}} &\left(\beta_{\mathrm{HeI}} n_e + \sum_{\mathrm{i=1}}^{M} \sigma_{iHeI}^{N} c N_i \right) + n_{\mathrm{HeIII}} \alpha_{\mathrm{HeIII}}^{A} n_e \\ &- n_{\mathrm{HeII}} \left(\beta_{\mathrm{HeII}} n_e + \alpha_{\mathrm{HeII}}^{A} n_e + \sum_{\mathrm{i=1}}^{M} \sigma_{iHeII}^{N} c N_i \right), \end{aligned} \tag{2.28}$$

$$n_{\mathrm{He}} \frac{\partial x_{\mathrm{HeIII}}}{\partial t} = n_{\mathrm{HeII}} \left(\beta_{\mathrm{HeII}} n_e + \sum_{\mathrm{i=1}}^{M} \sigma_{iHeII}^{N} c N_i \right) - n_{\mathrm{HeIII}} \alpha_{\mathrm{HeIII}}^{A} n_e, \tag{2.29}$$

where $\alpha_j^A(T)$ and $\alpha_j^B(T)$ represent case A and B recombination rates for species j (`H II, He II, He III`). The b_{ji}^{rec} is a boolean that states which photon group j-species recombinations emit into, and n_e is electron number density. Equation 2.26 describes the evolution of temperature via the photo-heating term ($\mathcal{H}$) and the radiative cooling term ($\mathcal{L}$). Equations 2.27, 2.28 and 2.29 describe the evolution of ionisation state x_{HII}, x_{HeII} and x_{HeIII} respectively. β_i gives the collisional ionisation rate for the given species and each of these equations account for photo-ionisation, recombinations and collisional excitation when relevant (see Rosdahl et al. (2013b) for full details of expressions used). For the stability of the solutions, no quantity can change by $> 10\%$ in a given timestep. If this occurs, timesteps are recursively split into smaller ones (sub-cycled) and thermochemisty is calculated until convergence in achieved.

Additionally, absorption of photons by hydrogen and dust can impart momentum to gas. The RHD solver in `RAMSES-RT` models (for full details of implementation see Rosdahl & Teyssier (2015b)) this via direct radiation pressure or in cases where a photon is absorbed by dust and re-emitted into lower energy groups ("multi-scattered photon"). Therefore, one can self-consistently model the emission, propagation, absorption along with feedback effects from radiation using `RAMSES-RT`. Combined with the sub-grid physics module available and developed for this thesis (see section 4.2.1), I run a suite of cosmological RHD simulations targeting galaxy formation and cosmic reionisation called `SPICE` which I introduce in the next chapter.

Chapter 3

SPICE: Connecting stellar feedback in the first galaxies and cosmic reionisation

"Because I am involved, they'll not think of Dune. They will somehow think it's named after the spice girls"

Dr. Tiago Costa

This work has been published in the Monthly Notices of the Royal Astronomical Society, Volume 531, Issue 3, July 2024, Pages 3406–3430

I present `SPICE`, a new suite of cosmological RHD simulations targeting the epoch of reionisation. The goal of these simulations is to systematically probe a variety of stellar feedback models, including "bursty" and "smooth" forms of supernova energy injection, as well as poorly-explored physical scenarios such as hypernova explosions and radiation pressure on dust. Subtle differences in the behaviour of supernova feedback drive profound differences in reionisation histories, with burstier forms of feedback causing earlier reionisation. However, some global galaxy properties, such as the dust-attenuated luminosity functions and star formation main sequence, remain degenerate between models. In particular, stellar feedback and its strength determine the morphological mix of galaxies emerging by $z = 5$ and that the reionisation history is inextricably connected to intrinsic properties such as galaxy kinematics and morphology. While star-forming, massive disks are prevalent if supernova feedback is "smooth", "bursty" feedback preferentially generates dispersion-dominated systems. Different modes of feedback produce different strengths of outflows, altering the ISM/CGM in different ways, and in turn strongly affecting the escape of Lyman continuum (LyC) photons. I establish a correlation between galaxy morphology and LyC escape fraction, revealing that dispersion-dominated systems have escape fractions 10-50 times higher than their rotation-dominated counterparts at all redshifts.

At the same intrinsic luminosity, dispersion-dominated systems should thus preferentially generate large H II regions as compared to their rotation-dominated counterparts. Since dispersion-dominated systems are more prevalent if stellar feedback is more explosive, reionisation occurs earlier in our simulation with burstier feedback. Statistical samples of post-reionisation galaxy morphologies probed with telescopes such as JWST, ALMA and MUSE can constrain stellar feedback at $z > 5$ and models of cosmic reionisation.

3.1 Introduction

About $380,000\,\mathrm{yr}$ after the Big Bang, protons and free electrons coalesce for the first time, leading to the formation of hydrogen and helium atoms. At this time, the Universe is mostly neutral. By $z = 5$ (e.g. Gaikwad et al., 2023), however, the vast majority of hydrogen has transitioned to an ionised state. This $\sim 1\,\mathrm{Gyr}$ period is known as the epoch of reionisation (EoR). Reionisation is brought about by the ionising flux generated by stellar populations in the first galaxies (Shapiro & Giroux, 1987; Madau et al., 1999; Gnedin, 2000; Robertson et al., 2010; Robertson et al., 2015; Eide et al., 2020), with quasars now thought to provide only a minor contribution (Kulkarni et al., 2019b; Mason et al., 2019b). The ionising photon budget is set by the abundance of young stars, while the ability of photons to escape from galaxies is governed by the structure of the interstellar medium (ISM), which, in turn, is shaped by a multitude of 'feedback' processes associated to star formation. Within the ΛCDM paradigm of galaxy formation, such processes must be invoked in order to prevent the overproduction of stars even at $z > 6$ (Hopkins et al., 2014; Costa et al., 2014; Somerville & Davé, 2015).

These feedback processes include massive stellar winds (Weaver et al., 1977; Mackey et al., 2015; Geen et al., 2020; Lancaster et al., 2021; Guszejnov et al., 2022), photo-ionisation and photo-heating (Geen et al., 2015; Peters et al., 2017a; Kim et al., 2018), radiation pressure (Murray et al., 2005; Menon et al., 2022) and supernova explosions (Dekel & Silk, 1986). The impact of stellar feedback on the phase structure of the ISM is well established (McKee & Ostriker, 1977; Chevalier & Clegg, 1985; Walch et al., 2015; Martizzi et al., 2016; Kim et al., 2017). Feedback in the form of ionising radiation suppresses radiative cooling (Efstathiou, 1992; Gnedin, 2000; Somerville, 2002; Okamoto et al., 2008). Strong radiation fields can also reduce the baryon fractions of galaxies via photo-heating, further suppressing growth (Wise & Abel, 2008; Okamoto et al., 2008; Hasegawa & Semelin, 2012; Wise et al., 2012; Pawlik et al., 2013). Supernova explosions heat the ISM (McKee & Ostriker, 1977) and launch galactic outflows, expelling ISM material that would otherwise form stars (e.g. Dubois & Teyssier, 2008; Puchwein & Springel, 2013; Fielding et al., 2018; Orr et al., 2019; Martizzi, 2019). Theoretical studies have for decades emphasised the importance of turbulence in shaping the ISM. Turbulence can be driven by processes such as gravitational instability (Klessen & Ballesteros-Paredes, 2004) and feedback from supernovae (Larson, 1981; Solomon et al., 1987; Heyer & Brunt, 2004; Federrath, 2016). Feedback-driven turbulence in the ISM can both inhibit and drive star formation by either providing support against gravitational collapse, or by creating strong density contrasts allowing for rapid collapse, hence strongly regulating star formation efficiency (Krumholz & McKee, 2005; Ostriker et al., 2010; Ostriker & Shetty, 2011; Faucher-Giguère et al., 2013; Gatto et al., 2016).

By influencing the structure of the ISM, stellar feedback plays a direct role in cosmic reionisation. Recent studies highlight the importance of supernova-driven outflows in facilitating Lyman continuum (LyC, photons with energy > 13.6eV) escape (Wise & Cen, 2009; Kimm & Cen, 2014; Trebitsch et al., 2017, 2018; Rosdahl et al., 2022a) through the creation of low-density channels. The impact of stellar radiation itself on the ISM, however, remains less clear. While studies agree that photo-ionisation feedback suppresses star formation bursts by counteracting the formation of high-density peaks in the ISM (Rosdahl et al., 2015; Peters et al., 2017b; Haid et al., 2018), the role of radiation pressure is less settled. Analytical arguments (Murray et al., 2005; Thompson et al., 2015) suggest that radiation pressure on dust should launch galactic winds if systems are sufficiently bright. Radiation-hydrodynamic (RHD) simulations, however, generally find that early stellar feedback (such as radiation pressure) acts to suppress outflows through a reduction in star formation and in supernova clustering (Kimm et al., 2018; Costa et al., 2019; Agertz et al., 2020; Smith et al., 2021). Recent observational evidence points to an 'effective Eddington limit' in star-forming galaxies at $z > 6.5$, observed through an absence of systems with high star formation rates and high optical depths (Fiore et al., 2023). Though possibly not a unique interpretation, such trends may suggest a link between dust obscuration and the strength of galactic outflows that is not captured by current models.

Besides questions surrounding the key feedback driving mechanisms, there are significant numerical uncertainties in the modelling of feedback in galaxy evolution simulations. An ab initio treatment of supernova feedback remains challenging in cosmological simulations due to prohibitive resolution requirements. Cosmological simulations thus have to resort to 'subgrid' models attempting to capture the impact of supernova feedback at the resolution scale, i.e. $\gtrsim 20\,\mathrm{pc}$[1]. While such subgrid models have become more sophisticated in the last decade (Rosdahl et al., 2017; Hopkins et al., 2018), uncertainties persist. For instance, while commonly adopted strategies account for unresolved 'PdV' work through a momentum boost (e.g. Kimm et al., 2015), current models may underproduce hot gas, essential for launching galactic outflows, if supernova explosions are not resolved (Hu, 2019). Even when enforcing the correct terminal momentum, many existing models have to boost supernova feedback in order to reproduce realistic galaxy star formation rates and masses. Missing physics, such as cosmic ray injection and transport (Diesing & Caprioli, 2018), have been proposed as possible ways to further strengthen stellar feedback (e.g. Martin-Alvarez et al., 2022).

Another possible approach to overcome limitations caused by insufficient resolution and decouple the impact of stellar radiation and supernova feedback from the host's ISM, is through the adoption of an effective model for galactic winds (Springel & Hernquist, 2003; Pillepich et al., 2017), with a prescribed mass outflow rate and velocity. While

[1] In this thesis, I denote comoving coordinates as "cpc, ckpc" etc and physical coordinates as "pc, kpc" etc.

this approach promotes good numerical convergence properties, it limits the simulations' insight into the detailed interaction between supernovae, stellar radiation and the ISM and properties of host galaxies, restricting its effects to the scale of the intergalactic medium (IGM). It also introduces difficulties in the generation of mock observables, such as Lyα or X-ray emission, to which the ISM contributes significantly.

The recent influx of observations from JWST has begun to provide statistical samples of galaxies at unprecedented resolution deep into reionisation. Probes such as spectral energy distribution (SED) fitting, emission line ratios and UV/Hα SFR indicators help constrain star formation properties of high redshift galaxies. While a large number of studies find that bursty star formation (Atek et al., 2023; Dressler et al., 2023a; Tacchella et al., 2023; Langeroodi & Hjorth, 2023; Endsley et al., 2023a; Asada et al., 2023a) dominates the histories of $M_* \leq 10^9$ M$_\odot$ galaxies, there is also evidence of a smoother star formation channel or even a combination of the two (Ciesla et al., 2023; Dressler et al., 2023b). Recently, a bursty star formation history (SFH) has been invoked to alleviate (Sun et al., 2023a,b; Steinhardt et al., 2023) the so-called "too many too bright" galaxies problem (Ferrara et al., 2023; Boylan-Kolchin, 2023). Other studies find that galaxies with bursty SFH could be the main drivers of reionisation (Simmonds et al., 2023a; Endsley et al., 2023a,b; Atek et al., 2023). Therefore, understanding the implications of different SFH in high redshifts galaxies is key, and careful theoretical modelling will help to interpret various observations. Theoretical studies such as Hartley & Ricotti (2016) and Furlanetto & Mirocha (2022) use semi-analytical models to understand the effect of a bursty SFH on reionisation, finding that the sizes of HII regions are strongly modulated by bursts.

Over the last decade, RHD simulations of reionisation such as `CROC` (Gnedin, 2014), `Renaissance` (O'Shea et al., 2015), `Aurora` (Pawlik et al., 2017), `Technicolor Dawn` (Finlator et al., 2018), `SPHINX` (Rosdahl et al., 2018; Katz et al., 2018; Rosdahl et al., 2022a), `CoDa` (Ocvirk et al., 2016, 2020; Lewis et al., 2022) and `THESAN` (Kannan et al., 2022; Garaldi et al., 2022; Smith et al., 2022) have used variations of the stellar feedback prescriptions previously described to simulate the high redshift universe (see Gnedin & Madau 2022 for a detailed review). Different simulations adopt varied approaches toward their modelling, with simulations like `THESAN`, `CoDa` and `CROC` focusing on the large scale reionisation process with fairly large volumes (though unable to resolve galaxy scale heights), whereas `SPHINX` focuses on resolving the internal structure of galaxies while compromising on volume. Due to the extreme cost of RHD simulations (tens of millions of cpu hours), most are performed for only a single fiducial model at the target resolution. The effect of variations of input baryonic physics has remained comparatively unexplored.

Available RHD simulations provide either a statistical sample of galaxies modeled within the same feedback prescription, or a variety of models for single, zoom-in galaxies (Pallottini & Ferrara, 2023; Katz et al., 2022b). A systematic and statistical study of the effect of different feedback models is thus missing. The approach taken in this chapter is to model galaxy formation and reionisation such that I maximize how well I resolve the multi-phase ISM (down to ≈ 28pc at $z = 5$) in a cosmological volume ($L_{\rm box} \approx 14.8$cMpc). The emphasis of these simulations is on the variations in supernova feedback prescriptions in order to quantify the impact of numerical uncertainties and to uncover observationally-testable connections between stellar feedback and the properties of the galaxies that drive reionisation. I introduce SPICE, a suite of simulations which include mechanical feedback from supernovae, stellar feedback in the form of ionising radiation (with on-the-fly radiation transport) and radiation pressure. Our simulations explore different models for supernova feedback with variations in explosion timing, supernova energies and the presence of hypernovae, predicted to exist in the pristine conditions of the early universe (Kobayashi et al., 2006). Within the SPICE framework, I aim to understand how the effect of different modes of feedback manifests in observable properties of galaxies. Indeed, by varying only the feedback prescription while keeping everything else constant, I am able to quantify *relative differences* between the feedback models.

This chapter is organised as follows. In Section 3.2 I describe the SPICE suite of simulations setup along with the physics prescriptions that are included. In Section 3.3 I present that results on the effect of stellar feedback on star formation, reionisation, UV luminosity functions, galaxy morphologies and LyC escape fractions. In Sections 4.5 and 3.5 I discuss and summarize my findings, respectively.

3.2 The SPICE simulations

In this section, I describe the simulations performed and post-processed for this study. I perform a total of three flagship simulations to study the effect of variations in supernova feedback. Relevant global simulation parameters are summarized in Table 3.1, while individual variations in feedback processes are briefly described in Table 3.2.

All simulations are performed with RAMSES-RT (Rosdahl et al., 2013a; Rosdahl & Teyssier, 2015b), which is a radiation-hydrodynamics extension of the Eulerian adaptive mesh refinement code RAMSES (Teyssier, 2002). RAMSES-RT solves the coupled gas hydrodynamics, radiative transfer of stellar radiation along with the self-gravity and N-body dynamics of gas, dark matter and stars. RAMSES-RT uses a first-order Godunov method with the M1 closure for the Eddington tensor (Levermore, 1984) to solve the radiation transport equation. I employ the 'Global–Lax–Friedrich' (GLF) Riemann solver to advect radiation between cells.

The adaptive mesh nature of the code allows for the grid to be dynamically refined in order to obtain higher numerical resolution within sub-regions of the simulation domain. I summarize the models used for our simulations below, with sections 3.2.1-3.2.5 describing global setup within RAMSES-RT and sections 3.2.6-3.2.11 describing the novel combination of galaxy formation and feedback models I include in the simulations.

3.2.1 Initial conditions

The initial conditions (ICs) for the simulations are setup at $z = 30$ using monofonIC[2] (Hahn et al., 2020; Michaux et al., 2020) with the 2PPT/2LPT approach. A ΛCDM cosmological model is adopted, with parameters $\Omega_\Lambda = 0.6901$, $\Omega_{\rm m} = 0.3099$, $\Omega_{\rm b} = 0.0489$, $H_0 = 67.74$

[2] https://bitbucket.org/ohahn/monofonic/

Name	Value	Description
$L_{\rm box}$	10 [cMpc/h]	Box size
$m_{\rm dm}$	6.38×10^5 [$\mathrm{M}_\odot$]	Mean mass of dark matter particles
$N_{\rm dm}$	512^3	Number of dark matter particles
m_*	975 [$\mathrm{M}_\odot$]	Minimum mass of stellar particles
$Z_{\rm floor}$	$3.2 \times 10^{-4}\ Z_\odot$	Metallicity floor at initial redshift
$f_{\rm esc}$	1.0	Stellar birth cloud escape fraction

Table 3.1: Basic properties of the simulated cosmological boxes, including the variable name, its adopted value and a short description.

Name	$\mathrm{t_{SNe}}$	$\mathrm{E_{SN/HN}}$ (erg)
`bursty-sn`	10 Myr	$2{\times}10^{51}$
`smooth-sn`	3-40 Myr	$2{\times}10^{51}$
`hyper-sn`	3-40 Myr	$10^{50} - 2 \times 10^{51}$(SN) + 10^{52}(HN)

Table 3.2: Description of various simulations and supernova feedback model variations. The columns list (from left to right) the name of the simulation, delay time for supernova events, energy per supernova event.

km/s/Mpc, $n_{\rm s} = 0.9682$, $\sigma_8 = 0.8159$ (Planck Collaboration et al., 2016a). A primordial gas mass fraction $X = 0.7545$ for Hydrogen (H) and $Y = 0.2455$ for Helium (He) is assumed, along with a metallicity floor (see 3.2.3). All simulation boxes have a length $L_{\rm box} = 10$ cMpc/h, with 512^3 dark matter particles, i.e. a mean mass $m_{\rm dm} = 6.38{\times}10^5$ $\mathrm{M}_\odot$. `MUSIC2-monofonIC` treats dark matter and baryons within the two-fluid approximation, using the novel 2nd order propagator perturbation theory (2PPT) (Uhlemann et al., 2019; Rampf et al., 2020). The 2PPT approach involves perturbing particle masses with a distribution centered at $m_{\rm dm}$ (see Hahn et al. 2020) which suppresses discreteness errors. `RAMSES-RT` evolves baryons from density and momentum fields which are discretised at fixed locations in Eulerian space. Traditionally, these Eulerian fields are generated from Lagrangian displacements and interpolated back onto Eulerian grids, thus introducing interpolation errors. The 2PPT approach directly yields these fields without ad-hoc interpolation (Porqueres et al., 2020), therefore providing accurate ICs for codes like `RAMSES-RT`.

3.2.2 Gravity and hydrodynamics

The Euler hydrodynamic equations are solved employing a second order Godunov scheme based on a MUSCL-Hancock method. I adopt the "HLLC" Riemann solver (Toro et al., 1994) to evaluate fluxes across all interfaces, and the MinMod slope limiter to construct gas variables at cell interfaces from their cell-centred values. To close the relation between gas pressure and internal energy, an adiabatic index of $\gamma = 5/3$ (for an ideal monatomic gas) is adopted. The dynamics of collisionless dark matter and stellar particles are computed using the Poisson equation with a particle-mesh solver. The dark matter and stellar particles are projected onto a grid with a cloud-in-cell interpolation (Guillet & Teyssier, 2011). I employ a multigrid solver (Guillet & Teyssier, 2011) to solve the Poisson equation up to a refinement level of 14 ($\Delta x \approx 100$pc), while at more refined levels I adopt a conjugate gradient solver to improve the computational speed.

3.2.3 Cooling and gas thermochemistry

Gas cooling and heating is calculated as described in Rosdahl et al. (2013a)[3]. `RAMSES-RT` evaluates the non-equilibrium ionisation states of H and He (HII , HeII , HeIII) in each computational cell, and advects them with the gas, as passive scalars (details of the quasi-implicit method can be found in Rosdahl et al. 2013a). They are fully coupled to the local ionising radiation field and for these primordial species, I include cooling and heating due to Bremsstrahlung, photoionisation, collisional ionisation, collisional excitation, Compton cooling off the cosmic microwave background, and di-electronic recombination.

The cooling contribution from metals at $T > 10^4$ K is computed using tables generated with CLOUDY (Ferland et al. 1998, version 6.02), assuming photoionisation equilibrium with a Haardt & Madau (1995) UV background. Instead, for $T \leq 10^4$ K I adopt the fine structure cooling rates from Rosen & Bregman (1995), allowing the gas to cool radiatively down to ≈ 300K. I also assume a homogeneous initial gas metallicity floor of $Z = 3.2 \times 10^{-4}\ Z_{\odot}$, which is used to mimic missing molecular hydrogen cooling channels and metal enrichment from Pop-III stars (Wise et al., 2011), and allows the gas to cool below $T = 10^4$ K. I also adopt the on-the-spot approximation, where emission of ionising photons from recombining gas is ignored, i.e. I assume that it is all absorbed locally, within the same cell.

3.2.4 Refinement strategy

The adaptive mesh refinement nature of `RAMSES-RT` allows for each parent gas cell to be split into 8 cells when certain conditions are satisfied (see below). The cell refinement level ℓ determines the width of each gas cell as $\Delta x_\ell = 0.5^\ell L_{\rm box}$. I allow refinement levels in the range $\ell = 9 - 16$. At the coarsest level ($\ell_{\rm min} = 9$) the minimum physical resolution of 4.8 kpc at $z = 5$ is achieved, while at the finest level ($\ell_{\rm max} = 16$) the maximum physical resolution is ≈ 28 pc at $z = 5$. Cells start at the coarsest level and are adaptively refined to higher levels to increase the numerical resolution of the simulation. A cell is refined if the following criteria are met:

1. if $M_{\rm dm} + \frac{\Omega_m}{\Omega b} M_{\rm b} > 8 \times m_{\rm dm}$ (quasi-Lagrangian refinement criterion), where $M_{\rm dm}$ and $M_{\rm b}$ are the total dark matter and baryonic (i.e. gas + stars) mass within the cell, and $m_{\rm dm}$ is the mean dark matter particle mass.

2. The cell width is larger than $\frac{1}{8}$ of the local Jeans length.

[3]Metal cooling is not currently modelled self-consistently with the local radiation, but see Katz (2022) for a development in this direction.

I adopt a constant comoving resolution throughout time, meaning that I allow for cells to be refined to $\ell_{\max}$ at all redshifts. This allows for the maximum physical resolution to be the highest at very high redshifts ($\approx$10.72 pc at $z = 20$).

3.2.5 Halo and galaxy finding

To identify dark matter haloes and galaxies, I use the AdaptaHOP halo finder (Aubert et al., 2004; Tweed et al., 2009) in the most massive submaxima mode. I fit a triaxial ellipsoid to each (sub-)halo and check that the virial theorem is satisfied within this ellipsoid, with the center corresponding to the location of the densest particle. If this condition is not satisfied, tje volume is iteratively decreased until one reaches an inner virialised region. From the volume of this largest ellipsoidal virialised region, I define the virial radius $R_{\rm vir}$ and mass $M_{\rm vir}$. For the halo finder, I require a minimum of 100 particles per halo. Halo finder parameters (as defined in Appendix B of Aubert et al. 2004) used are: $N_{\rm SPH} = 32$, $N_{\rm HOP} = 16$, $\rho_{\rm th} = 80$, and $f_{\rm poisson} = 4$. I also identify galaxies with AdaptaHOP. Here I require at least 100 stellar particles per galaxy. The galaxy-finder parameters are: $N_{\rm SPH} = 10$, $N_{\rm HOP} = 10$, $\rho_{\rm th} = 10^3$, and $f_{\rm poisson} = 4$.

3.2.6 Star formation

I employ the multi-freefall star formation model implemented by Kretschmer & Teyssier (2020). This includes a model for subgrid turbulence (as described in section 3.2.7), yielding a variable star formation efficiency that depends on local conditions described in terms of the virial parameter and the turbulent Mach number (see below). In each gas cell individually where the gas density is above a threshold of $n_{\rm H} \geq 10{\rm cm}^{-3}$, I adopt a standard Schmidt law, for which the star formation density is given as,

$$\dot{\rho}_* = \epsilon_{\rm ff}\frac{\rho}{t_{\rm ff}}, \tag{3.1}$$

where ρ is the gas density, $t_{\rm ff} = \sqrt{3\pi/(32G\rho)}$ is the freefall time, and $\epsilon_{\rm ff}$ is the star formation efficiency per freefall time. Typically, in galaxy formation simulations the value of $\epsilon_{\rm ff}$ is assumed to be a constant in the range 1-3 percent (Agertz et al., 2011), motivated by observations of inefficient star formation on galactic scales (Bigiel et al., 2008), as well as in Milky Way giant molecular clouds (GMCs) (Krumholz & Tan, 2007; Murray, 2011; Lee et al., 2016; Grisdale et al., 2019). This model can produce local (i.e. within a single computational cell) $\epsilon_{\rm ff}$ values as low as 0.1% likely suppressed by feedback (Ostriker & Shetty, 2011; Kim & Ostriker, 2015a), while also reaching values > 100% (i.e. star formation faster than freefall time). Feedback modulates star formation in different parts of the galaxy such that the global (averaged over the entire galaxy) $\epsilon_{\rm ff}$ values produced are in agreement with observations (see Fig. 6 in Kretschmer & Teyssier 2020).

I assume that the gas density within a supersonic turbulent medium such as the ISM is described by a log-normal probability distribution function (PDF) given as

$$p(s) = \frac{1}{\sqrt{2\pi\sigma_s^2}}\exp\frac{(s-\overline{s})^2}{2\sigma_s^2}, \tag{3.2}$$

where $s = \ln(\rho/\overline{\rho})$, σ_s is the variance of s, $\overline{s}$ is the mean logarithmic density $= -1/2\sigma_s^2$ and $\overline{\rho}$ is the mean density of the cell.

The local star formation efficiency $\epsilon_{\rm ff}$, as computed in Hennebelle & Chabrier (2011); Federrath & Klessen (2012), is

$$\begin{aligned} \epsilon_{\rm ff} &= \frac{\epsilon}{\phi}\int_{s_{\rm crit}}^{\infty}\frac{t_{\rm ff}(\overline{\rho})}{t_{\rm ff}(\rho)}\frac{\rho}{\overline{\rho}}p(s)ds & (3.3)\\ &= \frac{\epsilon}{2\phi}\exp\left(\frac{3}{8}\sigma_s^2\right)\left[1\ +\ \mathrm{erf}\left(\frac{\sigma_s^2 - s_{\rm crit}}{\sqrt{2\sigma_s^2}}\right)\right], & (3.4)\end{aligned}$$

where I assume that gas with density larger than a critical value, $s_{\rm crit}$, is converted into stars. The parameter $\phi = 1/0.49$ takes into account the uncertainty in free-fall timescales for gas with different densities and $\epsilon = 0.5$ accounts for the fact that not all gas above $s_{\rm crit}$ is converted into stars (both quantities are derived in Federrath & Klessen 2012). The critical density for star formation ($s_{\rm crit}$) is calculated using the model from Krumholz & McKee (2005). In order to extend the model to the subsonic regime, I allow star formation when a cell is gravitationally unstable ($\alpha_{\rm vir} < 1$) and $\mathcal{M} < 1$. The critical density accounting for both supersonic and subsonic regimes is

$$s_{\rm crit} = \ln\left[\alpha_{\rm vir}\left(1 + \frac{2\mathcal{M}^4}{1+\mathcal{M}^2}\right)\right] \tag{3.5}$$

Here,

$$\alpha_{\rm vir} = \frac{5\sigma^2}{3G\rho\Delta x^2} \tag{3.6}$$

is the local virial parameter, which is an indicator of local stability. Δx is the cell size, G is the gravitational constant, σ is the 1D turbulent velocity (see 3.2.7) and $\mathcal{M} = \sigma/c_s$ is the local Mach number, where c_s is the speed of sound.

This model therefore allows for two star formation channels. In the first channel, for which $\alpha_{\rm vir} < 1$ (independent of local $\mathcal{M}$), the entire computational cell is gravitationally unstable. In the second channel, collapse owing to large density fluctuations caused by supersonic turbulence, i.e. $\mathcal{M} \gg 1$ (see Figure 1 in Kretschmer & Teyssier 2020), becomes possible even if $\alpha_{\rm vir} > 1$. For reference, typical conditions for star-forming regions within the Milky way are $\alpha_{\rm vir} \simeq 3-10$ with $\mathcal{M} \simeq 10-20$ (Spilker et al., 2022), and correspond to $\epsilon_{\rm ff} \simeq 0.01-0.02$ (Murray, 2011; Grisdale et al., 2019).

Using the local star formation efficiency and the gas mass within the cell, I compute the number of new stellar particles in a given timestep by sampling a Poisson distribution.

The initial stellar mass of new stars is always an integer multiple of 970 $M_\odot$ ($\approx 95 - 97\%$ of stars in a simulation have a mass of 970 $M_\odot$), but it is capped such that a cell does not deplete more than 90% of its mass. I also assume that each stellar population represents a fully sampled Chabrier (2003) initial mass function (IMF).

3.2.7 Subgrid turbulence

Turbulence is modelled using a sub-grid scale approach (Schmidt et al., 2006). In the implementation of Kretschmer & Teyssier (2020), an additional equation for the turbulent kinetic energy is adopted to account for advection of turbulent energy and work done by turbulent pressure (Schmidt 2014 and Semenov et al. 2018). This is given by

$$\frac{\partial}{\partial t}K_{\mathrm{T}} + \frac{\partial}{\partial x_j}(K_{\mathrm{T}}\tilde{v}_j) + P_{\mathrm{T}}\frac{\partial \tilde{v}_j}{\partial x_j} = C_{\mathrm{T}} - D_{\mathrm{T}}, \tag{3.7}$$

where the turbulent kinetic energy $K_{\mathrm{T}} = 3/2\rho\sigma_{\mathrm{T}}^2$, is related to the turbulent pressure by $P_{\mathrm{T}} = 2/3K_{\mathrm{T}}$, with σ_{T} representing the 1D turbulent velocity dispersion. The left-hand side of the equation includes terms describing the time evolution, advection and compression. The right-hand side contains creation and destruction terms (C_T and D_T, respectively), which can be written as

$$C_T = 2\mu_T \sum_{ij}\left[\frac{1}{2}\left(\frac{\partial \tilde{v}_i}{\partial x_j} + \frac{\partial \tilde{v}_j}{\partial x_i}\right) - \frac{1}{3}(\nabla\cdot\tilde{v})\delta_{ij}\right]^2 = \frac{1}{2}\mu_T\left|S_{ij}\right|^2, \tag{3.8}$$

and

$$D_T = \frac{K_T}{\tau_{\mathrm{diss}}}, \tag{3.9}$$

where $\left|S_{ij}\right|$ is the mean flow viscous stress tensor (this term is evaluated as in Schmidt & Federrath 2011), $\tilde{v}$ is the mean flow variable (defined as $\tilde{v} = \overline{\rho v}/\overline{\rho}$) and the sum is calculated over the nearest neighbours of the computational cell in question. This model has two important parameters, the turbulent viscosity μ_T and the dissipation time-scale τ_{diss} , which are related to the cells' size by

$$\mu_T = \overline{\rho}\Delta x\sigma \quad \text{and} \quad t_{\mathrm{diss}} = \frac{\Delta x}{\sigma}. \tag{3.10}$$

Previous implementations of turbulent star formation sub-grid models consider an in-situ calculation (Kimm et al., 2017) of the turbulent velocity dispersion (Perret et al., 2015; Trebitsch et al., 2017, 2018; Hopkins et al., 2018), which can be thought of as the stationary limit of the model used in this work (i.e. the creation and destruction terms are considered to be equal). In our case, the model accounts for the non-equilibrium dissipation of the turbulent kinetic energy using the density and velocity fields without modifying the hydrodynamic solver. Turbulent velocity dispersion is estimated by solving Eq. 3.7 such that $\sigma = \sqrt{2K_{\mathrm{T}}/\overline{\rho}}$. The resulting velocity dispersion is adopted in Eq. 3.6 to evaluate the Mach number and the virial parameter entering the star formation efficiency computation (Eq. 3.4).

Group	ϵ_0 [eV]	ϵ_1 [eV]	$\langle\epsilon\rangle$ [eV]	$\sigma_{\rm HI}$ [cm^2]	$\sigma_{\rm HeI}$ [cm^2]	$\sigma_{\rm HeII}$ [cm^2]	$\kappa^0_{\rm abs}$	$\kappa^0_{\rm scat}$
IR	0.1	1	0.61	0	0	0	0	10
OP	1	13.6	5.51	0	0	0	10^3	0
UV I	13.6	24.59	17.9	3.19×10^{-18}	0	0	10^3	0
UV II	24.59	54.42	32.32	6.27×10^{-19}	4.78×10^{-18}	0	10^3	0
UV III	54.42	∞	67.77	7.37×10^{-20}	1.12×10^{-18}	8.71×10^{-19}	10^3	0

Table 3.3: *Columns left to right:* Photon groups, the lower and upper energies defining their energy interval, mean photon group energies , ionisation cross-sections to HI, HeI and HeII, absorption and scattering opacities to dust for each photon group.

3.2.8 Supernova feedback

I adopt the mechanical feedback scheme introduced by Kimm & Cen (2014) and implemented as in Kimm et al. (2015) see Hopkins et al. (2014) for a similar setup). The key idea behind this model is to correctly capture the terminal momentum associated to the snowplow phase of a SN remnant, by injecting into the surrounding cells a radial momentum $p_{\rm SN}$ which depends on whether the adiabatic (Sedov-Taylor) phase is resolved. The model introduces a parameter χ, which gives the ratio between the swept-up mass $M_{\rm swept}$ and the ejected mass $M_{\rm ej}$ for each neighbouring cell (number of neighbouring cells $N_{\rm nbor} = 48$) as

$$\chi \equiv dM_{\rm swept}/dM_{\rm ej}. \tag{3.11}$$

This is compared to a threshold value of

$$\chi_{\rm tr} \equiv 69.58\; n_{\rm H}^{-4/17} E_{51}^{-2/17} Z'^{-0.28}, \tag{3.12}$$

where E_{51} is the explosion energy of an individual SN in units of 10^{51} erg, $n_{\rm H}$ is the hydrogen number density in cm^{-3} and $Z' = \max[0.01, Z/{\rm Z}_\odot]$. Additionally,

$$dM_{\rm ej} = (1-\beta_{\rm sn})M_{\rm ej}/N_{\rm nbor}, \tag{3.13}$$

and

$$dM_{\rm swept} = \rho_{\rm nbor}\left(\frac{\Delta x}{2}\right)^2 + \frac{(1-\beta_{\rm sn})\rho_{\rm host}\Delta x^3}{N_{\rm nbor}} + dM_{\rm ej}. \tag{3.14}$$

Here $\rho_{\rm host}$ is gas density of the SN host cell, and $\beta_{\rm sn}$ determines what fraction of the gas mass ($M_{\rm ej} + \rho_{\rm host}\Delta x^3$) is re-distributed to the host cell of a SN (see Fig. 15 of Kimm & Cen 2014). The parameter $\beta_{\rm sn}$ is set to 4/52 to distribute the mass as evenly as possible to the host and neighbouring cells when the cells are on the same level of refinement.

If $\chi > \chi_{\rm tr}$ the adiabatic phase is not resolved and the momentum during the snowplow phase ($p_{\rm SN,snow}$) is injected to the neighbouring cells. Otherwise the momentum during the adiabatic phase ($p_{\rm SN,ad}$) is injected, i.e.

$$p_{\rm SN} = \begin{cases} p_{\rm SN,ad} = \sqrt{2\chi M_{\rm ej} f_{\rm e}(\chi) E_{\rm SN}} & \chi < \chi_{\rm tr}\ , \\ p_{\rm SN,snow} & \chi \geq \chi_{tr}\ , \end{cases} \tag{3.15}$$

where $f_{\rm e}(\chi) = 1 - \frac{\chi-1}{3(\chi_{\rm tr}-1)}$ smoothly connects the two regimes. The input momentum during the snowplow phase is

$$p_{\rm SN,snow} = 3\times10^{5}\ {\rm km\ s^{-1}M_{\odot}}\ E_{51}^{16/17}\ n_{\rm H}^{-2/17}\ Z'^{-0.14}, \tag{3.16}$$

following Blondin et al. (1998); Thornton et al. (1998); Geen et al. (2015); Kim & Ostriker (2015b). Geen et al. (2015) have shown that the final radial momentum from SN in the snowplow phase can be augmented by photoionisation of their environments by massive stars. Following their approach, for each SN event, the local Strömgen radius $r_{\rm S}$ is calculated and compared with the cell width Δx. If the Strömgen radius is not well resolved ($\Delta x >> r_{\rm s}$), I adopt a final input momentum of

$$p_{\rm SN,snow} = p_{\rm SN,snow}{\rm exp}\left(-\frac{\Delta x}{r_{\rm s}}\right) + p_{\rm SN+PH}\left(1-{\rm exp}\left[-\frac{\Delta x}{r_{\rm s}}\right]\right) \tag{3.17}$$

where $p_{\rm SN+PH}$ is obtained using a fit to the results of Geen et al. (2015).

Our assumption of a Chabrier (2003) IMF implies that a fraction $\eta_{\rm sn} = 0.31$ of the initial mass of the stellar particle is recycled back into the ISM. Out of the recycled mass, a fraction of 0.05 is in form of metals heavier than He (Chabrier, 2003). Due to computational cost, I do not store individual element abundances, but rather track the ejected metal mass as a metallicity per cell. Our choice of the IMF gives a fixed supernova rate of 0.01639 SN $M_{\odot}^{-1}$, which results in 15 SN per star particle for our minimum stellar mass of 970 $M_{\odot}$.

3.2.9 Supernova feedback variations

Given significant uncertainties in numerical models for supernova feedback (see Section 3.1), I explore a number of variations in the timing and energy injected per supernova event, keeping the basic implementation described in Section 3.2.8 fixed. The aim of these model variations is to quantify how the behaviour of stellar feedback affects reionisation and galaxy properties at high redshift.

Bursty supernova feedback

In our first model, labeled `bursty-sn` due to the bursty star formation behaviour it drives, energy from all SN events associated to a given stellar particle is injected simultaneously. Thus, I assume that each stellar particle hosts one single SN explosion event at 10 Myr, i.e. equivalent to the mean time at which SN occur for a Chabrier (2003) IMF. I adopt a progenitor mass of 19.1 $M_{\odot}$, and assume that each individual SN injects 2×10^{51} ergs into its neighbouring cells. Since large amounts of energy are deposited simultaneously at the same position, supernova feedback in `bursty-sn` is particularly efficient. A similar feedback scheme has been previously adopted by the `NewHorizonAGN` and `Obelisk` simulations (Dubois et al., 2021; Trebitsch et al., 2021).

Smooth supernova feedback

The second model I explore is referred to as `smooth-sn`, because, unlike `bursty-sn`, it produces a smooth star formation history. Previous studies (Kimm et al., 2015; Su et al., 2018; Keller et al., 2022; Keller & Kruijssen, 2022) have shown that discretising SN injections in time is crucial. Indeed, for a given stellar population, SN with progenitor masses $> 20\ \mathrm{M}_\odot$ can explode as early as 3 Myr, whereas SN with a progenitor mass of $8\ \mathrm{M}_\odot$ can explode as late as 40 Myr. In `smooth-sn`, the SN delay times are accounted for by randomly sampling the lifetimes of individual stars using the inverse sampling method of a polynomial fit for the integrated SN rate from `STARBURST99` (see Fig 2. in Kimm et al. 2015). As before, for each individual SN I assume an energy injection of 2×10^{51} ergs and a progenitor mass of $19.1\ \mathrm{M}_\odot$. This setup is a step toward a more physically-motivated feedback model as compared to `bursty-sn`, and a variation has been previously adopted by the `SPHINX` simulations (Rosdahl et al., 2018, 2022b).

Variable supernovae and hypernovae feedback

In this model, called `hyper-sn`, I vary the injected supernova energy per explosion event and, in addition, include a contribution from hypernova events. Indeed, a (metallicity-dependent) fraction of type-II SN is theorized to be associated to very large energies (Kobayashi et al., 2006), in the range $10^{51} - 10^{53}$ erg. Such events are referred to as hypernovae (HN), and are expected to be more frequent in low metallicity environments (Kitayama & Yoshida, 2005; Kobayashi et al., 2006, 2007; Smidt et al., 2014). Indeed, to explain chemical compositions observed in metal-poor stars, Grimmett et al. (2020) argue that the hypernova fraction (fraction of all type-II SN events) in the early universe needs to be $> 50\%$, while it decreases with increasing metallicity to reach the estimated rate of $\sim 1\%$ in the local universe (Podsiadlowski et al., 2004). Simulations of star-clusters and idealized galaxies have tested the effect of hypernova on small scales (Su et al., 2018; Brown & Gnedin, 2022), finding that HN feedback can quench dwarf galaxies for up to ~ 1 Gyr, hence making them relevant to study during reionisation.

In `hyper-sn`, I assign each stellar particle a metallicity dependant HN fraction f_{HN} given as

$$f_{\mathrm{HN}} = \max\left[0.5\ \exp\left(-\frac{Z_*}{0.001}\right), 0.01\right], \tag{3.18}$$

where Z_* is the metallicity of the stellar particle. f_{HN} represents the fraction of all SN events a stellar particle undergoes that are classified as HN. I assume an initial HN fraction of $f_{\mathrm{HN}} = 50\%$ to explore the extreme case of strong feedback in metal-free environments. In case of an HN event, I inject an explosion energy of 10^{52} erg. A constant progenitor mass of $30\ \mathrm{M}_\odot$ is assumed for all HN events (Grimmett et al., 2020).

For SN explosions, I assume that progenitors with different masses (between 8-40 $\mathrm{M}_\odot$, see Díaz-Rodríguez et al. 2018) explode at different times and inject different energies and masses into the surrounding medium. Thus, in addition to sampling the explosion times as described in the `smooth-sn` model, I also stochastically assign different energies to each SN event following a normal distribution centered at 1.2×10^{51} erg (best fit distribution using the Z9.6+W18 model as in Sukhbold et al. 2016), with minimum and maximum energies of 10^{50} and 2×10^{51} ergs, respectively (Sukhbold et al., 2016; Díaz-Rodríguez et al., 2018, 2021).

3.2.10 Radiative transfer

`RAMSES-RT` solves radiation transport by taking the first two moments of the radiative transfer equation and obtaining a system of conservation laws which is closed with the M1 closure of the Eddington tensor (Levermore, 1984). Further details of the methods used for the injection, propagation, and interaction of the ionising radiation with hydrogen and helium are described in Rosdahl et al. (2013a), while the diffusion of multi-scattering IR radiation is followed with the trapped/streaming photon scheme presented in Rosdahl & Teyssier (2015b). Each photon group, defined by a frequency interval, is described in each grid cell by the radiation energy density and the bulk radiation flux, which corresponds approximately to the radiation intensity integrated over all solid angles. `RAMSES-RT` solves the non-equilibrium evolution of the ionisation fractions of hydrogen and helium, along with photon fluxes and the gas temperature in each grid cell.

Since radiation is advected on the grid with an explicit solver, the simulation time-step is subject to the Courant condition. Since the RT time-step can become significantly smaller than the hydrodynamic time-step, I subcycle the RT on each AMR level, with a maximum of 500 RT steps performed after each hydro step (if the projected number of RT steps exceeds 500, the hydro time-step length is decreased accordingly). During the subcycling on each level, radiation is prevented from propagating to other levels and the radiation flux across boundaries is treated with Dirichlet boundary conditions. Details of the subcycling scheme in the context of flux-limited diffusion are given in Commerçon et al. (2014).

To prevent prohibitively small time-steps and a large number of RT subcycles, I adopt the 'reduced speed of light approximation' (RSLA) (Gnedin & Abel, 2001) with the global reduced speed of light set to $\tilde{c} = 0.1c$. Note that such approximation is used to advect the radiation field, while processes such as radiation pressure are treated with the full speed of light (Rosdahl & Teyssier, 2015b). Studies performed by Costa et al. (2018a,b) demonstrate a mild effect of the RSLA on the spatial extend of outflows driven by radiation pressure. When adopted in cosmological simulations targeting reionisation (Gnedin, 2016; Ocvirk et al., 2016; Deparis et al., 2019), the RSLA is found to affect mainly the post-reionisation neutral hydrogen fractions, which tend to be overestimated for a lower speed of light, while the differences are minimal during the overlap phase. Previous large scale simulations of reionisation (Rosdahl et al., 2018; Ocvirk et al., 2020; Kannan et al., 2021; Rosdahl et al., 2022b) adopt different values for $\tilde{c}$, in the range $(0.01 - 0.2)c$, while finding convergence with values as low as $\tilde{c} = 0.1c$ (Wu et al., 2019). Therefore, I use results from these studies and adopt $\tilde{c} = 0.1c$.

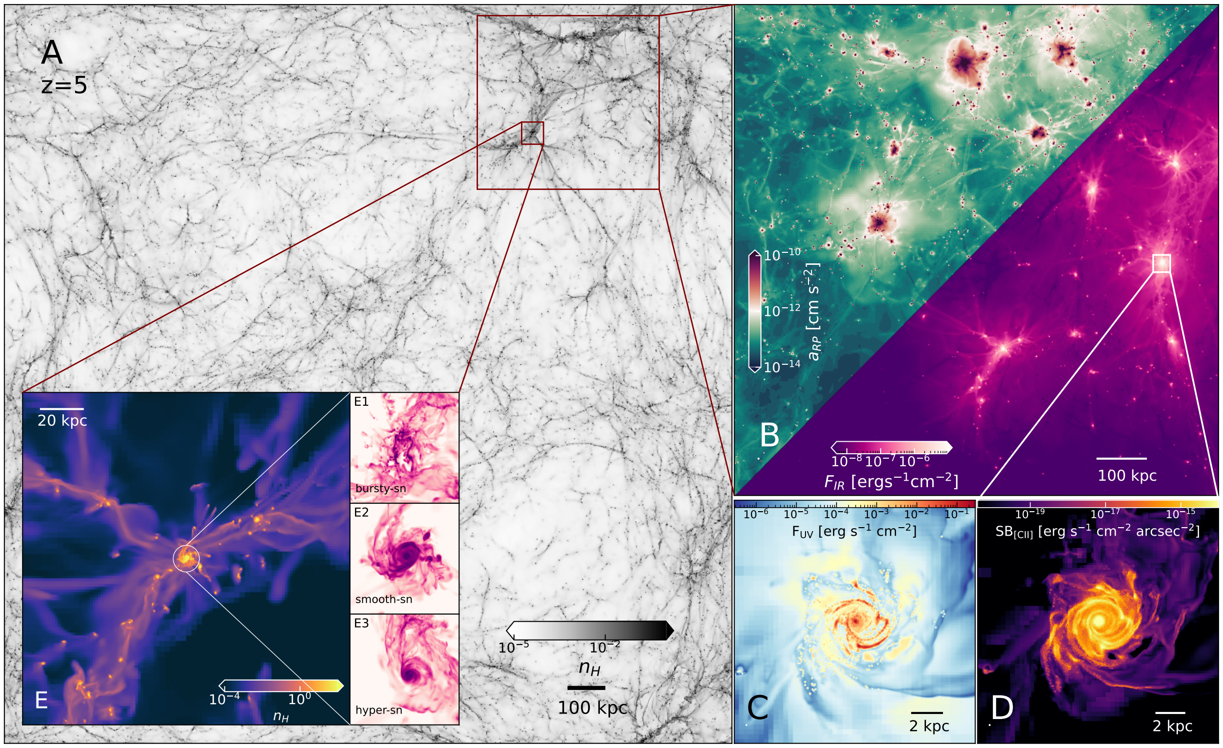

Figure 3.1: The `SPICE` simulations and their scope and dynamic range. In panel `A` I plot the volume-weighted gas density $z = 5$, showing the cosmic web on the largest scales captured by the simulations. Panel `B` shows a square region projected in two different quantities: the acceleration on gas produced by radiation pressure on dust (upper triangle), and infrared flux emergent from the galaxies (lower triangle). Panel `C` shows the flux of ionising radiation escaping from a disc galaxy. One can see channels of high (bright orange) LyC escape within the spiral arms of the galaxy and regions of inefficient escape (blue). `SPICE` traces LyC radiation escape on scales of $\Delta x \approx 28$pc. In panel `D` I show the surface brightness of the same galaxy in `[CII]`. In panel `E`, I zoom on a region of size $4 \times R_{\rm vir}$ (≈ 120kpc) centred on a $\approx 2.7 \times 10^{11} {\rm M}_{\odot}$ halo. The central galaxy is fed by large-scale cold inflows. Sub-panels `E1,E2,E3` highlight the very different gas density distributions emerging for this galaxy across our different simulations. In some simulations (e.g. `smooth-sn`, `hyper-sn`), gas has settled into a disc, while in others (`bursty-sn`), the gas component is strongly disrupted by strong outflows. Note that quantities shown in panels `A,B,C,D and E` are taken from `smooth-sn` and can vary between models.

3.2.11 Stellar radiative feedback

I sample radiation fluxes from stellar populations in five photon frequency groups, i.e. infrared, optical and three bands of ionising ultraviolet photons, whose widths are determined by the ionising potentials of HI, HeI and HeII. The frequency ranges, characteristic energies, ionisation cross-sections and dust opacities are listed in Table 3.3. Each of these radiation groups plays a key role in terms of radiative feedback on galaxy formation. For each stellar particle, the mass, age and metallicity-dependent stellar specific luminosities are extracted on-the-fly from the SED model of BPASSv2.2.1 (Eldridge et al., 2017; Stanway & Eldridge, 2018) assuming a Chabrier (Chabrier, 2003) IMF. The SED spectra (in units of $\mathrm{erg\,s^{-1}\,M_\odot^{-1}\,\AA^{-1}}$) are tabulated according to age- and metallicity-dependent luminosities for each radiation group by integrating over the energy intervals. I use this tabulated SED (single table for each simulation) to extract the number of photons emitted by each stellar particle. The photons in each group are directly injected in the host cell of the stellar particle. I update the photo-ionisation cross sections and energies at fixed intervals for the radiation groups to represent the luminosity-weighted average of all emitting sources (see Rosdahl et al. 2013a).

The photons in the UV groups not only interact with gas via photo-ionisation and photo-heating, but also via radiation pressure from photo-ionisation and dust. In contrast, the infrared and optical groups do not ionise hydrogen or helium, but interact with gas via radiation pressure on dust. In `SPICE` I do not model dust as an active ingredient but assume that the dust number density scales with the gas-phase metallicity and the gas thermal state. Following Nickerson et al. (2018), I assume a local dust number density $n_{\rm d} \equiv (Z/Z_\odot) f_d n_{\rm H}$, where Z is the local metallicity, $f_{\rm d} = 1 - x_{\rm HII}$ is the neutral fraction of gas that holds dust, and $n_{\rm H}$ is the hydrogen number density. This ensures that the dust density depends not only on enrichment but also on the local thermal state, since dust is not expected to survive in photo-ionised gas (Finkelman et al., 2012; Kannan et al., 2020). To each photon group, I assign dust absorption and scattering opacities as given in Table 3.3. If absorbed by dust, the photon flux from the group is added to the infrared group, where it will interact with gas via multi-scattered radiation pressure (Costa et al., 2018a).

3.3 Results

In this section I present our main results, starting with a qualitative overview of the simulations.

3.3.1 Overview

Primordial gas cools to form the first stellar particle at $z = 22.4$. Feedback from massive stars via photo-ionisation begins immediately, and supernova feedback kicks in as early as 3 Myr (10 Myr) after a stellar particle is born in `smooth-sn` and `hyper-sn` (`bursty-sn`). Galaxies continue to grow and the first $M_* > 10^7 \mathrm{M}_\odot$ dwarf galaxies form as early as $z = 12$. In Figure 3.1, I illustrate the dynamic range of the `SPICE` simulations. I note that the quantities shown in this figure are largely taken from `smooth-sn`, but they can vary dramatically between models.

Panel *A* shows the volume-weighted gas density distribution on Mpc scales, illustrating the cosmic web at $z = 5$. At this redshift, `SPICE` has produced a population of $\approx 13,000, 10,000, 7,000$ resolved (see Section 3.2.5) galaxies with $M_* > 10^5 \mathrm{M}_\odot$ for the `smooth-sn`, `bursty-sn` and `hyper-sn` models, respectively. The most massive halo at

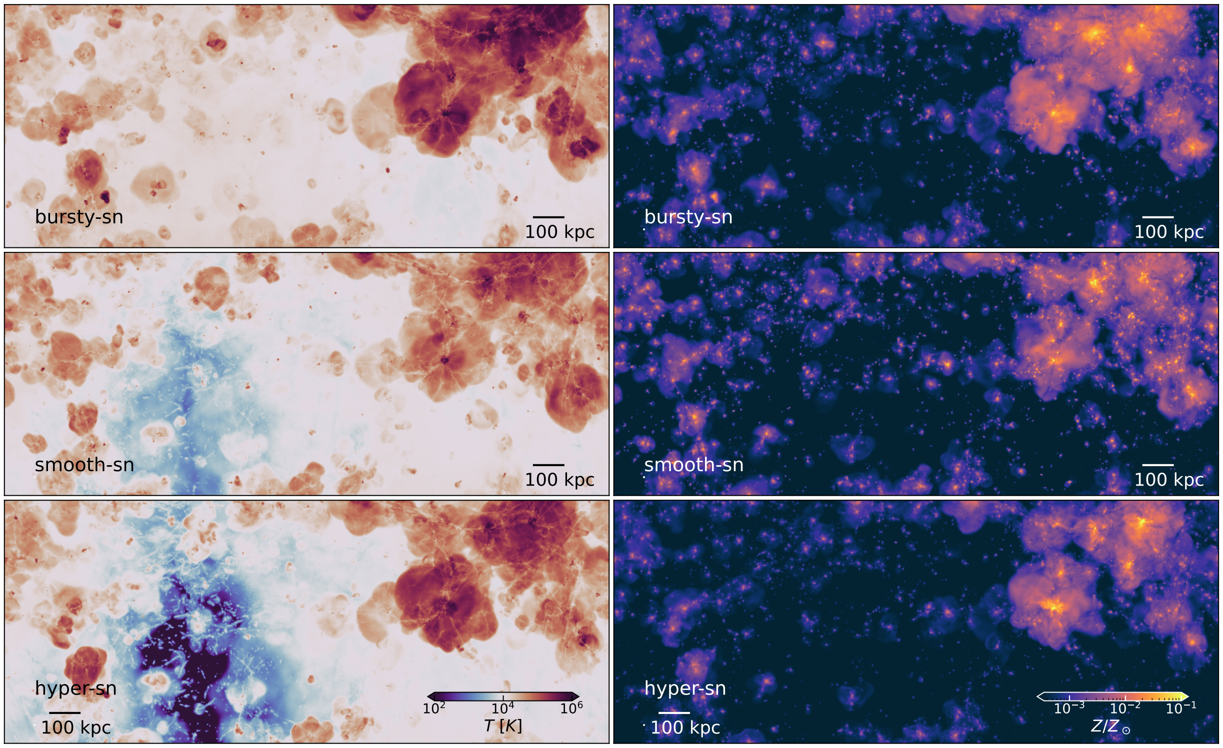

Figure 3.2: Temperature (left column) and gas-phase metallicity (right column) of the various simulations at $z = 5$. The projections shown cover a region spanning $L_{\rm box} \times L_{\rm box}/3 \times L_{\rm box}$. Consequences of varying the stellar feedback are imprinted in the thermal state and enrichment of the large-scale structure.

$z = 5$ in each simulation has a virial mass of $2.7 \times 10^{11}\mathrm{M}_\odot$ and hosts a stellar mass of $1.9 \times 10^{10}\,\mathrm{M}_\odot$, $2.1 \times 10^{9}\,\mathrm{M}_\odot$ and $1.7 \times 10^{10}\,\mathrm{M}_\odot$ for `smooth-sn`, `bursty-sn` and `hyper-sn`, respectively.

In panel `B`, I zoom onto an over-density in the simulations and highlight the quantities that describe the effect of novel physics included in `SPICE`, i.e, infrared radiation transport and consequently, radiation pressure on dust. The upper triangle in panel `B` shows the acceleration imparted to gas via radiation pressure on dust, with the highest radiation pressure observed very close to the centers of dusty galaxies. The lower triangle in panel `B` shows the infrared radial flux emerging from galaxies, which includes intrinsic emission from stars, dust emission and multi-scattered IR radiation. One can see a network of infrared-bright galaxies with a well established background by $z = 5$.

In panel `C` I zoom further into smaller scales, showing a single galaxy. I plot the radial flux of hydrogen-ionising radiation ($h\nu > 13.6\,\mathrm{eV}$) emerging from a $M_* = 2 \times 10^{10}\mathrm{M}_\odot$ galaxy. One can see the escape channels of LyC radiation, with bright orange/yellow colors representing HII regions through of which ionising radiation escapes most efficiently, and blue colours represent regions of inefficient escape. I investigate the connection between galaxy morphology and escape fractions of galaxies in Section 3.3.6.

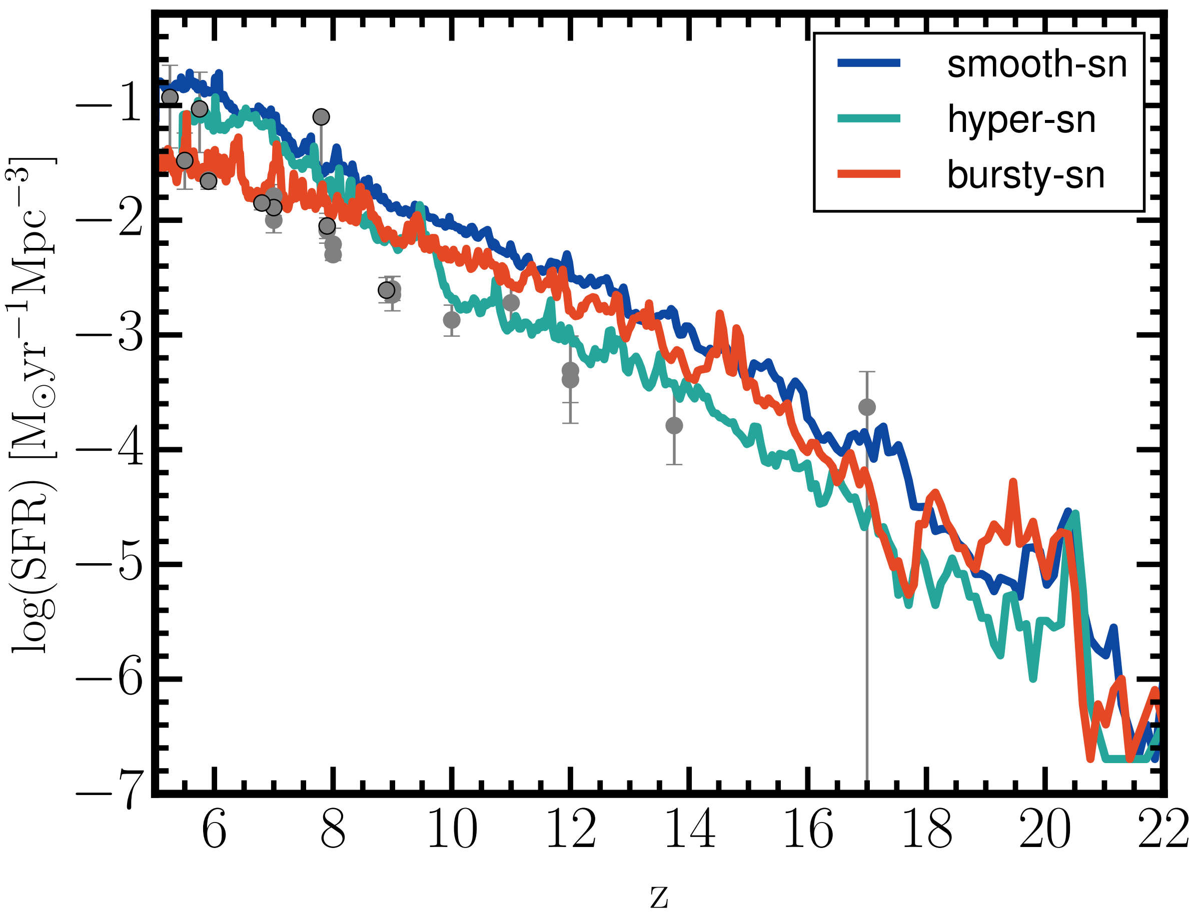

Figure 3.3: Cosmic star formation rate density as a function of redshift for the `bursty-sn` (red line), `smooth-sn` (blue) and `hyper-sn` (turquoise) models. Observational constraints (see text) are marked with grey circles. `hyper-sn` most closely reproduces the observed star formation density at $z \gtrsim 10$, while `bursty-sn` is closest to observational constraints at $z \lesssim 8$.

Panel `D` shows the surface brightness of the same galaxy in `[CII]` (a line which efficiently traces the cold phase of the ISM), calculated using a subgrid model which will be presented in detail in a follow-up study (Bhagwat et al, in prep). As `[CII]` is sensitive to the thermal state of the ISM, which is, in turn, shaped by feedback, this line can be potentially used to constrain feedback models.

Finally, panel E is a zoom onto a region of size $4 \times R_{\rm vir}$ ($\approx$ 120kpc) centred on a $\approx 2.7 \times 10^{11}M_\odot$ halo at $z = 5$. One can see this massive halo being fed by infalling gas filaments. I find further galaxies along the filaments, some with low mass companions. In `E1, E2 and E3`, I show the gas distribution of the central galaxies for our three different feedback models. The `bursty-sn` (`E1`) produces a highly irregular and disturbed gas distribution, in contrast to the `smooth-sn` (`E2`) model, which shows a well-formed disk galaxy. Finally, `hyper-sn` (`E3`) produces a compact disk-like density distribution. These distinct gas morphologies provide us with a first hint of the widely different effects of our feedback models on the morphology of the first galaxies.

In the left-hand panel of Figure 3.2, I show the gas temperature as obtained in the three feedback models at $z = 5$. The projections are calculated in a region of volume $L_{\rm box} \times L_{\rm box}/3 \times L_{\rm box}$. Bright red/maroon areas trace recent hot ($T > 10^6$ K) outflows driven by SN explosions, while the lighter brown regions ($T \approx 10^5$ K) trace older adiabatically-cooled ionised gas bubbles produced by previous star formation episodes. While these giant `HII` regions are present and co-spatial in all simulations, they are hottest and largest in `bursty-sn`, and least pronounced in `smooth-sn`. Beyond the SN-driven ionised gas lies a volume-filling, diffuse component with $T \sim 10^4$ K gas, shown by the bright white regions. This component consists of photoionised material which has been irradiated by stellar radiation at distances beyond those reached by feedback-powered ionised gas. The spatial scale of this diffuse component is set by the strength of SN feedback, as SN explosions create channels through which ionising photons can escape into the low density inter-galactic medium. A low volume-filling fraction of $T > 10^4$ K gas could arise from either inefficient feedback or a smaller ionising photon budget. However, I show in Sections 3.3.3 and 3.3.6 that the smaller volume-filling fractions seen in `smooth-sn` (middle-left panel) and `hyper-sn` (lower-left panel) arise in spite of a *higher* photon budget and are caused by low escape fractions. I see the presence of cold voids in both `smooth-sn` and `hyper-sn`, with the latter being colder and more extended. The difference between these two models is solely the SN feedback, highlighting the major role this plays in reionisation.

The right-hand panels of Figure 3.2 show metallicity projections for the various feedback models at $z = 5$. Simulation `bursty-sn` produces extended metal-enriched regions, again illustrating the stronger feedback present in this simulation. For instance, `smooth-sn` shows a larger number of compact enriched gas with typically higher maximum metallicities ($Z > 1Z_\odot$) at the very centers of halos. `hyper-sn` produces a distribution similar to `smooth-sn`, where the enriched regions are compact and with higher maximum metallicities [4]. However, `hyper-sn` contains visibly less structure than `smooth-sn` owing to the fact that low mass galaxies are much more effectively quenched (see section 3.3.2 and 3.3.4).

3.3.2 Cosmic star formation history

In Figure 3.3 I show the time evolution of the star formation rate density (SFRD) in the various feedback models calculated over the full simulation volume. One can see that the SFRD increases with decreasing redshift as massive galaxies assemble. The SFRD is consistently highest in the `smooth-sn` model, while it is more effectively suppressed in `bursty-sn`, particularly below $z = 8$. The SFRD is initially lowest in `hyper-sn` compared other models, owing to early strong feedback from HN. However, as the gas metallicity increases, the HN rate in the massive haloes is reduced exponentially (see Equation 3.18), and the weakening feedback results in a rapid increase in star formation at $z = 9 - 10$. I

[4] Gas phase metallicity of the most massive halo at $z = 5$ is $\sim 0.1Z_\odot$, $\sim 1Z_\odot$, $\sim 0.49Z_\odot$ for `bursty-sn`,`smooth-sn` and `hyper-sn` respectively

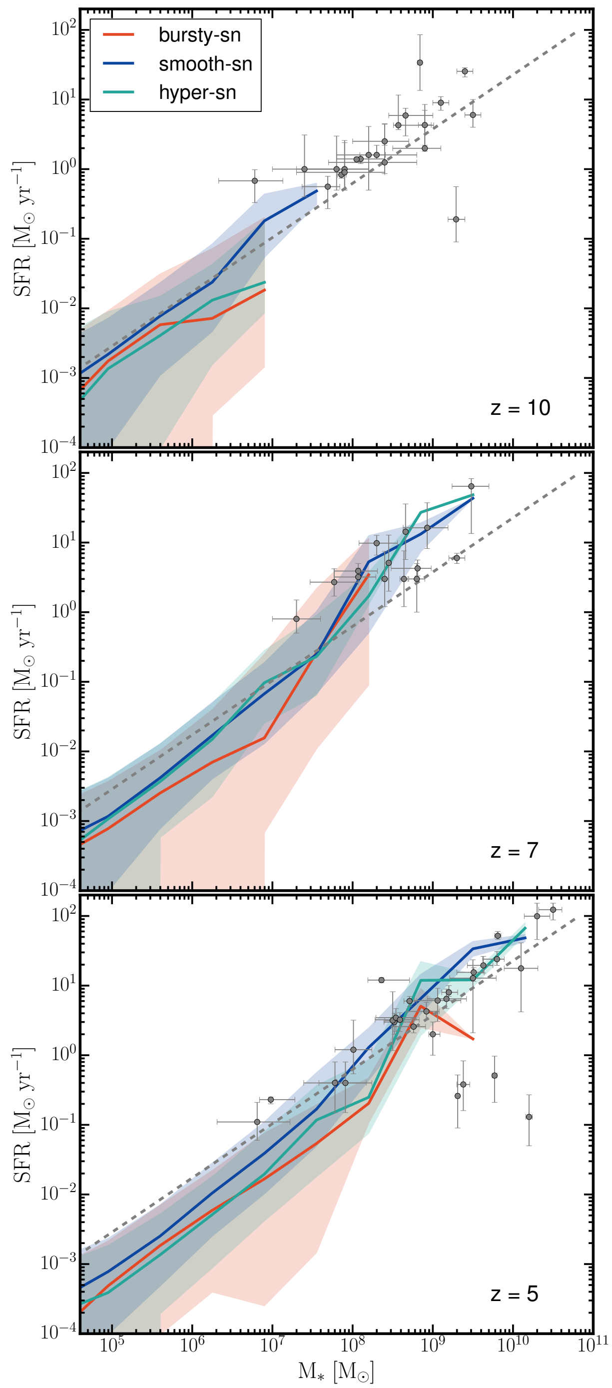

Figure 3.4: Star formation rate averaged over 10 Myr as a function of stellar mass for the `bursty-sn` (red line), `smooth-sn` (blue) and `hyper-sn` (turquoise) at z = 10, 7 and 5. Solid lines represent the median SFR, with the shaded regions covering the 16th and 84th percentiles. Observations from various JWST programs (see text) are shown with grey circles. The dashed line refers to the best fit relation for the main sequence at $z = 6$ (Iyer et al., 2018).

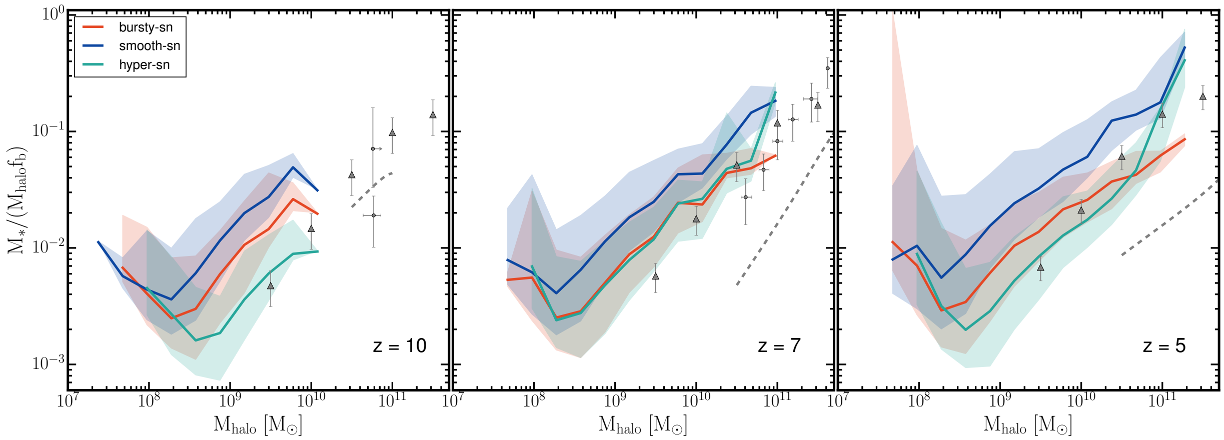

Figure 3.5: Star formation efficiency as a function of halo mass for `bursty-sn` (red line), `smooth-sn` (blue) and `hyper-sn` (turquoise) at redshift $z = 10$ (left panel), 7 (middle) and 5 (right). Solid lines represent the median SFE in each mass bin, with the shaded regions covering the 16th and 84th percentiles. Grey dots are observations from Stefanon et al. (2021), grey triangles abundance matching estimates from Tacchella et al. (2018), and the grey dashed line refers to the best fit from Behroozi et al. (2019).

note that the burstiness of star formation in the different models varies as mentioned in section 3.2.9. Both `bursty-sn` and `hyper-sn` have strong isolated bursts of star formation followed by relatively quiescent phases, whereas `smooth-sn` shows a comparatively smooth star formation history. The strength of the bursts increases with decreasing redshift for `bursty-sn`, while it decreases for `hyper-sn` and `smooth-sn`.

By comparing our models to observational constraints from multi-wavelength studies (Madau & Dickinson, 2014; Rowan-Robinson et al., 2016; Khusanova et al., 2021; Donnan et al., 2022; Asada & Ohta, 2022; Harikane et al., 2023; Algera et al., 2023), one can see that `hyper-sn` shows the best agreement at $z \gtrsim 10$, `bursty-sn` at $z \lesssim 8$, while `smooth-sn` is consistently higher than observations.

Figure 3.4 shows the SFR of galaxies (averaged over the previous 10 Myr) as a function of stellar mass for the three feedback models and redshifts. One can see that the median relations from all models roughly lie on a locus, forming a star formation main sequence (SFMS). Although the median relation does not vary significantly across models, the scatter differs. I quantify the scatter by fitting a Gaussian to the distributions of SFRs within bins of stellar mass. At $z = 10$, across the mass range, `bursty-sn` shows the largest scatter (≈ 0.8 dex) followed by `hyper-sn` (≈ 0.5 dex) and finally `smooth-sn` (≈ 0.3 dex). By $z = 7$, the scatter in `smooth-sn` and `hyper-sn` reduces to about $(0.2 - 0.3)$ dex, in agreement with observations from Speagle et al. (2014). However, `bursty-sn` continues to show a large scatter of $(0.8 - 0.9)$ dex with it being the largest below $M_* < 10^7 M_\odot$. While `smooth-sn` and `hyper-sn` show minimal evolution in scatter between $z = 7$ and $z = 5$, the scatter for `bursty-sn` drops to ≈ 0.4 dex.

I compare the SFMS from the three models with with observations from recent JWST programs (Fujimoto et al., 2023; Haro et al., 2023a; Jung et al., 2023a; Long et al., 2023; Haro et al., 2023b; Leethochawalit et al., 2023; Robertson et al., 2023; Heintz et al., 2023a; Jin et al., 2023; Helton et al., 2023; Atek et al., 2023; Treu et al., 2023; Heintz et al., 2023b; Asada et al., 2023b; Bouwens et al., 2023b; Looser et al., 2023; Papovich et al., 2023). Data is collected in bins of ±0.25 around the redshifts shown. At $z = 10$, the vast majority of observations lie in a mass range not probed well by `SPICE`, however, `smooth-sn` shows the best agreement with observations. At $z = 7$ and $z = 5$, the median relations from all models is in excellent agreement with data for galaxies with $M_* > 10^7 \mathrm{M}_\odot$.

Figure 3.5 shows the ratio between stellar mass and halo mass, which I use as a proxy for global star formation efficiency (SFE), $M_*/(M_{\mathrm{halo}} f_b)$, as a function of halo mass M_{halo}, where $f_{\mathrm{b}} = \Omega_{\mathrm{b}}/\Omega_{\mathrm{m}}$. I note that all the stellar mass within the virial radius of a halo is included in the calculation. The `smooth-sn` model produces the highest SFE at all times as compared to the other models, especially at the high-mass end. The `bursty-sn` model has only a weakly time-dependent SFE, while the SFE in `hyper-sn` starts at very low values at early times, but, following a starburst episode at $z \approx 9$, increases, and by $z = 7$ becomes comparable to the one of the `bursty-sn` model. The HN rate in haloes with $M_{\mathrm{halo}} > 10^{10}\,\mathrm{M}_\odot$ reaches 1% (by $z \approx 9$), therefore, the energetic component of feedback becomes negligible. Consequently, the SFE in these haloes increases rapidly due to inefficient feedback. Lower-mass halos have small SFEs, likely because the high HN rate combined with the shallower potential wells lead to more effective quenching. All three models show consistently higher ($\approx 0.6 - 1$ dex) SFEs as compared to best fit estimate from Behroozi et al. (2019). They are however in agreement with abundance matching estimates from Tacchella et al. (2018), and z=7 observations from (Stefanon et al., 2021).

Overall, the results shown in this section highlight how some observables (e.g SFRD, SFE) vary strongly with implementation of feedback, while others (e.g SFMS) are less affected. The explosiveness of the `bursty-sn` model highlights the need for sustained strong feedback to maintain a sufficiently low star formation rate. In contrast, the `smooth-sn` model, characterized by less energetic feedback, struggles to effectively regulate star formation, thus allowing for the formation of massive star-forming galaxies by $z = 5$. Finally, the `hyper-sn` model emphasizes the importance of striking a balance between bursty and smooth feedback mechanisms.

3.3.3 Reionisation histories

In Figure 3.6 I show the ionised fractions (x_{HII}) in the three feedback models representing the progress of reionisation, i.e, formation of ionised regions at high redshifts, overlap and post-overlap phase. The difference in their sizes and abundance is already evident at $z = 10$, when `bursty-sn` produces generally larger HII regions, while the `smooth-sn` and `hyper-sn` models show a combination of extended and localised regions, with `hyper-sn` exhibiting a larger number of small ones. The differences are amplified at $z = 7$, where one can observe that the bubbles in `bursty-sn` are already deep into the overlap phase, with islands of neutral hydrogen localised in voids with small volume-filling fractions, while both `smooth-sn` and `hyper-sn` still show mostly isolated HII regions with large neutral voids in

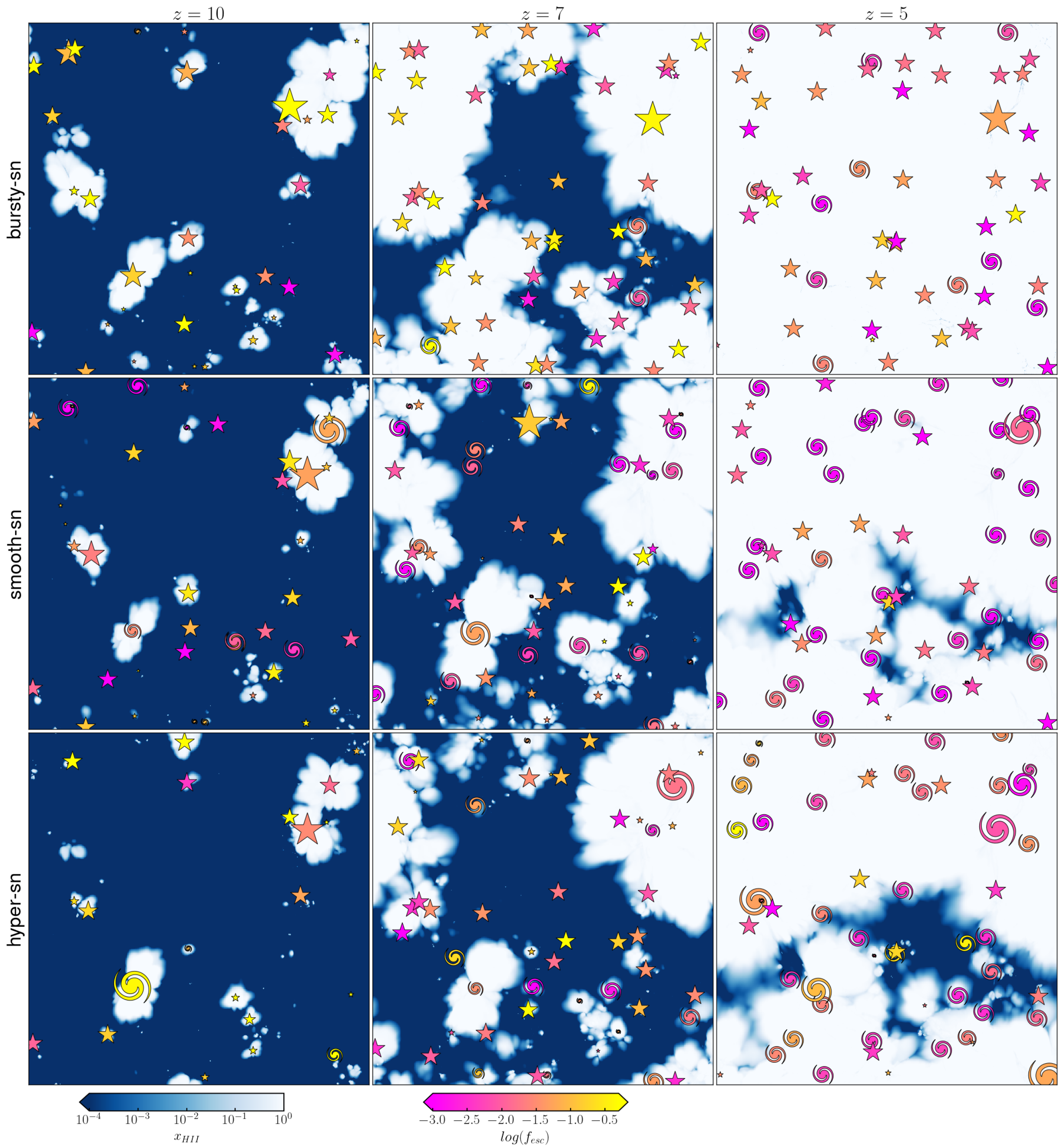

Figure 3.6: 100 kpc slices showing HII fraction in the `bursty-sn`, `smooth-sn` and `hyper-sn` models (from top to bottom) at $z = 10$, 7 and 5 (from left to right). Locations of galaxies are over-plotted (see text for selection criteria), with spiral (star) symbols representing rotationally- (dispersion-) dominated galaxies (gas morphologies; see section 3.3.5). Each symbol is color coded with the LyC escape fraction of the respective galaxy. Already at $z = 10$ ionised regions show differences in sizes, with `bursty-sn` and `hyper-sn` producing the largest and smallest, respectively. By $z = 5$, reionisation is complete in `bursty-sn`, whereas significant neutral patches persist in the other two models.

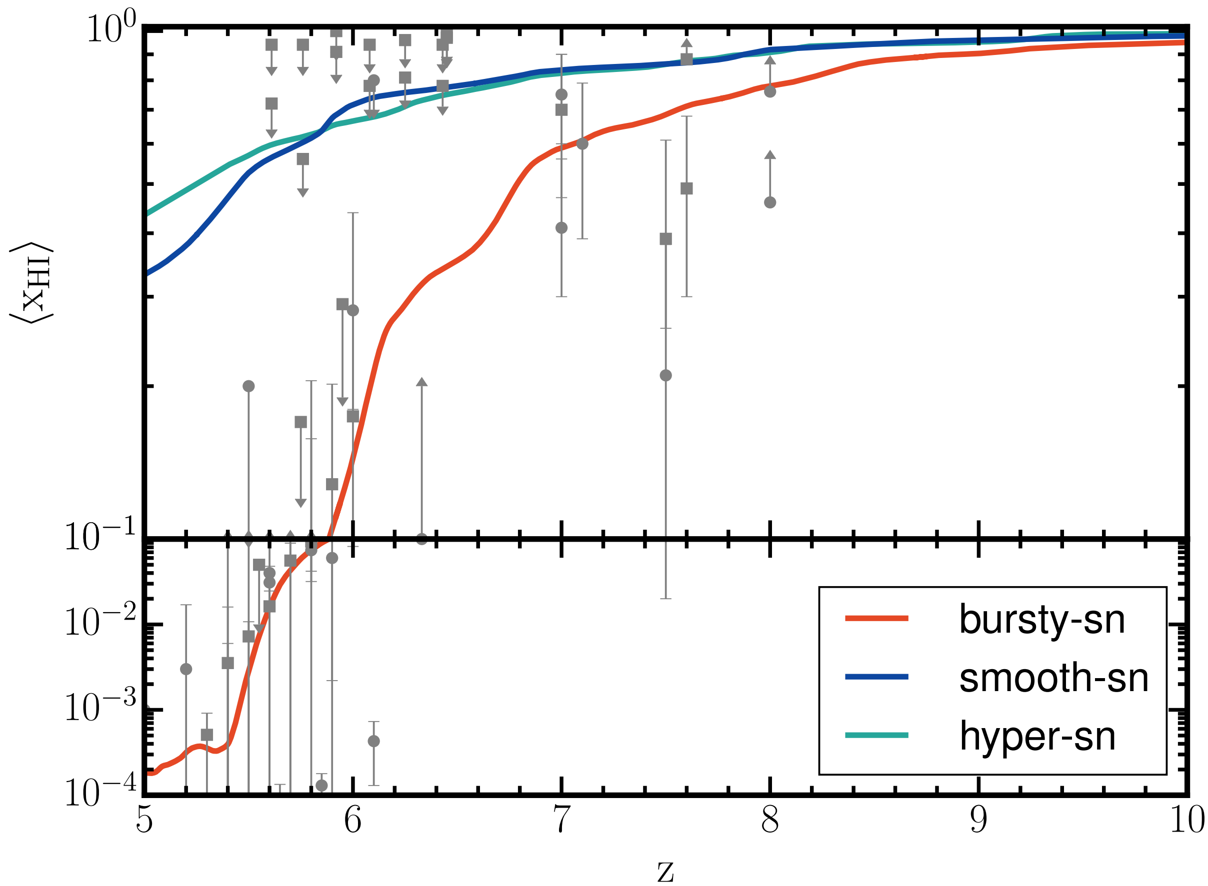

Figure 3.7: Volume-weighted neutral hydrogen fraction as a function of redshift for the three feedback models. Observational data shown in grey points are taken from Fan et al. (2006); McGreer et al. (2011); Ono et al. (2012); Schroeder et al. (2012); McGreer et al. (2015); Greig et al. (2017); Mason et al. (2018, 2019a); Greig et al. (2019); Hoag et al. (2019b); Yang et al. (2020); Wang et al. (2020); Lu et al. (2020); Jung et al. (2020a); Choudhury et al. (2021); Bosman et al. (2022); Zhu et al. (2022); Gaikwad et al. (2023). `bursty-sn` reionises within observational constraints whereas `smooth-sn` and `hyper-sn` reionise late.

between. By $z = 5$, the overlap phase is completed in `bursty-sn`, with neutral hydrogen present only in dense self-shielded structures, while in both `smooth-sn` and `hyper-sn` small neutral islands still persist.

To demonstrate the varied ability of galaxies to reionise their surroundings, in Figure 3.6 I divide each projection in a 4×4 grid and mark the location of the three most luminous galaxies within each grid sub-division. Each galaxy is coded by its morphology (stars and spirals represent dispersion- and rotation-dominated galaxies, respectively; see section 3.3.5 for details) and LyC escape fraction (different colors). In Section 3.3.6, I discuss in more detail the connection between galaxy morphology and LyC escape fractions.

In Figure 3.7 I show the resulting reionisation histories. I find that while `bursty-sn` reionises[5] the Universe by $z = 5.1$, this is not the case for `smooth-sn` and `hyper-sn` models. In `bursty-sn` the reionisation process starts early, with the hydrogen neutral fraction, x_{HI}, dropping to ≈ 0.9 already at $z \approx 10$. From $z \approx 7$, x_{HI} experiences a steep decline in a series of steps that are time-correlated with three star formation bursts clearly visible in Figure 3.3, and resulting in a 'late reionisation scenario' (Kulkarni et al., 2019a; Keating et al., 2020; Gaikwad et al., 2023), with x_{HI} becoming lower than 10^{-4} at $z \approx 5.1$. Despite producing more star-forming galaxies (see Section 3.3.2), `smooth-sn` and `hyper-sn` result in a much later reionisation, failing to bring the volume-weighted neutral fraction below 30% even by $z = 5$, the time when our simulations end. However, I note that the simulation volumes are not large enough to derive a converged mean reionisation history (Iliev et al., 2014; Gnedin & Madau, 2022), and a box size of $\gtrsim 100$ cMpc/h is required to better represent an average region of the universe and to account for the typical sizes of ionised regions in the late stages of reionisation, as these can be tens of cMpc in size.

The stellar masses integrated over the entire simulation volume at $z = 5$ for the `smooth-sn`, `bursty-sn` and `hyper-sn` model are $\approx 5 \times 10^{10}$ M$_\odot$, $\approx 2 \times 10^{11}$ M$_\odot$ and $\approx 1 \times 10^{11}$ M$_\odot$, respectively (a ratio of $1 : 4 : 2$). These estimates imply a different number of SN explosions and intrinsic ionising photon budget, as both increase for larger stellar masses. Therefore, `smooth-sn` and `hyper-sn` have a larger ionising photon budget as compared to `bursty-sn`, suggesting that the late reionisation is not a result of a lower ionising photon budget, but rather it is due to inefficient escape of photons.

Explosiveness of feedback affects star formation which determines the ionising photon budget and the extent to which gas is disturbed (modulation of escape fractions). `smooth-sn` and `hyper-sn` have a weaker feedback (especially at $z < 8$), which allows for the formation of stable gas configurations (see Figure 3.1) and the overproduction of stars (see Figures 3.3,3.5 and Section 3.3.2), but it is unable to significantly disrupt the gas configuration, hence suppressing the escape of radiation.

3.3.4 Luminosity functions at 1500 Å

In Figure 3.8 I show the evolution of the 1500 Å luminosity function, where the luminosities are calculated in a 10 Å bin around 1500 Å using the stellar SEDs. Solid and dashed lines refer to the intrinsic and dust-attenuated luminosity functions, respectively. The latter is calculated with the Monte Carlo line transfer code `RASCAS` (Michel-Dansac et al., 2020), by casting 100 rays from each stellar particle within a galaxy to the edge of the halo, and evaluating the solid angle-averaged attenuation per galaxy. The orientations of the rays are sampled randomly, and the dust attenuation along each ray is calculated using the dust model described in Section 3.2.11. I also show observational estimates of the luminosity functions from HST legacy fields and recent JWST programs (Finkelstein et al., 2015; Bouwens et al., 2015; Harikane et al., 2022; McLeod et al., 2023; Adams et al., 2023; Harikane et al., 2023; Bouwens et al., 2023b,a; Leung et al., 2023).

[5] I consider reionisation to be complete if the volume-averaged neutral hydrogen fraction of the simulation reaches 10^{-4}.

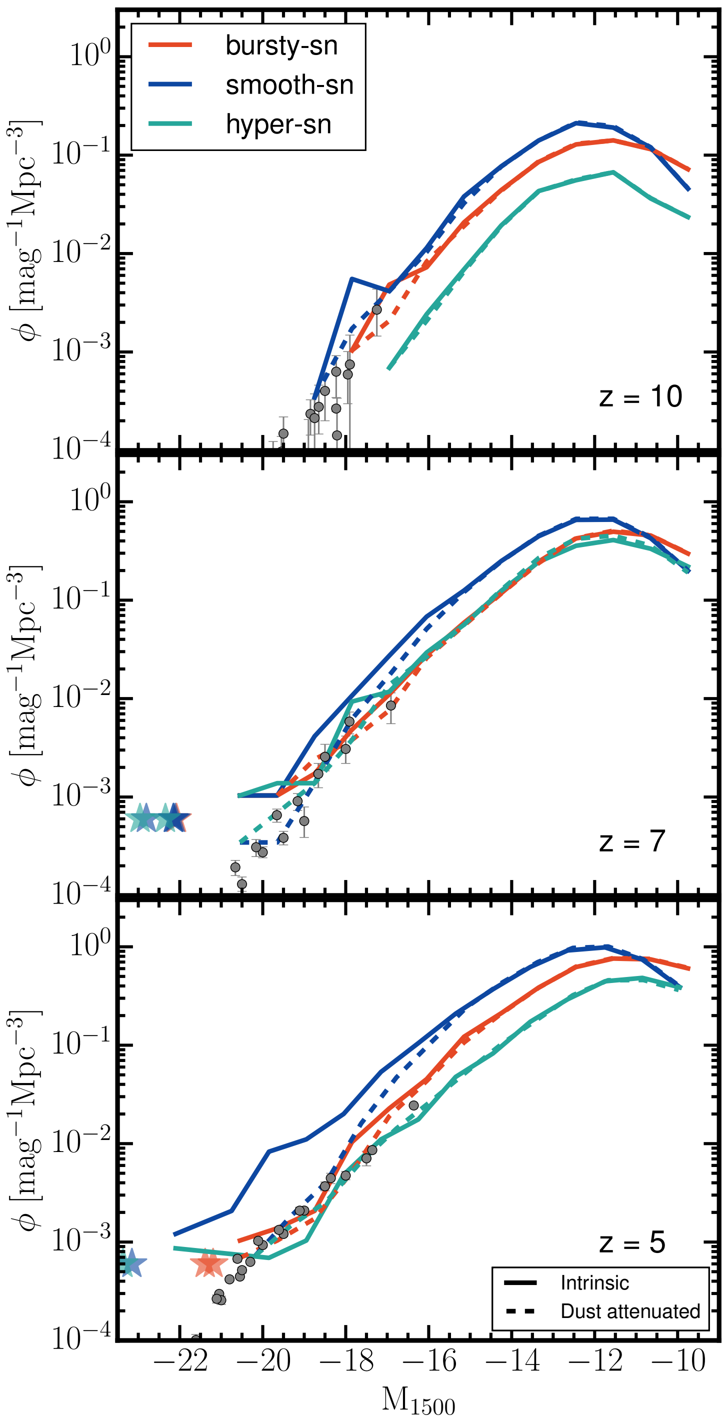

Figure 3.8: 1500 Å luminosity functions (LF) for the various feedback models at $z = 10$, 7 and 5 (from top to bottom). The solid and dashes lines refer to the intrinsic and dust-attenuated luminosity functions, respectively. Observations from HST and JWST fields are marked in grey (see text). Stars represent intrinsic luminosities in bins with fewer than 3 galaxies. Despite intrinsic LFs being different, dust-attenuated ones show minimal differences between models. Therefore, LFs *cannot* be used to constrain feedback models.

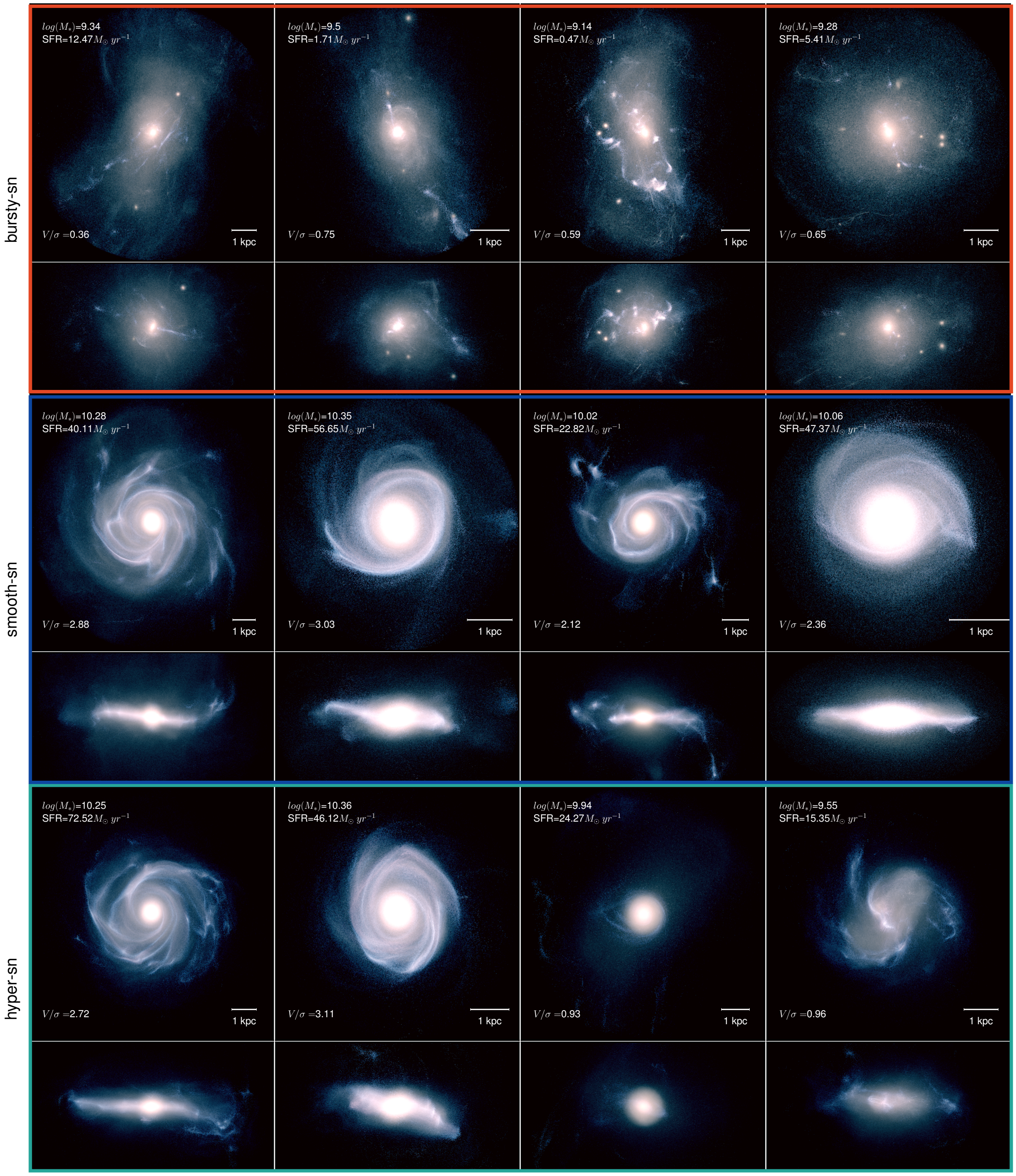

Figure 3.9: The columns show JWST RGB composite projections (face-on and edge-on) in the F200W, F277W and F444W filters for the four most massive galaxies at $z = 5$ in the `bursty-sn` (top two rows), `smooth-sn` (middle two rows), and `hyper-sn` (bottom two rows) model. Numbers in each panel indicate the stellar mass, SFRs and V/σ values for the stellar component. The `smooth-sn` model produces mainly rotationally supported, massive disk galaxies that are bulge-heavy; the `bursty-sn` model dispersion-supported, disturbed systems which are redder and less-massive; the `hyper-sn` model a combination of massive rotationally-supported spiral galaxies and dispersion-supported ellipsoids. Stellar feedback processes profoundly affect galaxy kinematics, colours and morphology.

From the top panel of Figure 3.8 one can see that at $z = 10$ `hyper-sn` produces fewer galaxies at all magnitudes compared to the other two models. The latter have similar luminosity functions, with `smooth-sn` producing the highest number of (intrinsically) bright objects. Following a decline of the HN rate in massive haloes in `hyper-sn`, the increase in star formation boosts the intrinsic LF, which becomes almost indistinguishable from the LF in the `bursty-sn` model at $z = 7$. Similarly to $z = 10$, `smooth-sn` shows a larger number (by 0.3-0.4 dex) of galaxies at all magnitudes compared to the other models.

By $z = 5$, `smooth-sn` produces extremely UV-bright ($M_{1500} \sim -23$) objects and an abundance of galaxies at all magnitudes. Also `hyper-sn` results in a similar abundance of objects at $M_{1500} \sim -23$, while showing less dimmer galaxies ($-20 < M_{1500} < -12$). Meanwhile, `bursty-sn` lies in between the other two models.

At $z = 10$ the dust-attenuated LFs are similar to the intrinsic ones for `bursty-sn` and `hyper-sn`, while one can observe significant attenuation for `smooth-sn` at $M_{1500} < -17$. Dust attenuation becomes more significant at $z = 7$ for `smooth-sn` and `hyper-sn`, when an effect is visible at the bright end of the LF. Indeed, it becomes relevant at $M_{1500} < -16$ for `smooth-sn`, and at $M_{1500} < -18$ for `hyper-sn`, while in `bursty-sn` dust attenuation is minor even at the brightest end of the LF. At $z = 5$, dust attenuation for `smooth-sn` is significant (> 1 dex) at $M_{1500} < -18$, while in `hyper-sn` it is present only at $M_{1500} < -20$. Finally, for `bursty-sn` it is minimal ($\approx$ 0.2dex) for $M_{1500} < -17$. At $z = 10$, while `bursty-sn` and `smooth-sn` agree very well with data, `hyper-sn` shows a deficit of bright galaxies. However, both at $z = 7$ and $z = 5$, dust-attenuated LFs from all three models are in excellent agreement with observations for $M_{1500} < -16$.

Overall, in this section I show that despite the intrinsic LFs being extremely different, the dust-attenuated ones are very similar below $M_{1500} < -16$, suggesting that UVLFs cannot be directly used to probe stellar feedback at high redshifts.

3.3.5 Galaxy morphologies

Figure 3.9 shows stellar light projections for the four most massive galaxies produced in each feedback model, which are matched across simulations using the IDs of the dark matter particles comprising their parent haloes (which remain identical across simulations). The images consist of RGB composites in the F200W(B) + F277W(G) + F444W(R) JWST filters. Each galaxy is shown both face-on (upper rows) and edge-on (bottom rows), where the total angular momentum vector was used to define the orientation. Note that dust attenuation is not taken into account, i.e. the images illustrate intrinsic stellar emission only.

The most massive galaxies in `smooth-sn` are blue, spiral galaxies (see Figure 3.9), which host also bright, red bulges, and have star formation rates reaching $\approx 50\,\mathrm{M_\odot\,yr^{-1}}$. Within the same haloes, `bursty-sn` generates systems with 10 times lower star formation rates and $(0.8 - 1)$ dex lower stellar mass. The host galaxies now show no evidence of disks, and appear much more irregular, hosting a number of stellar clumps and streams. Finally, the `hyper-sn` model results in a mixture of blue star-forming spirals with SFRs of $\approx 50\,\mathrm{M_\odot\,yr^{-1}}$, similar to those of `smooth-sn`, and irregular galaxies which also tend

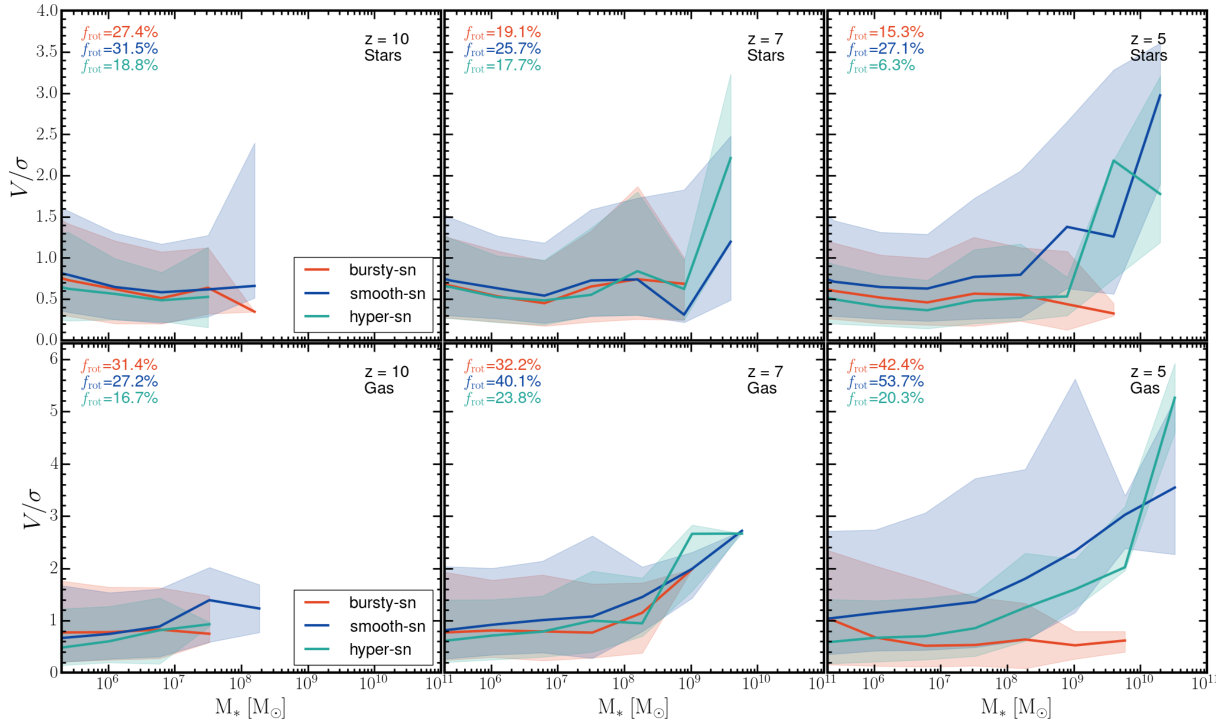

Figure 3.10: Median V/σ values for stars (top row) and gas (bottom row) as a function of stellar mass for galaxies in the various feedback models at $z = 10, 7$ and 5 (from left to right). The shaded regions show the 16th and 84th percentiles. Percentages in each panel refer to the number of rotationally-supported galaxies at a given redshift. Large differences emerge in the kinematics by $z = 5$, with `smooth-sn`, `bursty-sn` and `hyper-sn` producing mainly galaxies which are rotationally-supported, dispersion-supported, and mixed, respectively.

to be star-forming, unlike those in `bursty-sn`. Variations in supernova feedback have a particularly striking impact on galaxy morphology, with differences that are systematic and persist down to stellar masses of $\approx 10^7\ \mathrm{M}_\odot$ (see Figure 3.10).

While in Figure 3.9 I show the strong qualitative differences caused by feedback on the four most massive galaxies, I also quantify them for the entire galaxy population using the ratio V/σ (Dubois et al., 2016; Pillepich et al., 2019) as a proxy for morphology, where V is the rotational velocity and σ is the 3D velocity dispersion. This ratio classifies the degree to which a galaxy is supported by dispersion or rotation. I calculate V/σ for both stars and gas for each galaxy with $M_* > 10^5\ \mathrm{M}_\odot$. For stars, I construct a velocity dispersion radial profile, as well as the 3D rotation curve for all stars within twice the stellar half mass radius of each galaxy[6]. As for gas using all cells inside a fixed radius can lead to noisy calculations due to inflows and outflows, I select gas cells within R_{vir} adopting an Hα emissivity threshold. Indeed, recombination lines of atomic hydrogen from the ionised ISM are often used to measure gas kinematics in a wide redshift range (de Graaff et al.,

[6] I bin the rotation and dispersion curves at a fixed bin-width of 0.2 ckpc (∼8 times the maximum resolution of the simulation) to ensure statistical mean/medians in each bin.

2023). I evaluate the case-B recombination volume emissivity for each gas cell as (Hummer & Storey, 1987):

$$\epsilon_{\mathrm{H}\alpha} = h\nu\ P_{\mathrm{B}}(T)\ \alpha_B(T) n_{\mathrm{e}} n_{\mathrm{p}}, \tag{3.19}$$

where $\alpha_{\mathrm{B}} = 2.753 \times 10^{-14}\ \lambda^{1.5}/(1.0 + (\lambda/2.74)^{0.407})^{2.242}\ \mathrm{cm^3 s^{-1}}$ with $\lambda = 315614/T$ is the case-B recombination coefficient (Hui & Gnedin, 1997), T is the gas temperature, n_{e} and n_{p} are the number densities of electrons and protons, and $P_{\mathrm{B}}(T)$ is the conversion probability per recombination event, which is ≈ 0.451 for $T = 10^4$ K.

To calculate gas kinematics I select gas cells with $\epsilon_{\mathrm{H}\alpha} > 10^{-6}$ erg s^{-1} cm^{-3}, noting that this choice does not affect our qualitative results[7]. Following the process used in various theoretical and observational studies (Pillepich et al., 2019; Rizzo et al., 2020), V/σ is calculated using V at the peak of the rotation curve and σ as the mean velocity dispersion. I classify galaxies with $V/\sigma \geq 1$ (for both stars and gas) as rotationally-supported, otherwise as dispersion-supported.

In Figure 3.10 I show the median V/σ for stars (top row) and gas (bottom) as a function of stellar mass. The numbers in the various panels give the fraction of all galaxies that are rotationally-supported systems at a given redshift. The stellar component in `bursty-sn` and `hyper-sn` shows a consistent decrease with decreasing redshift in the fraction of rotationally-supported galaxies (`hyper-sn` exhibits a sudden drop from $\approx 18\%$ at $z = 7$ to $\approx 6\%$ $z = 5$), whereas the fraction does not change significantly in `smooth-sn`. The gas component behaves differently for all models. `bursty-sn` shows a steady increase in the fraction of rotationally-supported galaxies with decreasing redshift (from $\approx 31\%$ at $z = 10$ to $\approx 42\%$ at $z = 5$), `smooth-sn` has a similar trend but the increase is more drastic (from $\approx 27\%$ to $\approx 53\%$), while `hyper-sn` shows a mild increase in this fraction between $z = 10$ and 7, followed by a drop in the range $z = 7 - 5$.

At $z = 10$, both stellar and gas components are indistinguishable between models. Similarly at $z = 7$, with the only differences appearing at the highest masses, where `smooth-sn` and `hyper-sn` show formation of highly rotationally-supported systems. The differences between the various models become most pronounced at $z = 5$ for both stellar and gas components. `smooth-sn` shows a population of highly rotationally-supported galaxies ($V/\sigma > 2$) and very large scatter at $M_* \gtrsim 10^8 \mathrm{M}_\odot$, while `bursty-sn` produces a dispersion-supported galaxy population with a small scatter around the median. The `hyper-sn` model exhibits a transition at $M_* \approx 10^8 \mathrm{M}_\odot$: scatter is small and galaxies are mainly dispersion-supported for masses lower than this value, while more massive galaxies are typically rotationally-supported and scatter is more significant. I note that the gaseous component shows a larger degree of rotational support as compared to the stellar component (i.e. $V_{\mathrm{star}}/\sigma_{\mathrm{star}} < V_{\mathrm{gas}}/\sigma_{\mathrm{gas}}$), a trend particularly prominent in the `smooth-sn` and `hyper-sn` models. The number of galaxies classified as rotationally- vs dispersion-supported is also widely different for the three models, especially at $z = 5$, implying the presence of kinematic misalignment between the stellar and gas components in the galaxies.

Examining the galaxy morphologies, I show that feedback plays a key role in shaping

[7] This limit is taken using results on completeness estimates and theoretical studies from Belfiore et al. (2022) and Tacchella et al. (2022)

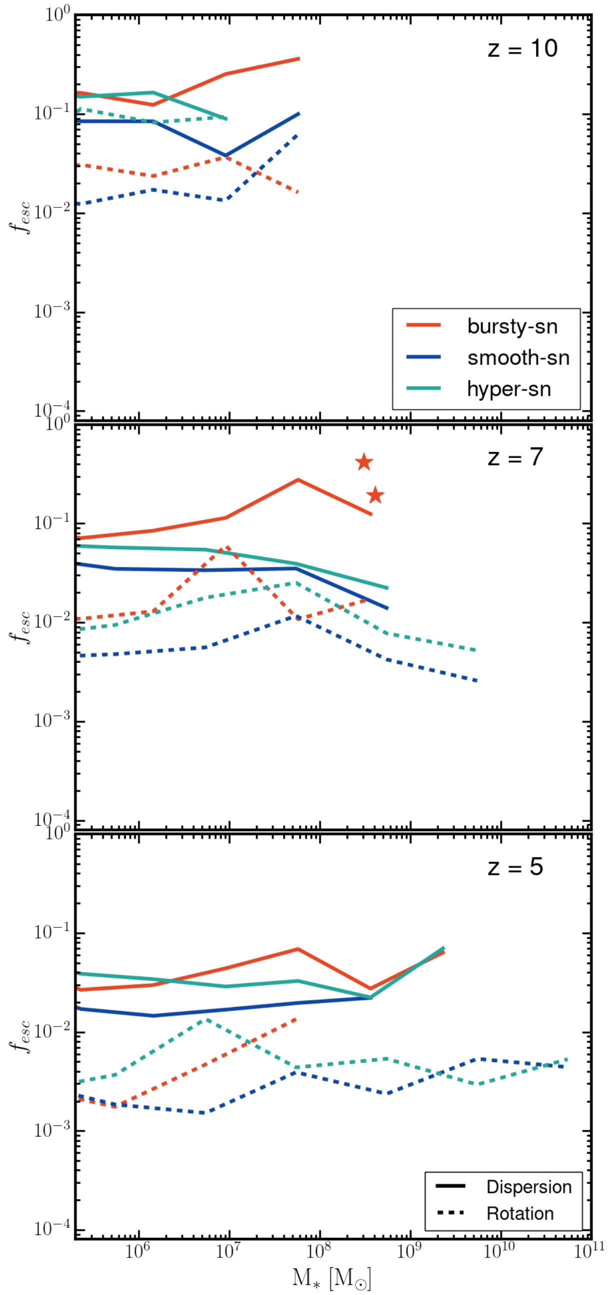

Figure 3.11: Luminosity-weighted mean escape fraction of `SPICE` galaxies as a function of stellar mass. Solid and dashed lines refers to dispersion- and rotation-dominated systems ($V_{\rm gas}/\sigma_{\rm gas}$), respectively. Solid (hollow) stars represent single dispersion-(rotation-) dominated galaxies in bins with fewer than 3 galaxies.

the morphological mix of galaxies that emerge post-reionisation. The populations are hard to distinguish using V/σ as an indicator at $z > 7$, except for the most massive galaxies. Below this redshift however, the morphological mixes diverge and hence can act as an indicator to distinguish feedback models.

3.3.6 Implications for LyC escape : What galaxies drive reionisation?

LyC escape can proceed either through low density channels created by stellar feedback, or if the ISM is highly ionised and optically thin (Zackrisson et al., 2013; Katz et al., 2022b). These scenarios are not mutually exclusive and previous studies (Trebitsch et al., 2017; Kimm et al., 2017; Rosdahl et al., 2018; Barrow et al., 2020; Katz et al., 2022b; Yeh et al., 2023) show that LyC escape fraction (f_{esc}) is strongly regulated by feedback through a complex multiphase ISM. Therefore, the morphology of the ISM holds signatures that can aid in the identification of the galaxies responsible for reionisation.

Here I connect the morphologies of galaxies as discussed in the previous section to their f_{esc}, which is calculated using `RASCAS` (Michel-Dansac et al., 2020). Photon packets are injected at the position of each stellar particle with a probability proportional to its LyC luminosity, evaluated using the stellar SEDs. I set the number of photon packets per halo to be 100 times the number of star particles, with a maximum of 10^7. Photons are propagated until they are absorbed or reach a distance equal to the virial radius of the host halo. The escape fraction is then defined as the ratio between the number of escaping and injected photons.

I assign a LyC f_{esc} to each galaxy, and use $V_{\mathrm{gas}}/\sigma_{\mathrm{gas}}$ (as calculated in section 3.3.5) to sort galaxies into rotationally- and dispersion-supported categories. In Figure 3.11, I show the luminosity-weighted mean LyC escape fractions as a function of stellar mass for dispersion- (solid lines) and rotationally-supported (dashed) galaxies. I observe a clear difference in the f_{esc} of rotation- and dispersion-dominated systems, with the latter exhibiting $\approx 10-50\times$ higher escape fractions as compared to their rotational counterparts. This trend holds for all three feedback models at all redshifts in consideration. The differences in f_{esc} imply that at the same intrinsic luminosity and in the same environment, dispersion-dominated systems produce ionised bubbles larger than those of their rotation-dominated counterparts. This effect is observed in Figure 3.6 and is particularly evident at $z = 10$ (left-column), where ionised regions surrounding dispersion-dominated galaxies (stars) are the largest (e.g in `bursty-sn`), while those around rotation-dominated galaxies (spirals) are the smallest (e.g in `smooth-sn`). The relative difference between the f_{esc} for rotation- vs dispersion- dominated systems is the largest for `smooth-sn`, followed by `bursty-sn` and `hyper-sn`. However, the morphological mix in the three models is redshift and stellar mass dependent. Since dispersion-dominated systems are more prevalent if stellar feedback is more explosive, reionisation occurs earlier in `bursty-sn` as compared to the other two models, where rotation-dominated systems are preferentially produced, especially at the highest masses.

I next quantify differences in reionisation histories by looking at the net intrinsic and escaping emissivities from all galaxies, defined as $f_{\mathrm{esc}}\dot{N}_{\mathrm{ion}}$, where $\dot{N}_{\mathrm{ion}}$ is the production rate of photons with $E_\gamma > 13.6\mathrm{eV}$ calculated by integrating the stellar SED, and $f_{\mathrm{esc}} = 1$ for

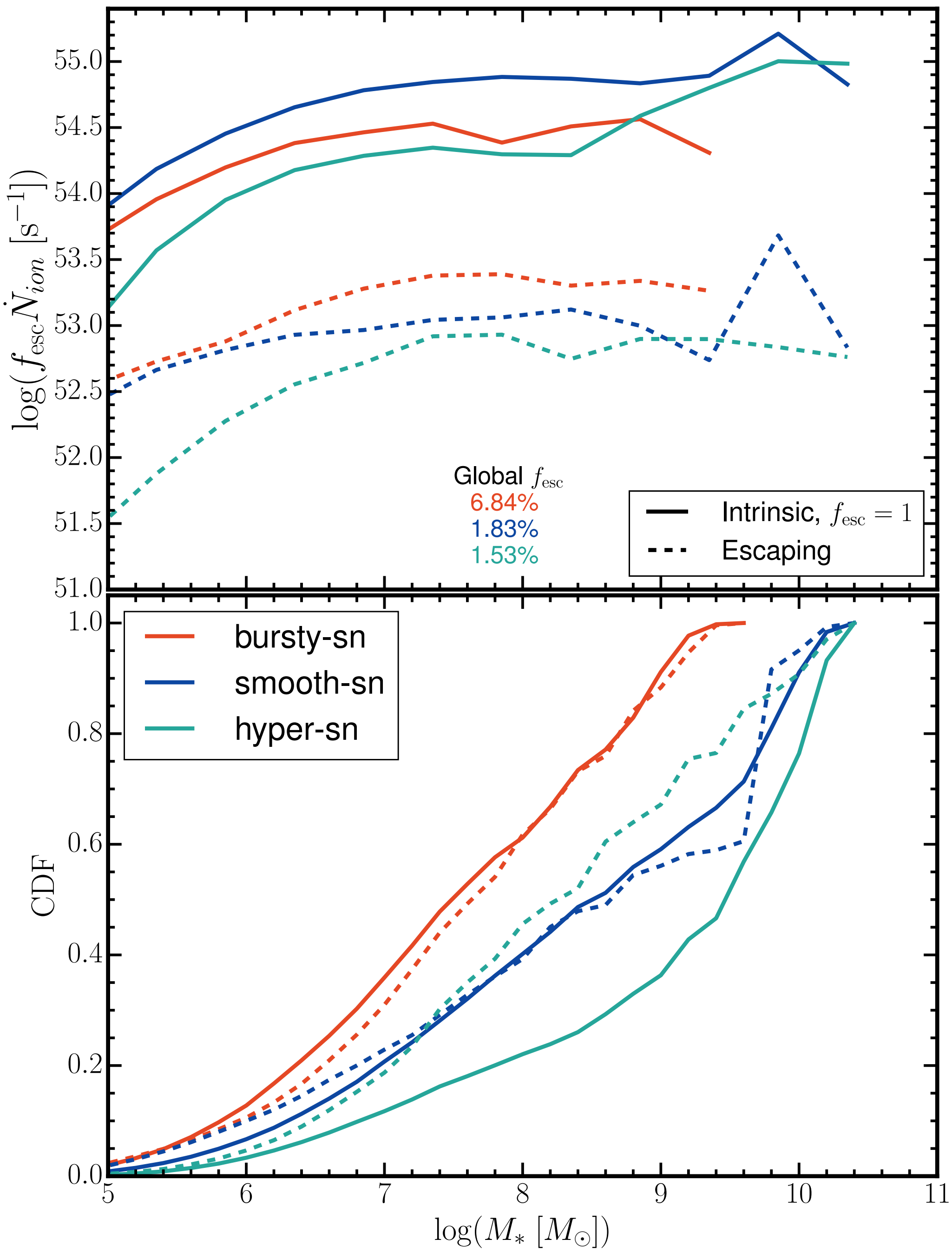

Figure 3.12: Top: Intrinsic (solid lines) and escaping (dashed line) ionising emissivity as a function of stellar mass for `bursty-sn` (red), `smooth-sn` (blue) and `hyper-sn` (turquoise). **Bottom**: Cumulative distribution of the above quantities indicating net contributions from galaxies in different mass bins. Emissivities are calculated over the full duration of the simulation.

the intrinsic emissivity. The top panel of Figure 3.12 shows the total intrinsic (solid lines) and escaping (dashed lines) emissivities of the galaxies over the entire duration of the simulation as a function of stellar mass. As previously discussed, the net intrinsic emissivity is the highest for `smooth-sn`, followed by `hyper-sn` and `bursty-sn`. The intrinsic contributions for `smooth-sn` and `hyper-sn` are largely dominated by the most massive galaxies (see also discussion below), whereas `bursty-sn` shows a more even distribution across the mass range. However, the net escaping emissivity is the highest for `bursty-sn`, followed by `smooth-sn` and finally `hyper-sn`. One can also use the total intrinsic and escaping emissivity to calculate a global escape fraction for each simulation, finding $\approx 6.8, 1.8$ and 1.5% for `bursty-sn`, `smooth-sn` and `hyper-sn`, respectively.

To understand which galaxies contribute the largest to reionisation, I look at the cumulative distribution of emissivities, which are shown in the bottom panel of Figure 3.12 as intrinsic (solid lines) and escaping (dashed lines). `bursty-sn` results in a fairly even contribution from galaxies with $M_* > 10^7 \mathrm{M}_\odot$ to both intrinsic and escaping emissivities. Differently, the intrinsic emissivity in `smooth-sn` and `hyper-sn` is largely dominated by galaxies with $M_* \gtrapprox 10^9 \mathrm{M}_\odot$ ($\approx 50\%$ and $\approx 65\%$, respectively). While the escaping emissivity shows a distribution similar to the intrinsic one (i.e. dominated by galaxies with $M_* \gtrapprox 10^9 \mathrm{M}_\odot$), `hyper-sn` exhibits an even contribution from galaxies with $M_* > 10^7 \mathrm{M}_\odot$. Therefore, in `bursty-sn` and `hyper-sn`, galaxies with $M_* > 10^7 \mathrm{M}_\odot$ contribute evenly to reionisation, whereas in `smooth-sn` $\approx 46\%$ of the escaping emissivity is produced by $M_* > 10^9 \mathrm{M}_\odot$ galaxies.

As measuring $\dot{N}_{\rm ion}$ at high redshifts is challenging, other quantities are used to evaluate the ionising photon production, such as the ionising photon production efficiency $\xi_{\rm ion,0} = \dot{N}_{\rm ion}/L_{1500}$, where L_{1500} is the intrinsic luminosity of the galaxy at 1500 Å. $\xi_{\rm ion,0}$ can give key insights about the stellar populations and dust obscuration and is used to study escape fractions of high redshift galaxies (Simmonds et al., 2023b). In Figure 3.13, I show $\xi_{\rm ion,0}$ as a function of stellar mass of galaxies calculated over the full duration of the simulation. All three models show comparable median trends with minor differences of $\approx (0.1 - 0.3)$ dex, however, `bursty-sn` has a very large scatter at all masses. Previous estimates from the HST surveys (Robertson et al., 2013) and more recent JWST programs (Atek et al., 2023; Simmonds et al., 2023b,a; Endsley et al., 2023a,b; Saxena et al., 2023a) find median values of $\log(\xi_{\rm ion,0}) \approx 24.8 - 25.7$ for galaxies in the range $z \sim 5 - 11$, which is in agreement with all three models.

Despite a very similar ionising photon production efficiency, the three models result in quite different reionisation histories (see section 3.3.3), suggesting that reionisation is strongly $f_{\rm esc}$ limited. Indeed, I show that different feedback models produce a different morphological mix (bottom panel in Figure 3.10), which in turn affects radiation escape depending on the relative predominance of rotation- or dispersion-dominated systems, and hence the escaping ionising emissivity budget. Therefore, models such as `smooth-sn` which preferentially produce rotationally-dominated systems (especially the most massive and luminous galaxies) show very low global escape fractions and produce very late reionisation histories. Meanwhile, `bursty-sn` produces a majority of dispersion-dominated systems (especially the most massive and luminous galaxies) which implies a high global $f_{\rm esc}$ ($\approx 4\times$

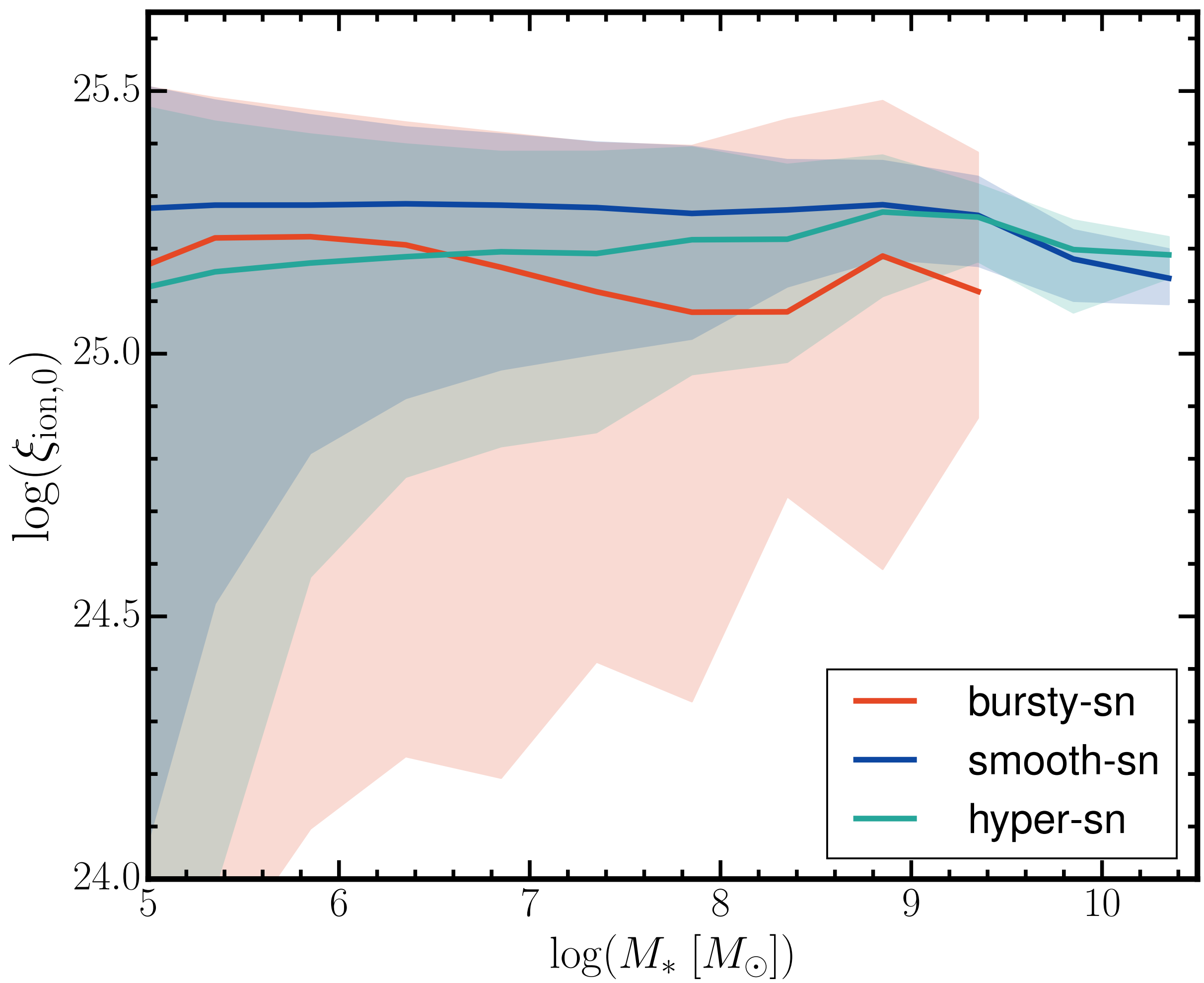

Figure 3.13: The median ionising photon production efficiency $\xi_{\mathrm{ion},0}$ as a function of stellar mass. Scatter around the median represents 16th and 84th percentiles. $\xi_{\mathrm{ion},0}$ is calculated over the full duration of the simulations. All models show very similar $\xi_{\mathrm{ion},0}$, although leading to very different reionisation histories suggesting that reionisation is f_{esc} limited.

higher than `smooth-sn`) and reionises the simulation volume by $z = 5.1$.

3.4 Discussion

Here I discuss the implications of feedback variations on galaxy properties, the prospects of constraining stellar feedback using observations, and the limitations of our work.

3.4.1 Connecting galaxy morphology and LyC escape: insights for observations

I have shown that the SN feedback mode hardly affects some observables (e.g SFMS, UVLF), while strongly altering others (e.g SFRD, SFE, reionisation, morphologies, $f_{\rm esc}$). A strong indicator to test feedback models I point to is the morphological mix that emerges post-reionisation, as feedback alters in a fundamental way stellar and gas morphologies. The gas morphologies in turn affect the $f_{\rm esc}$ of galaxies. As galactic morphology can be probed using different tracers (including stellar light and emission line kinematics), a multi-wavelength study of morphological characteristics provides a key insight to constrain feedback models (see Figure 3.6).

Telescopes like JWST and ALMA allow us to map galaxies at high angular resolutions ($\approx 0.1-0.2$ arcsec) deep into the epoch of reionisation. Studies using JWST observations have already started to produce galactic morphology statistics at various redshifts using e.g. stellar surface brightness profiles, Sersic indices, and Gini indices (Huertas-Company et al., 2023; Treu et al., 2023; Jacobs et al., 2023; Kartaltepe et al., 2023; Vega-Ferrero et al., 2023; Tacchella et al., 2023; Sun et al., 2023c). All find a rich morphological diversity of galaxies well established already at $z > 5$, and estimate a disk (pure disk + disks with bulges) fraction in the range $\sim 30-40\%$ at $z \sim 6$, in agreement with our `busty-sn` model. In this work I just consider dispersion- or rotation-dominated galaxies, finding that their relative distribution varies strongly depending on the feedback model. I defer to a future project a more direct comparison to observations, which will help to better constrain our models.

Recent studies have used SED fitting (Looser et al., 2023; Dressler et al., 2023a), [OIII]+Hβ equivalent width and Hα emission line luminosities (Endsley et al., 2023a,b; Simmonds et al., 2023a) to characterise modes of star formation in JWST galaxies, finding that a bursty SFH is prevalent in galaxies with masses $M_* \sim 10^{7-10}\mathrm{M}_\odot$ in the range $z = 6-12$. These studies also show that galaxies with a bursty SFH are likely to drive reionisation. In sections 3.3.3 and 3.3.5 I have discussed the strong influence that a bursty SFH has on galaxy morphology and on the reionisation history, supporting the claim that galaxies with bursty SFH are the likely drivers of reionisation. While observations have not yet connected galaxy morphologies to their ionising efficiencies, in `SPICE` I find that galaxies with a bursty SFH are largely dispersion-dominated (especially evident at $z = 5$), while galaxies with a non-bursty or smooth SFH are mainly rotation-supported and are unlikely to drive reionisation (see section 3.3.6). Such prediction can be tested with JWST observations.

The impact of cold streams (Dekel et al., 2009; Bournaud & Elmegreen, 2009; Oh et al., 2018), gas fractions (Barnes & Hernquist, 1996; Barnes, 2001; Naab et al., 2006), mergers (Toomre, 1977; Hopkins et al., 2009; Kannan et al., 2015; Velázquez et al., 2020), tidal effects (Bekki, 1998) and stellar feedback (Okamoto et al., 2005; Agertz & Kravtsov, 2016) on galaxy morphologies has been a topic of debate over the last few decades. While it is widely accepted that disk galaxies form due to gas accretion and transform to spheroidal galaxies via mergers (Toomre & Toomre, 1972; Toomre, 1977; Naab et al., 2006), the picture becomes unclear at high redshifts. For instance, the short dynamical timescales at high redshifts along with the long depletion timescales can allow for disk galaxies to stabilize even after major mergers (Robertson et al., 2006). As in all `SPICE` simulations the initial conditions are the same, I expect the timing of halo mergers as well as the cold streams feeding the haloes to be very similar across all models. Therefore, I argue that the stark differences in galaxy properties are a consequence of supernova feedback systematically altering the structure of galaxies on ISM/CGM scales. These differences translate not only to galaxy morphology (see section 3.3.5), but also to the LyC escape fractions (see section 3.3.6).

As a direct measurement of LyC escape fractions from high redshift galaxies is not possible because of the high IGM opacity, alternative indirect diagnostics have been suggested, such as metal line ratios (Wang et al., 2019; Chisholm et al., 2020; Saxena et al., 2022; Schaerer et al., 2022), Lyα peak separations (Verhamme et al., 2015a, 2017) and recent SFR (Calzetti, 2012; Kennicutt & Evans, 2012; Velázquez et al., 2020). While all these probes are sensitive to dust attenuation, line strengths and orientation effects, galaxy morphology can be reliably traced with high resolution observations, and could thus be used as a better proxy for the escape fraction. Indeed, here I show that a strong correlation exists between the morphology of galaxies (described in terms of V/σ) and their escaped radiation, with dispersion-dominated systems exhibiting the highest LyC escape fractions at all redshifts (by factor of 10-50). Our results also indicate that, as reionisation is limited by the escape fraction, it is strongly dependent on the behavior of stellar feedback, as this needs to be explosive and bursty (see section 3.3.3, 3.3.6).

Due to the differences in LyC $f_{\rm esc}$, at the same intrinsic luminosity, dispersion-dominated galaxies should preferentially create large expanding HII regions as compared to their rotation-dominated counterparts (see Figure 3.6). The growth of the HII regions is thus connected to the galaxy morphology, suggesting that concurrent observations of galaxy morphology and ionised regions could help to establish more firmly the connection between morphology and $f_{\rm esc}$, and to constrain stellar feedback. Observations of Lyα emitters (LAE) from HST/Keck-MOSFIRE (Stark et al., 2016; Matthee et al., 2018) suggest that bright LAEs are preferentially surrounded by large ionised regions, and also characterised by intense star formation. However, recent JWST observations of LAEs at $z \sim 7-9$ (Endsley et al., 2023a; Whitler et al., 2023; Tang et al., 2023a; Jung et al., 2023b; Saxena et al., 2023b) suggest a more diverse HII regions distribution, where not all strong LAEs lie within the largest ionised regions. Therefore, deep spectroscopic observations combined with imaging of LAEs will help to better constrain bubble sizes along with galactic properties. In a companion project I will investigate Lyα characteristics of galaxies in the three feedback models (see chapter 4).

Understanding the demographics of outflows driven by SN feedback and radiation pressure (Hayward & Hopkins, 2016; Li et al., 2017; Costa et al., 2018b; Menon et al., 2023) is key to constrain feedback models at high redshifts. Recent JWST observations (Zhang et al., 2023; Carniani et al., 2023) investigate the incidence of ionised outflows using Hα and `[O III]` in low mass galaxies ($M_* < 10^{10}\mathrm{M}_\odot$) in the range $z \sim 6-9$. These studies find that the inferred outflow velocities and mass loading factors are, respectively, 3 and 100 times larger than those observed for local dwarfs (Marasco et al., 2023). Multi-wavelength investigations combining JWST and ALMA data ([O III] and [C II], respectively; e.g. Fujimoto et al. 2022) suggest that the incidence of an outflow from a $M_* \approx 10^8 \mathrm{M}_\odot$ galaxy at $z \sim 8.5$ is likely associated to a starburst. This would then also promote a strong ionising photon escape. In SPICE I have shown how feedback affects the outflow characteristics (see Figure 3.2) suggesting that outflow properties and incidence rates can be a key tool to constrain feedback models.

3.4.2 Numerical uncertainties and physical limitations

The range of physics included in SPICE, along with a physical resolution of $\sim$ 28 pc, allows to make robust predictions for a variety of galaxy observables. However, due to approximations in numerical schemes, subgrid models and stochasticity, SPICE is affected by uncertainties. Understanding them is critical to improve models for future simulations, as well as the interpretation of their predictions.

While SPICE models metal line cooling, I do not include a molecular line cooling channel, which is relevant in the dense gas phase of the ISM. This can potentially impact, among others, the presence of cold gas in the outflows driven by SN feedback (Richings et al., 2014a,b; Biernacki & Teyssier, 2018), as well as the distribution and efficiency of star formation. While the refinement strategy adopted in SPICE allows us to resolve the CGM of galaxies at $\sim (28-84)$pc scales, the resolution deteriorates further away from the centers of haloes, with possible consequences on the correct modeling of the energy, mass loading and multiphase nature of outflows (Rey et al., 2023). This in turn can have important effects on the modeling of the escape of LyC radiation.

I attempted to improve the feedback modelling by making it increasingly physically based. `bursty-sn` represents the "IMF averaged" model, whereas `hyper-sn` includes realistic SN energies and explosion times, along with a theoretically supported prescription for hypernovae (Sukhbold et al., 2016; Kobayashi et al., 2006; Grimmett et al., 2020). However, I note that the latter, which is the most physically motivated model, is unable to complete reionisation by the end of the simulation, whereas `bursty-sn` (the least physically motivated model) is more consistent with observational constraints. While this could point to issues in the assumed HN rates or SN energy distributions, it could also indicate a potentially missing ingredient in the feedback modelling (e.g. runaway stars (Andersson et al., 2020; Steinwandel et al., 2023)), or the need for an improved numerical scheme for injection of energy and momentum.

The ISM model used in SPICE is a combination of subgrid prescriptions based on idealised simulations (e.g turbulence from Federrath 2016 and mechanical SN feedback from Kim & Ostriker 2015b). These prescriptions include a number of correction terms that are not predicted ab initio, but rather derived from smaller-scale simulations. Therefore, central assumptions such as log-normal density PDF and missing feedback processes at sub-resolution scale are a source of uncertainties.

Detailed studies of population synthesis models and SEDs have shown that the SED choice can strongly affect LyC escape fractions and reionisation histories (Ma et al., 2016;

Rosdahl et al., 2018; Ma et al., 2022; Rosdahl et al., 2022a). Further observational evidence (Götberg et al., 2019, 2020, 2023) suggests that e.g. the contribution from stripped binary stars could boost the ionising photon budget from massive stars. Hence, the SED and the ingredients of populations synthesis models are important uncertainties which should be further explored in future work.

`SPICE` employs the reduced speed of light approximation to advect radiation. This approximation produces converged reionisation histories as long as the speed of the ionisation fronts (I-fronts) remains below the value of the adopted reduced speed of light, which in `SPICE` is $0.1c$. I note that at the tail end of reionisation, the I-fronts can travel as fast as $0.1c$ as they traverse the voids (D'Aloisio et al., 2019), but the approximation is unavoidable because of the extreme computational costs of running simulations with the full speed of light.

I also note that the simulation volume is too small to study the global reionisation on large scales. Indeed, typical sizes of ionised regions can become tens of cMpc, suggesting that to produce converged reionisation histories boxes $\gtrsim 100\mathrm{cMpc}/h$ are required (Iliev et al., 2014; Gnedin & Madau, 2022). In follow-up studies I plan on extending the `SPICE` models to larger simulation volumes to get better galaxy statistics and to further improve numerical schemes of stellar feedback (see chapter 6).

`SPICE` addresses the effect of variations in stellar feedback models while including some poorly-explored physical processes, like radiation pressure on dust and dust itself. However, due to the computational costs involved, our models are far from complete, as processes such as cosmic rays (CRs), AGN feedback and magnetic fields are still missing. Magnetic fields and CRs can both affect the structure of the ISM which in turn affects galaxy obervables. Numerous studies have attempted to quantify the effect of magnetic fields (Gnedin et al., 2000; Marinacci & Vogelsberger, 2015; Krumholz & Federrath, 2019; McKee et al., 2020; Garaldi et al., 2021; Katz et al., 2021; Martin-Alvarez et al., 2020) and CRs (Sazonov & Sunyaev, 2015; Leite et al., 2017; Farcy et al., 2022; Martin-Alvarez et al., 2022) on galaxy formation and reionisation itself. However, the implications remain unclear.

Dust is relevant for various processes such as cooling, fragmentation, absorption and scattering of radiation and obscuration of UV photons. `SPICE` adopts a simplified dust model in which dust is hydrodynamically coupled to the gas and its creation and destruction are not accounted for. Additionally, I assume that dust opacities are independent of temperature, although in dense cold gas, they can scale as T^2 (Semenov et al., 2003). Scaling of opacities can also strongly affect the radiation pressure on dust, which I include as a feedback channel. Therefore, on-the-fly modelling of dust grain creation and destruction, as well as more accurate dust opacities, are important for a better modelling of the ISM structure and of the strength of radiation pressure driven feedback.

Theoretical studies have argued that AGN feedback can be important to understand the evolution of dwarf galaxies, even at very high redshifts (Dashyan et al., 2017; Koudmani et al., 2021, 2022; Sharma et al., 2022). At the same time, observational evidence is mounting supporting the presence of a population of $\sim (10^5 - 10^8)$ $\mathrm{M}_\odot$ black holes at very high redshifts (Scholtz et al., 2023; Mezcua et al., 2023; Schneider et al., 2023; Maiolino et al., 2023). Therefore, AGN feedback is a key missing ingredient worth exploring in the future to investigate when and in which galaxies it is relevant.

3.5 Conclusions

I introduced SPICE, a suite of radiation hydrodynamical simulations of galaxy formation and reionisation performed with RAMSES-RT. Our aim is to systematically study the effects of variations in stellar feedback on reionisation and properties of the first galaxies. SPICE resolves atomic cooling haloes and has a spatial resolution of ≈ 28 pc at $z = 5$. The galaxy formation model includes cooling, non-equilibrium chemistry, a multi-freefall star formation model, which employs a subgrid prescription for turbulence to evaluate the star formation efficiency in each computational cell, and a mechanical feedback scheme to inject energy and mass from supernovae. I include radiation transport (through gas and dust) in 5 frequency bands, i.e. IR, optical and three UV groups. Our base model remains identical across our different simulations with the sole exception of SN feedback, which is modelled in three different way (see Table 3.2): bursty (`bursty-sn`), smooth (`smooth-sn`) and smooth feedback with a time-evolving energetic component (`hyper-sn`).

In this chapter, I showcase the global properties of the simulations in terms of galaxy populations, reionisation histories, and connection between galaxy morphologies and LyC escape fractions. A summary of our key findings is presented below:

- Feedback strongly affects the burstiness and amplitude of the star formation rate density (SFRD; section 3.3.2). `bursty-sn` consistently exhibits bursts of SF, with a more pronounced intensity below $z = 8$. Conversely, `smooth-sn` has a minimal burstiness, consistently reaching the highest SFRD among the three models. Finally, in `hyper-sn`, the SFRD is the lowest at the highest redshifts because of the strong feedback from hypernovae. This also induces pronounced burstiness at $z > 9$, akin to `bursty-sn`. As the hypernova rate declines (due to metal enrichment), below $z \sim 9$ the model exhibits similarities with `smooth-sn` and shows a strong upswing in SFRD.

- I show the emergence of a star formation main sequence (SFMS; section 3.3.2) already by $z = 10$. The median SFMS remains very similar across models, however, `bursty-sn` exhibits a much larger scatter ($0.3 - 0.5$ dex higher) as compared to the other two models. All three models show good agreement with observations from various JWST programs.

- Feedback strongly affects reionisation histories (section 3.3.3). `bursty-sn` completes reionisation by $z = 5.1$, consistent with observational constraints. This is not the case for `smooth-sn` and `hyper-sn`, despite both models yielding an excess of ionising photons in comparison to `bursty-sn`. I thus confirm that reionisation is very sensitive to the modulation of $f_{\rm esc}$ due to feedback, rather than being driven solely by the number of available ionising photons.

- The impact of feedback is visible also in the intrinsic 1500 Å luminosity function (LF; section 3.3.4). While in `smooth-sn` and `hyper-sn` one can note an abundance of highly UV-bright galaxies ($M_{1500} < -23$), these are absent in `bursty-sn`. The `hyper-sn` (`smooth-sn`) model consistently yields the lowest (highest) galaxy counts at all redshifts.

- The evolution of the dust-attenuated LFs is different from that of the intrinsic ones (section 3.3.4). Interestingly, while only in `smooth-sn` one can observe signs of dust attenuation at $z = 10$, by $z = 7$ all models exhibit noticeable levels of attenuation, which becomes even more pronounced at $z = 5$. All three models show an excellent agreement with observations, especially at $z = 7$ and 5. Despite intrinsic LFs being different, dust-attenuated ones show minimal discrepancies across models. Therefore, LFs cannot be directly used to constrain feedback models.

- I note striking differences in post-reionisation galaxy morphologies, characterized by the ratio V/σ (section 3.3.5), where I classify galaxies with $V/\sigma \geq 1$ as rotationally-supported and dispersion-supported otherwise. `bursty-sn` exhibits a preference for dispersion-dominated systems, primarily at the higher mass end, while in `smooth-sn` most galaxies are rotationally-dominated at any mass. Finally, in `hyper-sn` galaxies with masses below (above) $M_* \approx 10^8 \mathrm{M}_\odot$ typically show strong dispersion (rotational) support.

- The differences in morphology translate into variations in Lyman continuum (LyC) escape fractions (f_{esc}; section 3.3.6 and Figure 3.11). I find that f_{esc} of dispersion-dominated systems is enhanced by a factor of $\approx 10 - 50$ in comparison to that of rotation-dominated ones at all redshifts.

- Galaxies that undergo strong bursts of feedback preferably produce dispersion-dominated systems (especially at the highest mass and luminosities), and hence higher f_{esc} as compared to galaxies that have smoother feedback, which allow for the formation of stable, rotationally-supported systems (in particular at the highest mass and luminosities). Therefore, feedback determines the global morphological mix of galaxies, and, as a consequence, the global f_{esc}. The connection between morphologies and f_{esc}, therefore, can potentially be an excellent probe not only of feedback models at high redshifts, but also of the galaxies that drive reionisation.

- The intrinsic contribution to ionising emissivity ($\dot{N}_{\mathrm{ion}}$; solid lines in Figure 3.12) is dominated by galaxies with $M_* \gtrsim 10^9 \mathrm{M}_\odot$ in `hyper-sn` ($\approx 65\%$) and `smooth-sn` ($\approx 50\%$), whereas `bursty-sn` shows a similar contribution from galaxies of all stellar masses above $\sim 10^7 \mathrm{M}_\odot$.

- The escaping emissivity ($f_{\mathrm{esc}}\dot{N}_{\mathrm{ion}}$, dashed lines Figure 3.12) in the three models is dominated by galaxies in different mass ranges. In `smooth-sn` the largest contribution ($\approx 46\%$) comes from $M_* > 10^9 \mathrm{M}_\odot$ galaxies, whereas `bursty-sn` and `hyper-sn` show roughly uniform contribution from galaxies in the range $M_* \approx 10^{7-10} \mathrm{M}_\odot$. Upon comparing the escaping and intrinsic emissivities, I find a global (i.e. from the entire galaxy populations at all redshifts) escape fraction of $\approx 6.8, 1.8$ and 1.5% for `bursty-sn`, `smooth-sn` and `hyper-sn`, respectively.

- The ionising photon production efficiency ($\xi_{\rm ion,0} = \dot{N}_{\rm ion}/L_{1500}$) evaluated over the full duration of the simulation shows comparable median trends (see Figure 3.13) for the three models, with differences of $\approx 0.1 - 0.3$ dex. Despite a very similar ionising photon production efficiency, the three models result in quite different reionisation histories, suggesting that reionisation is strongly $f_{\rm esc}$ limited.

The feedback variations as well as the high resolution of `SPICE` allow us to probe in detail the first sources of reionisation in their stellar, gas and radiative components. In this chapter, I focused on the morphology and LyC $f_{\rm esc}$ to connect feedback to reionisation using kinematics derived from stars and Hα bright gas. However, imprints of feedback will manifest in a wide range of observables. The multi-phase ISM model, along with the additional radiation transport in IR and optical, allows us to investigate a variety of emission lines (such as `H`α, `[C II]`, `[O III]` and Lyα). Indeed, all these probes offer a unique opportunity to make predictions for and comparisons to observations across a wide range of wavelengths, from state-of-the-art facilities such as JWST, ALMA and MUSE, as well as from planned ones such as SKA and ELT. Therefore, a comparison between synthetic `SPICE` observables and real data will help to disentangle and understand different feedback mechanisms at high redshifts. In particular, I study the Lyα emission line in Chapter 4 and the `[C II]` emission line in Chapter 5.

Chapter 4

Interpreting Lyα emission at z>5

"I think I finally understand my paper, but then I realize I don't"

Maja Lujan-Niemeyer

This work has been submitted for publication to Monthly Notices of the Royal Astronomical Society.

Lyα emission is key to understanding the process of cosmic reionisation. `JWST` is finally enabling us to measure Lyα emission deep into the epoch of reionisation for an increasing number of galaxies. However, discrepancies between measurements of Lyα equivalent widths (EW_0) of Lyα emitters (LAEs) have been noted between `JWST` and ground-based facilities. I employ `SPICE`, a suite of radiation-hydrodynamical simulations featuring different stellar feedback models, and investigate the impact of radiative transfer effects (e.g. extended emission, Lyα-UV spatial offsets) and observational systematics (such as slit placement) on the measured Lyα EW_0. I perform radiative transfer of Lyα and UV photons for `SPICE` galaxies to mimic slit spectroscopy for ground-based slits and `JWST-MSA` pseudo-slits. I find that spatial Lyα-UV offsets exist independently of feedback model, and are common ($> 70\%$ galaxies with $M_* > 10^8 M_\odot$) with median values of $\approx 0.07 - 0.11''$. The theoretical predictions from `SPICE` are consistent with the observed spatial offset distribution. In addition, spatial Lyα-UV offsets are identified as a major cause of loss of flux for `JWST-MSA` type observations, with median pseudo-slit losses of $\approx 65\%$, and $\approx 30\%$ cases suffering from $> 95\%$ pseudo-slit losses. Even in the absence of such spatial offsets, the presence of extended emission can cause median pseudo-slit losses of 40%, with 4% cases suffering from $> 95\%$ pseudo-slit losses. Finally, complex galaxy morphologies or misplaced `JWST-MSA` pseudo-slit can lead to under-estimated UV continuum, resulting in spuriously high estimates of EW_0 from `JWST` in $6 - 8\%$ of galaxies. I compare the predictions from `SPICE` to a sample of 25 galaxies with Lyα emission observations from both the ground and from `JWST`. The $EW_0^{\texttt{JWST}}$ and the $EW_0^{\texttt{Ground}}$ exhibit scatter in line with predictions from `SPICE`, indicating that both physical and systematic effects are likely at play.

4.1 Introduction

The Lyman alpha (Lyα) emission line is a key tool in our quest to understand the high-redshift Universe. Lyα radiation is produced both via recombinations around young stars and collisionally-excited hydrogen gas, and can be particularly bright (Partridge & Peebles, 1967). Due to its visibility and strength, the Lyα line has been used to spectroscopically confirm star-forming galaxies (e.g. Stark et al., 2010; Jung et al., 2020b), as a proxy for Lyman continuum (LyC) escape to pinpoint galaxies that drive cosmic reionisation (e.g. Verhamme et al., 2015b; Marchi et al., 2017), and to understand the physical properties of the high-redshift intergalactic medium (IGM; for an overview see Dijkstra, 2014; Ouchi et al., 2020).

The evolution of the fraction of Lyα emitters[1] (LAEs) relative to that of the UV continuum selected galaxies ($X_{\mathrm{Ly}\alpha}$) is often used to infer the IGM optical depth. To this aim, the distribution of intrinsic Lyα equivalent width in UV selected galaxies is assumed to be the one observed in the post-reionisation Universe, at $z \sim 5-6$ (Fontana et al., 2010; Stark et al., 2010; Pentericci et al., 2011; Jung et al., 2020b; Napolitano et al., 2024, hereafter N24). Indeed, several investigations (e.g. Pentericci et al., 2011; Caruana et al., 2014; Schenker et al., 2014) have reported a decline of $X_{\mathrm{Ly}\alpha}$ at high redshift, which becomes particularly rapid at $z > 6$, suggesting an increasingly neutral universe. However, the interpretation of this trend remains debated due to potential biases and systematics in observing strategies.

Conventional strategies to identify LAEs include narrow-band imaging (e.g. Ouchi et al., 2008; Zheng et al., 2016), integral field unit (IFU; e.g. Wisotzki et al., 2018), and slit spectroscopy (e.g. Pentericci et al., 2018). As the vast majority of instruments employed for these searches are ground-based, the sensitivity of the observations is limited by sky background and atmospheric telluric lines, in particular at $z > 7$. In addition, in the absence of Lyα the redshift confirmation of galaxies remains dubious, due to the lack of other features in the spectra of these galaxies. This renders the observed of the fraction of LAEs difficult to interpret and adds significant scatter to the available data. In the first two years of operation, the `James Ibb` Space Telescope's Near InfraRed Spectrograph (`JWST-NIRSpec`, Gardner et al., 2023; Jakobsen et al., 2022) has demonstrated its ability to successfully identify Lyα emission from high-redshift galaxies (e.g. Jung et al., 2023c; Tang et al., 2023b; Saxena et al., 2024), enabling the study of the Lyα visibility evolution during the Epoch of Reionisation (EoR; e.g. Chen et al., 2024; Jones et al., 2024; Nakane et al., 2024; Napolitano et al., 2024; Tang et al., 2024). Most notably, `JWST` allows for confirmation of redshifts of galaxies using optical bright emission lines (e.g. Balmer lines, [O III]). Therefore the absence of Lyα emission can be quantified in a very precise way along with the evaluation of $X_{Ly\alpha}$.

Crucially, various studies have reported discrepancies between the Lyα rest-frame equivalent width measured by `JWST` and the estimates from ground-based telescopes (Chen et al.,

[1] A galaxy is classified as a LAE if its Lyα equivalent width, EW_0, is > 25Å, where EW_0 is evaluated as the ratio between the Lyα flux and the UV continuum of the galaxy.

2024; Larson et al., 2023; Tang et al., 2023b), including a case in which JWST has reported a non-detection, while strong Lyα emission has been measured by VLT-MUSE (Jiang et al., 2023). These discrepancies in turn translate into $X_{\rm Ly\alpha}$ estimates from JWST significantly loIr than those from ground-based observations at $z = 5-6$. The loss of Lyα flux is mainly attributed to the small size ($0.12'' \times 0.46''$) of the micro-shutter assembly on JWST, which could potentially miss extended emission caused by resonant scattering of Lyα (Verhamme et al., 2012; Smith et al., 2015; Byrohl et al., 2021; Smith et al., 2022; Yuan et al., 2024). Another possible explanation is the presence of a spatial offset between the UV and Lyα emission, which would imply that if a pseudo-slit is oriented on the UV peak, the Lyα peak could fall outside of the collection area of the slit, leading to flux loss. In the latter respect, a few observational investigations have attempted to quantify the incidence and strengths of such spatial UV-Lyα offsets (Hoag et al., 2019a; Lemaux et al., 2021; Ning et al., 2024), finding that offsets exist with medians of $\sim 0.1''$, and their strength tends to decrease at higher redshifts. Furthermore, Ning et al. (2024) report a potential positive correlation between the offset strength and the Lyα equivalent width, implying that stronger emitters could be more susceptible to flux losses.

Interpreting the influx of ground- and space-based observations of galaxies during the EoR requires pinning down the magnitude and incidence of Lyα-UV offsets and spatially-extended emission. Attempts to forward-model slit-losses caused by spatial offsets (Nakane et al., 2024) have shown that losses are expected to be $\sim 20\%$. However, these estimates are based on isotropic 2D models of Lyα and UV emission, which most likely miss the complexity and strong directional dependencies associated to the multi-phase nature of the galactic interstellar medium (ISM) (see also Garel et al., 2021; Smith et al., 2022; Blaizot et al., 2023; Choustikov et al., 2024). Here, I quantify the incidence and importance of Lyα-UV offsets and spatially-extended emission in high redshift galaxies using SPICE (Bhagwat et al., 2024c, hereafter B24), a suite of three cosmological radiation-hydrodynamic simulations with different stellar feedback prescriptions, in which the Lyα and UV properties of galaxies can be modeled while accounting for resonant scattering and radiative transfer through a complex multi-phase ISM.

This chapter is organised as follows: in Section 4.2 I describe the SPICE simulations (4.2.1), the Lyα radiation transfer computation (4.2.2), and the construction of synthetic IFU observations (4.2.3). In Section 4.3 I introduce observations of high redshift LAEs with ground-based facilities (4.3.1) and JWST (4.3.2), and compare their Lyα EW$_0$ (4.3.3). In Section 4.4 I show theoretical predictions from SPICE. Finally, in Section 4.5 I discuss implications of our findings on interpretations of observations and summarise our key results.

4.2 Theoretical modeling

Here I briefly describe the simulations used for the analysis, as well as the methodology adopted to construct synthetic datacubes.

4.2.1 SPICE simulations

I use `SPICE` (B24), a suite of radiation-hydrodynamic simulations performed with the adaptive mesh refinement code `RAMSES-RT` (Rosdahl et al., 2013b; Rosdahl & Teyssier, 2015a). The simulations are run in a cosmological box of length $10h^{-1}$ cMpc, with 512^3 dark matter particles of mean mass $6.38 \times 10^5 \mathrm{M}_\odot$. I adopt a ΛCDM model with $\Omega_\Lambda = 0.6901$, $\Omega_\mathrm{b} = 0.0489$, $\Omega_\mathrm{m} = 0.3099$, $H_0 = 67.74$ km s^{-1} Mpc^{-1}, $\sigma_8 = 0.8159$, and $n_\mathrm{s} = 0.9682$ (Planck Collaboration et al., 2016b).

Metal line cooling is accounted for at $T > 10^4$K adopting `CLOUDY` tables (Ferland et al., 1998), while fine structure rates from Rosen & Bregman (1995) are employed for $T \leq 10^4$K. The non-equilibrium ionisation states of H and He are advected while being fully coupled to the local ionising radiation (see Rosdahl et al., 2013a). `SPICE` employs a star formation model with a variable star formation efficiency (Kretschmer & Teyssier, 2020) which depends on the local value of the gas turbulent Mach number and virial parameter, the latter being an indicator of the local stability. I refer the reader to B24 for more details of the model. I adopt a Chabrier initial mass function (Chabrier, 2003), which results in a Supernova (SN) rate of 0.016 SN $\mathrm{M}_\odot^{-1}$. SN mechanical feedback is implemented as in Kimm & Cen (2014) and Kimm et al. (2015). A unique feature of `SPICE` is the use of three different supernova feedback models, resulting in three highly-contrasting star formation and feedback behaviours. This is achieved by maintaining the implementation of the SN feedback, while varying the energy and timing of the SN explosions as follows (refer also to Table 2 of B24):

1. `bursty-sn`: When a stellar particle becomes 10 Myr old, all SN explode in a single event injecting an energy of 2×10^{51} ergs.

2. `smooth-sn`: As (i), but SN events now happen between 3 and 40 Myr since the stellar particle birth.

3. `hyper-sn`: As (ii), but a fraction f_HN of SN explodes as hypernovae, with an energy of 10^{52} ergs. I adopt a metallicity dependent $f_\mathrm{HN} = \max[0.5 \times \exp(-Z_*/0.001), 0.01]$, with Z_* stellar metallicity (Grimmett et al., 2020). The other SN events have an energy in the range $10^{50} - 2 \times 10^{51}$ ergs (Sukhbold et al., 2016).

I follow the on-the-fly radiative transfer of photons in five frequency bands, i.e. infrared (IR, $0.1 - 1$ eV), optical ($1 - 13.6$ eV) and three ionising UV bands (13.6-24.59 eV, 24.59-54.42 eV, and >54.42 eV). In addition to radiative feedback from photo-ionisation and photo-heating, I also include radiation pressure from UV photons and radiation pressure on dust from IR and optical photons.

Spectral energy distributions taken from `BPASSv2.2.1` (Eldridge et al., 2017; Stanway & Eldridge, 2018) are employed to evaluate the stellar particles' luminosity based on their metallicity, age and mass. I adopt a dust number density $n_\mathrm{d} \equiv (Z/Z_\odot) n_\mathrm{HI}$, where n_HI is the neutral hydrogen number density. Photons interact with gas through multi-scattered radiation pressure and can be re-processed into the IR according to dust absorption and scattering opacities assigned to each cell (see Rosdahl & Teyssier 2015b and Table 3 in B24).

4.2.2 Lyα radiative transfer

I perform Lyα radiative transfer (Lyα-RT) in post-process using the publicly available, resonant-line transfer code RASCAS (Michel-Dansac et al., 2020). This calculates the spatial and spectral diffusion of resonant-line photons using a Monte Carlo technique.

I model Lyα photon production from three emission channels: (i) recombination radiation from photo-ionised gas, (ii) Lyα cooling from collisionally-excited hydrogen, and (iii) direct injection from the stellar continuum. The emission from a recombination cascade from photo-ionised gas is modelled as in Cantalupo et al. (2008), with the number of Lyα photons emitted per unit time in a gas cell of proper length Δx given by

$$\dot{N}_{\mathrm{Ly}\alpha,\mathrm{rec}} = n_{\mathrm{e}} n_{\mathrm{p}} \epsilon^{\mathrm{B}}_{\mathrm{Ly}\alpha}(T) \alpha^{\mathrm{B}}(T) (\Delta x)^3, \tag{4.1}$$

where n_{e} and n_{p} are the electron and proton number densities, T is the gas temperature, $\alpha^{\mathrm{B}}(T)$ is the case-B recombination coefficient (Hui & Gnedin, 1997, Appendix A), and $\epsilon^{\mathrm{B}}_{\mathrm{Ly}\alpha}(T)$ is the number of Lyα photons produced per recombination event. The rate of Lyα photons emitted by collisionally-excited gas cell is given by

$$\dot{N}_{\mathrm{Ly}\alpha,\mathrm{col}} = n_{\mathrm{e}} n_{\mathrm{HI}} \left[\frac{6.58 \times 10^{-18}}{T^{0.185}} \right] \left[\frac{e^{-(4.86 \times 10^4)/T^{0.895}}}{h\nu_0} \right] (\Delta x)^3, \tag{4.2}$$

where $\nu_0 = 2.47 \times 10^{-15} s^{-1}$ is the rest frame frequency of a Lyα photon. The rate of collisional excitations is taken from the best fit parameters of Katz et al. (2022a, Supplementary data Fig. S1). The stellar continuum is modelled using the same spectral energy distributions of SPICE, and the Lyα photons emission rate of each star particle is estimated using a 2D interpolation in age and metallicity.

The Lyα radiation from recombination and collisionally-excited gas is sampled with $N_{\mathrm{ph,rec}} = N_{\mathrm{ph,col}} = 10^6$ photon packets, while for the stellar continuum I adopt $N_{\mathrm{ph,stc}} = 1.5 \times 10^7$ packets[2].

RASCAS models the interaction of the emitted Lyα photons with the hydrogen, deuterium and dust contained within each gas cell, assuming a deuterium abundance of D/H $= 3 \times 10^{-5}$, while the dust number density is provided by SPICE (see section 4.2.1 of B24 for details). The Lyα-RT calculation includes recoil due to deuterium, dust absorption (assuming a Small Magellanic Cloud composition[3]), as well as scattering with all three species. RASCAS adopts the phase functions from Hamilton (1940) and Dijkstra & Loeb (2008) for scattering of photons around the line centre, and Raleigh scattering in

[2]I note that the larger number of photon packets employed to sample the stellar continuum is due to the larger number of stellar particles in comparison to gas cells, as well as to the wider spectral band that needs to be sampled. Details and convergence tests will be provided in Bhagwat et al. (in prep.).

[3]The choice of dust composition does not affect our results (Costa et al. 2022).

the line wings. Lyα photons are scattered by dust with a probability given by an albedo $a_{\rm dust} = 0.32$ (Li & Draine, 2001) following a Henyey-Greenstein phase function (Henyey & Greenstein, 1941) with an asymmetry parameter $g = 0.73$. To reduce computational overhead in regions of high optical depth ($\gg 10^3$), `RASCAS` implements a core-skipping algorithm (see Smith et al. 2015) which shifts the photons to the line wings, facilitating their escape. Finally, `RASCAS` employs the "peeling off" algorithm (Zheng & Miralda-Escudé, 2002; Whitney, 2011) to collect Lyα flux along a given line-of-sight. I post-process all `SPICE` galaxies with $M_* > 10^8 {\rm M}_\odot$ at $z = 5, 6, 7$ which have UV magnitudes of $-23 < M_{\rm UV} < -16$ with median $M_{\rm UV} = -18.3$ and $\beta_{\rm UV}$ ranging between $-3 < \beta_{\rm UV} < -1.5$.

4.2.3 Synthetic IFU datacubes and associated observables

To compare the Lyα properties of `SPICE` galaxies to observations, I construct synthetic IFU datacubes of side length $3R_{\rm vir}$, where $R_{\rm vir}$ is the virial radius, centered on the halo. I follow the Lyα-RT of photons produced from the three emission channels mentioned in Section 4.2.2. I adopt $N \times N$ spatial bins of resolution $\Delta\theta$, and N_λ spectral bins of resolution $\Delta\lambda$ along the line-of-sight. Each 3D IFU datacube is thus constructed to have two spatial axes with $\Delta x = 0.05''$, and one wavelength axis with a rest-frame $\Delta\lambda \approx 0.13$Å.

Each photon packet contributes a luminosity of $L_{{\rm Ly}\alpha,i}/N_{{\rm ph},i}$, where $L_{{\rm Ly}\alpha,i}$ is the total Lyα luminosity produced via channel i. The probability that a photon escapes to an observer positioned at a luminosity distance $D_{\rm L}$ within a given wavelength bin is $P(\mu)e^{-\tau_{\rm esc}(\lambda)}$, where $\tau_{\rm esc}(\lambda)$ is the optical depth between the scattering event and the edge of the computational domain. The total flux within each pixel in the datacube is written as

$$F_{{\rm Ly}\alpha,{\rm pixel}} = \frac{L_\lambda/N_{\rm ph}}{4\pi D_{\rm L}^2(1+z)} \sum P(\mu)e^{-\tau_{\rm esc}(\lambda)}, \tag{4.3}$$

where $L_\lambda = L_{{\rm Ly}\alpha}/[\Delta\lambda(1+z)^{-1}]$, such that the flux in each pixel is integrated over all scattering events from all photon packets.

Calculations for collisional and recombination Lyα are carried out in the range $1205 - 1225$Å and the stellar continuum is calculate in the range $800 - 2600$Å. Henceforth, I refer to the UV continuum as flux estimated in range $1400 - 2600$Å. For each halo, I calculate the datacubes along 12 sightlines, where 4 are oriented at an angle of [0, 30, 60, 90] degrees to the halo's angular momentum vector (fixed ϕ with random θ), while the rest are drawn with random ϕ and θ.

From the IFU datacubes I evaluate the equivalent width (EW) and flux of Lyα and UV radiation. The flux is collected in apertures with sizes $0.2'' \times 0.46''$ and $0.7'' \times 8''$ to resemble the slit dimension on `JWST-NIRSpec` and ground-based settings, respectively. Note that ground based spectroscopy was performed using variable slit sizes, with width from $0.7''$ to $1.0''$ and length which was in some cases also greater than $10''$ (Pentericci et al., 2018; Schenker et al., 2014; Stark et al., 2011). While I always center the ground-based slits at the peak of the UV continuum, the `JWST-MSA` pseudo-slits are placed in two ways: either centered at the peak of the UV, or centered with offsets between $0''$ and $0.15''$ with respect to the UV peak in random directions to account for positional uncertainty in the MSA placement. This choice is motivated by the real offset in the observational data (see next section). I fit a poIr law to the UV continuum to obtain the β slope of a galaxy, and use the fit is used to estimate the continuum emission at the Lyα line center ($F_{\mathrm{Ly}\alpha}^{\mathrm{cont}}$). The rest-frame equivalent width (EW_0) for Lyα is then measured as:

$$\mathrm{EW}_0 = \frac{F_{\mathrm{Ly}\alpha}}{F_{\mathrm{Ly}\alpha}^{\mathrm{cont}}(1+z)}. \tag{4.4}$$

Finally, I quantify the spatial offsets, $d_{\mathrm{Ly}\alpha-\mathrm{UV}}$, between Ly$\alpha$ and UV by calculating the distance between the peak pixels in the respective surface brightness (SB) maps. I note that while this study focuses on the physical scenarios and systematics affecting interpretation of Lyα emission, a detailed study of Lyα properties of `SPICE` galaxies including radial surface brightness profiles, luminosities, line profiles will follow in a companion work (Bhagwat et al. in prep.).

4.3 Observational data

I note that the observational data in section 4.3 was collected by Dr. Laura Pentericci and Lorenzo Napolitano. I continue to use "I" this this section for consistency with the rest of the thesis.

As I aim to investigate potential systematics due to slit loss effects when comparing Lyα rest-frame equivalent widths from `JWST-NIRSpec` and ground-based measurements, I compile the largest possible sample of galaxies with Lyα measurements both from ground and space (i.e. `JWST-NIRSpec`) instrumentation. To minimise any possible calibration issue, I compare the Lyα EW_0 rather than the emission line flux.

4.3.1 Ground-based observations

I assemble a catalog of galaxies which Ire observed with the aim of detecting Lyα emission from ground-based facilities (`MUSE` and `FORS2` on the `VLT`, and `DEIMOS` and `MOSFIRE` on `Keck`) in the past ~ 15 years, targeting the GOODS-South, GOODS-North, EGS, UDS, COSMOS, and Abell 2744 fields. I consider the published catalogs with their spectroscopic redshift z_{spec}, Lyα EW_0 measurements, or upper limits, as presented in Pentericci et al. (2018), Jung et al. (2020b), Richard et al. (2021), Schmidt et al. (2021), Jung et al. (2022), Bacon et al. (2023), and Napolitano et al. (2023). I ensure that there are no systematics related to the ground-based instruments used and consider sources at $z_{\mathrm{spec}} \geq 5$, to match the redshifts probed by the `SPICE`.

4.3.2 `JWST` observations

I search for `JWST-NIRSpec` PRISM observations of targets which matched the sky position of the galaxies from the ground based catalog. To allow for positional uncertainties between

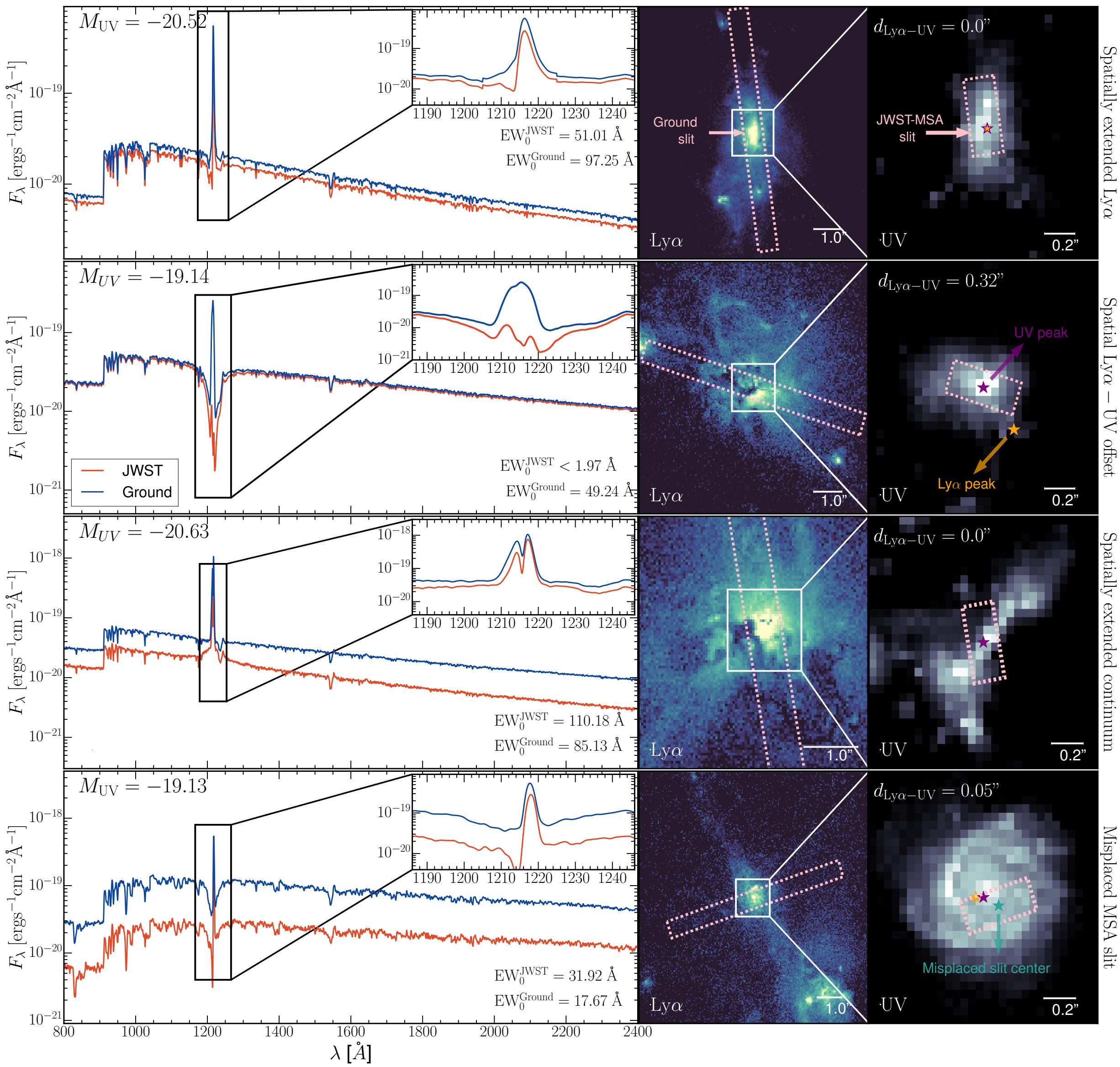

Figure 4.1: Four scenarios for EW_0 mismatch: *Left column:* Spectra extracted with ground-based slit (blue) and `JWST-MSA` pseudo-slit (red) from a reference galaxy in `SPICE`; the inset shows the spectra in the range 1180-1250 Å rest-frame. $M_{\rm UV}$ listed in each panel is the UV magnitude calculated between 1400-1500 Å, while EW_0 is the Lyα equivalent width (see section 4.2.3). *Middle column:* Lyα emission from the galaxy with the ground-based slit overplotted (dotted line). *Right column:* zoomed-in region on the UV continuum of the galaxy with the `JWST-MSA` pseudo-slit overplotted (dotted line). The position of the peak of the emission in UV (purple star) and Lyα (orange star) is shown to highlight the spatial Lyα-UV offset ($d_{\rm Ly\alpha-UV}$) . The rows refer to various cases in which a mismatch arises between the EW_0 measured by `JWST` and by ground-based telescopes; from top to bottom: extended Lyα emission in which the peaks of the Lyα and UV emission coincide, a large spatial Lyα-UV offset of $d_{\rm Ly\alpha-UV} = 0.32''$, `JWST` missing UV continuum due to complex galaxy morphologies with a spatially extended continuum, and `JWST` missing UV continuum due to errors in the pseudo-slit placement, with the true pseudo-slit position shown as green star.

different catalogs, I match objects using a 0.5" radius threshold. I employ all the spectra available from the CEERS data release (Arrabal Haro et al., 2023), from the JADES-DR3 (D'Eugenio et al., 2024) and from the DAWN `JWST` Archive[4] (DJA-Spec, Heintz et al., 2024). In particular, the observations include the Abell 2744 (PID 2561, 2756, Bezanson et al., 2022, and Mascia et al., submitted), JADES GOODS-North (GTO 1181, 1211, Bunker et al., 2023), JADES GOODS-South (GTO 1180, 1210, PID 3215, 6541, Bunker et al., 2023), EGS (ERS 1345, Arrabal Haro et al., 2023), COSMOS and UDS (PID 2565, Nanayakkara et al., 2024) fields. I visually inspect all the spectra and the z_{spec} provided by JADES-DR3 and DJA-Spec, while for CEERS I use the catalog presented in Napolitano et al. (2024). I also required the difference between the ground based and `JWST` spectroscopic redshift solutions to be less than 0.05 of each other (considering the low resolution of the PRISM observations). In total I obtained 60 matches.

For each `JWST` spectrum, I measure the UV magnitude, M_{UV}, in the 1400–1500Å rest-frame range without correcting for dust. The selected galaxies have a UV magnitude in the range $-21 < M_{\mathrm{UV}} < -18$. The Ly$\alpha$ EW$_0$ and uncertainties are derived as detailed in Napolitano et al. (2024). When the Lyα is not detected, I use the typically adopted 3EW$_{0,\mathrm{lim}}$ as an upper limit, where EW$_{0,\mathrm{lim}}$ is the loIst value that can be measured according to Equation (1) of Napolitano et al. (2024), which takes into account the spectral resolution and the noise spectrum.

4.3.3 `JWST` and ground-based equivalent widths

Out of the 60 galaxies selected above, the Lyα EW$_0$ from the `JWST` and ground based observations can be compared in a meaningful way in 25 cases, which include: (i) All galaxies with EW$_0$ measurements from both instruments (14 sources). (ii) All galaxies with a EW$_0$ measurement from `JWST` and for which the 3σ upper limit from ground-based instruments is below the `JWST` measure. In these cases I can conclude that the `JWST` measure is above the ground-based one (6 sources). (iii) All galaxies with a ground-based EW$_0$ measurement and for which Lyα is not detected in the `JWST` spectrum and its 3σ upper limit is below the ground-based EW$_0$. In these cases I can conclude that the ground-based measure is above the `JWST` one (5 sources). In all other cases, for example when both the `JWST` and ground-based spectra only give upper limits, the comparison is inconclusive.

Finally utilizing the "slitlet viewer" tool provided in the DJA archive, I check for the positional offset between the center of the MSA pseudo-slit and the peak of the UV continuum emission for the 25 sources just discussed. I found positional offsets varying between 0″ and 0.15″.

[4]https://dawn-cph.github.io/dja/

4.4 Results

SPICE galaxies often exhibit a mismatch between the EW_0 that would be measured by JWST and ground-based telescopes. I identified four main origin scenarios for such a mismatch: (i) spatially extended Lyα emission, (ii) spatial offsets between Lyα emission and the UV continuum, (iii) spatially extended young stellar populations and (iv) MSA misplacements.

In Figure 4.1 I illustrate these scenarios, using the ground-based slit (see Section 4.2.3) as a reference for the "true" measured EW_0. The system in the top row shows a spatially extended Lyα nebula in which the peak of the Lyα and UV emission coincide, i.e. $d_{\mathrm{Ly}\alpha-\mathrm{UV}} = 0''$. While the JWST-MSA pseudo-slit is able to capture the UV continuum to the same extent as the ground-based slit, the former misses part of the Lyα flux, leading to an underestimation of the EW_0 by a factor of ≈ 2. The second row illustrates a case in which there is a significant spatial Lyα-UV offset, with $d_{\mathrm{Ly}\alpha-\mathrm{UV}} = 0.32''$. While the UV continuum is captured by both slit and MSA pseudo-slit (as in the previous case), the majority of the Lyα emission lies outside of the JWST-MSA pseudo-slit boundaries due to the spatial offset. This effect translates into the estimation of a large Lyα EW_0 with ground-based facilities and a non-detection of Lyα with JWST (similar to the case reported by Jiang et al. 2023). The third row illustrates the case in which the continuum is produced by a system with spatially extended star formation, but without the presence of a spatial Lyα-UV offset. While the JWST-MSA pseudo-slit captures the majority of the Lyα emission, it fails to capture the full extent of the continuum emission. This leads to an estimate of EW_0 with JWST which is higher than the ground-based one, as the slit captures the full continuum emission. In this final scenario, if the pseudo-slit barycenter is not correctly placed at the peak of the UV continuum (bottom row), the small size of the JWST-MSA pseudo-slit can miss a large portion of the UV continuum flux, resulting in a loIr continuum estimate at the Lyα wavelength. As a consequence, JWST would overestimate EW_0 even if the Lyα emission Ire perfectly captured, while ground-based observations would instead correctly capture the full UV continuum as in the previous case, consequently, JWST would overestimate EW_0 as compared to ground-based slit. Therefore, both the systematics of observations and the underlying physical scenarios can affect the interpretation of measured EW_0.

As the presence of offsets can potentially lead to JWST missing a large portion of Lyα flux leading to a non-detection of Lyα emission, it is key to investigate their incidence and strength. In Figure 4.2 I show the cumulative distribution function of $d_{\mathrm{Ly}\alpha-\mathrm{UV}}$ at z=5 and 7[5]. For all models and at all redshifts analysed, over the full sample, I find non-zero offsets in $> 70\%$ galaxies, with median values of $0.07\pm0.06''(0.07\pm0.05'')$, $0.08\pm0.06''(0.10\pm0.07'')$ and $0.077 \pm 0.08''(0.11 \pm 0.08'')$ for bursty-sn, smooth-sn and hyper-sn, respectively at $z = 5$ (7). For the sub-sample of galaxies with non-zero offsets, the median values are $0.10\pm 0.05''(0.11\pm0.05'')$, $0.08\pm0.05''(0.12\pm0.05'')$ and $0.11\pm0.07''(0.12\pm0.07'')$ for bursty-sn, smooth-sn and hyper-sn, respectively at $z = 5$ (7). I note a slight redshift evolution in the smooth-sn and hyper-sn models, where the median offset decreases between $z = 7$

[5]I find similar results at z=6, but they are not shown to avoid overcrowding.

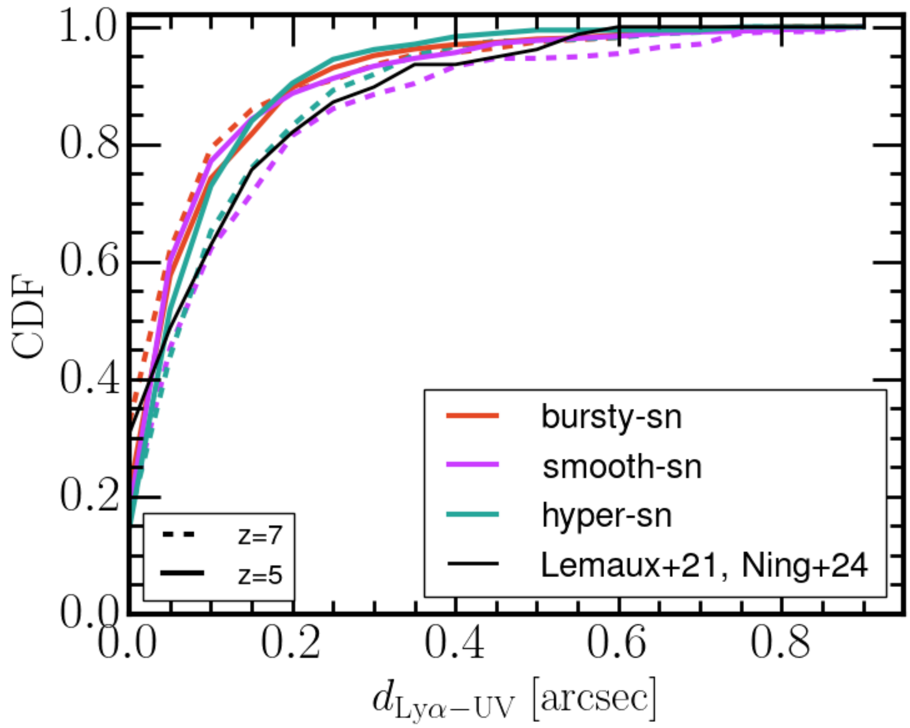

Figure 4.2: Cumulative distribution functions (CDF) of spatial Lyα-UV offsets, $d_{\mathrm{Ly}\alpha-\mathrm{UV}}$, for the three feedback models at $z = 7$ (dashed lines) and 5 (solid). The black solid line shows the cumulative distribution function of offsets obtained using the datasets of Lemaux et al. (2021) and Ning et al. (2024). Predictions from `SPICE` are consistent with observed spatial offsets independent of feedback model.

and 5, while `bursty-sn` shows no evolution. Median results are consistent with previous observations of high redshift galaxies (Hoag et al., 2019a; Ribeiro et al., 2020; Khusanova et al., 2020; Lemaux et al., 2021; Ning et al., 2024; Navarre et al., 2024). However, some of the observations show a mild decrease in offsets with increasing redshift, in contrast to what I obtain using the `smooth-sn` and `hyper-sn` models.

To assess the effect of slit-sizes on the estimated EW_0 of Lyα, in Figure 4.3 I show the EW_0 measured using the `JWST-MSA` pseudo-slit as a function of the value measured with a ground-based slit, for pseudo-slits centered on the peak of the UV. At $z = 7$ (left panel), in all models, the majority of galaxies has $\mathrm{EW}_0^{\texttt{JWST}} \ll \mathrm{EW}_0^{\texttt{Ground}}$ ($\approx 98\%$ in total), while only a small fraction has $\mathrm{EW}_0^{\texttt{JWST}} > \mathrm{EW}_0^{\texttt{Ground}}$ ($\approx 2\%$). At $z = 6$ (middle panel), the difference in the estimates reduces slightly, with all models moving closer to the 1:1 line (equal EW_0), and the fraction of galaxies with $\mathrm{EW}_0^{\texttt{JWST}} > \mathrm{EW}_0^{\texttt{Ground}}$ reducing to 1%. By $z = 5$ (right panel) this fraction has become negligible, while most galaxies still lie below the 1:1 line. The overall behaviour is maintained also with the inclusion of pseudo-slits misalignments, but the fraction of galaxies with $\mathrm{EW}_0^{\texttt{JWST}} > \mathrm{EW}_0^{\texttt{Ground}}$ increases to 9% (8%) at $z = 7(5)$. In the case where I include positional offsets in pseudo-slit placement, the scatter in the contours

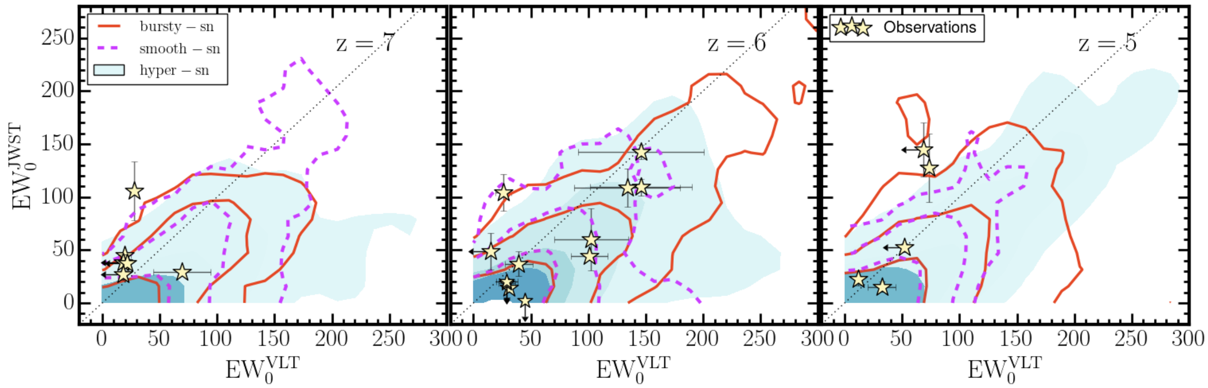

Figure 4.3: Lyα EW$_0$ measured by `JWST` as a function of the one measured by ground-based facilities for the three feedback models at $z = 7$ (left panel), 6 (middle), and 5 (right). Contours show regions covering 68%, 95% and 99% of all points. The black dotted line is the 1:1 relation, while the star symbols represent the 25 sources for which the comparison between $EW_0^{\texttt{JWST}}$ and $EW_0^{\texttt{Ground}}$ is conclusive (see Section 4.3 for details). Arrows refer to 3σ upper limits for non-detections. The majority of values derived from `SPICE` lie below the 1:1 line irrespective of the feedback model, implying a deficit of EW$_0$ as measured by `JWST`.

increases for all models, such that $\approx 6\%$ galaxies cross above the 1:1 at all redshifts.

In Figure 4.3 I also report the 25 galaxies selected in Section 4.3 at their respective redshifts. I find 14 cases where galaxies lie below the 1:1 line, with `JWST` measurements within a factor of $1-2$ of ground-based measurements; 6 galaxies have $EW_0^{\texttt{JWST}} > EW_0^{\texttt{Ground}}$ which could potentially be due to pseudo-slit position not being centered on the peak of the UV continuum; and in 5 cases `JWST-MSA` gives only a 3-sigma upper limit with confirmed strong Lyα detections from the ground. The observed data exhibits a scatter as predicted by `SPICE` ,therefore, all the physical and systematic effects illustrated in Figure 4.1 could potentially be at play. I defer a more detailed investigation of the relative importance of the various mechanisms to a future study once more observational data are available.

4.5 Summary and Conclusions

In this chapter, I use the SPICE simulations to show that the Lyα visibility can be strongly influenced by Lyα radiative transfer effects, and highlight the importance of considering spatial Lyα-UV offsets when performing MSA spectroscopic observations with `JWST`. Systematics such as pseudo-slit misalignments are also important to consider while interpreting observations. The combined information of rest-frame UV photometry and slit spectra can potentially correct for systematics.

I find that extended Lyα emission is present around every simulated galaxy in our sample (also shown in Verhamme et al., 2012; Byrohl et al., 2021; Smith et al., 2022; Yuan et al., 2024). If there is no spatial Lyα-UV offset, the emission radial profile determines whether EW$_0$ is correctly captured by `JWST` or not, since it will be underestimated if the

Lyα emission extends beyond the pseudo-slit size. Meanwhile, the larger slit sizes on the ground-based facilities allow to capture Lyα emission out to larger spatial scales. In the `bursty-sn` model, for galaxies without a spatial Lyα-UV offset, pseudo-slit losses are estimated to be $\approx 40\%$ at all redshifts with $\approx$4% (7.2%) of Lyα emitting galaxies suffering pseudo-slit losses of $> 95\%$ when observed by `JWST` at $z = 7$ ($z = 5$). For the `smooth-sn` and `hyper-sn` models, the pseudo-slit losses mildly evolve between 40% at $z = 7$ to 35% at $z = 5$, with $\approx$4% galaxies suffering pseudo-slit losses of $> 95\%$.

The Lyα EW_0, however, are mostly affected by spatial Lyα-UV offsets. For LAEs with spatial offsets, the pseudo-slit losses are estimated to be $\approx 65\%$ at all redshifts. This result appears to be robust as it holds throughout all `SPICE` simulations, i.e. irrespective of SN feedback model. Out of these galaxies, the fraction which suffer $> 95\%$ pseudo-slit loss in the `bursty-sn` models increases from 30% at $z = 7$ to 38% at $z = 5$, while it is 31% (30%) and 43% (44%) at $z = 5$ (7) for `smooth-sn` and `hyper-sn` models, respectively. Finally, $\approx 22-24\%$ of all LAEs show consistent EW_0 from both `JWST-MSA` and ground-based slits.

These results are obtained assuming that the `JWST-MSA` pseudo-slit is perfectly centered on the peak of the UV. This is not always the case, since the positions could be slightly misaligned to better optimize the total number of observed targets in the `JWST-MSA` configuration. If I include such placement uncertainties, of the order of $0.0''$–$0.15''$, as derived from the observations considered (see section 4.3), the fraction of galaxies with such high pseudo-slit losses drops by $5-7\%$ at all redshifts. These galaxies end up with overestimated EW_0 values (as shown in the bottom row of Figure 4.1). Overall, the EW_0 estimated by `JWST-MSA` increases relative to the ground-based values by a median factor of $\approx 4-5$ in the presence of slightly misaligned pseudo-slit positions for $\approx 25\%$ of galaxies. This effect is independent of feedback model and redshift considered.

Due to both pseudo-slit losses and misalignments, the scatter in the measured EW_0 distribution will lead to an uncertainty in the statistical visibility of Lyα that must be considered when using it to infer the neutral fraction of the IGM. Intrinsically, about $\approx 30\%$ LAEs will be missed by `JWST-MSA` as predicted by `SPICE` with the remainder being measured with mild to moderate pseudo-slit losses.

I summarize the key conclusions as follows:

- Radiative transfer effects leading to e.g. extended emission and Lyα-UV offsets, as well as observational systematics (e.g. off-centered pseudo-slit positions) affect EW_0 measurements from `JWST` introducing scatter in the EW_0 distributions.

- I find that $> 70\%$ `SPICE` galaxies have non-zero spatial Lyα-UV offsets, with a median offset of $0.07''$ ($0.07''$), $0.08''$ ($0.10''$) and $0.08''$ ($0.11''$) for the `bursty-sn`, `smooth-sn` and `hyper-sn` models, respectively, at $z = 5$ ($z = 7$).

- The distribution of offsets shows only a mild redshift evolution for the `smooth-sn` and `hyper-sn` models, where the median offset decreases between $z = 7$ and $z = 5$, while `bursty-sn` exhibits no redshift evolution in agreement with observations.

- In cases without spatial Lyα-UV offsets, extended Lyα emission can cause median pseudo-slit losses of $\approx 40\%$ with $\approx 4-7\%$ of LAEs suffering from $> 95\%$ losses.

- Spatial Lyα-UV offsets are the main cause of Lyα flux being underestimated from `JWST` observations, with median pseudo-slit losses of $\approx 65\%$ in galaxies with significant spatial offsets. About $30 - 40\%$ cases suffer from $> 95\%$ losses depending on redshift and feedback model.

- Complex galaxy morphologies as in the case of mergers or extended star-forming regions along with misplaced placement of the `JWST-MSA` pseudo-slits can lead to the UV continuum being under-sampled. In this scenario, the EW_0 estimated from `JWST` will exceed those estimated from the ground. About 2% (< 1%) galaxies exhibit $\mathrm{EW}_0^{\mathtt{JWST}} > \mathrm{EW}_0^{\mathtt{Ground}}$ without MSA placement offsets at $z = 7$ ($z = 5$) with the numbers increasing to $\approx 6\%$ (8%) galaxies with the inclusion of MSA placement offsets.

  While pseudo-slit losses add scatter to Lyα EW_0, the physical phenomena that lead to such losses also are sensitive to the state of the ISM and the CGM of high-z LAEs. Future observations such as those from the upcoming JWST large program CAPERS (The CANDELS-Area Prism Epoch of Reionization Survey; Dickinson et al., 2024) and RUBIES will provide larger samples of high redshift galaxies boosting both JWST and ground-based observations of the Lyα emission line. Such samples will be key to constrain the incidence and origin of extended emission and spatial offsets that affect the interpretation of Lyα emission visibility during cosmic reionisation.

Chapter 5

Imprints of stellar feedback on [C II] properties

"The computing gods are not on our side today....what a shame"

Hitesh Kishore Das

This work will be submitted for publication to Monthly Notices of the Royal Astronomical Society in the coming weeks.

5.1 Introduction

The 158μm emission line of singly ionised carbon ([C II] henceforth) has emerged as a key probe to study the interstellar medium (ISM) of high redshift galaxies. [C II] is one of the most dominant coolants in the ISM (Malhotra et al., 1997; Luhman et al., 1998) and accounts for a large fraction ($\sim$1%) of the total far-infrared (FIR) luminosity of galaxies (Russell et al., 1980; Spitzer, 1978; Crawford et al., 1985; Stacey et al., 1991). A wide range of ISM conditions ranging from diffuse ionised medium to cold neutral medium are thought to excite [C II] emission due to its low ionisation potential of 11.2eV (Madden et al., 1993; Pineda et al., 2013; Croxall et al., 2017; Tarantino et al., 2021). [C II] therefore could act as a diagnostic to characterise the structure of the multi-phase ISM in star-forming galaxies.

State-of-the-art observing facilities such as the Atacama Large Millimetre/sub-millimetre Array (ALMA) (Wootten & Thompson, 2009) and Northern Extended Millimeter Array (NOEMA) have allowed for observations of [C II] emitters up to $z \sim 8$ (Aravena et al., 2016), shedding light on the star-forming characteristics of galaxies. A strong correlation between [C II] luminosity ($L_{\rm CII}$) and the star formation rate (SFR) of galaxies has been shown by observations, particularly at low redshifts (Boselli et al., 2002; De Looze et al., 2011, 2014; Herrera-Camus et al., 2015; Hodge & da Cunha, 2020). At $z > 5$, however, a deficit in the $L_{\rm CII}$-SFR relation or a non-detection of [C II] in star-forming galaxies has raised tensions about interpreting [C II] as a tracer of star-forming gas (Ouchi et al., 2013b; Ota et al., 2014; Maiolino et al., 2015; Knudsen et al., 2016; Pentericci et al., 2016; Bradač et al., 2017; Laporte et al., 2019; Romano et al., 2022a). In this context, it has been theorised that bursty feedback could suppress [C II] immediately after a starburst (Ferrara et al., 2019; Katz et al., 2022c).

Multiple large ALMA programs such as `ALPINE` (Le Fèvre et al., 2020; Béthermin et al., 2020; Faisst et al., 2020), `REBELS` (Bouwens et al., 2022a) and `CRISTAL` (Solimano et al., 2024; Mitsuhashi et al., 2023) have observed hundreds of galaxies between $4 < z < 6$. The scientific goals of these programs revolve around understanding the physical origin of [C II] emission, incidence of outflows, metal enrichment of the CGM and star-formation. An interesting aspect of these studies is connecting observed broad [C II] kinematics to the incidence of outflows. Stacking of galaxies has become a norm in the last decade (Gallerani et al., 2018; Bischetti et al., 2019; Ginolfi et al., 2020a) to extract information from datacubes to mitigate lack of physical resolution in observations of single objects. Multiple studies using stacking data find evidence of broad [C II] lines, however, the origin of these lines remains debated. Physical scenarios such as satellite galaxies and mergers (Solimano et al., 2024; Posses et al., 2024), cold outflows (Pizzati et al., 2020; Ginolfi et al., 2020a; Pizzati et al., 2022) and cold streams and inflows (Fujimoto et al., 2022). Therefore, it is essential to forward-model the origin of [C ii] line emission and line kinematics and make robust predictions to guide observational efforts to disentangle the physical scenarios listed previously.

In this chapter, I exploit the high resolution radiation-hydrodynamical simulations `SPICE` to study and forward-model [C II] properties of high-redshift galaxies and attempt to quantify the imprints of effect stellar feedback on [C II] observables. The chapter is structured as follows: in section 5.2.1, I briefly describe the `SPICE` simulations employed in this work, in 5.2.2 and 5.2.3, I describe a novel model to predict [C II] luminosities from galaxies, in section 5.2.4, I describe details of synthetic observations modelled in this chapter, in section 5.3, I describe the relation between $L_{\rm CII}$ and SFR, surface brightness maps and profiles and origin of broad lines in `SPICE`. Finally, I summarize the results from this work in 5.4.

5.2 Methodology

Here I describe the cosmological radiation-hydrodynamical simulations employed in this work and introduce a post-processing model to estimate [C II] emission from simulated galaxies.

5.2.1 SPICE Simulations

I employ the `SPICE` suite of radiation-hydrodynamical (RHD) simulations to study the impact of different models of supernova feedback on [C II] properties of galaxies. We briefly introduce the simulations below, and refer the readers to Bhagwat et al. (2024a) for details. `SPICE` is a set of RHD simulations performed using `RAMSES-RT` (Rosdahl et al., 2013a; Rosdahl & Teyssier, 2015b), which is a coupled RHD extension of the adaptive mesh refinement (AMR) code `RAMSES` (Teyssier, 2002). `RAMSES-RT` solves the coupled gas hydrodynamics, self-gravity and radiative transfer of stellar radiation along with the N-body dynamics of dark matter and stars.

Initial conditions are generated using `MUSIC2-monofonIC` (Hahn et al., 2020; Michaux et al., 2020) at $z = 30$ with the 2PPT/2LPT approach in a cosmological box of length 10 cMpc/h. A ΛCDM cosmological model is adopted, with parameters $\Omega_\Lambda = 0.6901$, $\Omega_\mathrm{m} = 0.3099$, $\Omega_\mathrm{b} = 0.0489$, $H_0 = 67.74$ km/s/Mpc, $n_\mathrm{s} = 0.9682$, $\sigma_8 = 0.8159$ (Planck Collaboration et al., 2016b), where the symbols have their usual meaning. Primordial gas mass fractions are $X = 0.7545$ for Hydrogen (H) and $Y = 0.2455$ for Helium (He), along with a metallicity floor of $Z = 3.2 \times 10^{-4}\ \mathrm{Z}_\odot$. `SPICE` models the non-equilibrium metal line cooling at $T > 10^4$K using `CLOUDY` tables, while at $T \leq 10^4$K it adopts fine structure rates from Rosen & Bregman (1995). `SPICE` also follows the non-equilibrium ionisation states of H and He (HII , HeII , HeIII), which are advected as passive scalars and fully coupled to the local ionising radiation field (see Rosdahl et al., 2013a).

The local resolution of the AMR grid is increased if one of the two following criteria are met: (1) $M_\mathrm{dm} + \frac{\Omega_m}{\Omega b}\, M_\mathrm{b} > 8 \times m_\mathrm{dm}$ (quasi-Lagrangian refinement criteria), where M_dm and M_b are the total dark matter and baryonic (i.e. gas + stars) mass within the cell, and $m_\mathrm{dm} \approx 6 \times 10^5\ \mathrm{M}_\odot$ is the mean dark matter particle mass, or (2) the cell width is larger than $\frac{1}{8}$ of the local Jeans length. This allows for a maximum resolution of $\approx$ 32pc at $z = 5$ with a minimum resolution of $\approx$ 4.8kpc at the coarsest refinement levels.

`SPICE` employs the multi-freefall star formation model implemented by Kretschmer & Teyssier (2020), which includes a prescription to track sub-grid turbulence in each computational cell yielding a variable star formation efficiency (SFE) that depends on the physical state of gas in a cell as described by its virial parameter and turbulent mach number. Supernova (SN) feedback is included in the form of a mechanical feedback scheme introduced by Kimm & Cen (2014) (implemented as in Kimm et al. 2015). The model injects momentum in the surrounding cells based on the phase of the SN remnant that is resolved. Depending on whether the Strömgen radius is resolved or not, we additionally include a momentum correction to account for pre-processing of gas due to photo-ionisation (Geen et al., 2015). We assume a Chabrier (2003) initial mass function (IMF), which implies that a fraction $\eta_\mathrm{sn} = 0.31$ of the initial stellar mass is recycled back into the ISM, and 5% of this is ejected as metals heavier than He. The choice of IMF also results in a fixed SN rate of 0.016 SN $\mathrm{M}_\odot^{-1}$.

While keeping the global implementation of the SN feedback constant, we systematically vary the timing and energies of SN events, as briefly described below (see Table 2 in 3):

1. `bursty-sn`: All SN from a stellar particle are injected with a fixed energy of $E_\mathrm{SNII} = 2 \times 10^{51}$ ergs in a single event when the particle reaches an age of 10 Myr.

2. `smooth-sn`: SN from a stellar particle are injected with a fixed energy of $E_\mathrm{SNII} =$

2×10^{51} ergs, but the SN events occur with a delay time distribution, i.e. between 3 and 40 Myr after the birth of a particle.

3. `hyper-sn`: For each stellar particle a fraction $f_{\rm HN}$ of SN explodes as hypernovae, injecting an energy of 10^{52} ergs. Following Grimmett et al. (2020), we assume a metallicity dependent fraction $f_{\rm HN} = \max(0.5 \times \exp(-Z_*/0.001), 0.01)$, with Z_* stellar metallicity. The remainder of the SN events inject energies between $10^{50} - 2 \times 10^{51}$ ergs (Sukhbold et al., 2016). The SN time delay distribution remains such that explosions occur between 3 and 40 Myr.

`SPICE` also tracks the on-the-fly transport of radiation from stars in five photon frequency groups, i.e. infrared ($0.1 - 1$ eV), optical (OP; $1 - 13.6$ eV) and three bands of ionising ultraviolet radiation (UVI with $13.6 - 24.59$ eV, UVII with $4.59 - 54.42$ eV, UVIII with $54.42 - \infty$ eV). The luminosity of stellar particles is evaluated depending on their age, metallicity and mass using SED models of BPASSv2.2.1 (Eldridge et al., 2017; Stanway & Eldridge, 2018). Finally, `SPICE` includes radiative feedback via photo-ionisation, photo-heating and direct radiation pressure from UV photons and radiation pressure on dust from infrared and optical photons. The dust number density is modelled as a function of the local metallicity and HI number density, $n_{\rm d} \equiv (Z/Z_\odot) n_{\rm HI}$. Each cell is assigned dust absorption and scattering opacities (see Table 3 in 3), allowing for re-processing of photons into the infrared group and for interaction with gas via multi-scattered radiation pressure (Rosdahl & Teyssier, 2015b).

5.2.2 Modelling [C II] emission

As `SPICE` does not actively track the non-equilibrium chemistry and radiation coupling for the C II ionisation state, I post-process the snapshots to assign an emissivity to each computational cell and calculate the luminosity emanating from it. As a carbon atom can exist in multiple ionisation states depending on the strength of the radiation field[1] and physical conditions of a cell, for each cell I write the equilibrium equation for a three-level carbon atom (i.e. carbon can exist in singly, doubly and triply ionised states) as:

$$\begin{aligned} n_{\rm CI}\Gamma_{\rm CI} + n_{\rm CI} n_e \beta_{\rm CI} &= n_e n_{\rm CII} \alpha_{\rm CII} \\ n_{\rm CII}\Gamma_{\rm CII} + n_{\rm CII} n_e \beta_{\rm CII} &= n_e n_{\rm CIII} \alpha_{\rm CIII}, \end{aligned} \tag{5.1}$$

where $n_{\rm CI}$, $n_{\rm CII}$ and $n_{\rm CIII}$ are the number densities of the three ionisation states, $\Gamma_{\rm CI}$ and $\Gamma_{\rm CII}$ the are photo-ionisation rates of C I and C II, $\beta_{\rm CI}$ and $\beta_{\rm CII}$ are the collisional excitation rates of C I and C II (Tielens, 2005), $\alpha_{\rm CI}$ and $\alpha_{\rm CII}$ are the recombination rates (Badnell, 2006), and n_e is the electron number density. I additionally require that $n_{\rm CI} + n_{\rm CII} + n_{\rm CIII} = \mathcal{A}_{\rm C} n \equiv n_{\rm C}$, where $\mathcal{A}_{\rm C}$ is the abundance of carbon in a cell (Nomoto et al., 2006), n is the

[1]We note that C I and C II are ionised by photons with energies $h\nu > 11.2$eV and $h\nu > 24.4$eV, respectively.

number density of gas and $n_{\rm C}$ is the number density of carbon. Therefore, one can derive $n_{\rm CII}$ as:

$$n_{\rm CII} = \frac{n_{\rm C}}{\left(1 + \frac{\Gamma_{\rm CII} + n_{\rm C}\beta_{\rm CII}}{n_e \alpha_{\rm CIII}} + \frac{n_e \alpha_{\rm CII}}{\Gamma_{\rm CI} + n_e \beta_{\rm CI}}\right)}. \tag{5.2}$$

As `SPICE` performs an on-the-fly radiation transport, the photo-ionisation rates for C I and C II can be extracted directly from the simulations, without any further assumption. More specifically, as the OP frequency bin in `SPICE` tracks radiation in the range $(1-13.6)$eV, one can calculate the fraction of flux with $h\nu > 11.2$eV by interpolating the stellar SEDs based on the current age, mass and metallicity of all the stars in a given cell. I define a correction factor $f_{\rm CI} = N_{h\nu>11.2}/N_{\rm OP}$, where $N_{h\nu>11.2}$ and $N_{\rm OP}$ are the number of photons emitted for each star at $h\nu > 11.2$ eV and in the OP band, respectively. Within a given cell, the local photo-ionisation rate of C I can then be evaluated as $\Gamma_{\rm CI} = \sigma_{\rm CI}\overline{f}_{\rm CI}F_{\rm OP}$, where $\sigma_{\rm CI}$ is the flux-weighted ionisation cross-section of C I (Verner et al., 1996), $\overline{f}_{\rm CI}$ is the luminosity weighted correction factor defined previously, and $F_{\rm OP}$ is the flux from the optical frequency bin obtained in `SPICE`. Finally, the photo-ionisation rate of C II can be evaluated as $\Gamma_{\rm CII} = \sigma_{\rm CII}F_{\rm UVII+UVIII}$, where $\sigma_{\rm CII}$ is the flux-weighted ionisation cross-section of C II (Verner et al., 1996), and $F_{\rm UVII+UVIII}$ is the flux from the UV II and UV III frequency bins obtained in `SPICE`. In this case, no correction factor is needed as `SPICE` tracks already exactly radiation with $h\nu > 24.4$eV.

As [C II] emission is excited predominantly by collisions of C II atoms with electrons and HI atoms in the ISM (Goldsmith et al., 2012), the luminosity emitted by a computational cell with volume V is written as

$$L_{\rm CII} = \sum_{i}^{e^-,\rm HI} n_i n_{\rm CII}, \Lambda_i(T) V \tag{5.3}$$

where Λ_i is the cooling rate as a function of gas temperature for species i. Figure 5.1 shows the [C II] cooling rates as a function of temperature for collisions with H I and e^- (see Appendix B of Ferrara et al. 2019 for details). Finally, we ignore any optical depth effects as the [C II] emission remains optically thin for most galaxies and ISM phase structures (Osterbrock et al., 1992; Goldsmith et al., 2012).

5.2.3 CMB obscuration

The cosmic microwave background (CMB) sets the minimum temperature of the ISM (under the assumption of local equilibrium) to $T_{\rm CMB} = T^0_{\rm CMB}(1+z)$ where $T^0_{\rm CMB} = 2.73$K. Emission originating from the ISM is seen against the CMB background as shown by (da Cunha et al., 2013). The contrast between the CMB and the emitted radiation is written as

$$\Delta I_\nu = [B_\nu(T_s) - B_\nu(T_{\rm CMB})](1 - e^{-\tau_\nu}), \tag{5.4}$$

where T_s is the spin temperature and B_ν is the Planck function. As in most cases [C II] is optically thin in sub-millimeter wavelengths, $e^{-\tau_\nu} \approx 1 - \tau_\nu$. One can then define an

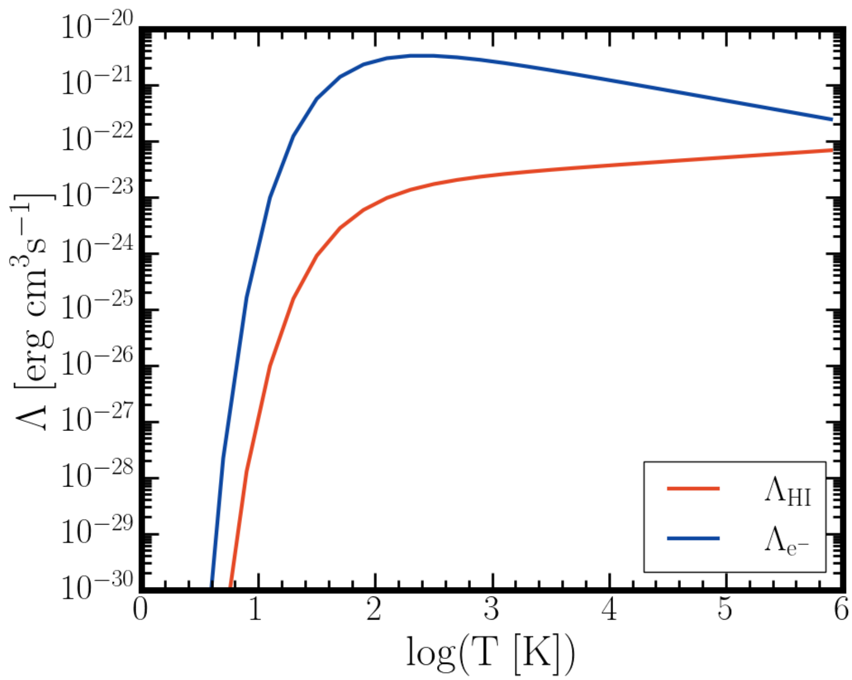

Figure 5.1: [C II] cooling rates as a function of gas temperature for excitations due to collisions with electrons (blue) and H I (red).

"obscuration" factor as the ratio of observed flux against the CMB to the intrinsic flux:

$$\zeta = \frac{F_{\rm obs}}{F_{\rm int}} = 1 - \frac{B_\nu(T_{\rm CMB})}{B_\nu(T_{\rm s})}. \tag{5.5}$$

As $T_{\rm CMB}$ approaches T_s, the observed flux tends to zero. Additionally, the spin temperature of [C II] is defined by the ratio of the population of the $^2P_{3/2}$ (labelled u) and $^2P_{1/2}$ (labelled l) levels of the 158 μm transition as (Goldsmith et al., 2012)

$$\frac{n_u}{n_l} = \frac{g_u}{g_l} e^{-T_*/T_s} = \frac{B_{lu} I_\nu + n_e C^e_{lu} + n_H C^H_{lu}}{B_{ul} I_\nu + A_{ul} + n_e C^e_{ul} + n_H C^H_{ul}}, \tag{5.6}$$

where $T_* = h\nu_{ul}/k_b = 91.92$K is the energy separation of the levels, and $g_u = 4, g_l = 2$ are the statistical weights of the levels, $A_{ul} = 2.36 \times 10^{-6} s^{-1}$ is the Einstein coefficient for spontaneous emission, B_{ul} (B_{ul}) gives the stimulated emission (absorption) coefficient, C^e_{lu} (C^H_{lu}) is the collisional excitation rate for collisions with $e^-(H)$, C^e_{ul} (C^H_{ul}) is the collisional de-excitation rate for collisions with $e^-(H)$ and finally, n_e and n_H are the e^- and H number densities (Dalgarno & McCray, 1972). The collisional excitation and de-excitation rates under local thermal equilibrium depends on the kinetic temperature and the rates can be written as

$$C^i_{lu} = \frac{g_u}{g_l} e^{(-T_*/T_s)} C^i_{ul}, \tag{5.7}$$

where i can be e^- and H. Combining equations 5.6 and 5.7 I obtain

$$\frac{T_*}{T_s} = ln\left(\frac{A_{ul}(1+\frac{c^2 I_\nu}{2h\nu^3}) + n_e C^e_{ul} + n_H C^H_{ul}}{A_{ul}(\frac{c^2 I_\nu}{2h\nu^3}) + n_e C^e_{ul} e^{-T_*/T} + n_H C^H_{ul} e^{-T_*/T}}\right). \tag{5.8}$$

Therefore, using equation 5.8 one can calculate the spin temperature for [C II] and using equation 5.5 for each cell, I estimate the CMB obscuration and correct the output luminosity as derived from equation 5.3 for each gas cell.

5.2.4 Synthetic observations and kinematic modelling

To fairly compare [C II] observables from `SPICE` galaxies to observations from ALMA and NOEMA, I construct 3D datacubes for each halo. Each constructed datacube has 2 spatial axes $\Delta x \approx 32$ pc and one velocity axis $\delta v = 30$km/s in the velocity range (-600,600) km/s. Each datacube is simulated for a region of side 25 kpc around the center of each halo using the positions ($\vec{x}$), velocity ($\vec{v}$) and $L_{\rm CII}$ calculated using equation 5.3 for each gas cell. Datacubes are constructed along 8 randomly drawn lines of sight per halo with the velocity dimension of a cube representing the line-of-sight velocity along the unit vector to the sightline drawn. The spectra and moment maps can then be derived using the [C II] datacube.

5.3 Results

In this section, I present the main results in terms of [C II] as a tracer of star-forming gas, surface brightness maps and broad lines as a tracer for stellar feedback.

5.3.1 $L_{\rm CII}$ vs SFR relation

In Figure 5.2, I show $L_{\rm CII}$ as a function of the SFR of a galaxy between $z = 10 - 5$ for the three feedback models. Overall, each model already establishes a "main-sequence" in the $L_{\rm CII} -$ SFR plane already at $z = 10$ which shows minimal evolution down to $z = 5$. I show a tight correlation between the SFR of a galaxy and $L_{\rm CII}$ for galaxies with smooth forms of feedback such that galaxies with the highest SFRs exhibit the highest $L_{\rm CII}$ values. The trends predicted by `SPICE` are in agreement with observations of [C II] emitting galaxies observed by ALMA and NOEMA at $z > 4$ as shown with gray points in each panel of figure 5.2. At SFR $\lesssim 10^{-2}$ M$_\odot$ yr^{-1}, the three feedback models are indistinguishable and show consistent median trends relative to each other. At SFR $\gtrsim 10^{-2}$ M$_\odot$ yr^{-1} however, `bursty-sn` consistently shows the lowest $L_{\rm CII}$ and the highest scatter out of the models by at all redshifts. The suppression in $L_{\rm CII}$ for `bursty-sn` is the most pronounced at $z = 7$ with a difference of ≈ 1.5 dex as compared to `smooth-sn`. `hyper-sn` closely follows `bursty-sn` with small differences in $L_{\rm CII}$ up to SFR $\approx 10^{-1}$ M$_\odot$ yr^{-1} at $z = 7$ and SFR $\gtrsim 1$ M$_\odot$ yr^{-1} at $z = 5$ above which it resembles `smooth-sn`.

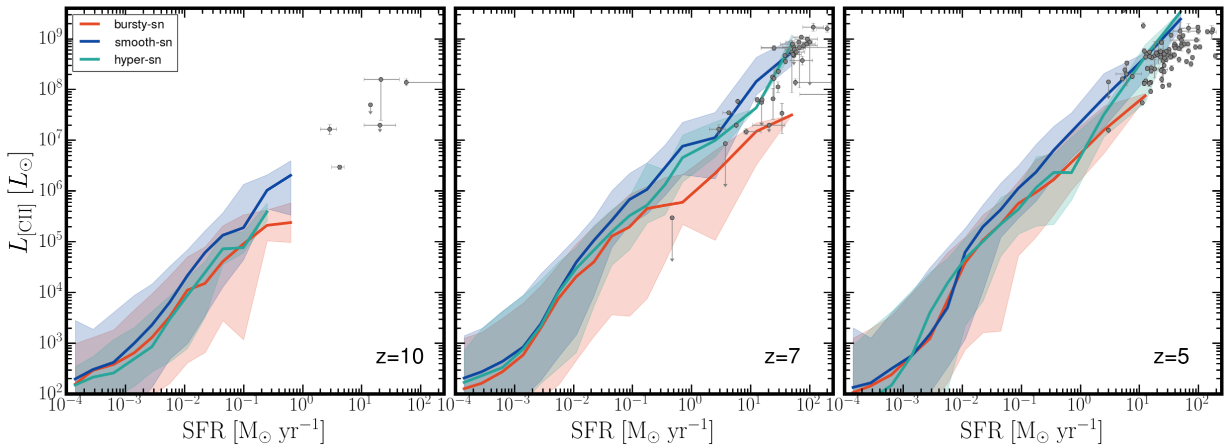

Figure 5.2: $L_{\rm CII}$ vs SFR relation for `SPICE` galaxies at $z = 10$ (left panel), $z = 7$ (middle panel) and $z = 5$ (right panel) for `bursty-sn` (red), `smooth-sn` (blue) and `hyper-sn` (turquoise).

The suppression of $L_{\rm CII}$ in `bursty-sn` is particularly interesting as it has been observed also in other works that employ different numerical schemes and simulation codes. Katz et al. 2022c find that "bursty leakers" exhibit lower $L_{\rm CII}$ as compared to "non-bursty leakers" in the `SPHINX20` simulations (Rosdahl et al., 2022a). Similarly, Casavecchia et al. 2024 also find a suppression in $L_{\rm CII}$ at similar SFR range as `bursty-sn` using the `ColdSIM` simulations (Maio et al., 2022). Therefore, understanding the origin of this luminosity deficit and its connection to burstiness is key. [C II] emission is theorised to originate mainly from photo-dissociation regions (PDRs) within the ISM. The abundance of PDR regions is shown to be sensitive to feedback which alters the porosity and ionisation state of the ISM (Cormier et al., 2019; Madden et al., 2020; Gurman et al., 2024). Resolving individual PDR regions in a simulations is however not feasible due to the extreme resolution demands. Therefore, in this work, I use H I regions as a proxy for PDRs.

Figure 5.3 shows the ratio of the H I surface density to the total gas surface density[2] as a function of $L_{\rm CII}$ between $z = 10 - 5$ for the three models. The ratio $\Sigma_{\rm HI}/\Sigma_{\rm gas}$ gives an idea of covering fraction of HI in a galaxy and gives information about the fraction of gas in a galaxy that is able to host PDRs and consequently emit [C II]. We see at at redshifts, `bursty-sn` exhibits the lowest $\Sigma_{\rm HI}/\Sigma_{\rm gas}$ at $L_{\rm CII} > 10^5 {\rm L}_\odot$, `smooth-sn` shows the highest values of $\Sigma_{\rm HI}/\Sigma_{\rm gas}$ while `hyper-sn` lies in between the other two models. At $z = 5$, `bursty-sn` shows a sudden drop in $\Sigma_{\rm HI}/\Sigma_{\rm gas}$ for galaxies with $L_{\rm CII} > 10^{6.5}{\rm L}_\odot$, implying a higher level of ionisation or a lower gas surface density. `bursty-sn` experiences a large upturn in star-formation (due to a starburst) at $z \sim 7$ (see Figure 3.3 in chapter 3) therefore, the reduced $\Sigma_{\rm HI}/\Sigma_{\rm gas}$ is likely a consequence of this starburst episode, consistent with previous findings (Asada et al., 2023a; Katz et al., 2022c; Casavecchia et al., 2024). The reduction in $\Sigma_{\rm HI}/\Sigma_{\rm gas}$ leads to a lower amount of available cold gas hosting PDRs which emit [C II] leading to the suppression in $L_{\rm CII}$ − SFR relation for `bursty-sn`.

[2]Surface density of the galaxy is defined as $\Sigma_i = \frac{M_i(<0.3R_{\rm vir})}{\pi(0.3R_{\rm vir})^2}$

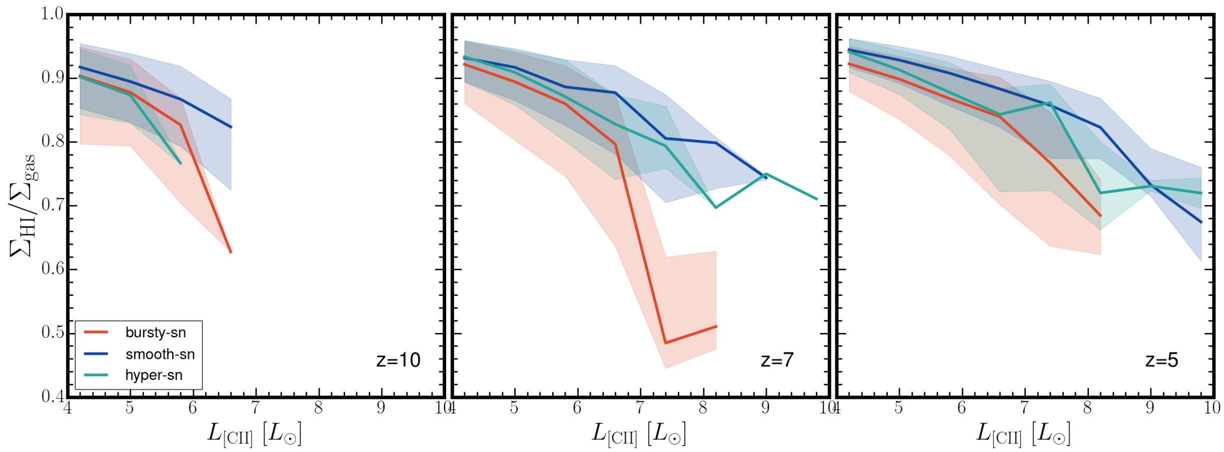

Figure 5.3: Ratio of the H I surface density to the total gas surface density as a as a function of the [C II] luminosity for `SPICE` galaxies at $z = 10$ (left panel), $z = 7$ (middle panel) and $z = 5$ (right panel) `bursty-sn` (red), `smooth-sn` (blue) and `hyper-sn` (turquoise).

Therefore, bursty feedback in `SPICE` regulates the cold gas content such that $L_{\rm CII}$ is suppressed for bursty star-forming galaxies. Observations from large ALMA surveys such as ALPINE have presented non-detections of [C II] in massive galaxies at $z > 5$ (Romano et al., 2022a; Romano et al., 2022b). Therefore, non-detections in [C II] for massive galaxies could potentially act as a tracer for feedback models such that their incidence will help constrain what fraction of galaxies with bursty star-formation histories.

5.3.2 Surface brightness maps and radial profiles

Interferometric observations often use surface brightness (SB) maps to constrain the origin of [C II] emission and comment on kinematics of the ISM (Fujimoto et al., 2019, 2022). In figure 5.4 I show the [C II] surface brightness and spectra for the four most massive halos in each feedback model. Both the SB maps and spectra show a large diversity of morphologies and shapes. [C II] emission is highly anisotropic and a diffuse component extends beyond the central regions of the galaxy likely due to enrichment of the CGM due to outflows (Ginolfi et al., 2020b). I note that `smooth-sn` and `hyper-sn` show highest luminosities at the very centers of the halos while `bursty-sn` shows a less drastic contrast as one goes outward into the halo. Additionally, `bursty-sn` is characterised by largely narrow line profiles (full-width half-maxima ($\rm FWHM_{broad}$) of $\approx 200-300$ km/s) with multiple sub-components highlighting complex kinematics of cold gas. `smooth-sn` and `hyper-sn` exhibit very broad lines ($\rm FWHM_{broad}$$> 600-700$ km/s) highlighting presence of fast cold gas motion. To understand if systematic differences in the feedback models persist statistically, I stack the SB maps and spectra for all galaxies with $M_* > 10^8$ $\rm M_\odot$ at $z = 5-6$[3]. Figure 5.5 shows the median stacked SB maps and spectra for the three

[3]The analysis is carried out at $z = 5-6$ to exploit the redshifts best suited for ALMA programs. An in-depth analysis for the full redshift range will follow in a future work.

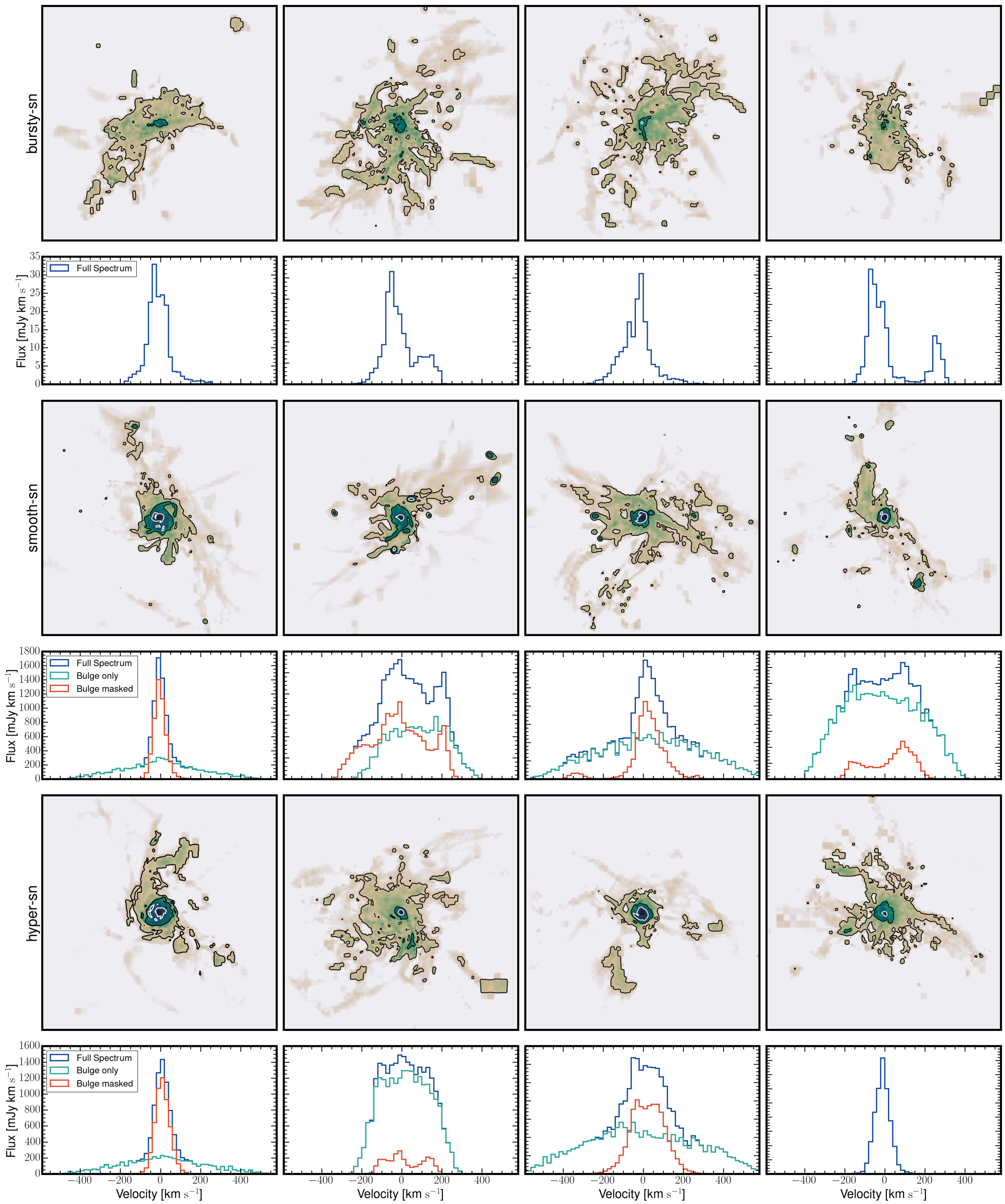

Figure 5.4: [C II] Surface brightness maps and spectra for the four most massive halos in the three feedback models. Top two rows: `bursty-sn`, middle two rows are `smooth-sn` and bottom two rows show `hyper-sn`. Surface brightness maps are calculated in the velocity range of [-800,800] km/s and the contours represent flux densities of $1, 100, 1000$ mJy km s^{-1}. Spectra shown for each model are calculated for the full galaxy (blue), just for the galactic bulge if present (turquoise) and the galaxy with the bulge region masked (red). Presence of galactic bulges correlates with presence of broad lines in [C II].

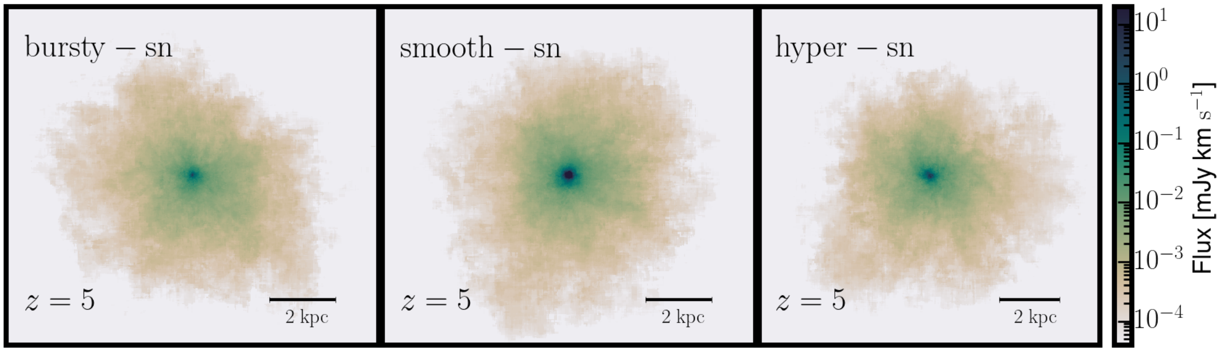

Figure 5.5: Median stacks of surface brightness maps of all galaxies with $M_* > 10^8$ M$_\odot$ at $z = 5 - 6$ for `bursty-sn` (left panel), `smooth-sn` (middle panel) and `hyper-sn` respectively.

feedback models. The extent of diffuse emission is similar across all the models, however, `smooth-sn` shows the highest concentration of flux at the center of the stacked image followed by `hyper-sn`. Meanwhile, `bursty-sn` does not exhibit a relatively flat SB map. This trend is quantified in figure 5.6, where I show the median radial SB profiles. As reflected by the stacked SB maps, `smooth-sn` shows a very sharp decline in the radial SB profile while `bursty-sn` remains relatively flat. Meanwhile, `hyper-sn` lies in between the other two models. The radial SB profiles for all the models converge at $\approx$ 3kpc scales highlighting the radial distance to which feedback impacts cold gas emission line tracers. A striking difference in the three feedback models can be seen in the median stacked spectral as shown in figure 5.7. `bursty-sn` exhibits a narrow [C II] line (FWHM$_{\rm broad}$$\approx$ 225 km/s) while `smooth-sn` and `hyper-sn` show very broad lines (FWHM$_{\rm broad}$$\approx$ 782 and 1090 km/s respectively). I discuss the origin of these broad lines in the following section. Therefore, owing to the strong relative differences, the slopes of the radial SB profiles and [C II] line kinematics can potentially provide constraints on stellar feedback at high-redshifts.

5.3.3 Origin of broad [C II] lines in SPICE

The presence of broad lines (FWHM$_{\rm broad}$ $\gtrsim$ 500km/s) in [C II] spectra are often used as a smoking gun for the presence of fast cooling outflows in high-redshift galaxies (Pizzati et al., 2020; Ginolfi et al., 2020a). In this section, I study if other factors such as feedback-regulated galactic dynamics can produce broad lines in [C II]. As previously shown, `smooth-sn` and `hyper-sn` are characterised by broad [C II] lines for galaxies with $M_* > 10^8$ M$_\odot$ whereas `bursty-sn` does not exhibit broad with FWHM$_{\rm broad}$$\gtrsim$ 500 km/s. A key difference I introduced in chapter 3 (section 3.3.5) in the galaxy populations produced by the various feedback models is that `smooth-sn` and `hyper-sn` preferentially produce disc galaxies with well formed bulges at the centers. Therefore, if these bulges are composed of fast rotating gas which can emit in [C II], one can produce broad line kinematics by invoking the presence of gas bulges at the centers of galaxies. Furthermore, rotating bulges have already been been detected at $z > 4$, albeit predominantly in QSO hosts using cold gas tracers such as CO (Prada et al., 1996; Kimball et al., 2015; Tripodi et al., 2023;

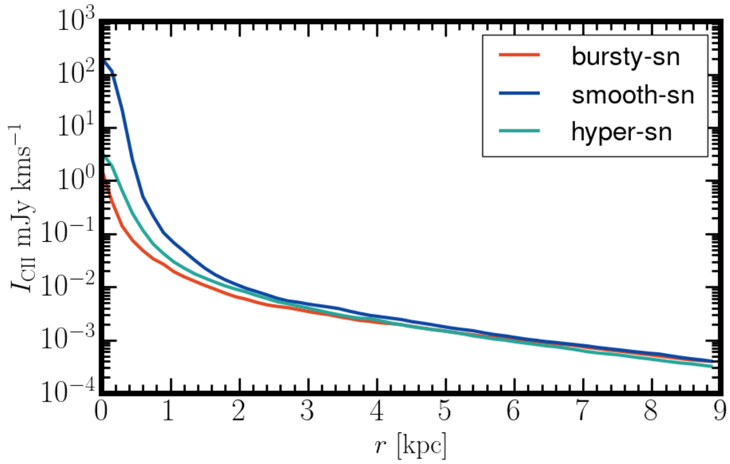

Figure 5.6: Median stacked radial surface brightness profiles of [C II] for `SPICE` galaxies at $z = 5 - 6$ for `bursty-sn` (red), `smooth-sn` (blue) and `hyper-sn` (turquoise) respectively.

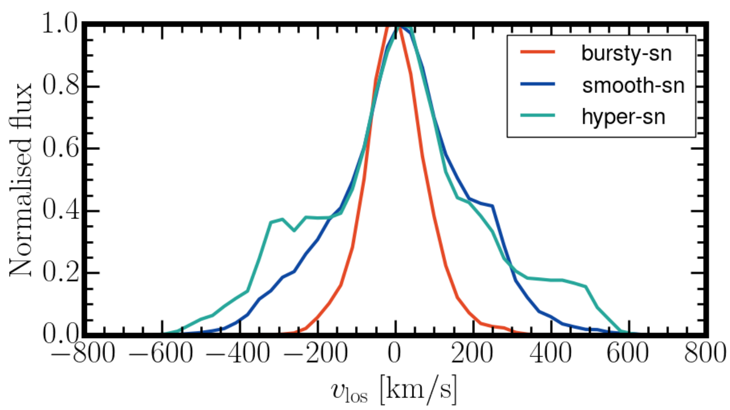

Figure 5.7: Median stacked of [C II] spectra of all galaxies with $M_* > 10^8$ M$_\odot$ at $z = 5 - 6$ for `bursty-sn` (left panel), `smooth-sn` (middle panel) and `hyper-sn` respectively. We see `bursty-sn` exhibits narrow line profiles while `smooth-sn` and `hyper-sn` exhibit broad line profiles.

D'Eugenio et al., 2023).

Therefore, I separate the population of galaxies into "bulge-heavy" and "bulge-less" galaxies. A galaxy is defined to be a bulge-heavy galaxy if the mass within 10% $R_{\rm vir}$ is greater than 25% of the total gas mass (e.g. Vudragović et al., 2022) of the galaxy ($M_{0.1\rm R_{vir}} > 0.25 M_{\rm tot}$). While this is a crude measure, I have tested different fractions and found the qualitative results remain unaffected. After diving the galaxy populations while being agnostic to the feedback model in question, I calculate their stacked SB maps and spectra. Figure 5.8 shows the stacked SB maps and spectra for bulge-heavy galaxies (left column) and bulge-less galaxies (right column). One can clearly see the absence of centrally bright [C II] regions and broad line features (FWHM$_{\rm broad} \approx 284$ km/s) in the bulge-less galaxy sample while the bulge-heavy galaxy sample shows centrally dominated SB maps

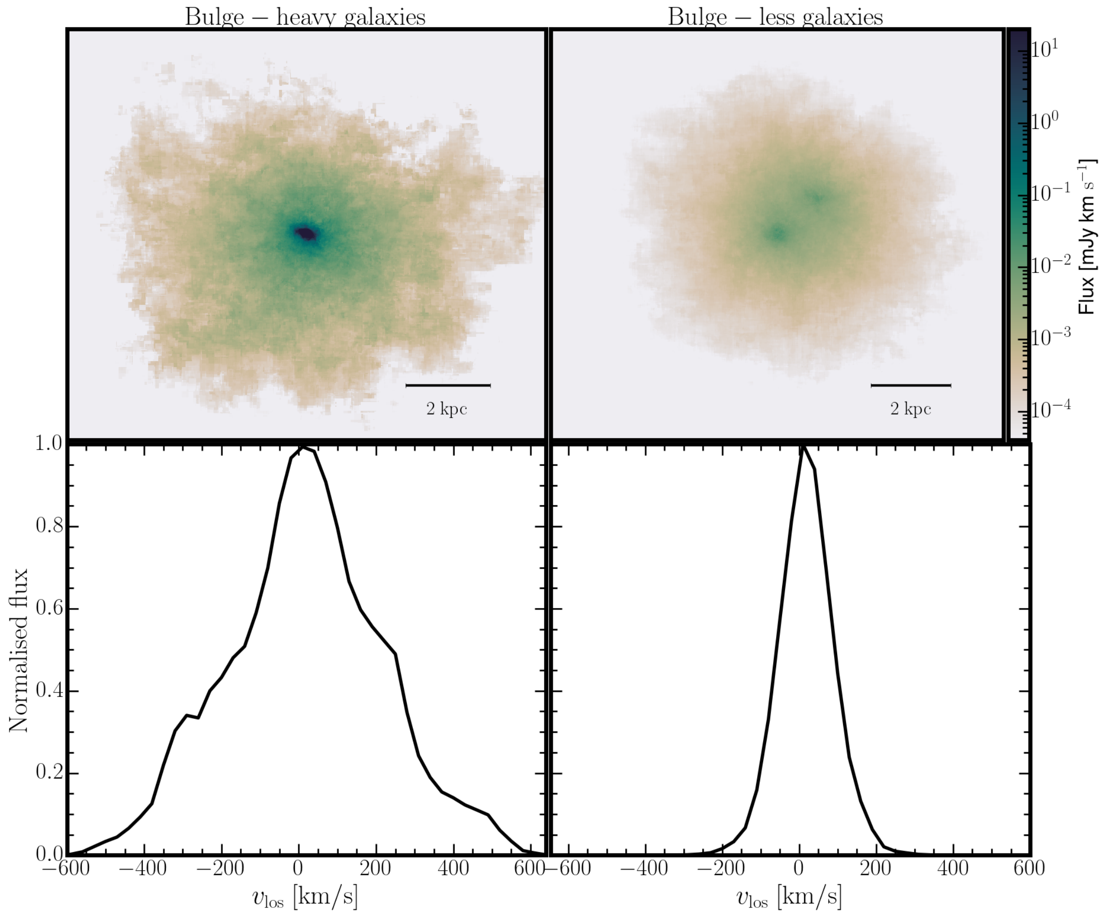

Figure 5.8: Left column: Median stacked surface brightness map (top) and median stacked spectra for bulge-heavy galaxies. **Right column**: Median stacked surface brightness map (top) and median stacked spectra for bulge-less galaxies. Bulge heavy galaxies exhibit centrally heavy SB maps and broad [C II] line kinematics while bulge-less galaxies show flat SB map with a narrow [C II] line.

and broad lines ($\mathrm{FWHM}_{\mathrm{broad}} \approx 966$ km/s). Additionally, in figure 5.4 I decompose the spectra of various galaxies into components as extracted from the full galaxy (blue), bulge component (turquoise) and galaxy with the bulge masked (red). One can clearly see the broad component in the spectra originates from the bulge while the galaxy itself largely produces spectra resembling narrow line as seen in `bursty-sn`. Therefore, the presence of galactic bulges at $z > 5$ can produce broad lines in [C II] and the incidence of these broad lines with bulge-like kinematics could provide constraints on stellar feedback models at high-redshifts.

5.4 Conclusions

In this chapter, I introduce a sub-grid model to post-process SPICE simulations with the goal or predicting [C II] emission line properties of high-redshift galaxies. I forward model 3D datacubes of SPICE galaxies to study the L_{CII}-SFR relation, surface brightness maps and profiles and finally the origin of broad [C II] lines in SPICE. I summarize my main conclusions below

- SPICE galaxies form a L_{CII}-SFR main sequence already at $z = 10$ which shows minimal evolution with redshift. I show a strong correlation between L_{CII} and SFR in smooth-sn and hyper-sn indicating [C II] is a good tracer for star-formation galaxies with smoother forms of feedback. Meanwhile, bursty-sn shows a relative suppression of L_{CII} at $L_{\mathrm{CII}} > 10^{6.5}$ $\mathrm{M}_{\odot}$ at $z = 7, 5$ indicating bursty feedback can suppress L_{CII}. Therefore, one can potentially use non-detections/deficits of [C II] in high-redshift galaxies as a tracer for bursty feedback

- Investigating the ratio of H I surface density to the total gas surface density ($\Sigma_{\mathrm{HI}}/\Sigma_{\mathrm{gas}}$) as a proxy for the covering fraction of H I reveals that galaxies with bursty feedback show strong suppression in $\Sigma_{\mathrm{HI}}/\Sigma_{\mathrm{gas}}$ (consequently H I covering fractions) as compared to galaxies with smoother forms of feedback. Since H I regions correlate to the sites of production of [C II], decrease in the covering fraction due to feedback in responsible for suppression of L_{CII}

- Surface brightness maps, radial profiles and spectra reveal a rich diversity in morphologies of [C II] extended emission and gas kinematics. smooth-sn exhibits centrally heavy SB maps while bursty-sn shows a relatively flat SB profile. hyper-sn predominantly lies in between the other models in terms of SB maps and radial profiles.

- The [C II] line spectra reveal the most striking differences between models with bursty-sn preferentially exhibiting narrow lines ($\mathrm{FWHM}_{\mathrm{broad}} \approx 200 - 300$ km/s) while smooth-sn and hyper-sn preferentially show broad lines ($\mathrm{FWHM}_{\mathrm{broad}} \gtrsim 500$ km/s). Therefore, kinematics of the [C II] could act as a strong tracer for bursty vs smooth feedback

- To understand the origin of broad lines in SPICE, I classify galaxies based on their morphologies. I divide the galaxy sample into "bulge-heavy" and "bulge-less" using mass enclosed within 10% R_{vir} as a metric. bulge-heavy galaxies preferentially show broad [C II] lines ($\mathrm{FWHM}_{\mathrm{broad}} \gg 500$ km/s) and centrally dominated SB maps while bulge-less galaxies prefer narrow [C II] lines ($\mathrm{FWHM}_{\mathrm{broad}} \approx 200 - 300$ km/s) and diffuse SB maps. As stellar feedback dictates the morphological mix of galaxies that emerges by $z = 5$, observations of broad [C II] lines that reveal bulge-like kinematics can therefore act as a tracer of different modes of feedback at high redshifts

Chapter 6

Summary and outlook

> "Our feedback models successfully reproduce galaxy properties, but we don't quite understand why these feedback models work"
>
> Dr. Rüdiger Pakmor

In this thesis, I presented a novel suite of cosmological radiation-hydrodynamical simulations called `SPICE` performed to systematically address the effect of stellar feedback on galaxy formation and cosmic reionisation. The emphasis was on studying variations in supernova feedback prescriptions with a goal of quantifying the effect of parameter choices and make observationally-testable connections between galaxy properties and reionisation scenarios. In addition to performing the simulations, I present a detailed analysis of global galaxy properties, reionisation histories, stellar and gas morphologies and show the connection between galaxy morphologies and LyC escape fractions (consequently quantifying galaxies that drive reionisation) in chapter 3. In chapter 4, I perform Monte Carlo radiation transport of Lyα and UV photons to probe the effect of physical mechanisms and observing systematics on the observaibility of Lyα emission from reionisation-era galaxies. And finally, in chapter 5, I introduce a sub-grid model to predict the [C II] 158μm emission line from RHD simulations such as `SPICE` and model emission properties and kinematics of [C II] for `SPICE` galaxies.

The post-processing carried out in the three projects uniquely quantifies the effect of variation of stellar feedback prescriptions on different observational tracers within of galaxy (e.g cold gas via [C II], photo-ionised gas via Lyα, stellar and Hα morphologies and LyC escape and UV continuum properties). These tracers combined in a multi-wavelength study ultimately will help answer the questions raised in chapter 1 such as: *Can we explain high-redshift galaxy properties and their evolution by invoking different modes of feedback? How do variations in stellar feedback models influence our interpretations of the high-redshift universe? how and to what extent choice of stellar feedback models impact the physical insights gained from simulations?*

Below, I summarise the main findings of this thesis.

6.1 Summary of the key results

1. Connecting stellar feedback in the first galaxies and cosmic reionisation

The first step in this thesis was to perform a suite of simulations that systematically probe the effect of stellar feedback variations in a volume such that one is able to simultaneously resolve the multi-phase ISM (i.e. sites of stellar feedback) and the effect of feedback on cosmological scales. For this purpose, I perform a suite of 3 radiation-hydrodynamical simulations called `SPICE` in a 14.78 cMpc cosmological box with a physical resolution of $\Delta x \approx 28$pc at $z = 5$. Each of these simulation volumes include sub-grid prescriptions for cooling, star-formation, stellar feedback, non-equilibrium thermochemistry and on-the-fly radiation transport in 5 frequency bins. While maintaining the same initial conditions and input physics prescriptions I step-by-step vary the timing of supernova explosions, the energies of supernova explosions and motivated poorly explored physical scenarios such as hypernovae (see tables 3.1,3.2 for details). The three models are labelled as `bursty-sn`, `smooth-sn` and `hyper-sn` to reflect the stellar feedback parameteres chosen in terms of supernova timing and energies (see 3.2).

The variations in feedback prescriptions strongly affect the burstiness and amplitude of star-formation rate density. The variations in feedback produce three distinct kinds of star-formation histories: bursty (as in `bursty-sn`), smooth (as in `smooth-sn`) and decreasing burstiness with decreasing redshift (as in `hyper-sn`). Burstiness of star-formation inversely correlates with its amplitude, i.e. if a model is highly bursty (e.g. `bursty-sn` at all z or `hyper-sn` at $z > 9$) it exhibits the lowest star-formation rates and vice-versa (`smooth-sn` at all z or `hyper-sn` at $z < 9$). Despite differences in star-formation rate evolution, the global galaxy properties such as the median star-formation main sequence and dust-attenuated luminosity functions remain degenerate between the different feedback models, therefore, cannot be used to constrain feedback models.

On the largest scales, subtle variations in the behaviour of supernova feedback strongly affect the reionisation histories. Burstier forms of feedback are able to complete reionisation by $z = 5.1$ (as in `bursty-sn`), consistent with observational constraints while smoother forms of feedback produce late reionisation scenarios (as in `smooth-sn` and `hyper-sn`). Therefore confirming that reionisation is sensitive to modulation of $f_{\rm esc}$ by feedback rather than bring driven by the number of of available ionising photons.

Stellar feedback and its strength determine the morphological make up of the galaxies that emerge by $z = 5$. Star-forming disc galaxies are prevalent if supernova feedback is 'smooth' (as in `smooth-sn` and `hyper-sn`) whereas 'bursty' feedback preferentially produces dispersion-dominated systems (as in `bursty-sn`). Additionally, cosmic reionisation is inextricably connected to intrinsic galaxy properties such as morphologies and kinematics. The varied strengths of outflows produced by different feedback models alter the CGM/ISM such that LyC $f_{\rm esc}$ of galaxies are strongly affected. Dispersion-dominated galaxies exhibit 10-50× higher $f_{\rm esc}$ as compared to rotation-dominated ones at all redshifts. Consequently, at the same intrinsic luminosity, dispersion-dominated systems should generate larger ionised regions around them as compared to their rotation-dominated counterparts.

Overall, feedback determines the global morphological mix of galaxies that emerges and as a consequence, the LyC $f_{\rm esc}$ of a simulated volume. Therefore, the connection between morphologies of galaxies and LyC $f_{\rm esc}$ can act as an excellent observable probe of galaxies that drive reionisation and provide constraints for feedback models at high-redshifts.

2. Impact of physical mechanisms and observational systematics on Lyα visibility

In chapter 4, I investigate the effect of radiative transfer and observational systematics on measured equivalent widths ($\rm EW_0$) of Lyα emitters in the EoR. The radiative transfer calculations performed through H I, D and dust reveal three physical scenarios and an observational systematic which can lead of erroneous $\rm EW_0$ estimates. The physical scenarios include extended Lyα emission, Lyα-UV spatial offsets and extended UV continuum from galaxies. Lyα-UV spatial offsets exist *independantly of feedback model* and are commonly seen with median values of $\approx 0.07 - 0.11''$, consistent with observational data. I identify Lyα-UV spatial offsets as the primary cause of loss of flux for `JWST-MSA` type observations with median slit-losses of $\approx 60\%$ such that $\approx 30\%$ galaxies suffer from $> 95\%$ loss of flux. Extended emission due to resonant scattering of Lyα can also cause loss of flux if the size of the extended emission exceeds the size of the `JWST-MSA` pseudo-slit. `SPICE` predicts median-losses of $\approx 40\%$ due to extended emission. The final physical scenario arises when observed galaxies exhibit complex morphologies which cannot be completely captured by `JWST-MSA` pseudo-slits, therefore the UV continuum is under-estimated. Therefore, the measured Lyα $\rm EW_0$ are erroneously over-estimated in such cases. The observational systematic we study is astrometry errors in the placement of the `JWST-MSA` pseudo-slitlet. Misplaced slits lead to under-estimated UV continuum therefore producing erroneously over-estimated Lyα $\rm EW_0$. The predictions made by `SPICE` stay constant irrespective of the feedback model in question, therefore providing for a robust result. Additionally, comparing predictions from `SPICE` to observations of 25 Lyα emitters confirms that all the predicted scenarios are likely at play. This work additionally strengthens the case for the use of the `JWST-NIRSpec` in the IFU observation mode and fully exploit the capabilities of `JWST` to understand cosmic reionisation using Lyα emitters.

3. Imprints of stellar feedback on [C II] observables

In chapter 5, I model the [C II] emission properties of `SPICE` galaxies using a novel sub-grid model. I show that [C II] presents as an excellent tracer of star-formation in galaxies with smooth forms of feedback. Bursty feedback suppresses $L_{\rm CII}$ for the brightest objects by lowering the covering fraction of H I which host photo-dissociation regions which emit [C II]. Additionally, radial profiles of surface brightness reveal different slopes for the different feedback models such that smoother forms of feedback exhibit a steep decline of the radial

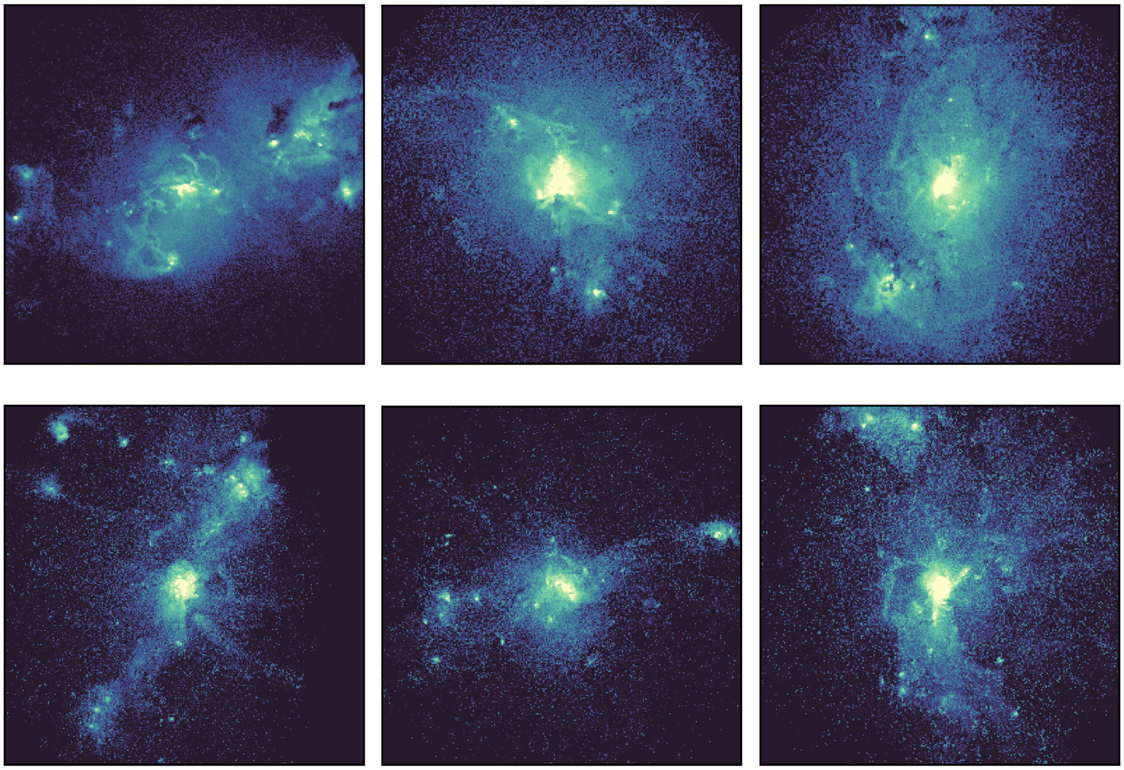

Figure 6.1: Top row: Lyα surface brightness maps for the three most massive halos in `bursty-sn` at $z = 5$. Bottom row:Lyα surface brightness maps for the three most massive halos in `smooth-sn` at $z = 5$. One can see a diversity of extended emission morphologies and extent of Lyα emission.

profile as compared to bursty galaxies. Finally, I probe the [C II] kinematics using the spectra extracted from synthetic 3D datacubes. `SPICE` predicts that galaxies with bursty feedback show disturbed morphologies in [C II] with narrow lines FWHM$\approx 200-250$ km/s whereas galaxies with smoother forms of feedback are able to form central bulges and therefore exhibit very broad wings with FWHM $\approx 600-800$ km/s. The broad component of the [C II] line in these galaxies originates from the fast rotating cold bulges at the centers of these galaxies as opposed to cooling outflows (Ginolfi et al., 2020a) or contribution from satellites (Devereaux et al., 2024) as suggested in literature. Overall, feedback models exhibit distinct differences in [C II] observables. Therefore, statistical samples of [C II] emitting galaxies from `ALMA` and `NOEMA` during the epoch of reionisation could provide strong constraints for stellar feedback models at high-redshifts.

6.2 Outlook

The `SPICE` suite along with the galaxy formation model developed for the simulations open up a wide range of possible extensions of this thesis.

A natural extension of the project presented in chapter 4 is to use the Lyα IFU datacubes to study the morpologies of the Lyα extended emission around galaxies. Understanding the impact of stellar feedback on the kinematics, luminosity-area relation, asymmetry of emission and radial emission profiles can provide valuable predictions for interpreting observations. Predicting these observables with `SPICE` would be very timely as `JWST` in the next year will observe Lyα emission from hundreds of Lyα emitting galaxies in the EoR using the IFU observing mode. In a similar manner, the sub-grid model I presented in chapter 5 to predict [C II] observables can be extended to various key emission lines such as [O III], Mg II, [N II] and C IV. Each of these emission lines trace different phases of gas in the galaxy. Additionally, influx of high-resolution data from various telescopes such as `JWST`, `MUSE` and `VLT` makes this study feasible. Therefore, I plan to model these lines toward a multi-wavelength study and systematically compare predicted observables with `SPICE` to data from these telescopes.

Numerically, while `SPICE` attempts to incrementally include a physically motivated ingredient (e.g SN delay time, hypernovae) in the three feedback models, a wide range of feedback physics is missing. `SPICE` does not include prescriptions for Pop III star-formation and feedback. Accurate modelling of feedback and metal enrichment from Pop III stars in idealised simulations with accurate modelling of primordial key could potentially be a key ingredient toward understanding high-redshift galaxies. Another feedback process that is included in `SPICE` is radiation pressure on dust, however, this process seems to be subdominant on galactic scales. However, treatment of dust in `SPICE` is approximate, better modelling of in dust could allow for radiation to couple to gas better and more accurately. Additionally, limited spatial resolution in `SPICE` ($\Delta x \approx 28$pc) could mean that dense optically thick clouds remain unresolved, therefore, underestimating the impact of radiation pressure in driving outflows and inducing starbursts (Costa et al., 2018a,b; Menon et al., 2023, 2024). Therefore, I plan to bridge scales between idealised simulations and `SPICE` with the goal of including feedback processes from Pop III stars and radiation pressure. Overall, this project will help improve our understanding of feedback at high-redshifts.

Furthermore, previous works have shown that mechanical feedback in cosmological simulations could potentially underestimate the fraction of hot gas produced (Hu, 2019). Therefore, it is imperative to improve schemes for feedback using predictions from `SPICE`. I showed in chapter 3, that to achieve cosmic reionisation by $z = 5.1$, galaxies need to produce consistently bursty feedback episodes. I also show that bursty feedback also effectively stops massive disc like galaxies from forming unlike in smoother forms of feedback. However, recent observations reveal that disc galaxies form already at $z > 6$ (Huertas-Company et al., 2023). Therefore, better schemes for feedback implementations will perhaps help simulations achieve both bursty and smooth feedback within the same simulation volume. I plan on exploring alternatives to strict momentum injection feedback models with `JWST` observations and predictions from `SPICE` in mind.

Finally, snapshots in `SPICE` are stored at a cadence of $8 - 10$ Myr between $z = 30 - 5$. Each snapshot contains information about the gravitational fields, hydrodynamic properties and radiation fields. By $z = 5$, due to the refinement strategy employed, the number of gas cells exceeds $\approx 10^9$ per snapshot per simulation box. Given the number of snapshots and cells per snapshot, `SPICE` provides a unique opportunity to apply machine learning algorithms on a very large training data set for different feedback models. One of the projects I plan to work with on is to train a convolutional neural network (CNN) to predict radiation fields and their feedback effects using the different feedback models as training sets. Each model produces a unique reionisation history driven by a different population of galaxies. Therefore, one could potentially train a neural network to on-the-fly predict radiation fields without the need for full radiation transport. Such modelling can be very useful to reduce cost and push volume sizes for large scale reionisation simulations.

Bibliography

Abel T., Anninos P., Zhang Y., Norman M. L., 1997, New Astron., 2, 181

Abel T., Norman M. L., Madau P., 1999, ApJ, 523, 66

Abel T., Bryan G. L., Norman M. L., 2002, Science, 295, 93

Adams N. J., et al., 2023, EPOCHS Paper II: The Ultraviolet Luminosity Function from $7.5 < z < 13.5$ using 110 square arcminutes of deep, blank-field data from the PEARLS Survey and Public Science Programmes (arXiv:2304.13721)

Agertz O., Kravtsov A. V., 2016, The Astrophysical Journal, 824, 79

Agertz O., Teyssier R., Moore B., 2011, Monthly Notices of the Royal Astronomical Society, 410, 1391

Agertz O., Kravtsov A. V., Leitner S. N., Gnedin N. Y., 2013, ApJ, 770, 25

Agertz O., et al., 2020, MNRAS, 491, 1656

Algera H. S. B., et al., 2023, MNRAS, 518, 6142

Alpher R. A., Herman R., 1948, Nature, 162, 774

Alpher R. A., Bethe H., Gamow G., 1948, Physical Review, 73, 803

Andersson E. P., Agertz O., Renaud F., 2020, MNRAS, 494, 3328

Angel P. W., Poole G. B., Ludlow A. D., Duffy A. R., Geil P. M., Mutch S. J., Mesinger A., Wyithe J. S. B., 2016, MNRAS, 459, 2106

Angulo R. E., Baugh C. M., Lacey C. G., 2008, MNRAS, 387, 921

Aravena M., et al., 2016, The Astrophysical Journal, 833, 71

Arrabal Haro P., et al., 2023, ApJ, 951, L22

Asada Y., Ohta K., 2022, ApJ, 924, 71

Asada Y., et al., 2023a, Bursty star formation and galaxy-galaxy interactions in low-mass galaxies 1 Gyr after the Big Bang (arXiv:2310.02314)

Asada Y., et al., 2023b, Monthly Notices of the Royal Astronomical Society: Letters, 523, L40

Atek H., et al., 2023, JWST UNCOVER: Discovery of $z > 9$ Galaxy Candidates Behind the Lensing Cluster Abell 2744 (arXiv:2305.01793)

Aubert D., Pichon C., Colombi S., 2004, Monthly Notices of the Royal Astronomical Society, 352, 376

Bacon R., et al., 2023, A&A, 670, A4

Badnell N. R., 2006, The Astrophysical Journal Supplement Series, 167, 334–342

Barnes J. E., 2001, in Hibbard J. E., Rupen M., van Gorkom J. H., eds, Astronomical Society of the Pacific Conference Series Vol. 240, Gas and Galaxy Evolution. p. 135 (arXiv:astro-ph/0010144), doi:10.48550/arXiv.astro-ph/0010144

Barnes J. E., Hernquist L., 1996, ApJ, 471, 115

Barrow K. S. S., Robertson B. E., Ellis R. S., Nakajima K., Saxena A., Stark D. P., Tang M., 2020, ApJ, 902, L39

Barrufet L., et al., 2023, Monthly Notices of the Royal Astronomical Society, 522, 449–456

Bauer A., Springel V., Vogelsberger M., Genel S., Torrey P., Sijacki D., Nelson D., Hernquist L., 2015, Monthly Notices of the Royal Astronomical Society, 453, 3594–3611

Becker G. D., Bolton J. S., 2013, MNRAS, 436, 1023

Becker G. D., Bolton J. S., Madau P., Pettini M., Ryan-Weber E. V., Venemans B. P., 2015, MNRAS, 447, 3402

Behroozi P., Wechsler R. H., Hearin A. P., Conroy C., 2019, Monthly Notices of the Royal Astronomical Society, 488, 3143

Bekki K., 1998, A&A, 334, 814

Belfiore F., et al., 2022, A&A, 659, A26

Bennett C. L., et al., 2003, The Astrophysical Journal, 583, 1–23

Bernardi M., Meert A., Sheth R. K., Vikram V., Huertas-Company M., Mei S., Shankar F., 2013, MNRAS, 436, 697

Bertschinger E., 1985, ApJS, 58, 39

Béthermin M., et al., 2020, A&A, 643, A2

Bezanson R., et al., 2022, arXiv e-prints, p. arXiv:2212.04026

Bhagwat A., Costa T., Ciardi B., Pakmor R., Garaldi E., 2024a, MNRAS,

Bhagwat A., Napolitano L., Pentericci L., Ciardi B., Costa T., 2024b, arXiv e-prints, p. arXiv:2408.16063

Bhagwat A., Costa T., Ciardi B., Pakmor R., Garaldi E., 2024c, MNRAS, 531, 3406

Biernacki P., Teyssier R., 2018, Monthly Notices of the Royal Astronomical Society, 475, 5688

Bigiel F., Leroy A., Walter F., Brinks E., De Blok W., Madore B., Thornley M. D., 2008, The Astronomical Journal, 136, 2846

Binney J., 1977, ApJ, 215, 483

Birnboim Y., Dekel A., 2003, MNRAS, 345, 349

Bischetti M., Maiolino R., Carniani S., Fiore F., Piconcelli E., Fluetsch A., 2019, A&A, 630, A59

Blaizot J., et al., 2023, MNRAS, 523, 3749

Blondin J. M., Wright E. B., Borkowski K. J., Reynolds S. P., 1998, The Astrophysical Journal, 500, 342

Blumenthal G. R., Pagels H., Primack J. R., 1982, Nature, 299, 37

Blumenthal G. R., Faber S. M., Primack J. R., Rees M. J., 1984, Nature, 311, 517

Bolton J. S., Becker G. D., Wyithe J. S. B., Haehnelt M. G., Sargent W. L. W., 2010, MNRAS, 406, 612

Boselli A., Gavazzi G., Lequeux J., Pierini D., 2002, Astronomy & Astrophysics, 385, 454–463

Bosman S. E. I., et al., 2022, MNRAS, 514, 55

Bournaud F., Elmegreen B. G., 2009, The Astrophysical Journal, 694, L158

Bouwens R. J., et al., 2015, The Astrophysical Journal, 803, 34

Bouwens R. J., et al., 2022a, ApJ, 931, 160

Bouwens R. J., Illingworth G., Ellis R. S., Oesch P., Stefanon M., 2022b, The Astrophysical Journal, 940, 55

Bouwens R., Illingworth G., Oesch P., Stefanon M., Naidu R., van Leeuwen I., Magee D., 2023a, Monthly Notices of the Royal Astronomical Society, 523, 1009

Bouwens R. J., et al., 2023b, Monthly Notices of the Royal Astronomical Society, 523, 1036

Bowman J. D., et al., 2013, Publ. Astron. Soc. Australia, 30, e031

Boylan-Kolchin M., 2023, Nature Astronomy, 7, 731

Bradač M., et al., 2017, The Astrophysical Journal Letters, 836, L2

Bromm V., Coppi P. S., Larson R. B., 1999, The Astrophysical Journal, 527, L5–L8

Bromm V., Ferrara A., Coppi P. S., Larson R. B., 2001, MNRAS, 328, 969

Brown G., Gnedin O. Y., 2022, Monthly Notices of the Royal Astronomical Society, 514, 280

Bunker A. J., et al., 2023, arXiv e-prints, p. arXiv:2306.02467

Byrohl C., et al., 2021, MNRAS, 506, 5129

Calzetti D., 2012, Star Formation Rate Indicators (`arXiv:1208.2997`)

Cantalupo S., Porciani C., Lilly S. J., 2008, ApJ, 672, 48

Carniani S., et al., 2017, Astronomy & Astrophysics, 605, A42

Carniani S., et al., 2023, JADES: The incidence rate and properties of galactic outflows in low-mass galaxies across 3 ¡ z ¡ 9 (`arXiv:2306.11801`)

Caruana J., Bunker A. J., Wilkins S. M., Stanway E. R., Lorenzoni S., Jarvis M. J., Ebert H., 2014, MNRAS, 443, 2831

Casavecchia B., Maio U., Péroux C., Ciardi B., 2024, Astronomy & Astrophysics, 689, A106

Castellano M., et al., 2017, ApJ, 839, 73

Chabrier G., 2003, Publications of the Astronomical Society of the Pacific, 115, 763

Chen Z., Stark D. P., Mason C., Topping M. W., Whitler L., Tang M., Endsley R., Charlot S., 2024, MNRAS, 528, 7052

Chevalier R. A., 1982, ApJ, 258, 790

Chevalier R. A., Clegg A. W., 1985, Nature, 317, 44

Chisholm J., Prochaska J. X., Schaerer D., Gazagnes S., Henry A., 2020, Monthly Notices of the Royal Astronomical Society, 498, 2554

Choudhury T. R., Paranjape A., Bosman S. E. I., 2021, MNRAS, 501, 5782

Choustikov N., et al., 2024, MNRAS, 532, 2463

Ciardi B., Ferrara A., 2005, Space Sci. Rev., 116, 625

Ciardi B., Ferrara A., Governato F., Jenkins A., 2000a, MNRAS, 314, 611

Ciardi B., Ferrara A., Abel T., 2000b, ApJ, 533, 594

Ciesla L., et al., 2023, Identification of a transition from stochastic to secular star formation around $z = 9$ with JWST (arXiv:2309.15720)

Colberg J. M., et al., 2000, MNRAS, 319, 209

Commerçon B., Debout V., Teyssier R., 2014, A&A, 563, A11

Cormier D., et al., 2019, Astronomy & Astrophysics, 626, A23

Costa T., Sijacki D., Trenti M., Haehnelt M. G., 2014, MNRAS, 439, 2146

Costa T., Rosdahl J., Sijacki D., Haehnelt M. G., 2018a, MNRAS, 473, 4197

Costa T., Rosdahl J., Sijacki D., Haehnelt M. G., 2018b, MNRAS, 479, 2079

Costa T., Rosdahl J., Kimm T., 2019, MNRAS, 489, 5181

Costa T., Arrigoni Battaia F., Farina E. P., Keating L. C., Rosdahl J., Kimm T., 2022, MNRAS, 517, 1767

Crawford M. K., Genzel R., Townes C. H., Watson D. M., 1985, ApJ, 291, 755

Croxall K. V., et al., 2017, The Astrophysical Journal, 845, 96

Curti M., et al., 2023, JADES: Insights on the low-mass end of the mass–metallicity–star-formation rate relation at $3 < z < 10$ from deep JWST/NIRSpec spectroscopy (arXiv:2304.08516), https://arxiv.org/abs/2304.08516

Cutler S. E., et al., 2024, Two Distinct Classes of Quiescent Galaxies at Cosmic Noon Revealed by JWST PRIMER and UNCOVER (arXiv:2312.15012), https://arxiv.org/abs/2312.15012

D'Aloisio A., McQuinn M., Maupin O., Davies F. B., Trac H., Fuller S., Upton Sanderbeck P. R., 2019, ApJ, 874, 154

D'Eugenio C., Daddi E., Liu D., Gobat R., 2023, A&A, 678, L9

D'Eugenio F., et al., 2024, arXiv e-prints, p. arXiv:2404.06531

Dalgarno A., McCray R. A., 1972, ARA&A, 10, 375

Dashyan G., Silk J., Mamon G. A., Dubois Y., Hartwig T., 2017, Monthly Notices of the Royal Astronomical Society, 473, 5698

Davis M., Efstathiou G., Frenk C. S., White S. D. M., 1985, ApJ, 292, 371

De Looze I., Baes M., Bendo G. J., Cortese L., Fritz J., 2011, MNRAS, 416, 2712

De Looze I., et al., 2014, A&A, 568, A62

Dekel A., Silk J., 1986, ApJ, 303, 39

Dekel A., Sari R., Ceverino D., 2009, The Astrophysical Journal, 703, 785

Deparis N., Aubert D., Ocvirk P., Chardin J., Lewis J., 2019, A&A, 622, A142

Devereaux T., et al., 2024, Astronomy & Astrophysics, 686, A156

Dewdney P. E., Hall P. J., Schilizzi R. T., Lazio T. J. L. W., 2009, Proceedings of the IEEE, 97, 1482

Díaz-Rodríguez M., Murphy J. W., Rubin D. A., Dolphin A. E., Williams B. F., Dalcanton J. J., 2018, The Astrophysical Journal, 861, 92

Díaz-Rodríguez M., Murphy J. W., Williams B. F., Dalcanton J. J., Dolphin A. E., 2021, Monthly Notices of the Royal Astronomical Society, 506, 781

Dicke R. H., Peebles P. J. E., Roll P. G., Wilkinson D. T., 1965, ApJ, 142, 414

Dickinson M., et al., 2024, The CANDELS-Area Prism Epoch of Reionization Survey (CAPERS), JWST Proposal. Cycle 3, ID. #6368

Diesing R., Caprioli D., 2018, Phys. Rev. Lett., 121, 091101

Dijkstra M., 2014, Publ. Astron. Soc. Australia, 31, e040

Dijkstra M., Loeb A., 2008, MNRAS, 391, 457

Donnan C. T., et al., 2022, Monthly Notices of the Royal Astronomical Society, 518, 6011

Draine B. T., 2011, Physics of the Interstellar and Intergalactic Medium

Dressler A., et al., 2023a, Building the First Galaxies – Chapter 2. Starbursts Dominate The Star Formation Histories of 6 ¡ z ¡12 Galaxies (arXiv:2306.02469)

Dressler A., et al., 2023b, The Astrophysical Journal Letters, 947, L27

Dubois Y., Teyssier R., 2008, A&A, 477, 79

Dubois Y., Peirani S., Pichon C., Devriendt J., Gavazzi R., Welker C., Volonteri M., 2016, Monthly Notices of the Royal Astronomical Society, 463, 3948

Dubois Y., et al., 2021, A&A, 651, A109

Duncan K., et al., 2014, Monthly Notices of the Royal Astronomical Society, 444, 2960–2984

Eddington A. S., 1933, The expanding universe

Efstathiou G., 1992, MNRAS, 256, 43P

Eide M. B., Ciardi B., Graziani L., Busch P., Feng Y., Di Matteo T., 2020, MNRAS, 498, 6083

Einasto J., Kaasik A., Saar E., 1974, Nature, 250, 309

Einstein A., 1916, Annalen der Physik, 354, 769

Einstein A., de Sitter W., 1932, Proceedings of the National Academy of Science, 18, 213

Eldridge J. J., Stanway E. R., Xiao L., McClelland L. A. S., Taylor G., Ng M., Greis S. M. L., Bray J. C., 2017, Publ. Astron. Soc. Australia, 34, e058

Endsley R., et al., 2023a, The Star-forming and Ionizing Properties of Dwarf z 6-9 Galaxies in JADES: Insights on Bursty Star Formation and Ionized Bubble Growth (arXiv:2306.05295)

Endsley R., Stark D. P., Whitler L., Topping M. W., Chen Z., Plat A., Chisholm J., Charlot S., 2023b, Monthly Notices of the Royal Astronomical Society, 524, 2312

Ewen H. I., Purcell E. M., 1951, Nature, 168, 356

Faber S. M., Gallagher J. S., 1979, ARA&A, 17, 135

Faisst A. L., et al., 2020, ApJS, 247, 61

Fall S. M., Efstathiou G., 1980, MNRAS, 193, 189

Fan X., et al., 2006, AJ, 132, 117

Farcy M., Rosdahl J., Dubois Y., Blaizot J., Martin-Alvarez S., 2022, MNRAS, 513, 5000

Faucher-Giguère C.-A., Quataert E., Hopkins P. F., 2013, Monthly Notices of the Royal Astronomical Society, 433, 1970

Federrath C., 2016, Journal of Physics: Conference Series, 719, 012002

Federrath C., Klessen R. S., 2012, The Astrophysical Journal, 761, 156

Ferland G., Korista K., Verner D., Ferguson J., Kingdon J., Verner E., 1998, Publications of the Astronomical Society of the Pacific, 110, 761

Ferrara A., Vallini L., Pallottini A., Gallerani S., Carniani S., Kohandel M., Decataldo D., Behrens C., 2019, MNRAS, 489, 1

Ferrara A., Pallottini A., Dayal P., 2023, Monthly Notices of the Royal Astronomical Society, 522, 3986

Field G. B., 1959, ApJ, 129, 536

Fielding D., Quataert E., Martizzi D., 2018, Monthly Notices of the Royal Astronomical Society, 481, 3325

Finkelman I., Brosch N., Funes J. G., Barway S., Kniazev A., Väisänen P., 2012, Monthly Notices of the Royal Astronomical Society, 422, 1384

Finkelstein S. L., et al., 2015, The Astrophysical Journal, 810, 71

Finlator K., Keating L., Oppenheimer B. D., Davé R., Zackrisson E., 2018, MNRAS, 480, 2628

Fiore F., Ferrara A., Bischetti M., Feruglio C., Travascio A., 2023, ApJ, 943, L27

Fontana A., et al., 2010, ApJ, 725, L205

Friedmann A., 1922, Zeitschrift fur Physik, 10, 377

Fujimoto S., et al., 2019, The Astrophysical Journal, 887, 107

Fujimoto S., et al., 2022, JWST and ALMA Multiple-Line Study in and around a Galaxy at $z = 8.496$: Optical to FIR Line Ratios and the Onset of an Outflow Promoting Ionizing Photon Escape (arXiv:2212.06863)

Fujimoto S., et al., 2023, The Astrophysical Journal Letters, 949, L25

Furlanetto S. R., 2006, MNRAS, 370, 1867

Furlanetto S. R., Mirocha J., 2022, Monthly Notices of the Royal Astronomical Society, 511, 3895

Gaikwad P., et al., 2023, arXiv e-prints, p. arXiv:2304.02038

Gallerani S., Pallottini A., Feruglio C., Ferrara A., Maiolino R., Vallini L., Riechers D. A., Pavesi R., 2018, MNRAS, 473, 1909

Gamow G., 1946, Phys. Rev., 70, 572

Garaldi E., Pakmor R., Springel V., 2021, MNRAS, 502, 5726

Garaldi E., Kannan R., Smith A., Springel V., Pakmor R., Vogelsberger M., Hernquist L., 2022, MNRAS, 512, 4909

Gardner J. P., et al., 2023, PASP, 135, 068001

Garel T., Blaizot J., Rosdahl J., Michel-Dansac L., Haehnelt M. G., Katz H., Kimm T., Verhamme A., 2021, MNRAS, 504, 1902

Gatto A., et al., 2016, Monthly Notices of the Royal Astronomical Society, 466, 1903

Geen S., Rosdahl J., Blaizot J., Devriendt J., Slyz A., 2015, Monthly Notices of the Royal Astronomical Society, 448, 3248

Geen S., Bieri R., Rosdahl J., de Koter A., 2020, Monthly Notices of the Royal Astronomical Society, 501, 1352

Ghara R., Choudhury T. R., Datta K. K., 2015, MNRAS, 447, 1806

Ginolfi M., et al., 2020a, A&A, 633, A90

Ginolfi M., et al., 2020b, A&A, 643, A7

Glover S. C. O., Brand P. W. J. L., 2001, Monthly Notices of the Royal Astronomical Society, 321, 385–397

Gnedin N. Y., 2000, The Astrophysical Journal, 542, 535

Gnedin O. Y., 2003, ApJ, 582, 141

Gnedin N. Y., 2014, The Astrophysical Journal, 793, 29

Gnedin N. Y., 2016, The Astrophysical Journal, 833, 66

Gnedin N. Y., Abel T., 2001, New Astronomy, 6, 437

Gnedin N. Y., Hui L., 1998, MNRAS, 296, 44

Gnedin N. Y., Madau P., 2022, Modeling Cosmic Reionization (`arXiv:2208.02260`)

Gnedin N. Y., Ostriker J. P., 1997, ApJ, 486, 581

Gnedin N. Y., Ferrara A., Zweibel E. G., 2000, The Astrophysical Journal, 539, 505

Goldsmith P. F., Langer W. D., Pineda J. L., Velusamy T., 2012, ApJS, 203, 13

Götberg Y., de Mink S. E., Groh J. H., Leitherer C., Norman C., 2019, A&A, 629, A134

Götberg Y., de Mink S. E., McQuinn M., Zapartas E., Groh J. H., Norman C., 2020, A&A, 634, A134

Götberg Y., et al., 2023, arXiv e-prints, p. arXiv:2307.00074

Gottumukkala R., et al., 2024, Monthly Notices of the Royal Astronomical Society, 530, 966–983

Grazian A., et al., 2015, Astronomy & Astrophysics, 575, A96

Greig B., Mesinger A., Haiman Z., Simcoe R. A., 2017, MNRAS, 466, 4239

Greig B., Mesinger A., Bañ ados E., 2019, Monthly Notices of the Royal Astronomical Society, 484, 5094

Grimmett J., Karakas A. I., Heger A., Müller B., West C., 2020, Monthly Notices of the Royal Astronomical Society, 496, 4987

Grisdale K., Agertz O., Renaud F., Romeo A. B., Devriendt J., Slyz A., 2019, Monthly Notices of the Royal Astronomical Society, 486, 5482

Grissom R. L., Ballantyne D. R., Wise J. H., 2014, A&A, 561, A90

Guillet T., Teyssier R., 2011, Journal of Computational Physics, 230, 4756

Gunn J. E., Gott J. Richard I., 1972, ApJ, 176, 1

Gurman A., Hu C.-Y., Sternberg A., van Dishoeck E. F., 2024, [CII] Emission in a Self-Regulated Interstellar Medium (arXiv:2308.07338), https://arxiv.org/abs/2308.07338

Guszejnov D., Grudić M. Y., Offner S. S. R., Faucher-Giguère C.-A., Hopkins P. F., Rosen A. L., 2022, Monthly Notices of the Royal Astronomical Society, 515, 4929

Guth A. H., 1981, Phys. Rev. D, 23, 347

Haardt F., Madau P., 1995, arXiv preprint astro-ph/9509093

Haardt F., Madau P., 2012, The Astrophysical Journal, 746, 125

Hahn O., Rampf C., Uhlemann C., 2020, Monthly Notices of the Royal Astronomical Society, 503, 426

Haid S., Walch S., Seifried D., Wünsch R., Dinnbier F., Naab T., 2018, Monthly Notices of the Royal Astronomical Society, 482, 4062

Haiman Z., Thoul A. A., Loeb A., 1996, ApJ, 464, 523

Hamilton D. R., 1940, Physical Review, 58, 122

Harikane Y., et al., 2018, ApJ, 859, 84

Harikane Y., et al., 2022, The Astrophysical Journal Supplement Series, 259, 20

Harikane Y., et al., 2023, The Astrophysical Journal Supplement Series, 265, 5

Haro P. A., et al., 2023a, Spectroscopic confirmation of CEERS NIRCam-selected galaxies at $\boldsymbol{z \simeq 8 - 10}$ (arXiv:2304.05378)

Haro P. A., et al., 2023b, Spectroscopic verification of very luminous galaxy candidates in the early universe (arXiv:2303.15431)

Hartley B., Ricotti M., 2016, Monthly Notices of the Royal Astronomical Society, 462, 1164

Hasegawa K., Semelin B., 2012, Monthly Notices of the Royal Astronomical Society, 428, 154

Hayward C. C., Hopkins P. F., 2016, Monthly Notices of the Royal Astronomical Society, 465, 1682

Heintz K. E., et al., 2023a, Dilution of chemical enrichment in galaxies 600 Myr after the Big Bang (arXiv:2212.02890)

Heintz K. E., et al., 2023b, Extreme damped Lyman-α absorption in young star-forming galaxies at $z = 9 - 11$ (arXiv:2306.00647)

Heintz K. E., et al., 2024, arXiv e-prints, p. arXiv:2404.02211

Helton J. M., et al., 2023, The JWST Advanced Deep Extragalactic Survey: Discovery of an Extreme Galaxy Overdensity at $z = 5.4$ with JWST/NIRCam in GOODS-S (arXiv:2302.10217)

Hennebelle P., Chabrier G., 2011, The Astrophysical Journal Letters, 743, L29

Henyey L. G., Greenstein J. L., 1941, ApJ, 93, 70

Herrera-Camus R., et al., 2015, ApJ, 800, 1

Herschel W., 1802, Philosophical Transactions of the Royal Society of London Series I, 92, 477

Heyer M. H., Brunt C. M., 2004, ApJ, 615, L45

Hoag A., et al., 2019a, MNRAS, 488, 706

Hoag A., et al., 2019b, The Astrophysical Journal, 878, 12

Hodge J. A., da Cunha E., 2020, Royal Society Open Science, 7, 200556

Holtzman J. A., 1989, ApJS, 71, 1

Hopkins P. F., et al., 2009, Monthly Notices of the Royal Astronomical Society, 397, 802

Hopkins P. F., Quataert E., Murray N., 2012, Monthly Notices of the Royal Astronomical Society, 421, 3522–3537

Hopkins P. F., Kereš D., Oñorbe J., Faucher-Giguère C.-A., Quataert E., Murray N., Bullock J. S., 2014, Monthly Notices of the Royal Astronomical Society, 445, 581

Hopkins P. F., et al., 2018, Monthly Notices of the Royal Astronomical Society, 477, 1578

Hoyle F., 1953, ApJ, 118, 513

Hu C.-Y., 2019, MNRAS, 483, 3363

Hubble E. P., 1926, ApJ, 64, 321

Hubble E., 1929a, Proceedings of the National Academy of Science, 15, 168

Hubble E., 1929b, Contributions from the Mount Wilson Observatory / Carnegie Institution of Washington, 376, 1

Huertas-Company M., et al., 2023, Galaxy Morphology from $z \sim 6$ through the eyes of JWST (arXiv:2305.02478)

Hui L., Gnedin N. Y., 1997, MNRAS, 292, 27

Hummer D. G., Storey P. J., 1987, MNRAS, 224, 801

Hutter A., Dayal P., Yepes G., Gottlöber S., Legrand L., Ucci G., 2021, MNRAS, 503, 3698

Iliev I. T., Mellema G., Pen U. L., Merz H., Shapiro P. R., Alvarez M. A., 2006, MNRAS, 369, 1625

Iliev I. T., Mellema G., Ahn K., Shapiro P. R., Mao Y., Pen U.-L., 2014, Monthly Notices of the Royal Astronomical Society, 439, 725

Ishigaki M., Kawamata R., Ouchi M., Oguri M., Shimasaku K., Ono Y., 2018, ApJ, 854, 73

Ito K., et al., 2024, Size - Stellar Mass Relation and Morphology of Quiescent Galaxies at $z \geq 3$ in Public *JWST* Fields (arXiv:2307.06994), https://arxiv.org/abs/2307.06994

Iyer K., et al., 2018, The Astrophysical Journal, 866, 120

Jacobs C., et al., 2023, ApJ, 948, L13

Jakobsen P., et al., 2022, A&A, 661, A80

Janka H.-T., 2012, Annual Review of Nuclear and Particle Science, 62, 407

Jeans J. H., 1902, Philosophical Transactions of the Royal Society of London Series A, 199, 1

Jenkins A., et al., 1998, ApJ, 499, 20

Jiang H., et al., 2023, arXiv e-prints, p. arXiv:2312.04151

Jin S., et al., 2023, A&A, 670, L11

Jones G. C., et al., 2024, A&A, 683, A238

Joung M. K. R., Mac Low M.-M., 2006, ApJ, 653, 1266

Jung I., et al., 2020a, ApJ, 904, 144

Jung I., et al., 2020b, ApJ, 904, 144

Jung I., et al., 2022, arXiv e-prints, p. arXiv:2212.09850

Jung I., et al., 2023a, CEERS: Diversity of Lyman-Alpha Emitters during the Epoch of Reionization (arXiv:2304.05385)

Jung I., et al., 2023b, arXiv e-prints, p. arXiv:2304.05385

Jung I., et al., 2023c, arXiv e-prints, p. arXiv:2304.05385

Kahn F. D., Woltjer L., 1959, ApJ, 130, 705

Kannan R., Macciò A. V., Fontanot F., Moster B. P., Karman W., Somerville R. S., 2015, Monthly Notices of the Royal Astronomical Society, 452, 4347

Kannan R., Vogelsberger M., Marinacci F., McKinnon R., Pakmor R., Springel V., 2019, MNRAS, 485, 117

Kannan R., Marinacci F., Vogelsberger M., Sales L. V., Torrey P., Springel V., Hernquist L., 2020, Monthly Notices of the Royal Astronomical Society, 499, 5732

Kannan R., Garaldi E., Smith A., Pakmor R., Springel V., Vogelsberger M., Hernquist L., 2021, Monthly Notices of the Royal Astronomical Society, 511, 4005

Kannan R., Garaldi E., Smith A., Pakmor R., Springel V., Vogelsberger M., Hernquist L., 2022, MNRAS, 511, 4005

Kant I., 1755, Allgemeine Naturgeschichte und Theorie des Himmels

Karlsson T., Bromm V., Bland-Hawthorn J., 2013, Reviews of Modern Physics, 85, 809–848

Kartaltepe J. S., et al., 2023, The Astrophysical Journal Letters, 946, L15

Kashikawa N., et al., 2015, ApJ, 798, 28

Kashino D., Lilly S. J., Matthee J., Eilers A.-C., Mackenzie R., Bordoloi R., Simcoe R. A., 2023, The Astrophysical Journal, 950, 66

Katz H. B., 2017, PhD thesis, Apollo - University of Cambridge Repository, doi:10.17863/CAM.14367, https://www.repository.cam.ac.uk/handle/1810/268166

Katz H., 2022, Monthly Notices of the Royal Astronomical Society, 512, 348

Katz N., White S. D. M., 1993, ApJ, 412, 455

Katz N., Hernquist L., Weinberg D. H., 1992, ApJ, 399, L109

Katz H., Kimm T., Haehnelt M. G., Sijacki D., Rosdahl J., Blaizot J., 2018, Monthly Notices of the Royal Astronomical Society, 483, 1029

Katz H., et al., 2021, Monthly Notices of the Royal Astronomical Society, 507, 1254

Katz H., et al., 2022a, MNRAS, 515, 4265

Katz H., et al., 2022b, Monthly Notices of the Royal Astronomical Society, 518, 270

Katz H., et al., 2022c, Monthly Notices of the Royal Astronomical Society, 518, 270–285

Keating L. C., Weinberger L. H., Kulkarni G., Haehnelt M. G., Chardin J., Aubert D., 2020, MNRAS, 491, 1736

Keller B. W., Kruijssen J. D., 2022, Monthly Notices of the Royal Astronomical Society, 512, 199

Keller B. W., Kruijssen J. D., Chevance M., 2022, Monthly Notices of the Royal Astronomical Society, 514, 5355

Kennicutt Robert C. J., 1989, ApJ, 344, 685

Kennicutt R. C., Evans N. J., 2012, Annual Review of Astronomy and Astrophysics, 50, 531

Khaire V., Srianand R., Choudhury T. R., Gaikwad P., 2016, MNRAS, 457, 4051

Khusanova Y., et al., 2020, A&A, 634, A97

Khusanova Y., et al., 2021, A&A, 649, A152

Kim C.-G., Ostriker E. C., 2015a, Proceedings of the International Astronomical Union, 11, 38

Kim C.-G., Ostriker E. C., 2015b, The Astrophysical Journal, 802, 99

Kim C.-G., Ostriker E. C., Raileanu R., 2017, ApJ, 834, 25

Kim J.-G., Kim W.-T., Ostriker E. C., 2018, ApJ, 859, 68

Kimball A. E., Lacy M., Lonsdale C. J., Macquart J. P., 2015, MNRAS, 452, 88

Kimm T., Cen R., 2014, The Astrophysical Journal, 788, 121

Kimm T., Cen R., Devriendt J., Dubois Y., Slyz A., 2015, Monthly Notices of the Royal Astronomical Society, 451, 2900

Kimm T., Katz H., Haehnelt M., Rosdahl J., Devriendt J., Slyz A., 2017, Monthly Notices of the Royal Astronomical Society, 466, 4826

Kimm T., Haehnelt M., Blaizot J., Katz H., Michel-Dansac L., Garel T., Rosdahl J., Teyssier R., 2018, MNRAS, 475, 4617

Kitayama T., Yoshida N., 2005, The Astrophysical Journal, 630, 675

Klessen R. S., Ballesteros-Paredes J., 2004, Gravoturbulent Fragmentation (arXiv:astro-ph/0402038)

Klypin A. A., Trujillo-Gomez S., Primack J., 2011, The Astrophysical Journal, 740, 102

Knudsen K. K., Richard J., Kneib J.-P., Jauzac M., Clément B., Drouart G., Egami E., Lindroos L., 2016, MNRAS, 462, L6

Kobayashi C., Umeda H., Nomoto K., Tominaga N., Ohkubo T., 2006, The Astrophysical Journal, 653, 1145

Kobayashi C., Springel V., White S. D., 2007, Monthly Notices of the Royal Astronomical Society, 376, 1465

Koudmani S., Henden N. A., Sijacki D., 2021, Monthly Notices of the Royal Astronomical Society, 503, 3568

Koudmani S., Sijacki D., Smith M. C., 2022, Monthly Notices of the Royal Astronomical Society, 516, 2112

Kretschmer M., Teyssier R., 2020, Monthly Notices of the Royal Astronomical Society, 492, 1385

Krumholz M. R., Federrath C., 2019, The Role of Magnetic Fields in Setting the Star Formation Rate and the Initial Mass Function (arXiv:1902.02557)

Krumholz M. R., McKee C. F., 2005, The astrophysical journal, 630, 250

Krumholz M. R., Tan J. C., 2007, The Astrophysical Journal, 654, 304

Kulkarni G., Keating L. C., Haehnelt M. G., Bosman S. E. I., Puchwein E., Chardin J., Aubert D., 2019a, MNRAS, 485, L24

Kulkarni G., Worseck G., Hennawi J. F., 2019b, MNRAS, 488, 1035

Lancaster L., Ostriker E. C., Kim J.-G., Kim C.-G., 2021, The Astrophysical Journal Letters, 922, L3

Langeroodi D., Hjorth J., 2023, Ultraviolet Compactness of High-Redshift Galaxies as a Tracer of Early-Stage Gas Infall, Stochastic Star Formation, and Offset from the Fundamental Metallicity Relation (arXiv:2307.06336)

Laporte N., et al., 2019, MNRAS, 487, L81

Larson R. B., 1981, MNRAS, 194, 809

Larson R. B., 1998, MNRAS, 301, 569

Larson R. L., et al., 2023, The Astrophysical Journal Letters, 953, L29

Latif M. A., Whalen D., Khochfar S., 2022, The Astrophysical Journal, 925, 28

Laursen P., 2023, Galaxy Formation from a Timescale Perspective. Springer International Publishing, p. 105–145, doi:10.1007/16618˙2023˙71, http://dx.doi.org/10.1007/16618_2023_71

Laursen P., Sommer-Larsen J., Milvang-Jensen B., Fynbo J. P. U., Razoumov A. O., 2019, A&A, 627, A84

Le Fèvre O., et al., 2020, A&A, 643, A1

Lee E. J., Miville-Deschênes M.-A., Murray N. W., 2016, The Astrophysical Journal, 833, 229

Leethochawalit N., et al., 2023, The Astrophysical Journal Letters, 942, L26

Leite N., Evoli C., D'Angelo M., Ciardi B., Sigl G., Ferrara A., 2017, Monthly Notices of the Royal Astronomical Society, 469, 416

Leitherer C., et al., 1999, The Astrophysical Journal Supplement Series, 123, 3

Lemaître G., 1927, Annales de la Société Scientifique de Bruxelles, 47, 49

Lemaître G., 1931a, MNRAS, 91, 483

Lemaître G., 1931b, MNRAS, 91, 490

Lemaître G., 1931c, Nature, 127, 706

Lemaitre G., 1949, Publications du Laboratoire d'Astronomie et de Geodesie de l'Universite de Louvain, 12, D1

Lemaux B. C., et al., 2021, MNRAS, 504, 3662

Leung G. C. K., et al., 2023, NGDEEP Epoch 1: The Faint-End of the Luminosity Function at $z \sim$ 9-12 from Ultra-Deep JWST Imaging (arXiv:2306.06244)

Levermore C. D., 1984, Journal of Quantitative Spectroscopy and Radiative Transfer, 31, 149

Lewis J. S. W., et al., 2022, Monthly Notices of the Royal Astronomical Society, 516, 3389

Li A., Draine B. T., 2001, ApJ, 554, 778

Li M., Bryan G. L., Ostriker J. P., 2017, The Astrophysical Journal, 841, 101

Lindley D., 1989, Nature, 342, 329

Long A. S., et al., 2023, Efficient NIRCam Selection of Quiescent Galaxies at 3 ¡ z ¡ 6 in CEERS (arXiv:2305.04662)

Looser T. J., et al., 2023, JADES: Differing assembly histories of galaxies – Observational evidence for bursty SFHs and (mini-)quenching in the first billion years of the Universe (arXiv:2306.02470)

Lu T.-Y., et al., 2020, ApJ, 893, 69

Luhman M. L., et al., 1998, ApJ, 504, L11

Lynden-Bell D., 1967, MNRAS, 136, 101

Ma X., Hopkins P. F., Kasen D., Quataert E., Faucher-Giguère C.-A., Kereš D., Murray N., Strom A., 2016, Monthly Notices of the Royal Astronomical Society, 459, 3614

Ma Q.-B., Fiaschi S., Ciardi B., Busch P., Eide M. B., 2022, MNRAS, 513, 1513

Machacek M. E., Bryan G. L., Abel T., 2001, ApJ, 548, 509

Mackey J., Bromm V., Hernquist L., 2003, The Astrophysical Journal, 586, 1–11

Mackey J., Gvaramadze V. V., Mohamed S., Langer N., 2015, A&A, 573, A10

Madau P., Dickinson M., 2014, ARA&A, 52, 415

Madau P., Haardt F., Rees M. J., 1999, ApJ, 514, 648

Madden S. C., Geis N., Genzel R., Herrmann F., Jackson J., Poglitsch A., Stacey G. J., Townes C. H., 1993, ApJ, 407, 579

Madden S. C., et al., 2020, Astronomy & Astrophysics, 643, A141

Maio U., Ciardi B., Dolag K., Tornatore L., Khochfar S., 2010, MNRAS, 407, 1003

Maio U., Khochfar S., Johnson J. L., Ciardi B., 2011, MNRAS, 414, 1145

Maio U., Péroux C., Ciardi B., 2022, Astronomy & Astrophysics, 657, A47

Maiolino R., et al., 2015, MNRAS, 452, 54

Maiolino R., et al., 2023, JADES. The diverse population of infant Black Holes at 4¡z¡11: merging, tiny, poor, but mighty (`arXiv:2308.01230`)

Maity B., Choudhury T. R., 2023, Monthly Notices of the Royal Astronomical Society, 521, 4140–4155

Malhotra S., et al., 1997, ApJ, 491, L27

Marasco A., et al., 2023, A&A, 670, A92

Marchi F., et al., 2017, A&A, 601, A73

Marinacci F., Vogelsberger M., 2015, Monthly Notices of the Royal Astronomical Society: Letters, 456, L69

Martin-Alvarez S., Slyz A., Devriendt J., Gó mez-Guijarro C., 2020, Monthly Notices of the Royal Astronomical Society, 495, 4475

Martin-Alvarez S., Sijacki D., Haehnelt M. G., Farcy M., Dubois Y., Belokurov V., Rosdahl J., Lopez-Rodriguez E., 2022, arXiv e-prints, p. arXiv:2211.09139

Martizzi D., 2019, Monthly Notices of the Royal Astronomical Society, 492, 79

Martizzi D., Fielding D., Faucher-Giguère C.-A., Quataert E., 2016, Monthly Notices of the Royal Astronomical Society, 459, 2311

Mason C. A., Treu T., Dijkstra M., Mesinger A., Trenti M., Pentericci L., de Barros S., Vanzella E., 2018, ApJ, 856, 2

Mason C. A., et al., 2019a, MNRAS, 485, 3947

Mason C. A., Naidu R. P., Tacchella S., Leja J., 2019b, MNRAS, 489, 2669

Mathews W. G., 1978, ApJ, 219, 413

Matthee J., Sobral D., Gronke M., Paulino-Afonso A., Stefanon M., Röttgering H., 2018, A&A, 619, A136

McDonald P., Miralda-Escude J., Rauch M., Sargent W. L. W., Barlow T. A., Cen R., 2001, The Astrophysical Journal, 562, 52–75

McDowell M. R. C., 1961, The Observatory, 81, 240

McGreer I. D., Mesinger A., Fan X., 2011, MNRAS, 415, 3237

McGreer I. D., Mesinger A., D'Odorico V., 2015, MNRAS, 447, 499

McKee C. F., Ostriker J. P., 1977, ApJ, 218, 148

McKee C. F., Stacy A., Li P. S., 2020, Monthly Notices of the Royal Astronomical Society, 496, 5528

McLeod D. J., et al., 2023, The galaxy UV luminosity function at $\mathbf{z \simeq 11}$ from a suite of public JWST ERS, ERO and Cycle-1 programs (arXiv:2304.14469)

Mellema G., Iliev I. T., Pen U.-L., Shapiro P. R., 2006, Monthly Notices of the Royal Astronomical Society, 372, 679–692

Menon S. H., Federrath C., Krumholz M. R., 2022, MNRAS, 517, 1313

Menon S. H., Federrath C., Krumholz M. R., 2023, Monthly Notices of the Royal Astronomical Society, 521, 5160

Menon S. H., Burkhart B., Somerville R. S., Thompson T. A., Sternberg A., 2024, Bursts of star formation and radiation-driven outflows produce efficient LyC leakage from dense compact star clusters (arXiv:2408.14591), https://arxiv.org/abs/2408.14591

Mesinger A., 2010, MNRAS, 407, 1328

Mesinger A., Furlanetto S., Cen R., 2010, Monthly Notices of the Royal Astronomical Society, 411, 955–972

Messier C., 1781, Catalogue des Nébuleuses et des Amas d'Étoiles (Catalog of Nebulae and Star Clusters), Connoissance des Temps ou des Mouvements Célestes, for 1784, p. 227-267

Mezcua M., Siudek M., Suh H., Valiante R., Spinoso D., Bonoli S., 2023, ApJ, 943, L5

Michaux M., Hahn O., Rampf C., Angulo R. E., 2020, Monthly Notices of the Royal Astronomical Society, 500, 663

Michel-Dansac L., Blaizot J., Garel T., Verhamme A., Kimm T., Trebitsch M., 2020, A&A, 635, A154

Mihalas D., Mihalas B. W., 1984, Foundations of radiation hydrodynamics

Milgrom M., 1983, ApJ, 270, 365

Miralda-Escudé J., Haehnelt M., Rees M. J., 2000, ApJ, 530, 1

Mirocha J., Furlanetto S. R., 2018, Monthly Notices of the Royal Astronomical Society, 483, 1980–1992

Mitsuhashi I., et al., 2023, The ALMA-CRISTAL survey: Widespread dust-obscured star formation in typical star-forming galaxies at z=4-6 (arXiv:2311.17671)

Molaro M., Davé R., Hassan S., Santos M. G., Finlator K., 2019, MNRAS, 489, 5594

Moore B., Katz N., Lake G., Dressler A., Oemler A., 1996, Nature, 379, 613

Morishita T., et al., 2023, ApJ, 947, L24

Mukhanov V. F., Chibisov G. V., 1981, ZhETF Pisma Redaktsiiu, 33, 549

Murray N., 2011, The Astrophysical Journal, 729, 133

Murray N., Quataert E., Thompson T. A., 2005, ApJ, 618, 569

Mutch S. J., Geil P. M., Poole G. B., Angel P. W., Duffy A. R., Mesinger A., Wyithe J. S. B., 2016, MNRAS, 462, 250

Naab T., Ostriker J. P., 2017, ARA&A, 55, 59

Naab T., Jesseit R., Burkert A., 2006, Monthly Notices of the Royal Astronomical Society, 372, 839

Nakajima K., Ouchi M., Isobe Y., Harikane Y., Zhang Y., Ono Y., Umeda H., Oguri M., 2023, JWST Census for the Mass-Metallicity Star-Formation Relations at z=4-10 with the Self-Consistent Flux Calibration and the Proper Metallicity Calibrators (arXiv:2301.12825), https://arxiv.org/abs/2301.12825

Nakane M., et al., 2024, ApJ, 967, 28

Nanayakkara T., et al., 2024, Scientific Reports, 14, 3724

Napolitano L., et al., 2023, A&A, 677, A138

Napolitano L., et al., 2024, arXiv e-prints, p. arXiv:2402.11220

Narayanan D., et al., 2024a, arXiv e-prints, p. arXiv:2408.13312

Narayanan D., et al., 2024b, ApJ, 961, 73

Navarre A., et al., 2024, ApJ, 962, 175

Navarro J. F., Frenk C. S., White S. D. M., 1996, ApJ, 462, 563

Neben A. R., et al., 2016, The Astrophysical Journal, 826, 199

Nickerson S., Teyssier R., Rosdahl J., 2018, Monthly Notices of the Royal Astronomical Society, 479, 3206

Ning Y., et al., 2024, ApJ, 963, L38

Nomoto K., Tominaga N., Umeda H., Kobayashi C., Maeda K., 2006, Nuclear Phys. A, 777, 424

Norman C. A., Ikeuchi S., 1989, ApJ, 345, 372

O'Shea B. W., Norman M. L., 2007, ApJ, 654, 66

O'Shea B. W., Bryan G., Bordner J., Norman M. L., Abel T., Harkness R., Kritsuk A., 2004, Introducing Enzo, an AMR Cosmology Application (arXiv:astro-ph/0403044), https://arxiv.org/abs/astro-ph/0403044

O'Shea B. W., Wise J. H., Xu H., Norman M. L., 2015, ApJ, 807, L12

Ocvirk P., et al., 2016, Monthly Notices of the Royal Astronomical Society, 463, 1462

Ocvirk P., et al., 2020, Monthly Notices of the Royal Astronomical Society, 496, 4087

Oh S. P., Haiman Z., 2002, ApJ, 569, 558

Oh S., et al., 2018, The Astrophysical Journal Supplement Series, 237, 14

Okamoto T., Eke V. R., Frenk C. S., Jenkins A., 2005, Monthly Notices of the Royal Astronomical Society, 363, 1299

Okamoto T., Gao L., Theuns T., 2008, Monthly Notices of the Royal Astronomical Society, 390, 920

Omukai K., Nishi R., 1999, The Astrophysical Journal, 518, 64–68

Omukai K., Tsuribe T., Schneider R., Ferrara A., 2005, ApJ, 626, 627

Ono Y., et al., 2012, ApJ, 744, 83

Orr M. E., Hayward C. C., Hopkins P. F., 2019, Monthly Notices of the Royal Astronomical Society, 486, 4724

Osterbrock D. E., Tran H. D., Veilleux S., 1992, ApJ, 389, 305

Ostriker J. P., McKee C. F., 1988, Rev. Mod. Phys., 60, 1

Ostriker E. C., Shetty R., 2011, The Astrophysical Journal, 731, 41

Ostriker E. C., McKee C. F., Leroy A. K., 2010, ApJ, 721, 975

Ota K., et al., 2014, ApJ, 792, 34

Ouchi M., et al., 2008, ApJS, 176, 301

Ouchi M., et al., 2013a, The Astrophysical Journal, 778, 102

Ouchi M., et al., 2013b, The Astrophysical Journal, 778, 102

Ouchi M., Ono Y., Shibuya T., 2020, ARA&A, 58, 617

Padoan P., Nordlund Å., 2011, The Astrophysical Journal, 730, 40

Pallottini A., Ferrara A., 2023, A&A, 677, L4

Papovich C., et al., 2023, ApJ, 949, L18

Parsons A. R., et al., 2010, AJ, 139, 1468

Partridge R. B., Peebles P. J. E., 1967, ApJ, 148, 377

Pawlik A. H., Milosavljević M., Bromm V., 2013, ApJ, 767, 59

Pawlik A. H., Rahmati A., Schaye J., Jeon M., Dalla Vecchia C., 2017, MNRAS, 466, 960

Peebles P. J. E., 1965, ApJ, 142, 1317

Peebles P. J. E., 1967, in Ehlers J., ed., , Vol. 8, Relativity Theory and Astrophysics. Vol.1: Relativity and Cosmology. p. 274

Peebles P. J. E., 1968a, in Origin and Distribution of the Elements. pp 31–37

Peebles P. J. E., 1968b, ApJ, 153, 1

Peebles P. J. E., 1982, ApJ, 263, L1

Pentericci L., et al., 2011, ApJ, 743, 132

Pentericci L., et al., 2016, ApJ, 829, L11

Pentericci L., et al., 2018, A&A, 616, A174

Penzias A. A., Wilson R. W., 1965, ApJ, 142, 419

Perret V., Teyssier R., Devriendt J., Rosdahl J., Slyz A., 2015, in IAU General Assembly. p. 2257403

Peters T., et al., 2017a, MNRAS, 466, 3293

Peters T., et al., 2017b, MNRAS, 466, 3293

Petkova M., Springel V., 2009, MNRAS, 396, 1383

Pillepich A., et al., 2017, Monthly Notices of the Royal Astronomical Society, 473, 4077

Pillepich A., et al., 2019, MNRAS, 490, 3196

Pineda J. L., Langer W. D., Velusamy T., Goldsmith P. F., 2013, A&A, 554, A103

Pizzati E., Ferrara A., Pallottini A., Gallerani S., Vallini L., Decataldo D., Fujimoto S., 2020, Monthly Notices of the Royal Astronomical Society, 495, 160–172

Pizzati E., Ferrara A., Pallottini A., Sommovigo L., Kohandel M., Carniani S., 2022, Monthly Notices of the Royal Astronomical Society, 519, 4608–4621

Planck Collaboration et al., 2016a, A&A, 594, A13

Planck Collaboration et al., 2016b, A&A, 594, A13

Podsiadlowski P., Mazzali P., Nomoto K., Lazzati D., Cappellaro E., 2004, The Astrophysical Journal, 607, L17

Poole G. B., Angel P. W., Mutch S. J., Power C., Duffy A. R., Geil P. M., Mesinger A., Wyithe S. B., 2016, MNRAS, 459, 3025

Porqueres N., Hahn O., Jasche J., Lavaux G., 2020, A&A, 642, A139

Posses A., et al., 2024, arXiv e-prints, p. arXiv:2403.03379

Prada F., Gutiérrez C. M., Peletier R. F., McKeith C. D., 1996, The Astrophysical Journal, 463, L9–L12

Press W. H., Schechter P., 1974, ApJ, 187, 425

Prieto-Lyon G., et al., 2023, Astronomy & Astrophysics, 672, A186

Primack J. R., Blumenthal G. R., 1984, in Audouze J., Tran Thanh Van J., eds, NATO Advanced Study Institute (ASI) Series C Vol. 117, Formation and Evolution of Galaxies and Large Structures in the Universe. p. 163

Puchwein E., Springel V., 2013, MNRAS, 428, 2966

Rampf C., Uhlemann C., Hahn O., 2020, Monthly Notices of the Royal Astronomical Society, 503, 406

Reddy N. A., Topping M. W., Sanders R. L., Shapley A. E., Brammer G., 2023, The Astrophysical Journal, 952, 167

Rees M. J., Ostriker J. P., 1977, MNRAS, 179, 541

Rey M. P., Katz H. B., Cameron A. J., Devriendt J., Slyz A., 2023, Boosting galactic outflows with enhanced resolution (arXiv:2302.08521)

Ribeiro B., et al., 2020, arXiv e-prints, p. arXiv:2007.01322

Richard J., et al., 2021, A&A, 646, A83

Richings A. J., Schaye J., Oppenheimer B. D., 2014a, MNRAS, 440, 3349

Richings A. J., Schaye J., Oppenheimer B. D., 2014b, MNRAS, 442, 2780

Riess A. G., et al., 1998, The Astronomical Journal, 116, 1009–1038

Rinaldi P., et al., 2023, The Astrophysical Journal, 952, 143

Rizzo F., Vegetti S., Powell D., Fraternali F., McKean J. P., Stacey H. R., White S. D. M., 2020, Nature, 584, 201

Roberts-Borsani G., et al., 2024, Between the Extremes: A JWST Spectroscopic Benchmark for High Redshift Galaxies Using 500 Confirmed Sources at $z \geqslant 5$ (arXiv:2403.07103), https://arxiv.org/abs/2403.07103

Robertson H. P., 1935, ApJ, 82, 284

Robertson B. E., 2022, Annual Review of Astronomy and Astrophysics, 60, 121–158

Robertson B., Bullock J. S., Cox T. J., Di Matteo T., Hernquist L., Springel V., Yoshida N., 2006, ApJ, 645, 986

Robertson B. E., Ellis R. S., Dunlop J. S., McLure R. J., Stark D. P., 2010, Nature, 468, 49

Robertson B. E., et al., 2013, The Astrophysical Journal, 768, 71

Robertson B. E., Ellis R. S., Furlanetto S. R., Dunlop J. S., 2015, ApJ, 802, L19

Robertson B. E., et al., 2023, Nature Astronomy, 7, 611

Romano M., et al., 2022b, Astronomy & Astrophysics, 660, A14

Romano M., et al., 2022a, A&A, 660, A14

Rosdahl J., Teyssier R., 2015a, MNRAS, 449, 4380

Rosdahl J., Teyssier R., 2015b, Monthly Notices of the Royal Astronomical Society, 449, 4380

Rosdahl J., Blaizot J., Aubert D., Stranex T., Teyssier R., 2013a, Monthly Notices of the Royal Astronomical Society, 436, 2188

Rosdahl J., Blaizot J., Aubert D., Stranex T., Teyssier R., 2013b, MNRAS, 436, 2188

Rosdahl J., Schaye J., Teyssier R., Agertz O., 2015, MNRAS, 451, 34

Rosdahl J., Schaye J., Dubois Y., Kimm T., Teyssier R., 2017, Monthly Notices of the Royal Astronomical Society, 466, 11

Rosdahl J., et al., 2018, MNRAS, 479, 994

Rosdahl J., et al., 2022a, MNRAS, 515, 2386

Rosdahl J., et al., 2022b, MNRAS, 515, 2386

Rosen A., Bregman J. N., 1995, The Astrophysical Journal, 440, 634

Rowan-Robinson M., et al., 2016, Monthly Notices of the Royal Astronomical Society, 461, 1100

Roškar R., Teyssier R., Agertz O., Wetzstein M., Moore B., 2014, Monthly Notices of the Royal Astronomical Society, 444, 2837–2853

Rubin V. C., Ford W. Kent J., 1970, ApJ, 159, 379

Russell R. W., Melnick G., Gull G. E., Harwit M., 1980, ApJ, 240, L99

Salpeter E. E., 1955, ApJ, 121, 161

Sanders R. L., Shapley A. E., Topping M. W., Reddy N. A., Brammer G. B., 2023, Excitation and Ionization Properties of Star-forming Galaxies at z=2.0-9.3 with JWST/NIRSpec (`arXiv:2301.06696`), `https://arxiv.org/abs/2301.06696`

Saxena A., et al., 2022, MNRAS, 517, 1098

Saxena A., et al., 2023a, JADES: The production and escape of ionizing photons from faint Lyman-alpha emitters in the epoch of reionization (`arXiv:2306.04536`)

Saxena A., et al., 2023b, A&A, 678, A68

Saxena A., et al., 2024, A&A, 684, A84

Sazonov S., Sunyaev R., 2015, Monthly Notices of the Royal Astronomical Society, 454, 3464

Scalo J., Elmegreen B. G., 2004, Annual Review of Astronomy and Astrophysics, 42, 275–316

Schaerer D., de Barros S., 2010, Astronomy and Astrophysics, 515, A73

Schaerer D., et al., 2022, A&A, 658, L11

Schaye J., Theuns T., Rauch M., Efstathiou G., Sargent W. L., 2000, Monthly Notices of the Royal Astronomical Society, 318, 817–826

Schenker M. A., Ellis R. S., Konidaris N. P., Stark D. P., 2014, ApJ, 795, 20

Schmidt M., 1959, ApJ, 129, 243

Schmidt W., 2014, Numerical Modelling of Astrophysical Turbulence. Springer

Schmidt W., Federrath C., 2011, Astronomy & Astrophysics, 528, A106

Schmidt W., Niemeyer J., Hillebrandt W., Röpke F., 2006, Astronomy & Astrophysics, 450, 283

Schmidt K. B., et al., 2021, A&A, 654, A80

Schneider R., Ferrara A., Natarajan P., Omukai K., 2002, The Astrophysical Journal, 571, 30–39

Schneider R., Valiante R., Trinca A., Graziani L., Volonteri M., 2023, arXiv e-prints, p. arXiv:2305.12504

Scholtz J., et al., 2023, GN-z11: The environment of an AGN at z =10.603 (arXiv:2306.09142)

Schroeder J., Mesinger A., Haiman Z., 2012, Monthly Notices of the Royal Astronomical Society, 428, 3058

Scott D., Rees M. J., 1990, MNRAS, 247, 510

Sedov L. I., 1959, Similarity and Dimensional Methods in Mechanics

Semenov D., Henning T., Helling C., Ilgner M., Sedlmayr E., 2003, A&A, 410, 611

Semenov V. A., Kravtsov A. V., Gnedin N. Y., 2018, The Astrophysical Journal, 861, 4

Shapiro P. R., Giroux M. L., 1987, ApJ, 321, L107

Sharma R. S., Brooks A. M., Tremmel M., Bellovary J., Quinn T. R., 2022, arXiv e-prints, p. arXiv:2211.05275

Sheth R. K., Tormen G., 2002, MNRAS, 329, 61

Silk J., 1977a, ApJ, 211, 638

Silk J., 1977b, ApJ, 214, 152

Silk J., 1977c, ApJ, 214, 718

Simmonds C., et al., 2023a, Low-mass bursty galaxies in JADES efficiently produce ionising photons and could represent the main drivers of reionisation (arXiv:2310.01112)

Simmonds C., et al., 2023b, Monthly Notices of the Royal Astronomical Society, 523, 5468

Smidt J., Whalen D. J., Wiggins B. K., Even W., Johnson J. L., Fryer C. L., 2014, The Astrophysical Journal, 797, 97

Smith B. D., Sigurdsson S., 2007, ApJ, 661, L5

Smith A., Safranek-Shrader C., Bromm V., Milosavljević M., 2015, MNRAS, 449, 4336

Smith M. C., Bryan G. L., Somerville R. S., Hu C.-Y., Teyssier R., Burkhart B., Hernquist L., 2021, MNRAS, 506, 3882

Smith A., Kannan R., Garaldi E., Vogelsberger M., Pakmor R., Springel V., Hernquist L., 2022, MNRAS, 512, 3243

Solimano M., et al., 2024, arXiv e-prints, p. arXiv:2401.04919

Solomon P. M., Rivolo A. R., Barrett J., Yahil A., 1987, ApJ, 319, 730

Somerville R. S., 2002, ApJ, 572, L23

Somerville R. S., Davé R., 2015, ARA&A, 53, 51

Somerville R. S., Hopkins P. F., Cox T. J., Robertson B. E., Hernquist L., 2008, MNRAS, 391, 481

Song M., et al., 2016, The Astrophysical Journal, 825, 5

Speagle J. S., Steinhardt C. L., Capak P. L., Silverman J. D., 2014, ApJS, 214, 15

Spilker A., Kainulainen J., Orkisz J., 2022, A&A, 667, A110

Spitzer L., 1978, Physical processes in the interstellar medium, doi:10.1002/9783527617722.

Springel V., 2010, MNRAS, 401, 791

Springel V., Hernquist L., 2003, MNRAS, 339, 289

Springel V., et al., 2005, Nature, 435, 629

Stacey G. J., Geis N., Genzel R., Lugten J. B., Poglitsch A., Sternberg A., Townes C. H., 1991, ApJ, 373, 423

Stanway E. R., Eldridge J. J., 2018, MNRAS, 479, 75

Stark D. P., Ellis R. S., Chiu K., Ouchi M., Bunker A., 2010, MNRAS, 408, 1628

Stark D. P., Ellis R. S., Ouchi M., 2011, ApJ, 728, L2

Stark D. P., Schenker M. A., Ellis R., Robertson B., McLure R., Dunlop J., 2013, ApJ, 763, 129

Stark D. P., et al., 2016, Monthly Notices of the Royal Astronomical Society, 464, 469

Stefanon M., Bouwens R. J., Labbé I., Muzzin A., Marchesini D., Oesch P., Gonzalez V., 2017, ApJ, 843, 36

Stefanon M., Bouwens R. J., Labbé I., Illingworth G. D., Gonzalez V., Oesch P. A., 2021, The Astrophysical Journal, 922, 29

Steidel C. C., Giavalisco M., Pettini M., Dickinson M., Adelberger K. L., 1996, ApJ, 462, L17

Steinhardt C. L., Sneppen A., Clausen T., Katz H., Rey M. P., Stahlschmidt J., 2023, The Highest-Redshift Balmer Breaks as a Test of ΛCDM (arXiv:2305.15459)

Steinwandel U. P., Bryan G. L., Somerville R. S., Hayward C. C., Burkhart B., 2023, MNRAS, 526, 1408

Su K.-Y., et al., 2018, Monthly Notices of the Royal Astronomical Society, 480, 1666

Sukhbold T., Ertl T., Woosley S., Brown J. M., Janka H.-T., 2016, The Astrophysical Journal, 821, 38

Sun G., Faucher-Giguère C.-A., Hayward C. C., Shen X., Wetzel A., Cochrane R. K., 2023b, Bursty Star Formation Naturally Explains the Abundance of Bright Galaxies at Cosmic Dawn (arXiv:2307.15305)

Sun G., Faucher-Giguère C.-A., Hayward C. C., Shen X., 2023a, Seen and unseen: bursty star formation and its implications for observations of high-redshift galaxies with JWST (arXiv:2305.02713)

Sun W., Ho L. C., Zhuang M.-Y., Ma C., Chen C., Li R., 2023c, The Structure and Morphology of Galaxies during the Epoch of Reionization Revealed by JWST (arXiv:2308.09076)

Susa H., Umemura M., 2004, The Astrophysical Journal, 610, L5–L8

Suto Y., Cen R., Ostriker J. P., 1992, ApJ, 395, 1

Tacchella S., Bose S., Conroy C., Eisenstein D. J., Johnson B. D., 2018, The Astrophysical Journal, 868, 92

Tacchella S., et al., 2022, Monthly Notices of the Royal Astronomical Society, 513, 2904

Tacchella S., et al., 2023, The Astrophysical Journal, 952, 74

Tanaka T., Hasegawa K., 2021, Monthly Notices of the Royal Astronomical Society, 502, 463–471

Tang M., et al., 2023a, JWST/NIRSpec Spectroscopy of $z = 7 - 9$ Star Forming Galaxies with CEERS: New Insight into Bright Lyα Emitters in Ionized Bubbles (arXiv:2301.07072)

Tang M., et al., 2023b, MNRAS, 526, 1657

Tang M., Stark D. P., Topping M. W., Mason C., Ellis R. S., 2024, arXiv e-prints, p. arXiv:2408.01507

Tarantino E., et al., 2021, ApJ, 915, 92

Tashiro M., Nishi R., 2000, The Astrophysical Journal, 536, 277–283

Taylor G., 1950, Proceedings of the Royal Society of London Series A, 201, 159

Tegmark M., Silk J., Rees M. J., Blanchard A., Abel T., Palla F., 1997, ApJ, 474, 1

Teyssier R., 2002, Astronomy & Astrophysics, 385, 337

Teyssier R., Commerçon B., 2019, Frontiers in Astronomy and Space Sciences, 6, 51

Thomas R. M., Zaroubi S., 2008, MNRAS, 384, 1080

Thompson T. A., Fabian A. C., Quataert E., Murray N., 2015, MNRAS, 449, 147

Thornton K., Gaudlitz M., Janka H.-T., Steinmetz M., 1998, The Astrophysical Journal, 500, 95

Thoul A. A., Weinberg D. H., 1996, ApJ, 465, 608

Tielens A. G. G. M., 2005, The Physics and Chemistry of the Interstellar Medium

Toomre A., 1977, in Tinsley B. M., Larson Richard B. Gehret D. C., eds, Evolution of Galaxies and Stellar Populations. p. 401

Toomre A., Toomre J., 1972, ApJ, 178, 623

Toro E. F., Spruce M., Speares W., 1994, Shock waves, 4, 25

Trac H., Chen N., Holst I., Alvarez M., Cen R., 2022, AMBER: Abundance Matching Box for the Epoch of Reionization, Astrophysics Source Code Library, record ascl:2211.003

Trebitsch M., Blaizot J., Rosdahl J., Devriendt J., Slyz A., 2017, Monthly Notices of the Royal Astronomical Society, 470, 224

Trebitsch M., Volonteri M., Dubois Y., Madau P., 2018, Monthly Notices of the Royal Astronomical Society, 478, 5607

Trebitsch M., et al., 2021, Astronomy & Astrophysics, 653, A154

Treu T., et al., 2023, The Astrophysical Journal Letters, 942, L28

Tripodi R., Lelli F., Feruglio C., Fiore F., Fontanot F., Bischetti M., Maiolino R., 2023, A&A, 671, A44

Tweed D., Devriendt J., Blaizot J., Colombi S., Slyz A., 2009, A&A, 506, 647

Uhlemann C., Rampf C., Gosenca M., Hahn O., 2019, Phys. Rev. D, 99, 083524

Vanzella E., et al., 2023, A&A, 678, A173

Vega-Ferrero J., et al., 2023, On the nature of disks at high redshift seen by JWST/CEERS with contrastive learning and cosmological simulations (arXiv:2302.07277)

Velázquez J. A. F., et al., 2020, Monthly Notices of the Royal Astronomical Society, 501, 4812

Ventura E. M., Qin Y., Balu S., Wyithe J. S. B., 2024, Semi-analytic modelling of Pop. III star formation and metallicity evolution – I. Impact on the UV luminosity functions at z = 9-16 (arXiv:2401.07396), https://arxiv.org/abs/2401.07396

Verhamme A., Dubois Y., Blaizot J., Garel T., Bacon R., Devriendt J., Guiderdoni B., Slyz A., 2012, A&A, 546, A111

Verhamme A., Orlitová I., Schaerer D., Hayes M., 2015a, A&A, 578, A7

Verhamme A., Orlitová I., Schaerer D., Hayes M., 2015b, A&A, 578, A7

Verhamme A., Orlitová I., Schaerer D., Izotov Y., Worseck G., Thuan T. X., Guseva N., 2017, A&A, 597, A13

Verner D. A., Ferland G. J., Korista K. T., Yakovlev D. G., 1996, ApJ, 465, 487

Vogelsberger M., Marinacci F., Torrey P., Puchwein E., 2020, Nature Reviews Physics, 2, 42

Vudragović A., Petraš I., Jovanović M., Knežević S., Samurović S., 2022, Astronomy & Astrophysics, 662, A17

Walch S., et al., 2015, MNRAS, 454, 238

Walker A. G., 1937, Proceedings of the London Mathematical Society, 42, 90

Wang B., Heckman T. M., Leitherer C., Alexandroff R., Borthakur S., Overzier R. A., 2019, ApJ, 885, 57

Wang F., et al., 2020, ApJ, 896, 23

Wang T., et al., 2024, The true number density of massive galaxies in the early Universe revealed by JWST/MIRI (arXiv:2403.02399), https://arxiv.org/abs/2403.02399

Weaver T. A., Zimmerman G. B., Woosley S. E., 1977, Presupernova evolution of massive stars

Weaver J. R., et al., 2023, Astronomy & Astrophysics, 677, A184

White S. D. M., Rees M. J., 1978, MNRAS, 183, 341

White S. D. M., Frenk C. S., Davis M., Efstathiou G., 1987a, ApJ, 313, 505

White S. D. M., Davis M., Efstathiou G., Frenk C. S., 1987b, Nature, 330, 451

Whitler L., Stark D. P., Endsley R., Chen Z., Mason C., Topping M. W., Charlot S., 2023, Insight from JWST/NIRCam into galaxy overdensities around bright Lyα emitters during reionization: implications for ionized bubbles at $z \sim 9$ (arXiv:2305.16670)

Whitney B. A., 2011, Bulletin of the Astronomical Society of India, 39, 101

Willott C. J., et al., 2010, The Astronomical Journal, 140, 546–560

Wise J. H., 2019, Contemporary Physics, 60, 145–163

Wise J. H., Abel T., 2008, The Astrophysical Journal, 685, 40

Wise J. H., Cen R., 2009, ApJ, 693, 984

Wise J. H., Turk M. J., Norman M. L., Abel T., 2011, The Astrophysical Journal, 745, 50

Wise J. H., Abel T., Turk M. J., Norman M. L., Smith B. D., 2012, Monthly Notices of the Royal Astronomical Society, 427, 311

Wisotzki L., et al., 2018, Nature, 562, 229

Wootten A., Thompson A. R., 2009, Proceedings of the IEEE, 97, 1463

Wright T., 1750, An original theory or new hypothesis of the universe : founded upon general phaenomena of the visible creation; and particularly the Via the laws of nature, and solving by mathematical principles : the Lactea ...compris'd in nine familiar letters from the author to his friendand : illustrated with upward of thirty graven and mezzotinto plates ..., doi:10.3931/e-rara-28672.

Wright A. H., et al., 2017, MNRAS, 470, 283

Wu X., McQuinn M., Kannan R., D'Aloisio A., Bird S., Marinacci F., Davé R., Hernquist L., 2019, MNRAS, 490, 3177

Xu H., Norman M. L., O'Shea B. W., Wise J. H., 2016, The Astrophysical Journal, 823, 140

Yang J., et al., 2020, The Astrophysical Journal, 897, L14

Yeh J. Y. C., et al., 2023, MNRAS, 520, 2757

Yoshii Y., Sabano Y., 1980, PASJ, 32, 229

Yuan Y., Martin-Alvarez S., Haehnelt M. G., Garel T., Sijacki D., 2024, MNRAS, 532, 3643

Zackrisson E., Inoue A. K., Jensen H., 2013, The Astrophysical Journal, 777, 39

Zaroubi S., 2012, The Epoch of Reionization. Springer Berlin Heidelberg, p. 45–101, doi:10.1007/978-3-642-32362-1˙2, http://dx.doi.org/10.1007/978-3-642-32362-1_2

Zhang Y., Ouchi M., Nakajima K., Harikane Y., Isobe Y., Xu Y., Ono Y., Umeda H., 2023, Statistics for Galaxy Outflows at $z \sim 6-9$ with Imaging and Spectroscopic Signatures Identified with JWST/NIRCam and NIRSpec Data (arXiv:2306.07940)

Zheng Z., Miralda-Escudé J., 2002, ApJ, 578, 33

Zheng Z.-Y., Malhotra S., Rhoads J. E., Finkelstein S. L., Wang J.-X., Jiang C.-Y., Cai Z., 2016, ApJS, 226, 23

Zhu Y., et al., 2022, ApJ, 932, 76

Zwicky F., 1933, Helvetica Physica Acta, 6, 110

Zwicky F., 1937, ApJ, 86, 217

da Cunha E., et al., 2013, The Astrophysical Journal, 766, 13

de Graaff A., et al., 2023, Ionised gas kinematics and dynamical masses of $z \gtrsim 6$ galaxies from JADES/NIRSpec high-resolution spectroscopy (arXiv:2308.09742)

van Haarlem M. P., et al., 2013, A&A, 556, A2

Acknowledgements

I am deeply thankful to my supervisor Benedetta Ciardi, for not only giving me a job when no one else did but also for her constant support and guidance over the last $\sim$7 years. Her constant reminders to stay the course and not get distracted by the next cool project along with being supportive during Covid lockdown and my numerous injuries was of tremendous help to keep up good spirits and stay motivated. I am also deeply grateful to Tiago Costa for adopting me after my first project crashed, teaching me how to use `RAMSES-RT`, the ways of being a good simulator and instilling a level of thoroughness which has helped me develop as a scientist.

I also extend a great deal of gratitude to Rüdiger Pakmor for motivating me, helping me use HPC systems and teaching good computing practices that ultimately were crucial toward running my simulations. And to Volker Springel and Klaus Dolag for examining my thesis. Many thanks go to the wonderful roster of secretaries at MPA: Maria, Gabi, Sonja, Cornelia, Solvejg, Isabel and Lena; whose hard work made bureaucratic life easy and ensured lack of headaches outside of the PhD itself.

Surviving the pandemic and carrying out my research would not have been possible without an absolutely amazing group of friends who I have found myself surrounded by. I'm thankful for Christian for doing interior design in my office every second day and for being a cocktail enthusiast. Miha for always being up for something and Miha things, Enrico, Daniela and Adam for the epic hike and always being supportive during the best and the worst times. A huge deal of gratitude to Maria W. for all the epic adventures in Munich and at conferences. Tiago for the amusing stories, fun chats and great recommendations for everything from restaurants to perfumes. Big thanks to Alex, Teresa, Hitesh and for the good vibes, fun parties, foosball and listening to me rant all the time. Anna, Tiara for always being down for a beer at 3 PM on a Wednesday and of course, karaoke. Benny for being my metaphorical mother and bringing me fruits during my thesis writing. I'm very thankful for Eileen and for her constant support and encouragement, all the amazing discussions and for reminding me to drink my coffee.

Finally, I want to thank my parents and my brother for their encouragement and unwavering support throughout my PhD. You've helped me get to this level of success.